

University of Strathclyde

Department of Naval Architecture, Ocean and
Marine Engineering

**Development of Computational and
Experimental Techniques
to Investigate the Effect of Biofouling on
Ship Hydrodynamic Performance**

Soonseok Song

A thesis presented in fulfilment of the
requirements for the degree of Doctor of
Philosophy

2020

This thesis is the result of the author's original research. It has been composed by the author and has not been previously submitted for examination which has led to the award of a degree.

The copyright belongs to the author under the terms of the United Kingdom Copyright Acts as qualified by University of Strathclyde Regulation 3.50. Due acknowledgement must always be made of the use of any material contained in, or derived from, this thesis.

Signed:

Date:

Acknowledgements

I have spent the most important time of my life during my PhD study in Glasgow. The journey was not always easy, with many ups and downs, sometimes with sunshine but also with many occasional rains. Without a doubt, it would not have been possible to reach the end of this journey without the help of the people that I would like to acknowledge.

First of all, my deep gratitude goes to my first supervisor, mentor, and all-around role model, Doctor Yigit Kemal Demirel, for giving me the opportunity of the PhD study. I appreciate him for not only supervising my PhD study, but also for mentoring me for the past two and half years to prepare myself for the academic environment, by giving additional opportunities and responsibilities. His constant support, patience, and encouragement drove me to keep on track and finish this journey on time.

I would like to express my appreciation to my second supervisor, Professor Mehmet Atlar for his unconditional support, advice and insights. His valuable inspirations and encouragement helped me to move forward. I would like to thank my ex-supervisor Professor Sang-Hyun Kim for his encouragement and constant guidance with care.

I would also like to thank Professor Sandy Day and the staffs at the Kelvin Hydrodynamics Laboratory, Steven Black, Grant Dunning, Bill Wright, and Rebecca McEwan. Without their support, I could not have finished my experiments safely. My acknowledgement extends to my colleague and friends for their continuous support during my days in Glasgow: Doctor Saishuai Dai (a.k.a David), Alessandro Marino, Kaan Ilter, Margot Cocard, Roberto Ravenna.

I would like to express my deepest gratitude to my mother and father, Mi-Ja Bae, and Jae-Ha Song, for their unyielding supports and belief in me. Without their dedication, I could not finish this journey.

Last, but certainly not least, I would like to thank the best friend of my life, the rock of my family, the love of my life, my wife, Solip, for her unconditional love and support. Of course, I love you too, my lovely dog, Soondori.

Contents

List of Figures.....	viii
List of Tables.....	xvii
Abstract	xx
1. Introduction.....	1
1.1. Introducton	1
1.2. General perspectives	1
1.3. Motivations.....	5
1.4. Research aim and objectives	7
1.5. Structure of the thesis.....	9
1.6. Chapter summary.....	11
2. Literature review	12
2.1. Introduction	12
2.2. Marine biofouling.....	13
2.2.1. Definition of biofouling	13
2.2.2. Microfouling.....	14
2.2.3. Macrofouling.....	15
2.3. Fouling-control coatings	17
2.4. The effect of biofouling on ship performance.....	21
2.4.1. On ship resistance.....	21
2.4.2. On propeller performance	26
2.5. Roughness effect on turbulent flow	29
2.5.1. Turbulent boundary layer.....	29
2.5.2. Roughness effect in the turbulent boundary layer	34
2.5.3. Determination of roughness functions.....	37

2.6.	Prediction methods for the roughness effect on full-scale ship resistance ..	43
2.6.1.	Boundary layer similarity law analysis.....	43
2.6.2.	Application of CFD	44
2.7.	Prediction methods for the roughness effect on propulsion performance ...	47
2.8.	Literature gap identification	49
2.9.	Chapter summary and conclusion.....	51
3.	Methodology.....	52
3.1.	Introduction	52
3.2.	Methodology	52
3.3.	Chapter summary.....	55
4.	Experimental and theoretical investigation into the roughness effect on ship resistance	56
4.1.	Introduction	56
4.2.	Methodology	58
4.2.1.	Approach.....	58
4.2.2.	Experimental setup	59
4.2.3.	Roughness function determination	63
4.2.4.	Granville’s boundary layer similarity law scaling.....	65
4.2.5.	Uncertainty analysis.....	66
4.3.	Results.....	67
4.3.1.	Flat plate towing test.....	67
4.3.2.	Model ship towing test.....	68
4.3.3.	Roughness function determination	70
4.3.4.	Extrapolation of the frictional resistance	72
4.3.5.	Prediction of the total resistance and comparison with the experimental data	74

4.4.	Chapter summary and conclusions	76
5.	Validation of the CFD method for predicting the roughness effect.....	78
5.1.	Introduction	78
5.2.	Methodology	79
5.2.1.	Approach.....	79
5.2.2.	Mathematical formulations	80
5.2.3.	Modified wall-function approach.....	82
5.2.4.	Roughness function model.....	82
5.2.5.	Geometry and boundary conditions.....	84
5.2.6.	Mesh generation	86
5.2.7.	Uncertainty analysis.....	87
5.3.	Results.....	91
5.3.1.	Validation against experiment.....	91
5.3.2.	Effect of hull roughness on the ship resistance components	94
5.3.3.	Effect of hull roughness on the flow characteristics.....	98
5.4.	Chapter summary and conclusions	104
6.	CFD prediction of the effect of biofouling on full-scale ship resistance	106
6.1.	Introduction	106
6.2.	Methodology	107
6.2.1.	Approach.....	107
6.2.2.	Roughness function of barnacles.....	108
6.2.3.	Numerical modelling	110
6.2.4.	Mesh generation	112
6.3.	Verification and validation.....	113
6.3.1.	Verification study	113
6.3.2.	Validation study.....	116

6.4.	Results.....	118
6.4.1.	Total resistance and effective power	118
6.4.2.	Frictional resistance and residuary resistance	119
6.4.3.	Viscous pressure and wave-making resistance	122
6.4.4.	Contribution of resistance components.....	124
6.4.5.	Wave profile.....	125
6.4.6.	Pressure distribution	126
6.4.7.	Velocity field.....	128
6.4.8.	Nominal wake.....	131
6.5.	Chapter summary and conclusions	133
7.	CFD prediction of the effect of biofouling on full-scale propeller performance...	135
7.1.	Introduction	135
7.2.	Methodology	137
7.2.1.	Approach.....	137
7.2.2.	Modified wall-function approach for barnacle fouling.....	138
7.2.3.	Numerical modelling	138
7.2.4.	Mesh generation	140
7.3.	Verification and validation.....	142
7.3.1.	Verification study	142
7.3.2.	Validation study.....	143
7.4.	Results.....	144
7.4.1.	Roughness effect on the open water coefficients	144
7.4.2.	Roughness effect on flow characteristics.....	150
7.5.	Chapter summary and conclusions	156

8.	CFD prediction of the effect of biofouling on ship self-propulsion performance .	158
8.1.	Introduction	158
8.2.	Methodology	159
8.2.1.	Approach.....	159
8.2.2.	Modified wall-function approach for barnacle fouling.....	160
8.2.3.	Numerical modelling	160
8.2.4.	Fouling conditions	163
8.2.5.	Propeller controller.....	164
8.3.	Verification and validation study	166
8.3.1.	Verification study	166
8.3.2.	Validation study.....	168
8.4.	The effect of biofouling on ship self-propulsion characteristics.....	174
8.4.1.	Effect on total resistance coefficient.....	176
8.4.2.	Effect on propeller rotational speed.....	179
8.4.3.	Effect on thrust and torque coefficients	180
8.4.4.	Effect on advance coefficient.....	182
8.4.5.	Effect on thrust deduction factor	183
8.4.6.	Effect on wake fraction.....	184
8.4.7.	Effect on relative rotative efficiency and open water efficiency.....	185
8.4.8.	Effect on hull efficiency and behind-hull efficiency	186
8.4.9.	Effect on propulsive efficiency	188
8.4.10.	Power penalty	189
8.5.	The effect of biofouling on flow characteristics.....	192
8.5.1.	Effect on velocity distribution.....	192
8.5.2.	Effect on surface pressure	194

8.5.3.	Effect on wave pattern	196
8.5.4.	Effect on vorticity field.....	197
8.6.	Chapter summary and conclusions	198
9.	Effect of heterogeneous distribution of hull roughness on ship resistance	200
9.1.	Introduction	200
9.2.	Methodology	201
9.2.1.	Approach.....	201
9.2.2.	Experimental setup	203
9.2.3.	Uncertainty analysis.....	205
9.3.	Result	206
9.3.1.	Verification of model symmetry.....	206
9.3.2.	Effect of heterogeneous hull roughness.....	207
9.3.3.	Rationale of the differences	209
9.4.	New prediction method for heterogeneous hull roughness.....	211
9.4.1.	Resistance prediction and comparison against EFD.....	212
9.5.	Chapter summary and conclusions	216
10.	Fouling effect on resistance of different ship types	218
10.1.	Introduction.....	218
10.2.	Methodology	219
10.2.1.	Approach	219
10.2.2.	Modified wall-function approach for barnacle fouling	220
10.2.3.	Numerical modelling.....	221
10.2.4.	Mesh generation.....	225
10.3.	Result.....	226
10.3.1.	Verification study.....	226
10.3.2.	Double-body simulations.....	228

10.3.3.	Free-surface simulations.....	234
10.3.4.	Roughness effect on the flow field	240
10.4.	Chapter summary and conclusions.....	248
11.	Conclusions and discussions.....	249
11.1.	Introduction.....	249
11.2.	Achievement of research aim and objectives	249
11.3.	Main conclusions	253
11.4.	Novelties and contributions	255
11.5.	General discussion	257
11.6.	Recommendations for future research.....	259
11.7.	Research outputs	261
References	264

List of Figures

Figure 2.1 Classification of marine fouling types, adapted from Atlar (2008)	13
Figure 2.2 Formation of biofilm, adapted from Chambers et al (2006)	15
Figure 2.3 Typical macroorganisms, adapted from Bressy and Lejars (2014)	16
Figure 2.4 Comparison of the performance and price of the key biocidal antifouling coatings, adapted from Atlar (2008).....	20
Figure 2.5 Resistance of destroyer ‘Yudachi’ towed at different speeds after various periods, adapted from Redfield et al. (1952).....	22
Figure 2.6 Testing panels installed on twin strut assembly (left) and the strut system deployed under the moon-pool plug of the research vessel (right), adapted from Chang et al. (2019).....	26
Figure 2.7 The efficiency of a model propeller in the smooth condition and after roughening by stippling a wet paint coating, adapted from McEntee (1916).....	27
Figure 2.8 Boundary layer at a flat plate at zero incidences, adapted from Schlichting (2017).....	30
Figure 2.9 Sketch of laminar-turbulent transition in the boundary layer on a flat plate, adapted from White (2006)	31
Figure 2.10 Velocity profile in a typical turbulent boundary layer, adapted from Shapiro (2004)	32
Figure 2.11 Velocity profile on smooth and rough walls, adapted from Shapiro (2004)	34
Figure 2.12 Collapse of velocity defect profiles for different surfaces, adapted from Schultz and Flack (2009)	36
Figure 2.13 Local method with displacement thickness, adapted from Granville (1987)	38
Figure 2.14 Local method without displacement thickness, adapted from Granville (1987).....	39
Figure 2.15 Overall method, adapted from Granville (1987)	41
Figure 2.16 Indirect method for pipe flow, adapted from Granville (1987).....	42
Figure 3.1 Methodology followed in the thesis.....	53
Figure 4.1 Schematic illustration of the methodology in Chapter 4.....	59

Figure 4.2 The towing carriage of the Kelvin Hydrodynamics Laboratory.....	60
Figure 4.3 Experimental setup for flat plate towing test.....	61
Figure 4.4 Flat plate used in this study, (a) smooth condition, (b) rough condition ..	61
Figure 4.5 Experimental set up for model ship towing test	63
Figure 4.6 KCS model used in this study (a) smooth condition, (b) rough condition	63
Figure 4.7 Schematic of Granville’s similarity law scaling procedure.....	66
Figure 4.8 C_T and C_F values of the flat plate in smooth and rough conditions	68
Figure 4.9 C_T values of the model ship in smooth and rough conditions	69
Figure 4.10 τ and σ values for the model ship in smooth and rough conditions.....	70
Figure 4.11 Roughness functions, based on the different choices of the representative roughness height	71
Figure 4.12 $C_{F,r}$ values for the rough plate and the extrapolated $C_{F,r}$ for the rough KCS model using Granville’s similarity law scaling	73
Figure 4.13 C_T and C_F values for the model ship in smooth and rough conditions ...	73
Figure 4.14 $C_{T,r}$ values predicted from the two different methods, and those measured from the model ship towing test	76
Figure 5.1 Schematic illustration of the methodology in Chapter 5.....	80
Figure 5.2 Experimental roughness function of the sand-grain surface and the proposed roughness function model	83
Figure 5.3 The dimensions and boundary conditions for the flat plate simulation model, (a) the flat plate, (b) profile view, (c) top view	84
Figure 5.4 Computational domain and boundary conditions of the KCS model ship simulation, (a) double-body simulation, (b) free-surface simulation	86
Figure 5.5 Volume mesh of the flat plate simulation	87
Figure 5.6 Volume mesh of the KCS model ship simulation.....	87
Figure 5.7 Total resistance coefficient, C_T , of the towed flat plate in the smooth and rough surface conditions, predicted from the current CFD simulations and the results of the towing test in Chapter 4	92
Figure 5.8 Total resistance coefficient, C_T , of the KCS model ship in the smooth and rough surface conditions, predicted from the current CFD simulations and the results of the towing test in Chapter 4	93

Figure 5.9 C_F and C_R values of the KCS model in the smooth and rough surface conditions	96
Figure 5.10 C_R , C_{VP} and C_W values of the KCS model in the smooth and rough surface conditions	98
Figure 5.11 Mean axial velocity contours at $y = 0.006L_{pp}$	100
Figure 5.12 Mean axial velocity contours at $x = 0.0175L_{pp}$	100
Figure 5.13 Boundary layer representation by slices limited to axial velocity ($V_x/ V_{model} = 0.9$)	101
Figure 5.14 Local wake fraction, wn' , at the propeller plane	101
Figure 5.15 Pressure distribution on the KCS model ship	102
Figure 5.16 Wave pattern around the KCS model	103
Figure 5.17 Wave elevation along a line with constant $y = 0.1509L_{pp}$	103
Figure 6.1 Schematic illustration of the methodology in Chapter 6	108
Figure 6.2 The dimensions and boundary conditions for the full-scale flat plate simulation model, (a) the plate, (b) profile view of the computational domain, (c) top view of the computational domain	112
Figure 6.3 Volume mesh of full-scale KCS hull simulation model, (a) top view, (b) profile view, (c) stern refinement, (d) bow refinement	113
Figure 6.4 C_T values of flat plates towed with different fouling conditions obtained from the simulations and the experiments by Demirel et al. (2017a), (a) $Rn=2.79E+06$, (b) $Rn=3.19E+06$, (c) $Rn=4.51E+06$, (d) $Rn=4.70E+06$	116
Figure 6.5 C_T values obtained by the full-scale CFD simulations	118
Figure 6.6 C_F values obtained by the full-scale CFD simulations and Granville's similarity law extrapolation at (a) 24knots and (b) 19knots	121
Figure 6.7 Residuary resistance coefficients versus roughness heights, obtained from full-scale KCS hull simulations at 24 knots and 19 knots	122
Figure 6.8 Comparison of the residuary resistance, viscous pressure resistance and wave-making resistance versus the representative roughness height of the fouling conditions, (a) 24 knots, (b) 19 knots	123
Figure 6.9 Percentage bar diagram of the resistance components, at (a) 24 knots, (b) 19 knots	125

Figure 6.10 Wave profile along a line with constant $y = 0.1509L_{pp}$ for smooth and fouled (B20%) cases, (a) full-scale, (b) model-scale.....	126
Figure 6.11 Pressure distribution on the KCS hull, (a) smooth case, (b) fouled case (B20%), (c) difference (rough-smooth), at 24 knots	127
Figure 6.12 Pressure distribution on the plane with constant $y = 0.006L_{pp}$, (a) smooth case, (b) fouled case (B20%), at 24 knots.....	128
Figure 6.13 Boundary layer represented by slices limited to $V_x/ V_{model} = 0.9$, (a) smooth case, (b) fouled case (B20%)	129
Figure 6.14 Contours of mean axial velocity at $y = 0.006L_{pp}$, (a) smooth case, (b) fouled case, at 24 knots	130
Figure 6.15 Contours of mean axial velocity at $x = 0.0175L_{pp}$, (a) smooth case, (b) fouled case, at 24 knots	130
Figure 6.16 Nominal wake distribution, w'_x , and transvers velocity vector, V_{xy} , at the propeller plane in smooth and fouled cases, at 24 knots.....	132
Figure 7.1 Schematic illustration of the methodology in Chapter 7.....	137
Figure 7.2 KP505 propeller.....	139
Figure 7.3 Computational domain and boundary conditions of the simulation model	140
Figure 7.4 Grid system of KP505 simulation.....	141
Figure 7.5 Comparison of the propeller open water curves obtained from the current CFD and EFD (Fujisawa et al., 2000).....	144
Figure 7.6 Thrust coefficients decreasing with the level of surface fouling.....	145
Figure 7.7 Torque coefficients increasing with the level of surface fouling.....	146
Figure 7.8 Propeller efficiency decreasing with the level of surface fouling	147
Figure 7.9 Comparison of the Propeller open water curves in smooth and rough (B20%) conditions	148
Figure 7.10 Contribution of the thrust coefficient components, at $J=0.7$	149
Figure 7.11 Contribution of the torque coefficient components, at $J=0.7$	149
Figure 7.12 Pressure distribution on $y=0$ plane, at $J=0.7$	150
Figure 7.13 Pressure distribution on the propeller surface, at $J=0.7$	151
Figure 7.14 Wall Shear stress coefficients, at $J=0.7$	152
Figure 7.15 Axial velocity on $y = 0$ plane, at $J=0.7$	153

Figure 7.16 Transverse velocity on $y = 0$ plane, at $J=0.7$	153
Figure 7.17 Vorticity magnitude on $y = 0$ plane, at $J=0.7$	155
Figure 7.18 Isosurface of Q-criterion, at $J=0.7$	155
Figure 8.1 Schematic illustration of the methodology in Chapter 8.....	160
Figure 8.2 Geometry of the KCS with rudder and propeller.....	161
Figure 8.3 Computational domain and boundary conditions used in Chapter 8	162
Figure 8.4 Volume mesh and surface of the simulation model (a) two view, (b) profile view, (c) rear view, (d) stern, (e) bow.....	163
Figure 8.5 Rotational speed of the propeller controlled by the PI controller.....	165
Figure 8.6 Schematic diagram of the process of the validation study	169
Figure 8.7 Total resistance coefficient, C_T , values obtained from the present CFD simulation (model-scale without a rudder), and EFD (Hino, 2005), and other CFD results from the CFD workshop Tokyo 2015.....	170
Figure 8.8 Propeller rotational speed, n , values obtained from the present CFD simulation (model-scale without a rudder), and EFD (Hino, 2005), and other CFD results from the CFD workshop Tokyo 2015.....	170
Figure 8.9 Thrust coefficient, K_T , values obtained from the present CFD simulation (model-scale without a rudder), and EFD (Hino, 2005), and other CFD results from the CFD workshop Tokyo 2015	171
Figure 8.10 Torque coefficient, K_Q , values obtained from the present CFD simulation (model-scale without a rudder), and EFD (Hino, 2005), and other CFD results from the CFD workshop Tokyo 2015	171
Figure 8.11 Geometries representing (a) KCS with a rudder and (b) and without a rudder	172
Figure 8.12 C_T , n , K_T and K_Q values at self-propulsion points obtained from the model-scale and full-scale simulations with and without a rudder.....	173
Figure 8.13 Self-propulsion parameters and propeller efficiencies at self-propulsion points obtained from the model-scale and full-scale simulations with and without a rudder	174
Figure 8.14 Total resistance coefficient, C_T , at self-propulsion point under the given fouling conditions, plotted against the representative roughness heights of the surface fouling conditions in Table 6.1.....	177

Figure 8.15 Frictional resistance coefficient, C_F , at self-propulsion point under the given fouling conditions, plotted against the representative roughness heights of the surface fouling conditions in Table 6.1	178
Figure 8.16 Residuary resistance coefficient, C_R , at self-propulsion point under the given fouling conditions, plotted against the representative roughness heights of the surface fouling conditions in Table 6.1	178
Figure 8.17 Propeller rotational speed, n , at self-propulsion point under the given fouling conditions, plotted against the representative roughness heights of the surface conditions in Table 6.1	179
Figure 8.18 Thrust coefficient, K_T , at self-propulsion point under the given fouling conditions, plotted against the representative roughness heights of the surface conditions in Table 6.1	181
Figure 8.19 Torque coefficient, K_Q , at self-propulsion point under the given fouling conditions, plotted against the representative roughness heights of the surface conditions in Table 6.1	181
Figure 8.20 Advance coefficient, J , at self-propulsion point under the given fouling conditions, plotted against the representative roughness heights of the surface conditions in Table 6.1	182
Figure 8.21 Thrust deduction factor, $1 - t$, at self-propulsion point under the given fouling conditions, plotted against the representative roughness heights of the surface fouling conditions in Table 6.1	184
Figure 8.22 Wake fraction, $1 - w_T$, at self-propulsion point under the given fouling conditions, plotted against the representative roughness heights of the surface fouling conditions in Table 6.1	185
Figure 8.23 Relative rotative efficiency, η_R , and propeller open water efficiency, η_O , at self-propulsion point under the given fouling conditions, plotted against the representative roughness heights of the surface fouling conditions in Table 6.1	186
Figure 8.24 Hull efficiency, η_H , and behind-hull propeller efficiency, $\eta_{H'}$, at self-propulsion point under the given fouling conditions, plotted against the representative roughness heights of the surface fouling conditions in Table 6.1	187

Figure 8.25 Propulsive efficiency, η_D , at self-propulsion point under the given fouling conditions, plotted against the representative roughness heights of the surface fouling conditions in Table 6.1	189
Figure 8.26 Required shaft power, SP , at self-propulsion point under the given fouling conditions, obtained from the current CFD and using the towed ship and propeller open water simulations (Chapter 6 and 7), plotted against the representative roughness heights of the surface fouling conditions in Table 6.1	191
Figure 8.27 Velocity contour of V_{xz}/V_{ship} at $y = 0.006L_{pp}$, (a) clean-hull/clean-propeller, (b) fouled-hull/clean-propeller, B20%, (c) clean-hull/fouled-propeller, B20%, (d) fouled-hull/fouled-propeller, B20%.....	193
Figure 8.28 Axial velocity contour of V_x/V_{ship} at $x = 0.0089L_{pp}$, (a) clean-hull/clean-propeller, (b) fouled-hull/clean-propeller, B20%, (c) clean-hull/fouled-propeller, B20%, (d) fouled-hull/fouled-propeller, B20%.....	193
Figure 8.29 Boundary layer represented by slices limited to the turbulent kinetic energy, (a) clean-hull/clean-propeller, (b) fouled-hull/clean-propeller, B20%, (c) clean-hull/fouled-propeller, B20%, (d) fouled-hull/fouled-propeller, B20%, (e) towed ship, clean-hull, (f) towed ship, fouled-hull, B20%	194
Figure 8.30 Surface pressure distribution at the stern (a) clean-hull/clean-propeller, (b) fouled-hull/clean-propeller, B20%, (c) clean-hull/fouled-propeller, B20%, (d) fouled-hull/fouled-propeller, B20%, (e) towed ship, clean-hull, (f) towed ship, fouled-hull, B20%.....	195
Figure 8.31 Wave pattern around the ship, (a) clean-hull/clean-propeller, (b) fouled-hull/clean-propeller, B20%, (c) clean-hull/fouled-propeller, B20%, (d) fouled-hull/fouled-propeller, B20%.....	196
Figure 8.32 Vorticity contour around the propeller (bottom-up view), (a) clean-hull/clean-propeller, (b) fouled-hull/clean-propeller, B20%, (c) clean-hull/fouled-propeller, B20%, (d) fouled-hull/fouled-propeller, B20%.....	197
Figure 9.1 Schematic illustration of the methodology in Chapter 9.....	202
Figure 9.2 Wigley model with different surface conditions.....	202
Figure 9.3 The towing carriage of the Kelvin Hydrodynamics Laboratory and the Wigley model; (a) ½-bow-rough condition, (b) ½-aft-rough condition	203
Figure 9.4 Experimental set up of the towing test	204

Figure 9.5 C_T values of smooth and full-rough conditions with different towing directions	207
Figure 9.6 C_T values of Wigley model in smooth and $\frac{1}{4}$ -rough condition	208
Figure 9.7 C_T values of Wigley model in smooth and $\frac{1}{2}$ -rough condition	208
Figure 9.8 Local skin friction on the flat plate along the line of $z = -2/T$ in smooth and (homogeneously) rough condition with the towing speed of $V = 4.5 \text{ m/s}$, obtained from the flat plate simulation in Chapter 5.	210
Figure 9.9 Roughness Reynolds number, k^+ , on the rough flat plate with the towing speed of $V = 4.5 \text{ m/s}$, obtained from the flat plate simulation in Chapter 5.	210
Figure 9.10 C_F predictions of the Wigley hull with different surface conditions	213
Figure 9.11 Form factor calculation based on the test data of Ju (1983).....	214
Figure 9.12 C_T values from the towing test and the predictions for the Wigley model with $\frac{1}{4}$ -rough condition.....	215
Figure 9.13 C_T values from the towing test and the predictions for the Wigley model with $\frac{1}{2}$ -rough condition.....	215
Figure 9.14 C_T values from the towing test and the predictions for the Wigley model with full-rough condition	216
Figure 10.1 Schematic illustration of the methodology in Chapter 10.....	220
Figure 10.2 Geometry of KCS hull with a rudder	222
Figure 10.3 Geometry of KVLCC2 hull with a rudder.....	222
Figure 10.4 Computational domain and the boundary conditions of KCS simulations	224
Figure 10.5 Computational domain and the boundary conditions of KVLCC2 simulations	225
Figure 10.6 Mesh structure of the computational domain of KCS and KVLCC2 simulations (free-surface models).....	226
Figure 10.7 C_F and C_V of KCS with different hull conditions at model ($\lambda=31.6$), moderate ($\lambda=10$) and full-scale ($\lambda=1$)	230
Figure 10.8 C_F and C_V of KVLCC2 with different hull conditions at model ($\lambda=58$), moderate ($\lambda=10$) and full-scale ($\lambda=1$)	230
Figure 10.9 k^+ on the hulls of KCS and KVLCC2 with B20% fouling condition.	231
Figure 10.10 $1 + k$ of KCS and KVLCC2 for different surface conditions.....	233

Figure 10.11 $\% \Delta C_F$ vs $\% \Delta C_{VP}$ due to the fouling conditions of KCS (left) and KVLCC2 (right)	233
Figure 10.12 C_T of KCS with different hull conditions	235
Figure 10.13 C_T of KVLCC2 with different hull conditions	235
Figure 10.14 C_T of KCS with different hull conditions	237
Figure 10.15 C_T of KVLCC2 with different hull conditions	237
Figure 10.16 C_{VP} and C_W of KCS with different hull conditions	239
Figure 10.17 C_{VP} and C_W of KVLCC2 with different hull conditions	239
Figure 10.18 Axial velocity (V_x/V_{ship}) around KCS hulls in different scales with smooth and B20% surface conditions (on $y = 0.006L_{pp}$)	241
Figure 10.19 Axial velocity (V_x/V_{ship}) around KVLCC2 hulls in different scales with smooth and B20% surface conditions (on $y = 0.006L_{pp}$)	241
Figure 10.20 Axial velocity (V_x/V_{ship}) behind KCS (left) and KVLCC2 (right) in different scales with smooth and B20% surface conditions (on $x = 0.0175L_{pp}$ plane)	242
Figure 10.21 Local wake fraction, w'_x , at the propeller plane of KCS in different scales with smooth and B20% surface conditions	242
Figure 10.22 Local wake fraction, w'_x , at the propeller plane of KVLCC2 in different scales with smooth and B20% surface conditions	243
Figure 10.23 Boundary layer represented by slices limited to axial velocity ($V_x/V_{ship} = 0.9$) around KCS hulls in different scales with smooth and B20% surface conditions	244
Figure 10.24 Boundary layer represented by slices limited to axial velocity ($V_x/V_{ship} = 0.9$) around KVLCC2 hulls in different scales with smooth and B20% surface conditions	244
Figure 10.25 Pressure coefficient on stern region of KCS in different scales with smooth and B20% surface conditions	245
Figure 10.26 Pressure coefficient on stern region of KVLCC2 in different scales with smooth and B20% surface conditions	246
Figure 10.27 Kelvin wave pattern around KCS hulls at low and high speeds with smooth (upper) and B20% (lower) surface conditions	247

Figure 10.28 Kelvin wave pattern around KCS hulls at low and high speeds with smooth (upper) and B20% (lower) surface conditions	247
--	-----

List of Tables

Table 2.1 Performance comparison for the key antifouling systems used, adapted from Chamber et al. (2006)	19
Table 2.2 Kempf's Roughness Coefficients (C_k), adapted from Redfield et al. (1952)	23
Table 4.1 Principal particulars of the KCS in full-scale adapted from Kim et al. (2001) and Larsson et al. (2013).....	62
Table 4.2 Overall uncertainties of the measurements with 95% confidence level, where τ and σ are trim and sinkage, respectively	67
Table 5.1 Principal particulars of the KCS in full-scale and model-scale, adapted from Kim et al. (2001) and Larsson et al. (2013)	85
Table 5.2 Parameters used for the discretisation error for the spatial convergence study, key variable: C_T	89
Table 5.3 Parameters used for the discretisation error for the temporal convergence study, key variable: C_T	90
Table 5.4 C_V , C_{VP} and k values obtained from the double-body simulations	97
Table 6.1 Roughness length scales of the barnacle fouling conditions, adapted from Demirel et al. (2017a)	109
Table 6.2 Parameters used for the calculation of the discretization error for the spatial convergence study, key variable: C_T	114
Table 6.3 Parameters of the calculation of the discretization error for the temporal convergence study, key variable: C_T	115
Table 6.4 C_T values obtained from the CFD simulations and the experiments (Demirel et al., 2017a; Kim et al., 2011)	117
Table 6.5 C_T values obtained from full-scale KCS hull simulation	119

Table 6.6 Comparison of the frictional resistance coefficients and the residuary resistance coefficients computed from the full-scale KCS hull simulations at 24 knots and 19 knots.....	121
Table 6.7 Form factor calculation from the double-body simulations	124
Table 6.8 Mean nominal wake fractions computed from the simulations	132
Table 7.1 Principal particulars of KP505 propeller	138
Table 7.2 Parameters used for the calculation of the discretization error for the spatial convergence study, key variable: K_T , $10K_Q$, and η_O	143
Table 8.1 Fouling conditions of different fouling scenarios and surface conditions	164
Table 8.2 Parameters used for the calculation of the discretisation error for the spatial convergence study.....	167
Table 8.3 Parameters used for the calculation of the discretisation error for the temporal convergence study	168
Table 8.4 Self-propulsion parameters obtained from the model-scale and full-scale simulations with and without a rudder.....	173
Table 8.5 Self-propulsion parameters under ‘fouled-hull/clean-propeller’ conditions	175
Table 8.6 Self-propulsion parameters under ‘clean-hull/fouled-propeller’ conditions	175
Table 8.7 Self-propulsion parameters under ‘fouled-hull/fouled-propeller’ conditions	175
Table 9.1 Principal particulars of the Wigley model and test conditions	204
Table 9.2 Overall uncertainties of C_T with 95% confidence level	205
Table 10.1 Principal particulars and conditions of the KCS simulations, adapted from Kim et al. (2001) and Larsson et al. (2013)	223
Table 10.2 Principal particulars and conditions of the KVLCC2 simulations, adapted from Kim et al. (2001) and Larsson et al. (2013).....	223
Table 10.3 Simulation cases.....	224
Table 10.4 Spatial and temporal convergence study of the KCS simulations	227
Table 10.5 Spatial and temporal convergence study of KVLCC2 simulations.....	228

Abstract

Hull and propeller roughness can be caused by various factors such as mechanical causes, chemical and electrochemical processes (e.g. corrosion), and finally the colonisation of biofouling, which is often the most critical. The associated economic and environmental problems include increases in ship resistance, fuel consumption, and greenhouse gas emissions. The mitigation measures are also associated with costly antifouling coatings and drydocking. Therefore, accurate predictions of the roughness effect on ship performance are of great importance in the economic and environmental perspectives.

Although many studies have been carried out to investigate the roughness effect since the age of William Froude, our understanding in this field is still limited. More specifically, the validations of the two most prevalent prediction methods are not complete. Also, the conventional studies have mainly focussed on the roughness effect on ship resistance, whereas the impact on propulsion performance has been less highlighted. Furthermore, the hull surfaces have been treated as uniformly rough in the conventional studies, while real ships' surfaces are not uniform as they are exposed to heterogeneous fouling accumulation.

Based on the above background, this PhD study aims to develop computational and experimental techniques to investigate the effect of biofouling on ship hydrodynamic performance. This aim has been realised by achieving several milestones using Computational Fluid Dynamics (CFD) and Experimental Fluid Dynamics (EFD).

This PhD thesis consists of three distinct parts. Part I includes experimental validations by means of tank testing to demonstrate the suitability of the methods for the added resistance prediction due to hull roughness: Granville's similarity law scaling method and the CFD method involving modified wall-functions.

Part II presents the full-scale applications of the CFD approach to predict the effect of biofouling on the full-scale ship hydrodynamic problems, including ship resistance, propeller performance and ship self-propulsion performance.

Finally, extended investigations are presented in Part III, including the investigations into the effect of heterogeneous distributions of hull roughness on ship resistance as well as the roughness effect with the variations of hull forms, ship lengths and speeds.

1. Introduction

1.1. Introduction

This chapter introduces the general perspectives of the subjects covered in this PhD thesis, presents the motivations behind the study, defines the aim and objectives of the study and finally outlines the structure of the thesis.

1.2. General perspectives

To meet the needs of the globalised world, there has been a rapid expansion of maritime transportation. According to the United Nations Conference on Trade and Development (UNCTAD, 2017), the seaborne trade volumes have more than tripled during the last four decades. While marine transport is considered as more fuel-efficient than other freight methods, its greenhouse gas emissions are still substantial and growing fast. The International Maritime Organization (IMO) forecasted maritime CO₂ emissions to increase by 50% to 250% in the period to 2050 depending on the scenarios of future economic and energy developments (IMO, 2014). Consequently, some regulations and recommended practices have been implemented in recent times to limit Green House Gas (GHG) emissions from ships; e.g. the Energy Efficiency Design Index (EEDI) for new ships and the Ship Energy Efficiency Management Plan (SEEMP) for all ships (IMO, 2011). Within this framework, the importance of energy efficient shipping is being highlighted.

When energy efficiency is concerned, the prediction of ships' in-service performance is important. It is because ships' energy efficiency can vary with different factors in operation, such as the loading conditions, weather, and hull surface conditions. In particular, the effect of hull roughness is known to increase the frictional resistance of ships. Considering that the frictional resistance often takes the largest portion of the total resistance, hull roughness can cause a significant efficiency loss (Schultz, 2007).

The surface roughness of a ship's hull and propeller increases by time due to various factors including mechanical causes (e.g. mechanical damage, sand-blasting, plate waviness, welds, mechanical damage to the marine coatings), chemical and electrochemical processes (i.e. corrosion), and finally the colonisation of biofouling, which is often the most critical (Townsin, 2003; Tezdogan and Demirel, 2014).

Marine biofouling is the undesirable growth of marine organisms on the surfaces of submerged or semi-submerged objects (Lewis, 1998). This inevitable process often begins with the accumulation of microfouling organisms, which forms sticky coatings commonly referred to as 'biofilms' (Gehrke and Sand, 2003). Biofilms do not only decrease the energy efficiency of ships, but also provide a rich basis for larger organisms (i.e. macrofouling), which can result in even more drastic impacts. In particular, the hard-shell fouling, i.e. barnacles, mussels and tubeworms, results in dramatic increases in the surface roughness. Therefore, its impact on ship performance is particularly critical and greatly dependent on the type and coverage of fouling (McEntee, 1915; Kempf, 1937; Schultz, 2004; 2007). Transportation of invasive species is another problem associated with biofouling. Some fouling species can remain alive during the journey of commercial vessels and be released to other ecosystems. These exotic species may survive to establish a reproductive population in the host environment, becoming invasive, out-competing native species and multiplying into pest proportions. Eventually, they can cause the extinction of some species and may harm biodiversity and/or transport various diseases (Ulman, 2019).

Considering the above mentioned economic and environmental penalties of biofouling, it is essential to mitigate the accumulation of biofouling on ship hulls. The most prevalent mitigation method is the application of antifouling paints on the hull surfaces. Most of the conventional antifouling paints contain toxic chemicals, which are often called as biocides. Toxic antifouling coatings are recognised as the most cost-effective over many types of antifouling methods, because of their advantages, such as ease of manufacture, high speed and low-cost application, durability, and applicability to a variety of structural forms and compositions (Little and Depalma, 1988). However, these biocides may also impact non-target species. Also, modern research revealed that

these chemicals contaminate the food chain and persist in the environment (Maréchal and Hellio, 2009).

The awareness of such environmental problems of the conventional antifouling coatings resulted in legislative measures, such as the ban of tributyltin (TBT) based antifouling paints in 2003 (IMO, 2001). The regulatory authorities now require testing of new active substance before marketing authorisation, and these new restrictions unavoidably resulted in significant increases in the total costs for the development of new antifouling coatings (Maréchal and Hellio, 2009). Consequently, the costs of antifouling activities are becoming more and more expensive.

Within this framework, from a naval architect or a ship owner's point of view, a proper life cycle assessment is now of great importance. In other words, the economic penalties associated with the increased fuel consumption and/or the speed loss of ships should be accurately predicted and compared with the costs associated with the antifouling activities.

Currently, there are two mainstream methods for assessing ship performance with biofouling:

- Extrapolating the roughness effect on frictional resistance using the similarity law scaling of Granville (1958, 1978)
- Modelling the roughness effect in Computational Fluid Dynamics (CFD) simulations

The similarity law scaling, which was proposed by Granville (1958, 1978), has been widely used to predict the roughness effect on ship frictional resistance. The benefit of using this method is that once the roughness function, ΔU^+ , of the surface is known, the skin friction with the same roughness can be extrapolated for flat plates with arbitrary lengths and speeds. Accordingly, many researchers used this method to predict the effect of hull fouling (Schultz, 2002, 2004, 2007; Flack and Schultz, 2010; Schultz et al., 2011; Demirel, 2015; Demirel et al., 2017a, 2019; Li et al., 2019; Uzun

et al., 2019, 2020). However, this method has several limitations due to its assumption of flat plate (Atlar et al., 2018). In other words, this method only considers the roughness effect on the frictional resistance. However, recent studies claim that the hull roughness not only affects the frictional resistance but also the other pressure-related resistance components (Demirel et al., 2017b; Farkas et al., 2018, 2019; Andersson et al., 2020). Therefore, it is now timely to revise the validity of Granville's method for predicting the effect of biofouling on ship resistance.

Recently, the use of CFD is considered as an effective alternative to predict the roughness effect on ship resistance, as it can overcome the shortcomings of Granville's method. The mainstream is using modified wall-functions by employing the roughness function in the CFD model (Demirel et al., 2014, 2017b; Vargas and Shan, 2016; Farkas et al., 2018, 2019; Seok and Park, 2020). However, the validations of these studies were merely performed against flat plates with zero pressure gradient. Therefore, it cannot guarantee the validity of it for other resistance components originating from the 3D shape of the hulls. Therefore, the validity of the CFD approach for 3D hulls still remains to be demonstrated.

Also, the investigations should be extended to increase our understanding in this field. The previous studies were mainly focussing on the effect of hull fouling on ship resistance. However, the roughness effect on the propulsion performance is also important for better predictions of the energy efficiency of ships in operation. Furthermore, there has been a major simplification in the conventional studies. That is, the hull surfaces have been treated as uniformly rough, while the real ships' surfaces are not uniform as they are exposed to heterogeneous fouling accumulation. This difference can introduce uncertainties in the added resistance predictions, as claimed by Demirel et al. (2017a).

1.3. Motivations

Before detailing the specific objectives of this PhD study, an overview of the general motivations is presented in this section.

- The accuracy of the roughness allowance formula of Townsin and Dey (1990) has been questioned since the 23rd ITTC meeting (ITTC, 2002) and one of the terms of reference for the 29th ITTC Resistance and Propulsion Committee is “*Investigate the need of change of standard hull and propeller roughness. Develop and propose new roughness correction methods for both hull and propeller*”. Therefore, it is essential to develop new experimental and computational techniques to contribute to this task.
- As will be discussed in Chapter 2, the predictions of the roughness effect on ship resistance have been performed mainly using either Granville’s similarity law scaling method or the CFD methods in recent studies. However, the validations of these methods are still incomplete. To the best of the author’s knowledge, there exists no specific study validating these prediction methods against experimental data obtained from tank testing using a ship model with a rough surface. Therefore, it is worthwhile to conduct ship model towing tests for validations of these prediction methods.
- There have been a few studies investigating the effect of biofouling on full-scale ship resistance using CFD. However, the investigations can be extended for better understanding. For example, the roughness effect on different resistance components can be examined, as well as the effect on other

hydrodynamic characteristics (e.g. form factor, nominal wake, etc). Also, analysis of the flow characteristics around the hull can be useful to correlate the findings.

- There have been only a few studies devoted to the roughness effect on propeller performance. The CFD method could be useful to determine the impact of propeller fouling. However, to the best of the author's knowledge, there exists no specific study to investigate the roughness effect on a full-scale marine propeller using CFD. This gap can be filled by performing CFD simulations.
- For more accurate predictions of ships' energy consumption, it is needed to investigate the hull-propeller-rudder interaction with the presence of biofouling. However, to the best of the author's knowledge, there exists no specific study investigating the effect of hull and/or propeller fouling on the power consumption and propulsion efficiency. Therefore, it is worthwhile to investigate the effect of hull and/or propeller fouling on full-scale ship self-propulsion performance using CFD.
- In the conventional studies, the hull surfaces have been treated as uniform rough surfaces while the real ships' hulls are exposed to heterogeneous fouling accumulation, which can result in differences. To the best of the author's knowledge, there is no specific study exists investigating the effect of the heterogeneous hull roughness on ship resistance. Therefore, conducting a ship model towing test with heterogeneous hull roughness can be effective to identify the effect of heterogeneous hull roughness.

- It is well known that different ships have different ship hydrodynamic characteristics. Therefore, the roughness effect can also vary with different ships. To the best of the author's knowledge, there exists no specific study investigating the differences between the roughness effects on different ships. Therefore, CFD simulations of different ships with hull fouling can be used to fill this gap.

1.4. Research aim and objectives

Based on the motivations given in the previous section, which will be supported further by the literature review in Chapter 2, the main aim of this PhD thesis is:

- To develop computational and experimental techniques to investigate the effect of biofouling on ship hydrodynamic performances

In order to achieve the above aim, the following objectives are specified:

- Objective 1: To conduct a literature survey to review the state-of-the-art literature and the background knowledge in the field of the effect of hull and propeller fouling on ship hydrodynamic performance (Chapter 2).
- Objective 2: To perform an experimental study using a towed flat plate and a ship model in smooth and rough surface conditions, to investigate the effect of hull roughness on ship resistance and also to validate the similarity law scaling of Granville (1958; 1978) (Chapter 3).

- Objective 3: To develop a CFD model to predict the effect of hull roughness on ship resistance and to perform a validation study by comparing the CFD prediction with the experimental result obtained from the ship model towing test (Chapter 5).
- Objective 4: To develop a CFD model of a full-scale towed ship to investigate the effect of biofouling on the resistance components and other hydrodynamic characteristics (Chapter 6).
- Objective 5: To develop a CFD model of a full-scale marine propeller to investigate the effect of propeller fouling on the propeller performance in open water (Chapter 7).
- Objective 6: To develop a CFD model of a full-scale self-propelled ship to investigate the effect of hull and/or propeller fouling on ship self-propulsion characteristics (Chapter 8).
- Objective 7: To perform an experimental study using a ship model with different configurations of hull roughness to investigate the effect of heterogeneous hull roughness on ship resistance and propose a new prediction method for heterogeneous hull fouling (Chapter 9).
- Objective 8: To perform CFD simulations of different hull forms in different scales and speeds to investigate the effect of hull fouling on different ships (Chapter 10).

1.5. Structure of the thesis

The structure of this PhD thesis is organised as follows:

Chapter 2 presents a comprehensive literature review on relevant topics including, a brief background of biofouling and marine coatings, historical observations of the roughness effect on ship performances, theoretical information regarding the roughness effect in the turbulent boundary layer, and the state-of-the-art literature in the field. The literature gaps are also identified.

Chapter 3 explains the general methodology used in the PhD thesis.

Chapter 4 presents an experimental investigation into the effect of hull roughness on ship resistance and provides a validation of the similarity law scaling, by using tank testing of a flat plate and a KRISO Container Ship (KCS) model. Both the plate and ship model were tested in smooth and rough (sand-grain) surface conditions. The roughness functions of the rough surface were derived by using the results of the flat plate towing tests. Using the obtained roughness function, the frictional resistance was extrapolated to the length of the ship model following the similarity law scaling procedure. The total resistance of the rough ship model was predicted using the extrapolated frictional resistance and the result of the smooth ship model and then compared with the results of the rough ship model.

Validation of the CFD approach for modelling the roughness effect on ship resistance is presented in Chapter 5. CFD models of the towed flat plate and the KCS model were developed and compared with the towing test results in Chapter 4. To represent the effect of hull roughness, the roughness function of the sand-grain surface, which was determined in Chapter 4, was employed in the wall-function of the CFD model. The result of the CFD simulations was compared with the experimental result, to validate the CFD approach.

Full-scale applications of the CFD approach (i.e. modified wall-function approach) are presented in Chapters 6-8. In Chapter 6, the roughness function of barnacles (Demirel

et al., 2017a) was employed in the wall-function of the CFD model to represent the surface roughness of barnacle fouling with varying barnacle sizes and coverage densities. For validation of the modified wall-function approach, towed-flat plate simulations were carried out and compared against the experimental data. The modified-wall function approach was then applied to full-scale ship hydrodynamic problems (i.e. towed KCS, KP505 propeller in open water, and self-propelled KCS). From the full-scale KCS simulations in Chapter 6, the effect of barnacle fouling was examined on the ship resistance components, form factors and wake fractions as well as the flow characteristics around the hull. From the full-scale KP505 propeller simulations in Chapter 7, the effect of barnacles on the propeller open water performance was predicted. In Chapter 8, full-scale KCS self-propulsion simulations were conducted with various configurations of hull and/or propeller fouling. The effects of barnacle fouling on the ship resistance, delivered power and other propulsion efficiencies were investigated.

Chapter 9 involves towing tests of a ship model of the Wigley hull with heterogeneous hull roughness. The differences in the added resistance between the heterogeneous hull roughness conditions were discussed. Also, a new prediction method was proposed to predict the added resistance due to the heterogeneous hull roughness based on Granville's similarity law scaling and the predictions were compared with the experimental result.

Chapter 10 presents the extension of the CFD approach for better understanding of the fouling effect on ship resistance performance. Using the same CFD approach as in Chapter 6-8, ship resistance simulations were conducted using two different hull forms, KRISO Containership (KCS) and KRISO Tanker (KVLCC2). Each hull form was modelled in three different scales (i.e. model-scale, moderate-scale and full-scale) with a range of Froude numbers. From the simulations, the effect of hull fouling on ship hydrodynamic characteristics was investigated for the different ships, scales and speeds.

Finally, Chapter 11 provides a comprehensive summary of this PhD thesis, including the achievement of the research aim and objectives, main conclusions, novelties and contributions to the field, and the recommended future works.

1.6. Chapter summary

The general perspectives, the motivations behind the PhD study, the aim and objectives, and the structure of the thesis have been presented in this chapter.

2. Literature review

2.1. Introduction

An extensive literature survey was conducted in the relevant field to identify the literature gaps and justify the aim and objectives of the PhD study.

In section 2.2, a brief review on the marine biofouling is presented, including the definition of the terms, classification of marine biofouling and the process of the marine biofouling formation. Section 2.3 reviews the fouling control coatings. Section 2.4 presents pieces of evidence of the critical impacts of biofouling on ship resistance and propulsion performances. Section 2.5 gives general information of the relevant background theories, including the boundary layer concept, roughness effect in the turbulent boundary layer and different methods for the roughness function determination. Section 2.6 and 2.7 present state-of-the-art studies predicting the fouling effect on ship resistance and propulsion performances, respectively. Finally, research gaps are identified in section 2.8.

2.2. Marine biofouling

2.2.1. Definition of biofouling

At one time, the term ‘fouling’ was used to distinguish the unwanted marine organisms on artificial structures from those occurring on rocks, stones, and other natural objects. Later, however, the definition of ‘fouling’ has been expanded to encompass the process of adsorption, colonisation and development of living and non-living material on any solid surface (Redfield et al., 1952; Lewis, 1998). Redfield et al. (1952) claimed that there are nearly 2,000 species of animals and plants reported to cause biofouling. These include 615 types of plants and 1,361 varieties of animals. Figure 2.1 illustrates the typical plant and animal fouling types detailed by Atlar (2008).

The marine organisms may be categorised by their sizes into microfouling and macrofouling. Microfouling is the accumulation of microbial forms such as bacteria, fungi, and microalgae and their secretions, whereas macrofouling is the accumulation of macroscopic organisms such as oysters and barnacles on submerged surfaces (Little and Depalma, 1988).

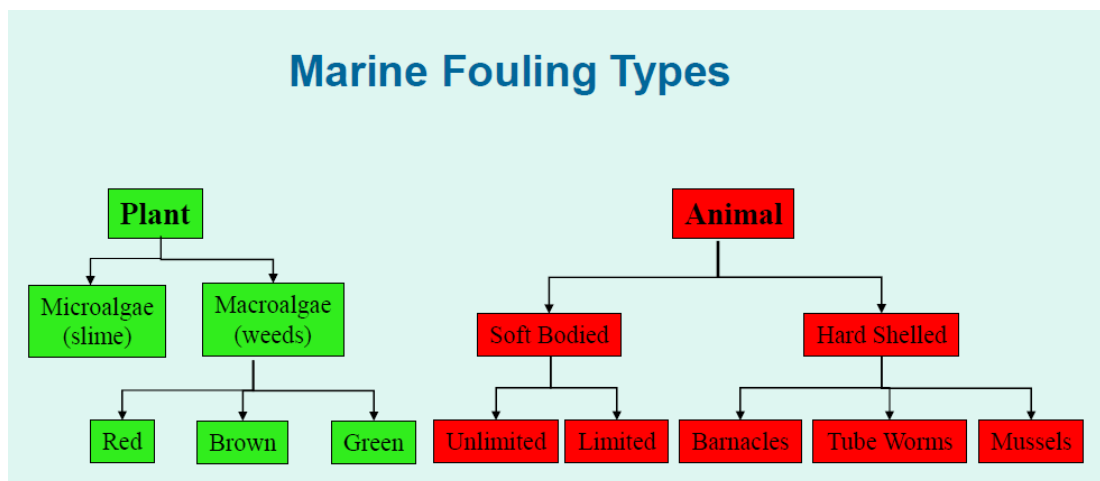


Figure 2.1 Classification of marine fouling types, adapted from Atlar (2008)

2.2.2. Microfouling

Biofouling process often begins with the accumulation of microfouling organisms. Where the conditions are met, bacteria such as Thiobacilli, and/or other microorganisms quickly colonise any substrate placed in seawater (Gehrke and Sand, 2003). They form sticky coatings commonly referred to as 'biofilms'. The accumulation of biofilms is often a precursor to subsequent fouling by macrofoulers (Chambers et al., 2006).

Little and Depalma (1988) identified the four stages in the formation of the biofilm; (i) *conditioning*, (ii) *colonisation by 'pioneer species' (attachment)*, (iii) *colonisation by other microorganisms (colonisation)*, and (iv) *growth*. Figure 2.2 illustrates the four stages in the formation of the biofilm (Chambers et al., 2006). The first stage, *conditioning*, begins within seconds of a surface being immersed with the formation of a film of both organic and inorganic matter adsorbed from the aquatic phase. The 'pioneering species' can now colonise the surface. These primary colonisers are often small, rod-shaped bacteria, which attach within several hours. The early attachment is weak and reversible until the bacteria secrete extracellular adhesive polysaccharide and secure non-reversible attachment. Once the primary colonisers settle down on the surface, they start to assimilate nutrients and synthesise extracellular polymeric substances (EPS), which accumulates in the surface deposit. The third and fourth stages, then proceed rapidly. The secondary colonisers, such as stalked or filamentous bacteria, diatoms, other microalgae, and protozoa. The colonisers grow, reproduce, and synthesise EPS, which plays essential roles in the growth of biofilms. It creates a gel matrix providing enzymatic interaction, exchange of nutrients in the biofilms, protection against environmental stress and increased resistance to biocides (Videla, 1996; Morton et al., 1998). The formation of biofilms provides both a food source and a convenient interface to which the larger organisms can adhere (Titah-Benbouzid and Benbouzid, 2015).

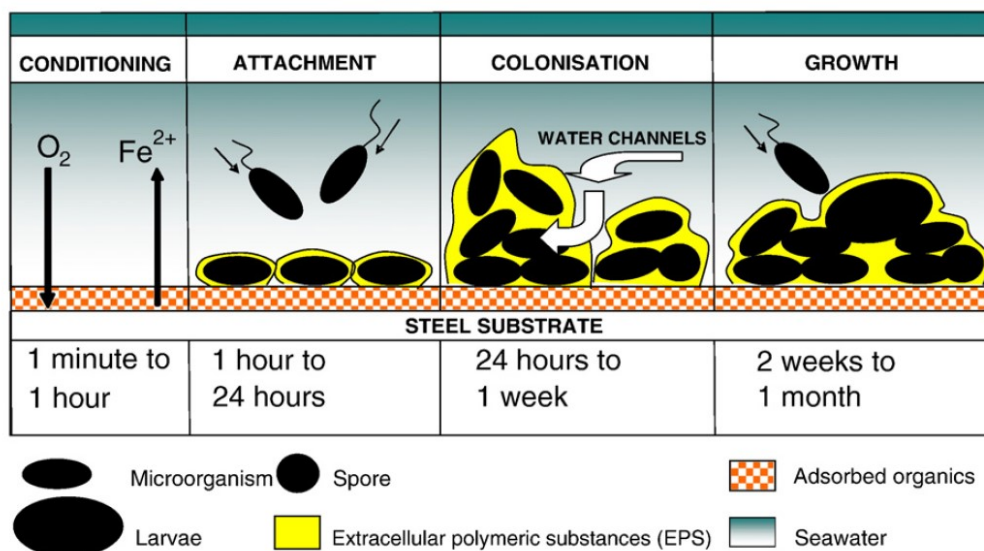


Figure 2.2 Formation of biofilm, adapted from Chambers et al (2006)

2.2.3. Macrofouling

Several days to weeks after the first exposure of a surface, the last and longest phase of fouling colonisation, i.e. macrofouling, begins with the settlement, attachment and growth of multicellular organisms (Lewis, 1998). A macrofouling community (Figure 2.3), consisting of ‘soft’ and ‘hard’ fouling, develops and grows above the microfouling community. Soft fouling organisms include algae and invertebrates, such as soft corals, sponges, anemones, tunicates and hydroids, while hard fouling organisms comprise invertebrates such as barnacles, mussels and tubeworms. Animal species of macrofouling consists of amphipods, barnacles, bryozoans, corals, echinoderms, hydroids, isopods, mussels, nemerteans, Platyhelminthes, sea anemones, serpulid worms, sponges, and tunicates (Callow and Callow, 2002; Kumar and Doble, 2014). Some of these species produce an adhesive to attach to the immersed surface.

The adhesion techniques of these macrofoulers are diverse and can often be a two-component process consisting of temporary and permanent adhesion. At the stage of the critical larval development of those animal foulers, the larvae explore a surface to determine its acceptability before permanently settling on it. During this phase, the

larvae use temporary adhesives to maintain a hold on the surface. If the surface is found to be unacceptable, the adhesions are released to explore alternative settlement sites. The temporary attachment mechanism can be by either a suction apparatus or a secreted sticky substance. Once the surface is determined as acceptable, permanent adhesion is used for settling on the surface. Permanent attachment is by a hardened or cured adhesive cement, sometimes reinforced with calcareous deposits (Lewis, 1998).

The adhesion and settlement is a key stage in the life cycle of the marine organisms, and it is also an important aspect in the perspective of antifouling. If this process could be prevented, fouling could be controlled (Chambers et al., 2006).



Figure 2.3 Typical macroorganisms, adapted from Bressy and Lejars (2014)

2.3. Fouling-control coatings

The fouling of ship hulls is often prolific as vessels move between a diverse range of environments and remain in the most productive region, i.e. the photic zone, of the water column (Chambers, et al., 2006). Hull fouling causes significant costs to ship operations. The increase in hull roughness due to hull fouling results in increased ship resistance and corresponding fuel consumption as well as the cost associated with drydocking. In the environmental perspective, the increased drag results in increased greenhouse gas (GHG) emission, as well as translocation of invasive alien species (Bouyssou and Madjidian, 2013).

In this context, fouling-control systems are essential to minimise the fore-mentioned impacts of marine biofouling.

Although many non-chemical methods, including ultrasonics, electric currents, magnetic fields and optical methods have been proposed, toxic coatings have been the most popular antifouling method due to their unbeatable antifouling performance and low cost. Toxic antifouling coatings are recognised as the most cost-effective over the many types of antifouling methods. Their advantages include ease of manufacture, high speed and low-cost application, durability, and applicability to a variety of structural forms and compositions (Little and Depalma, 1988). Toxic antifouling coatings contain toxic chemicals, which are termed as a biocide. Biocide in the paint surface is gradually released into seawater, such that a toxic layer is formed around the hull. This layer prevents fouling species from attaching to the hull, either by killing the fouling organisms or deterring their settlement.

Coatings must maintain a certain level of biocide release. Once the leach rate falls below this level, whether through biocide depletion in the coating or by the formation of insoluble precipitates on the coating surface, the antifouling action will cease and the marine organisms will start to settle on the surface. As a result, the effective life of typical copper-based biocidal coatings rarely exceeds 18 months (Lewis, 1998).

In the late 1960's organotin compounds replaced the traditional copper-containing antifouling paints, because of their unbeatable antifouling ability and numerous other advantages, such as an effective life of 5 years or more, controllable biocide release rate, and ability to overcoat without loss of activity (Lewis, 1998). Tributyltin (TBT) is the most used organotin compound but also Triphenyltin (TPT) is used.

When these organotin compounds were first introduced, they were thought to be environmentally safe because they degraded rapidly to harmless inorganic forms of tin. Unfortunately, research revealed that the TBT exposure causes severe impacts on marine ecosystems including the malformation of oyster shells and imposex of gastropod molluscs (Alzieu et al., 1986; Gibbs and Bryan, 1986). Eventually, the International Maritime Organization (IMO) banned the application of antifouling coatings which contain TBT in 2003 and banned the operation of ships coated with TBT paints in 2008 (IMO 2001; Champ 2003).

Modern fouling-control coatings can be classified into two main groups by their compositions: 'biocidal' and 'non-biocidal'. Biocidal coatings include Controlled Depletion Polymer (CDP), Self-Polishing Copolymer (SPC), and Hybrid SPC and Non-biocidal coatings. Non-biocidal coatings can be listed as foul-release coatings (FR), which is also termed as non-stick coatings.

A comprehensive review of the modern approaches to environmentally-friendly antifouling systems can be found in Chambers et al. (2006). Table 2.1 compares the performances for the key antifouling systems.

Table 2.1 Performance comparison for the key antifouling systems used, adapted from Chamber et al. (2006)

Antifouling system	Leaching rate	Lifetime	Erosion rate	Cost per m ²	Problems
(TBT) self-polishing copolymer paints	Chemical reaction through hydrolysis. Reaction zone of ablation 5 µm deep.	4-5 years	<3 µm month ⁻¹ . Polishing leads to smoothing, reducing fuel consumption.	\$680,884	Banned 2008
(Tin-free) self-polishing copolymers	Chemical reaction through hydrolysis of copper, zinc, and silyl acrylate	5 years	Polishing leads to smoothing, reducing fuel consumption.	\$1,382,670	Life time shorter than TBT-based paint systems. Increasing the overall cost of ship maintenance. Hard non-polishing performance leads to coating build up.
(Tin-free) conventional paint	10 µg cm ⁻² d ⁻¹	12-18 months	N/A	N/A	Performance only suitable for low fouling environments
Control depletion polymers (CDPs) – copper paint	Physical dissolution, works by having a soluble matrix	3 years	Matrix erodes due to dissolution of coating binder	\$1,357,786	Biocide release not constant, poor self-smoothing, little activity during idle times, higher costs due to necessity of sealer coat on recoats. Slow drying time.
Foul release	Low energy surface, some use leached silicone oils	2-5 years	N/A	N/A	In-water cleaning difficult as brushes may damage silicone, foul release coatings are prone to abrasion damage

The rosin-based Controlled Depletion Polymer (CDP) uses the hydration process to release biocides into the seawater. Seawater migrates into the CDP paint film which in turn dissolves rosin and biocides, which leach into the sea. The rate of biocide release falls exponentially with time. Initially, the rate of release is wastefully high, then falls rapidly towards a point at which insufficient biocide is released to prevent the settlement of the fouling species (Lewis, 1998). The leached layers can become thick and increase the hull roughness. In general, the performance of CDP is considered as poor, but they are still preferred for vessels which have short drydock intervals and those operating in low fouling regions due to their low cost (Atlar, 2008).

The banning of TBT led to the development of tin-free Self-Polishing Copolymers (SPC). SPCs have good initial hydrodynamic performance due to their smooth surface

and the self-polishing action. The dissolution rate of biocides is controlled via hydrolysis, resulting in better antifouling performances. SPCs can remain effective for up to 5 years. Accordingly, they are preferred for vessels which have longer drydock intervals (Atlar, 2008; van Rompay, 2012).

The biocide release mechanism of Hybrid SPCs may be regarded as a hybrid of hydrolysis and hydration, combining SPC acrylic polymer with a certain amount of Rosin. The performance and price of Hybrid SPCs, therefore, are mid-way between the CDP (rosin-based) and SPC (Acrylic based). Figure 2.4 compares the prices and performances of these three biocidal antifouling coatings.

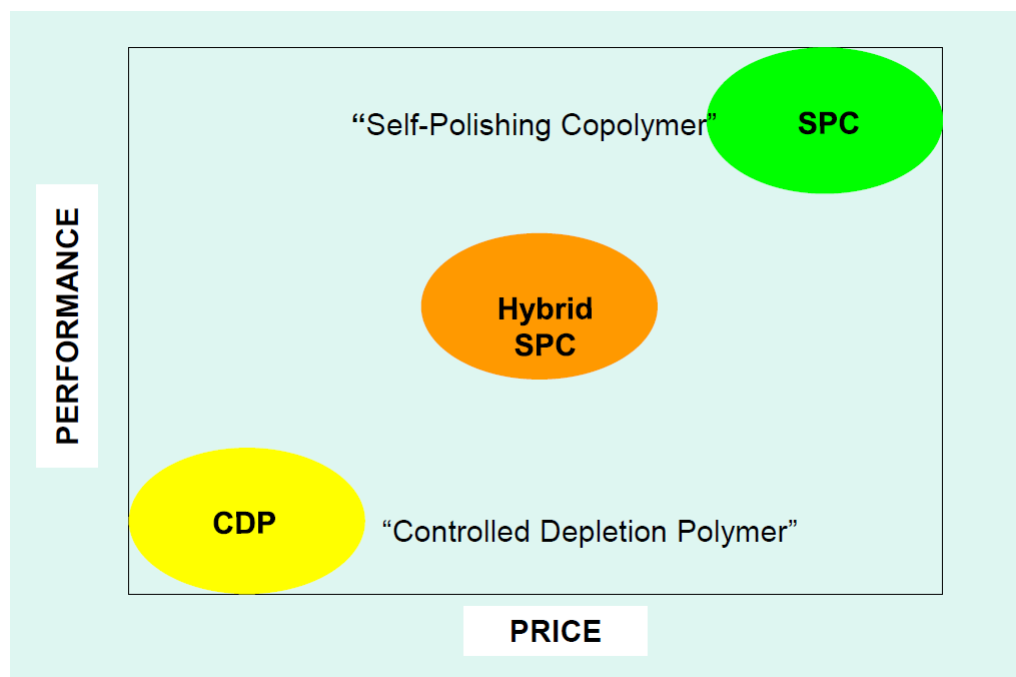


Figure 2.4 Comparison of the performance and price of the key biocidal antifouling coatings, adapted from Atlar (2008)

Foul release (FR) coatings, on the other hand, are a biocide-free solution to control fouling. FR coatings function due to low surface energy which degrades the organisms adhesion strength. Consequently, the organism detaches under its own weight or is dislodged by the friction of water (Lewis, 1998). However, due to its releasing mechanism, FR coatings are not effective for low form biofoulers (e.g. diatoms) which experience relatively lower shear stress, and the antifouling performance is highly

dependent on the ship speed. For this reason, FR coatings are not appropriate for slow ships and for ships spending a long time in ports (Candries, 2001; Candries et al., 2003). Recently, Hunsucker et al. (2014) compared the antifouling performances of a copper-based SPC coating and an FR coating, by applying them on two in-service cruise ships with the same cruise cycles. Greater richness of diatom species was found on the ship hull coated with the FR system compared to the copper-based SPC coating.

2.4. The effect of biofouling on ship performance

2.4.1. On ship resistance

The penalty of increased hull roughness due to biofouling is ship speed loss at constant power or power increase at a constant speed. Either of which results in economic and environmental penalties (Townsin, 2003).

The critical impacts of hull roughness on ship resistance has been noted over the past 150 years, since the very first experimental investigation of the effect of hull roughness on a destroyer by Froude (1872, 1874), as reported by van Manen and van Ooossanen (1988). As reviewed by Redfield et al. (1952), the first comprehensive tests of the effect of fouling on the frictional drag were conducted by McEntee (1915). Flat plates were coated with anticorrosive paints, exposed in the Chesapeake Bay, and then towed periodically to determine the frictional resistance. The results showed that the resistance of the plate increased up to four times due to the barnacles on the surface after twelve months. Hiraga (1934) reported the effect of biofouling on the resistance of a towed brass plate coated with *Veneziani* composition. The plate was towed after 24 days of immersion and showed a 20% increase in the total drag with grown slime and barnacles on the surface. Izubuchi (1934) conducted a full-scale towing test to examine the effect of fouling on ship resistance using the Japanese ex-destroyer, *Yudachi*. This vessel was docked, painted, and had the propeller removed and immediately subjected to a towing test. The towing tests were repeated at intervals to

show the effect of hull fouling by time. Figure 2.5 shows the significant increases in the resistance of the destroyer, *Yudachi*, after various periods. The increase in the resistance at 16 knots, for example, is more than 100% after 375 days due to the surface fouling. Unfortunately, any information about the fouling condition of the destroyer, *Yudachi*, during the test periods is not reported.

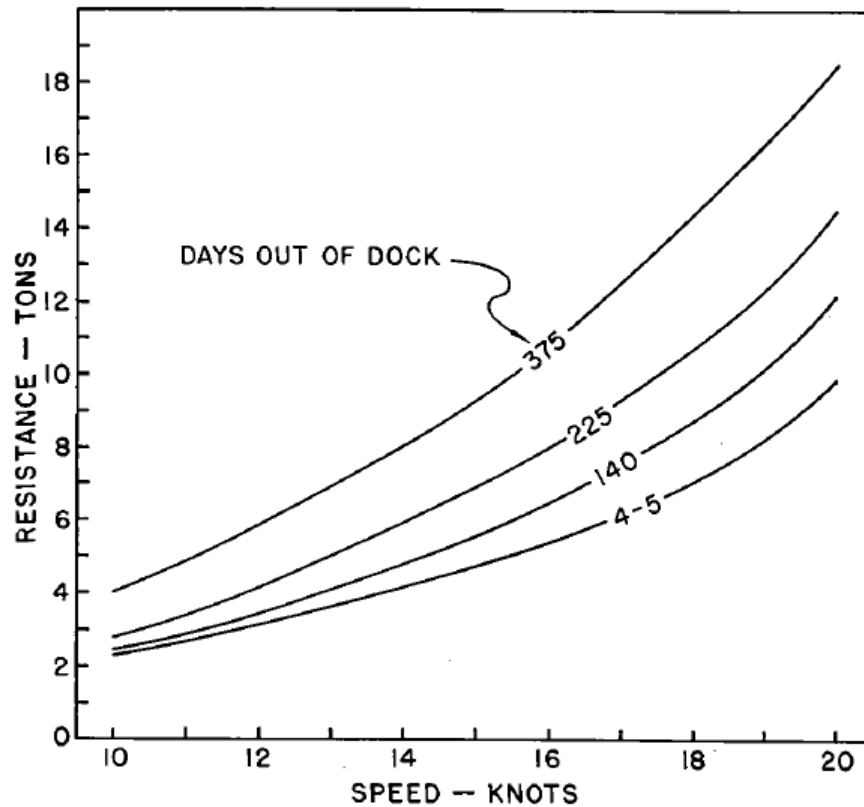


Figure 2.5 Resistance of destroyer 'Yudachi' towed at different speeds after various periods, adapted from Redfield et al. (1952)

Kempf (1937) investigated the effect of fouling on the frictional resistance of a 77-metre long pontoon. By conducting a series of towing tests, he developed a Roughness Coefficient, C_k , to quantify the effect on frictional resistance. The C_k values are given in Table 2.2, which are to be added to smooth surface coefficients, C_f , given by Equation 2.1.

$$R_f = (C_f + C_k) \left(\frac{\rho}{2}\right) S V^2 \quad (2.1)$$

where, R_f denotes the frictional resistance of the rough pontoon, ρ is the water density, S and V is the wetted surface area and the velocity of the pontoon, respectively. Utilising this data, Redfield et al. (1952) showed that the frictional resistance of a surface with 0.118 to 0.157-inch barnacles covering 25% of the area is more than 100% larger than the frictional resistance of the smooth surface.

Table 2.2 Kempf's Roughness Coefficients (C_k), adapted from Redfield et al. (1952)

Surface	C_k
Plane, smooth surface of steel plates, with new paint but without rivets, butts, and straps. Average roughness about 0.012-inch	0.1×10^{-3}
Same as 1, but with butts 0.79-inch high, spaced every	0.4×10^{-3}
Old copper-sheathed	0.75×10^{-3}
New hull with new paint in normal condition with rivets, butts, and straps	0.75×10^{-3}
Normal hull surface like 4, but after 22 years of service, newly painted but with roughening from rust	0.75×10^{-3}
Plane surface with sand particles 0.0394-inch in diameter, covering 100 per cent of area	1.0×10^{-3}
Plane surface with barnacles 0.118 to 0.157- inch high, covering 25 per cent of area	3.0×10^{-3}

There have been studies devoted to the effect of biofilms on ship resistance. The effect of slime film on the frictional resistance was surveyed by Benson et al. (1938), using towed plates covered with slime. Denny (1951) observed a 5% increase in the skin friction on the *Lucy Ashton* after the vessel was moored for 40 days. The increase was attributed to the thin coat of slime and deterioration of the bituminous aluminium paint on the hull. Experiments on slime-coated concentric cylinders, rotating disks and a ship model were conducted by Watanabe et al. (1969). Extrapolating the experimental

result, they predicted an increase in full-scale ship resistance of 9-10% due to the slime fouling.

There have been studies investigating the effect of slimes with background roughness, with a hypothesis that thin slime films on rough surfaces may reduce the frictional resistance by effectively smoothing it. However, it was found that the slime on the rough surface increases the frictional resistance even more. Loeb et al. (1984) conducted rotating disk tests to verify the hypothesis. They measured the frictional resistance of a pre-roughened rotating disk before and after biofilm formation. The result showed 10% higher frictional resistance for the fouled disk. Lewkowicz and Das (1986) showed a similar result, by conducting towing tests using uniformly distributed nylon tufts attached to a rough flat plate to mimic a marine slime growth. They found 18% higher frictional resistance for the model slime with a background roughness compared to that of the background roughness alone.

Lewthwaite et al. (1985) carried out an experiment measuring the boundary layer velocity profiles on a 23m fleet tender. An 83% increase in the frictional resistance and a 15% reduction in ship speed were observed over the 2-year exposure. Haslbeck and Bohlander (1992) conducted a full-scale trial on a Knox class frigate which was coated with an ablative antifouling paint. The delivered power and ship speed were measured after 22 months being moored in Pearl Harbour. With a slime film and little macrofouling on the hull, an 18% increase in the delivered power was observed.

Schultz and Swain (1999) conducted experiments to study the effect of biofilms and algae on skin friction. The experiment involves boundary layer measurements in a recirculating water tunnel using a Laser Doppler Velocimeter (LDV). The result showed up to 370% increase in the skin friction due to the slime and algae on the plates. Schultz (2004) carried out towing tests using flat plates exposed to seawater and concluded that the most dominant effect on resistance was the height of the largest barnacles on the plates. Andrewartha et al. (2010) conducted an experimental study to investigate the effect of biofilm on skin friction using a recirculating water tunnel. The test plates were deployed in the open channels of a hydroelectric power station (Tarraleah Power Scheme, Tasmania, Australia) for varying durations for biofilm

growth. They measured up to 99% increase in the drag of the test plates due to the biofilms on the plates.

Hunsucker et al. (2016) conducted static and dynamic immersion tests to examine the role of hydrodynamic wall shear stress on the growth of biofilms. The immersed test panels were exposed to three different conditions; one static condition and two dynamic conditions (with different wall shear stress). As expected, the static and dynamic panels showed significantly different fouling community compositions after 35 days of exposure. Despite the existence of different fouling community composition, the skin frictions measured on the panels were very similar, suggesting that the frictional drag of low form and soft fouling communities are similar and that there may be a stepwise increase in frictional drag associated with the presence of mature calcareous organisms.

Li et al. (2019) investigated the effect of marine biofilm on the surfaces coated with different sized cuprous oxide (Cu_2O) particles. In order for the biofilms to develop under 'in-service' conditions, the test panels were installed on a detachable twin strut system, which was designed by Atlar et al. (2015), as shown in Figure 2.6. The strut system was deployed under the moon-pool plug of a catamaran research vessel, *Princess Royal*, and exposed in the sea with various periods. The frictional drag of the test panels was measured using a turbulent flow channel after every 6-week deployment period. The result showed up to 83% increase in frictional drag due to the biofilm developed for 6 months.



Figure 2.6 Testing panels installed on twin strut assembly (left) and the strut system deployed under the moon-pool plug of the research vessel (right), adapted from Li et al. (2019)

Recently, there have been active studies using replicated fouling geometries, which are recreated through casting, 3D scanning and printing, etc., to investigate the effect of biofouling without introducing the real fouling into experimental facilities. Monty et al. (2016) scanned light calcareous tubeworm fouling, scaled and reproduced for wind-tunnel testing to determine the equivalent sand grain roughness, k_s . Using the obtained equivalent sand grain roughness, they predicted a 23% increase in the total resistance of a frigate due to the light calcareous fouling. Demirel et al. (2017a) conducted an extensive series of towing test of flat plates covered with artificial barnacle patches to obtain the roughness functions of barnacles with varying sizes and coverages. Different sizes of real barnacles were 3D scanned and printed into artificial barnacle patches. The result showed a 119% increase in skin friction with the most severe fouling condition (i.e. big barnacles, 20% coverage). Uzun et al. (2020) extended the study of Demirel et al. (2017a) to investigate the effect of the settlement pattern of barnacles. A chaotic settlement, which is called ‘natural settlement’, was designed to represent real barnacle settlement in nature. The result showed that changes in settlement pattern alone can cause up to 10.5% additional frictional resistance.

2.4.2. On propeller performance

There have been relatively few studies investigating the roughness effect on propeller performances. Bengough and Shephard (1943) reasoned that the case of *HMS Fowey* which failed to reach to its designed speed can be attributed its fouled propeller. When subsequently docked, the propellers were found to be almost completely covered with calcareous tubeworms. The target speed could be finally achieved after cleaning the propeller. McEntee (1916) conducted experiments on artificially roughened model propellers to compare the efficiencies of similar propellers in different surface conditions. A model propeller was painted and stippled while the coating was wet to

roughen the surface. As shown in Figure 2.7, the efficiency loss was about 20% due to the roughened surface. In another test, they used a propeller covered with ground cork, which resulted in an efficiency drop of 35%. Taylor (1943) insisted that even the ships operating with a propeller in moderately good condition can suffer a power loss in order of 10%. Townsin et al. (1981) recognised that propeller fouling can be as destructive as hull fouling but the remedy is much cheaper. Mosaad (1986) claimed that although the impact of propeller fouling may seem less severe than hull fouling, the losses per unit area are much greater.

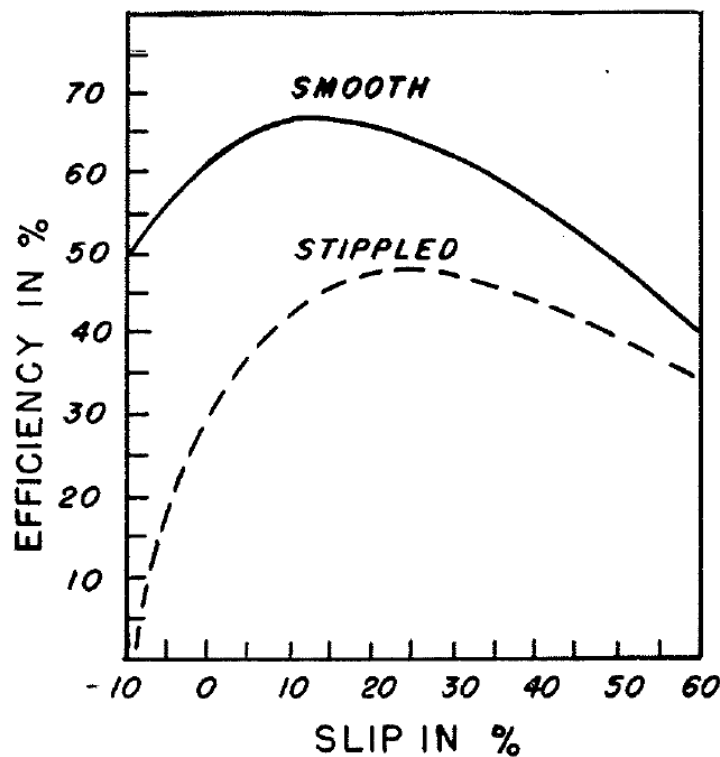


Figure 2.7 The efficiency of a model propeller in the smooth condition and after roughening by stippling a wet paint coating, adapted from McEntee (1916)

Mutton et al. (2005) compared the propeller open water performances in intact and damaged coating conditions and showed reduced propeller efficiency under the damaged scenarios. Korkut and Atlar (2009) conducted experiments to examine the roughness effect of foul release coatings on the propeller open water performances.

An interesting finding from their experiment is that whilst the applied foul release coating increased the roughness amplitudes, it also reduced the texture amplitude, which results in slight decreases in both of thrust and torque, and a small reduction in overall efficiency.

2.5. Roughness effect on turbulent flow

As reviewed in section 2.4, it is evident that the effect of biofouling deteriorates the ship performance. In order to find the rationale behind the roughness effect on ship hydrodynamics, understanding the turbulent boundary layer concept is essential. This section, therefore, briefs the theoretical information including the turbulent boundary layer, roughness effect on the velocity profile and the definition of the roughness functions as well as the experimental techniques for the roughness function determinations.

2.5.1. Turbulent boundary layer

The boundary layer concept was first introduced by Ludwig Prandtl in 1904, as a thin region near the surface of an object in a fluid flow (Schlichting, 2017). He reasoned that, in the fluid flow around an object, the velocity at the surface of an object is zero (i.e. no-slip condition) whereas the velocity of the fluid flow is the freestream value at some distance away from the object (i.e. free-stream velocity). Accordingly, a velocity gradient occurs in the thin layer between two. Prandtl defined this as the ‘boundary layer’. The thickness of the boundary layer, δ , increases as the fluid moves downstream. Figure 2.8 illustrates the velocity gradient in the boundary layer and the growth of the boundary layer thickness, δ , schematically. This thickness, δ , is usually described as the distance between the wall and the point where the velocity magnitude of the flow reaches 99% of the free-stream velocity, U_e .

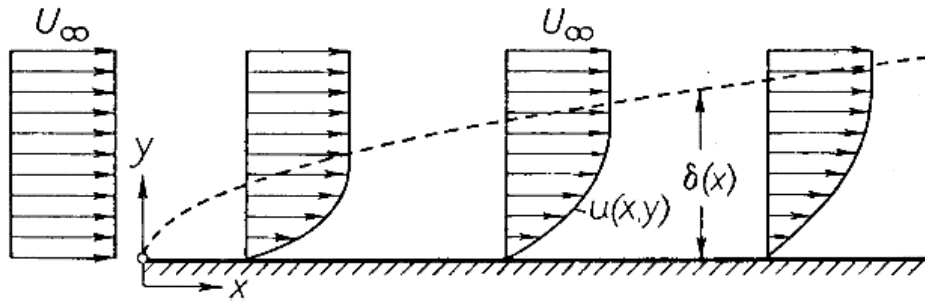


Figure 2.8 Boundary layer at a flat plate at zero incidences, adapted from Schlichting (2017)

The development of the boundary layer is dependent on Reynolds number, Re (i.e. Rn) defined as

$$Re = \frac{U_{\infty} x}{\nu} \quad (2.2)$$

where, U_{∞} , x and ν are the freestream fluid velocity, downstream distance, and kinematic viscosity of the fluid, respectively. Figure 2.9 gives an example of a boundary layer developing over a flat plate. As shown in the figure, the flow remains laminar for a distance downstream. In this laminar region, the flow creates less skin friction than turbulent flow. After a certain distance from the leading edge of the plate (i.e. $x = x_{crit}$), instabilities arise and the flow begins to transition to a turbulent flow.

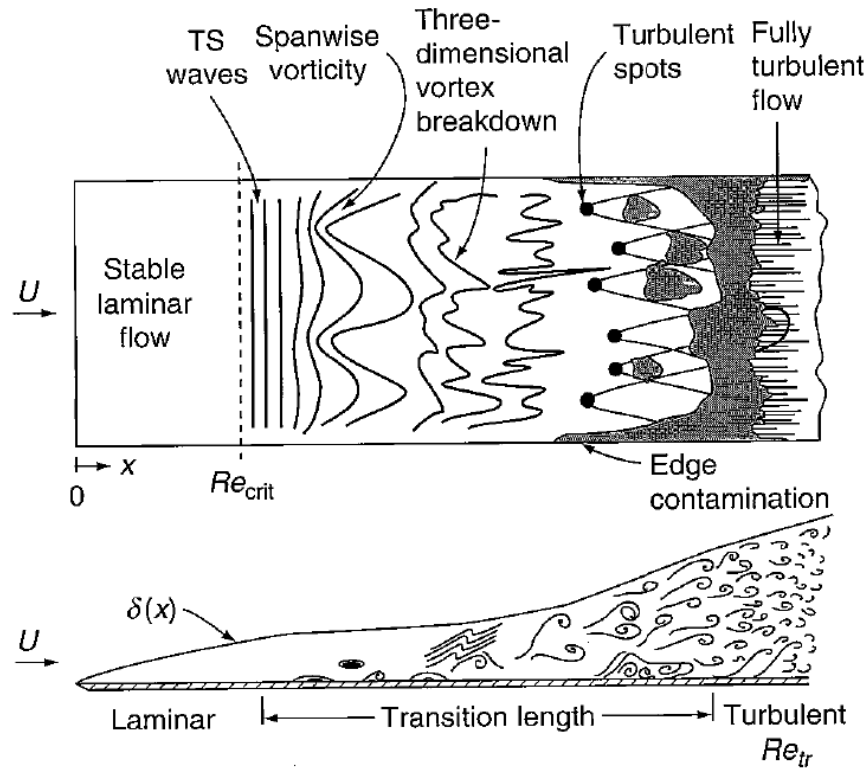


Figure 2.9 Sketch of laminar-turbulent transition in the boundary layer on a flat plate, adapted from White (2006)

In the flow around a ship, the laminar region takes a very small portion while the turbulent boundary layer covers the majority of the hull. For example, when the critical Reynolds number for a typical flat plate, $Re_{crit} = 5 \times 10^5$ is used, the transition for a 230m-long container ship cruising at 24 knots occurs after 5cm from the leading edge.

As illustrated in Figure 2.10, the turbulent boundary layer can be divided into several regions. In the inner region, consisting of the viscous sublayer and log-law region, about 70% of velocity variation occurs, although this layer is as thin as only 10-20% of the turbulent boundary layer thickness (Schultz and Swain, 2000).

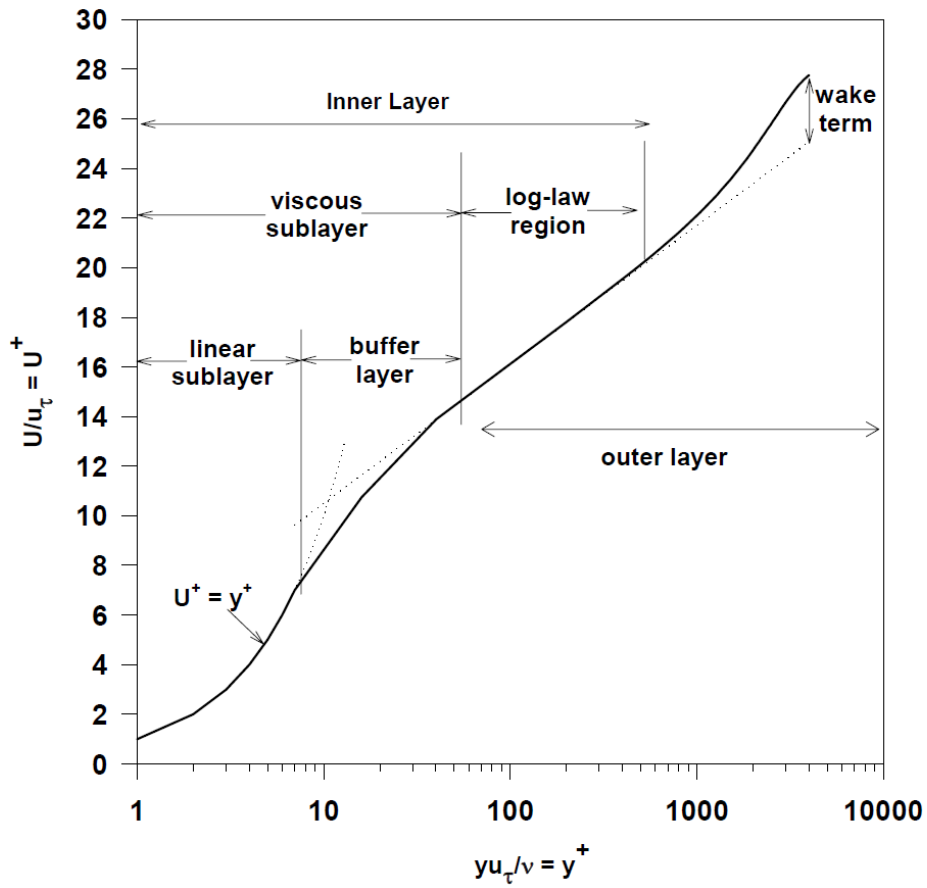


Figure 2.10 Velocity profile in a typical turbulent boundary layer, adapted from Shapiro (2004)

The mean velocity profile in the inner region can be expressed by using the non-dimensional velocity and length, given by

$$U^+ = \frac{U}{U_\tau} \quad (2.2)$$

$$y^+ = \frac{yU_\tau}{\nu} \quad (2.3)$$

Where U is the mean velocity at the normal distance of y from the wall, U_τ is the friction velocity defined as $\sqrt{\tau_w/\rho}$, τ_w is the wall shear stress, and ν is the kinematic viscosity defined as the ratio of dynamic viscosity and the fluid density, μ/ρ .

The viscous sublayer can be further divided into the linear sublayer and the buffer layer. In the linear sublayer, the wall restricts the eddy motion, therefore, no turbulence is expected and therefore this layer is also referred to linear sublayer. In the linear sublayer, the velocity profile can be expressed by

$$U^+ = y^+ \quad (2.4)$$

In the buffer region, the velocity profile begins to lose its linearity. The velocity profile in the log-law region, as the name suggests, follows the log-law. For a smooth surface, the log-law is given by

$$U^+ = \frac{1}{\kappa} \ln y^+ + B \quad (2.5)$$

where, κ is the von Karman constant and B is the log-law intercept. The remaining 80-90% of the turbulent boundary layer is referred to the outer region. The fluid motions in the outer region ($y/\delta > 0.1$ to 0.2) are assumed to be independent of the fluid viscosity or surface roughness while the velocity profile in the inner region is certainly affected by them (Karman, 1934). That is to say, the mean velocity and the turbulence intensity in this region are assumed not to be affected by the surface conditions, i.e. Townsend's hypothesis (Townsend, 1976). The velocity defect law can be expressed by the following equation.

$$\frac{U_e - U}{U_\tau} = f\left(\frac{y}{\delta}\right) \quad (2.6)$$

In the outer region, the velocity profile starts to depart from the log-law, and this is termed as the wake. Coles (1956) introduced the law of the wake to correlate the effect of the turbulent wake defect with the velocity profile. Using Coles wake function, the velocity profile in the wake region can be expressed as

$$U^+ = \frac{1}{\kappa} \ln y^+ + B + \frac{2\Pi}{\kappa} \sin^2\left(\frac{\pi y}{2\delta}\right) \quad (2.7)$$

where, Π is the wake parameter, which is generally a function of the pressure gradient (Schetz, 1993).

2.5.2. Roughness effect in the turbulent boundary layer

The surface roughness causes an increase in the turbulence. As consequences, the turbulent stress, wall shear stress and finally the skin friction increases. The increase in skin friction decreases the momentum of the flow, and this momentum loss due to the roughness effect can be observed in the velocity profile in the log-law region. Clauser (1954) showed that the roughness effect results in a downward shift in the velocity profile in the log-law region, as seen in Figure 2.11. This downward shift is termed the roughness function, ΔU^+ .

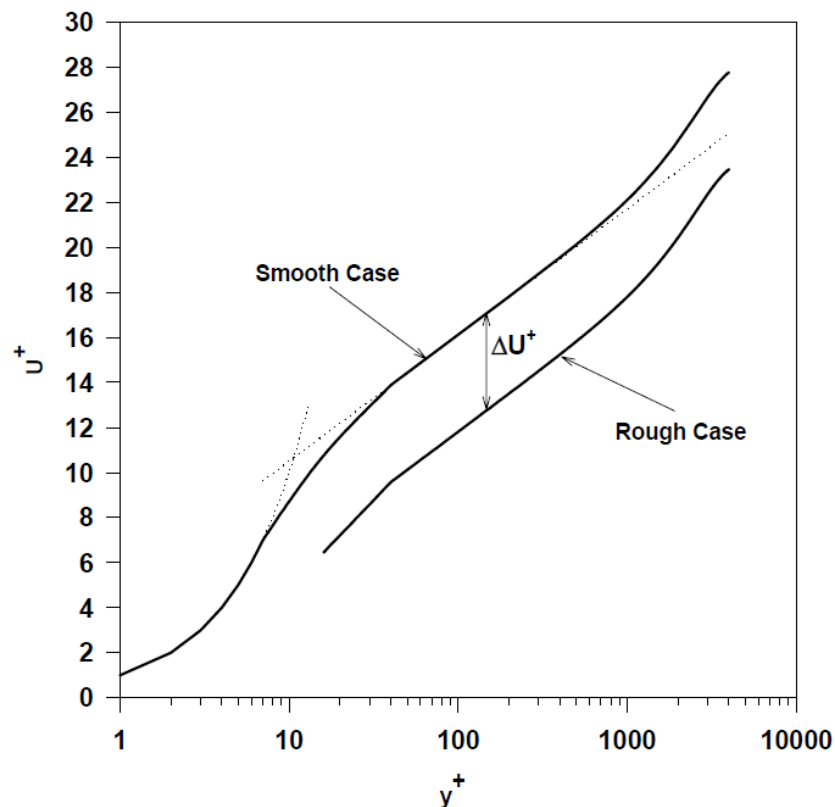


Figure 2.11 Velocity profile on smooth and rough walls, adapted from Shapiro (2004)

The generalised velocity profile in the log-law region for a rough surface is then given as

$$U^+ = \frac{1}{\kappa} \ln y^+ + B - \Delta U^+ \quad (2.8)$$

The roughness function, ΔU^+ can be expressed as a function of the roughness Reynolds number, k^+ , defined as

$$k^+ = \frac{kU_\tau}{\nu} \quad (2.9)$$

It should be borne in mind that ΔU^+ simply vanishes in the case of a smooth condition, such that the velocity profile collapses to the smooth velocity profile, and Equation 2.8 becomes Equation 2.5.

Once the roughness function, $\Delta U^+ = f(k^+)$, of a certain roughness surface is known, it can be utilised with the boundary layer similarity law analysis (Granville, 1958, 1978) or directly embedded into a CFD solver to predict the roughness effect on the frictional resistance of a ship covered with the given roughness (Demirel et al., 2014).

Another interesting point to note is that the rough wall does not affect the shape of the mean velocity profile of the outer region (Hama, 1954; Clauser, 1954). As a result, the mean velocity profiles for smooth and rough walls collapse with each other in the overlap and outer regions of the boundary layer. That is to say, the turbulence outside the inner layer is not a function of surface roughness. This suggests that the hypotheses of Townsend (1976), and Perry and Li (1990) is valid for rough walls.

Although there have been several studies showing the changes in the velocity defect law due to the surface roughness (Krogstad et al., 1992; Tachie et al., 2000; Keirsbulck et al., 2001; Acharya et al., 1986), the majority of the studies experimentally demonstrate the validity of this hypothesis (Bandyopadhyay, 1987; Raupach et al.,

1991; Krogstad and Antonia, 1999; Antonia and Krogstad, 2001; Schultz and Flack, 2003; Shapiro, 2004; Schultz and Flack, 2005; Flack et al., 2005; Kunkel and Marusic, 2006; Schultz and Flack, 2007; Schultz and Flack, 2009; Ünal et al., 2012; Flack et al., 2016). An example of the velocity defect profiles of smooth and rough walls collapsing each other is shown in Figure 2.12.

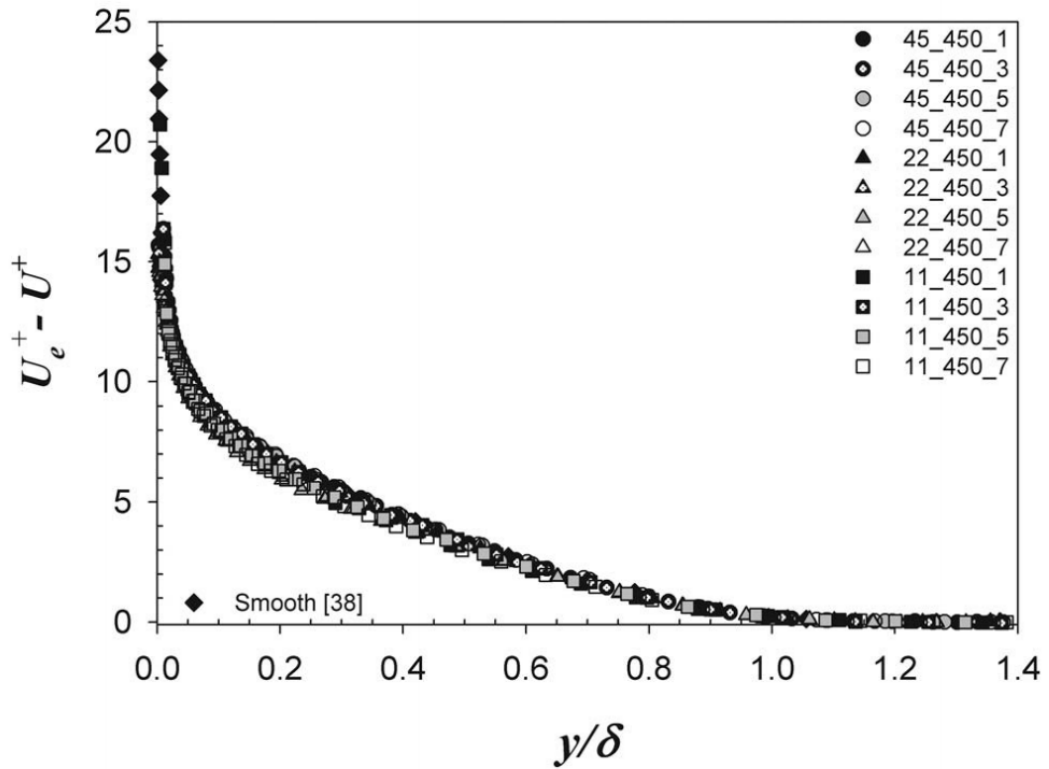


Figure 2.12 Collapse of velocity defect profiles for different surfaces, adapted from Schultz and Flack (2009)

2.5.3. Determination of roughness functions

Roughness functions are of practical importance, as the frictional resistance of any structure covered with a specific roughness can be predicted using the turbulent boundary layer similarity law analysis (Granville, 1958, 1978). Furthermore, it enables the use of CFD methods by avoiding the most difficult barrier of describing the actual hull surface numerically in CFD (Atlar et al., 2018). However, since the roughness function is not universal for all roughness types, the roughness functions need to be determined for individual roughness types (Schultz and Myers, 2003).

The determination methods of roughness functions can be categorised into direct and indirect methods. The direct method involves the measurement of the velocity profile of the logarithmic similarity law close to the specified rough wall (Granville, 1987). Using this method, the shift of the velocity profile due to the roughness effect can be compared and the roughness function of the surface is directly obtained. However, the direct method requires the measurement of the boundary layer profiles, which requires more accessible channels and costly set-up systems (e.g. Laser Doppler Anemometry). Furthermore, using direct methods the determination of U_τ (for non-dimensionalisation of the velocity profile) for a rough-wall profile is more prone to error, since the choice of the y -origin will directly affect the ΔU^+ values (Schultz and Myers, 2003).

On the other hand, indirect methods are generally simpler and more convenient as they are more readily attainable and require a less expensive investment to measure compared to the direct methods (Granville, 1987). Granville derived several indirect methods including local method with displacement thickness (Granville, 1987) based on the work of Hama (1954), the overall method for towed plates (Granville 1958, 1987), the indirect method for rotating disks (Granville, 1982, 1978), a local method without displacement thickness (Granville, 1987) and finally the indirect method for pipes (Granville, 1987).

2.5.3.1. Local method with displacement thickness

The local method with displacement thickness (Figure 2.13) involves measurements of the displacement thickness, δ^* , and local skin friction coefficients, $c_f = 2\tau_w/\rho U_e^2$, of both a smooth and rough surface. The roughness functions can then be obtained by subtracting U_{rough}^+ from U_{smooth}^+ at the same value of displacement thickness Reynolds number, $Re_{\delta^*} = U_e \delta^*/\nu$, as

$$\Delta U^+ = \left(\sqrt{\frac{2}{c_f}} \right)_s - \left(\sqrt{\frac{2}{c_f}} \right)_r \quad (2.10)$$

where, the subscript 's' and 'r' denote smooth and rough surfaces, respectively.

The corresponding roughness Reynolds number, k^+ , is calculated as

$$k^+ = Re_{\delta^*} \left(\sqrt{\frac{2}{c_f}} \right)_r \left(\frac{k}{\delta^*} \right) \quad (2.11)$$

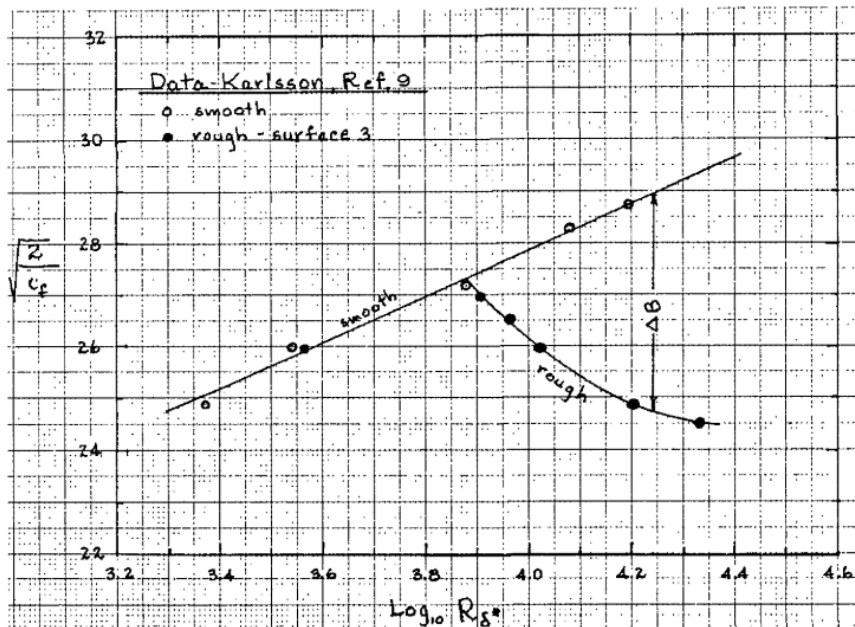


Figure 2.13 Local method with displacement thickness, adapted from Granville (1987)

2.5.3.2. Local method without displacement thickness

Granville (1987) proposed a local method which does not require the measurement of displacement thickness (Figure 2.14). This method involves measurements of the local skin friction coefficients, c_f , and the Reynolds numbers of the smooth and rough surfaces. The roughness function can be obtained by comparing the c_f of the smooth and rough surfaces at the same value of Rec_f , as given by

$$\Delta U^+ = \left(\sqrt{\frac{2}{c_f}} \right)_s - \left(\sqrt{\frac{2}{c_f}} \right)_r - 19.7 \left[\left(\sqrt{\frac{c_f}{2}} \right)_s - \left(\sqrt{\frac{c_f}{2}} \right)_r \right] \quad (2.12)$$

The corresponding roughness Reynolds number, k^+ , is calculated as

$$k^+ = Rec_f \left(\sqrt{\frac{2}{c_f}} \right)_r \left(\frac{k}{2x} \right) \quad (2.13)$$

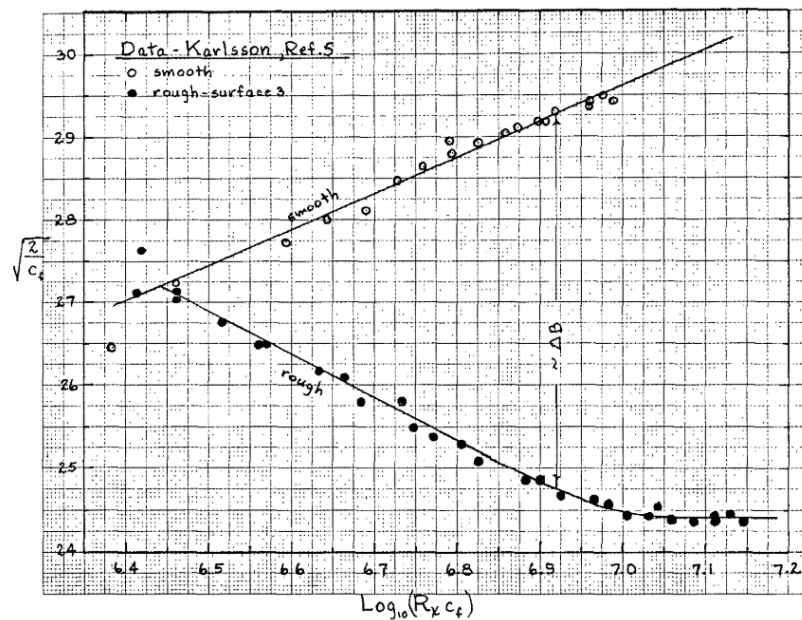


Figure 2.14 Local method without displacement thickness, adapted from Granville (1987)

2.5.3.3. Overall method

Overall method (Figure 2.15) can be used for a flat plate towing test. This method involves the measurement of the global frictional resistance of the towed plate, $C_F = \frac{R_F}{1/2\rho SV^2}$. The roughness function and corresponding roughness Reynolds number can be obtained as

$$\Delta U^+ = \left(\sqrt{\frac{2}{C_F}} \right)_s - \left(\sqrt{\frac{2}{C_F}} \right)_r - 19.7 \left[\left(\sqrt{\frac{C_F}{2}} \right)_s - \left(\sqrt{\frac{C_F}{2}} \right)_r \right] - \frac{1}{\kappa} \Delta U^{+'} \left(\sqrt{\frac{C_F}{2}} \right)_r \quad (2.14)$$

$$k^+ = \left(\frac{k}{L} \right) \left(\frac{Re_L C_F}{2} \right) \left(\sqrt{\frac{2}{C_F}} \right)_r \left[1 - \frac{1}{\kappa} \left(\sqrt{\frac{2}{C_F}} \right)_r + \frac{1}{\kappa} \left(\frac{3}{2\kappa} - \Delta U^{+'} \right) \left(\frac{C_F}{2} \right)_r \right] \quad (2.15)$$

where, L is the length of the towed plate, Re_L is the Reynolds number based on the plate length and the towing speed, $\Delta U^{+'}$ is the slope of the roughness function against $\ln k^+$. It is of note that the C_F values of smooth and rough conditions are the values at the same value of $Re_L C_F$ (Granville, 1987). As the equations are implicit, those values need to be determined in an iterative manner.

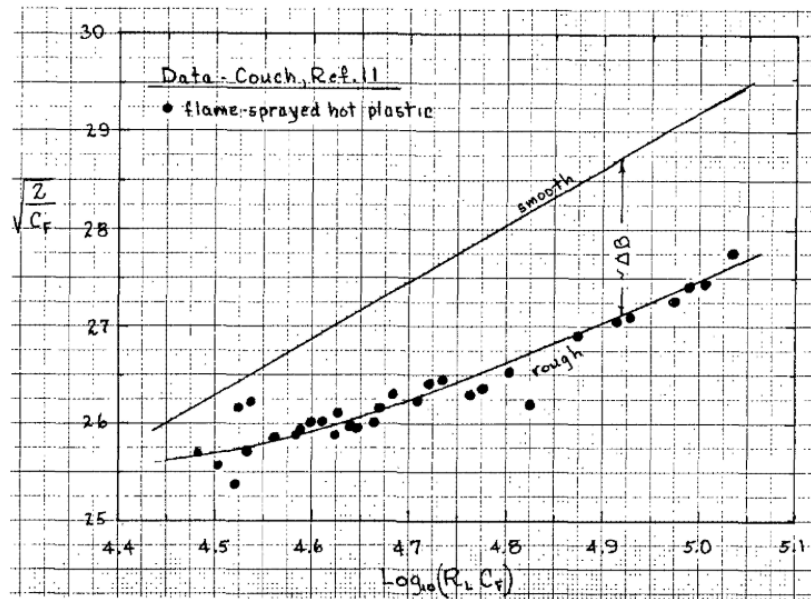


Figure 2.15 Overall method, adapted from Granville (1987)

2.5.3.4. Indirect method for pipes

The indirect method for pipes (Figure 2.16) involves measurements of pressure drop and the mean bulk velocity, \bar{U} , of smooth and rough pipes. The roughness function and corresponding roughness Reynolds number can be obtained as

$$\Delta U^+ = \sqrt{\frac{2}{f_{F,s}}} - \sqrt{\frac{2}{f_{F,r}}} \quad (2.16)$$

$$k^+ = \frac{1}{\sqrt{2}} Re_D \sqrt{f_{F,r}} \left(\frac{k}{D} \right) \quad (2.17)$$

where, $f_{F,s}$ and $f_{F,r}$ are the Fanning friction factors measured in the smooth and rough pipes at the same value of $Re_D \sqrt{f_F}$, Re_D is the Reynolds number based on the pipe diameter and bulk velocity. D is the pipe diameter. It is of note that these equations

can be also used with the pressure drop measurement in 2D channel flow by calculating the hydraulic diameter, D_h , of the channel (Schultz et al., 2015; Li et al., 2019).

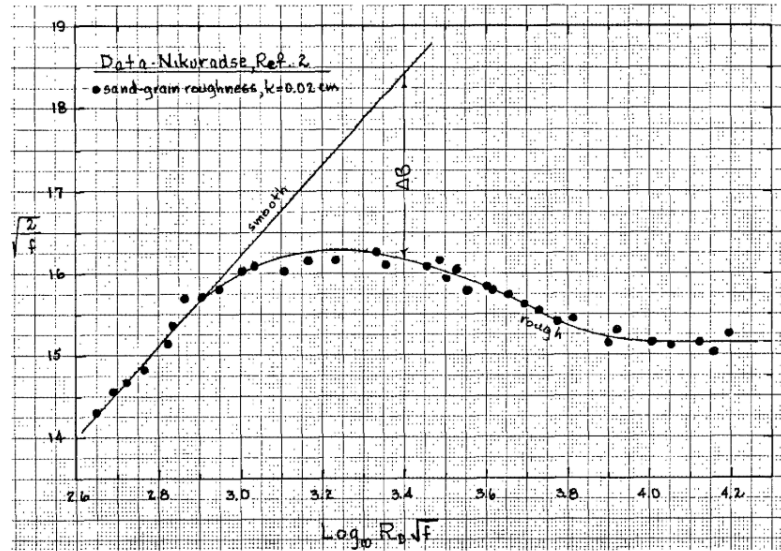


Figure 2.16 Indirect method for pipe flow, adapted from Granville (1987)

There have been a large number of experimental studies to determine the roughness functions, ΔU^+ , and the corresponding roughness Reynolds number, k^+ , using the indirect methods derived by Granville (1958; 1978; 1982; 1987), including the local method with displacement thickness (Schultz and Swain, 1999; Flack et al., 2005; Schultz et al., 2015), the local method without displacement thickness (Karlsson, 1978; Li et al., 2019), the overall method (Schultz and Myers, 2003; Schultz, 2004; Shapiro, 2004; Demirel, 2015; Demirel et al. 2017a), the rotating disk method (Schultz and Myers, 2003; Holm et al., 2004), or the turbulent channel flow method (Schultz et al., 2015; Li et al., 2019).

2.6. Prediction methods for the roughness effect on full-scale ship resistance

2.6.1. Boundary layer similarity law analysis

The boundary layer similarity law analysis, which was proposed by Granville (1958; 1978), can extrapolate the skin friction over a rough surface. The merit of using this method is that once the roughness function of the surface is given, the full-scale roughness effect on an arbitrary length of the body covered with the same roughness can be predicted.

There have been many studies using this method to predict the frictional resistance of a ship with hull fouling or marine coatings (Schultz, 2002, 2004, 2007; Shapiro, 2004; Flack and Schultz, 2010; Schultz et al., 2011; Demirel, 2015; Demirel et al., 2017a, 2019; Li et al., 2019). More specifically, Schultz (2004) compared the frictional resistance of a 150 m flat plate with different antifouling surfaces in unfouled, fouled and cleaned conditions. The increases in the frictional resistance of such surfaces were predicted using Granville's method utilising experimentally obtained roughness functions. The increase in the frictional resistance of the surfaces in fouled condition ranged from 50% for an SPC TBT coating to 217% for a silicone coating. Using the same method, Schultz (2007) predicted the power penalty of an *Oliver Hazard Perry class* frigate of 144 m with different coating and fouling conditions. The increase in the required shaft power at a constant speed (30 knots) due to the heavy calcareous fouling condition was 59%, while the speed loss at a fixed power was 10.7%. Shapiro (2004) used Granville's method to estimate the added fuel cost of a *DDG-51 class* destroyer of 150 m length due to different roughness conditions. The added annual fuel cost due to fouled ship bottom paint was estimated to be 3.0 million USD. Schultz et al. (2011) investigated the overall economic impact of hull fouling on a 142 m *Arleigh Burke-class* destroyer. The fuel costs due to different fouling conditions were estimated based on the similarity law analysis and compared with other costs associated with antifouling activities. The results indicated that the costs related to hull

cleaning and painting are much lower than the added fuel costs due to hull fouling. Demirel et al. (2019) generated added resistance diagrams to be used for the prediction of the effect of different hull fouling conditions on the resistance and powering of ships with arbitrary lengths and speeds. The similarity law analysis was conducted using the roughness length scales of different fouled surfaced proposed by Schultz (2007).

However, Granville's similarity law scaling has several limitations due to its assumption of flat plate (Atlar et al., 2018). In other words, this method only considers the roughness effect on frictional resistance. However, recent studies claim that the hull roughness not only affects the frictional resistance but also the other pressure-related resistance components (Demirel et al., 2017b; Farkas et al., 2018, 2019; Andersson et al., 2020). Another restriction of this scaling method is that only a constant roughness Reynolds number, k^+ , (i.e. uniform k^+ over the flat plate) is taken into account in the calculation to represent the roughness effect on the whole flat plate, which is not realistic as the local friction velocity, u_τ , varies by the flow being developed along with the flat plate in reality (White, 2011).

2.6.2. Application of CFD

Implementation of computational fluid dynamics (CFD) is an effective way to overcome the limits of the similarity law scaling (i.e. flat plate assumption and uniform distribution of k^+). In CFD simulations the distribution of the local friction velocity, u_τ , is dynamically computed for each discretised cell, and therefore the dynamically varying roughness Reynolds number, k^+ , and corresponding roughness function, ΔU^+ , are dynamically calculated in the simulations, and hence the roughness effect on ship resistance can be more accurately predicted (Demirel et al. 2017b; Atlar et al., 2018). The simulations are free from the scale effects if they are modelled in full-scale. The 3D effects can be also taken into account. Therefore, the roughness effect on other resistance components and the effect on the propeller performance can be simulated.

There have been several studies investigating the roughness effect of marine coatings and biofouling on ship resistance using CFD simulations. Patel (1998) remarked that once the roughness function model, $\Delta U^+ = f(k^+)$, of the roughness type is known, the given roughness function model can be employed into the wall-function in the CFD so that the wall boundary condition in the simulation represents the roughness on the surface. Date and Turnock (1999) proposed a numerical approach modifying the wall-function coefficient to predict the roughness effect on frictional resistance of a flat plate. However, their method cannot directly represent the viscous flow over the rough surface as the dynamically changing values of ΔU^+ , is not considered in the CFD computation. Izaquirre-Alza et al. (2010) conducted a CFD simulation of a flat plate coated with marine coatings using SST $k-\omega$ turbulence model and showed a good agreement with the experimental result. However, they did not provide any information about the roughness function model employed in their CFD model and valid evidence of the selection of the roughness height of the coatings. Eça and Hoekstra (2011) examined the effect of sand-grain roughness on skin friction of a ship-length flat plate and further asserted that the roughness can be accurately simulated using either wall-functions or near-wall resolution. However, there is a continuing concern by ITTC (2011) in the use of sand grain roughness since the real ships' surfaces do not show the behaviour of closely packed sand roughness.

Demirel et al. (2014), on the other hand, developed a CFD model for the prediction of skin friction of antifouling coatings. They employed roughness functions obtained from a series of towing tests of flat plates coated with antifouling coatings and validated the modified wall-function approach by comparing the results obtained by CFD with the experimental data. They applied the same approach to ship-length flat plate simulations to predict the frictional resistance of the ships with the antifouling coatings. Vargas and Shan (2016) implemented a modified wall-function in their CFD models based on the equivalent sand-grain roughness approach in conjunction with the SST $k - \omega$ turbulence model. The roughness model was validated against the experiments on rough towed plates covered with sand-grain using towing tank and flow channel (Schultz, 2004; Flack et al., 2007).

There have been fewer studies carried out for the examination of the effect of the surface roughness on 3D hull shapes. Castro et al. (2011) conducted full-scale simulations of the KRISO container ship (KCS) modifying the wall-function coefficients according to the roughness height of the coating. However, they used a fixed value of the roughness function as the case of Date and Turnock (1999). Demirel et al. (2017b) conducted simulations of a full-scale KCS. They proposed a roughness function model representing a typical coating and different fouling conditions based on the roughness functions of Schultz and Flack (2007) and employed the roughness function into the wall-function of the CFD software. The result showed up to a 107.5% increase in the effective power of KCS due to the heavy calcareous fouling condition. Also, they showed that the hull roughness affects the wave-making resistance for the first time. Farkas et al. (2018, 2019) conducted CFD simulations to investigate the effect of biofilm on the resistance a full-scale KCS, using a modified-wall function with the implementation of the roughness functions of diatomaceous biofilm of Schultz et al. (2015). By comparing the 3D KCS simulations with and without the presence of free surface, they decomposed the ship resistance into individual components. The result showed that the total resistance and frictional resistance of KCS increase with the presence of biofilm, whereas the wave-making resistance showed decreases. Seok and Park (2020) also used the modified wall-function approach to analyse the variation in resistance performance of three different containership models. The simulation results were compared with the predictions based on Townsin's formula (Townsin and Dey, 1990) and showed a satisfactory agreement.

2.7. Prediction methods for the roughness effect on propulsion performance

As reviewed in section 2.4.2, it is evident that the propeller fouling deteriorates the efficiency of marine propellers. Therefore, accurately predicting the effect of surface roughness of marine propeller is also critical as ship energy consumption depends on not only the hull resistance, but also the propulsion efficiency.

Although there have been several lab-scale experimental studies investigating the effect of surface roughness on marine propeller performances, as reviewed in section 2.4.2, relating the model-scale experiments to the full-scale roughness effect is not an easy task owing to the unique feature of the roughness effect. That is, the size of surface roughness cannot be scaled up or down (Franzini, 1997).

While the roughness effect on skin friction can be extrapolated using the boundary layer similarity law analysis of Granville (1958; 1978), this method may not be appropriate for propellers as the boundary layer similarity law analysis is limited by the assumption of zero pressure gradient. In other words, this method cannot consider the three-dimensional effect and inevitably it cannot properly consider the roughness effect on the pressure field around the blades, which dominates the thrust and torque of the propeller.

For this reason, the roughness effect on the full-scale propeller performance is not well established yet. Atlar et al. (2002) conducted numerical calculations to determine the roughness effect on the propeller open water characteristics. They used a propeller roughness comparator to represent the blade roughness after several years in service. The increment of the blade section drag coefficient due to the roughness was calculated utilising the early work of Mosaad (1986) and used in the numerical computation. The result indicates that the loss of the propeller efficiency can be as high as 12 % with the increase in torque and decrease in thrust due to the surface roughness of the blades.

Seo et al. (2016) conducted numerical predictions of full-scale propeller efficiency loss due to surface fouling on the blades. They predicted the increased drag coefficient of the blade section based on the boundary layer similarity law analysis derived by Granville (1958, 1978). Utilising the drag coefficients of different fouling conditions, they estimated a 14.6% loss in propeller efficiency with small calcareous fouling condition.

In these studies, however, the roughness effect on the propeller is only considered by using increased blade section drag coefficients rather. Thus, these studies do not consider the roughness effect on the fluid field around the propeller, which is closely related to the surface pressure distribution on the blades. In consequence, they could not observe a considerable roughness effect on the thrust coefficients, while significant increases in the torque coefficients were observed from the calculation results.

Recently, Owen et al. (2018) investigated the roughness effect of biofouling on propeller characteristics using CFD. A roughness function model representing different fouling conditions was employed in the wall-function of the CFD software. The simulation results indicate that severe calcareous fouling can result in 30.3% of efficiency loss compared to the smooth case. However, as the simulations were conducted in the model-scale only, it is still questionable if their results can realistically represent the full-scale effect of biofouling on real marine propellers.

Farkas et al. (2020) conducted full-scale CFD simulations of a self-propelled containership with different types of biofilms on the hull and propeller to predict their impact on the ship propulsion characteristics. They used the modified wall-function approach with roughness function models representing surface conditions of biofilms. They quantified the increases in delivered power at the constant speeds as well as the speed loss at the same power due to the biofilms on the hull and propeller surface. However, they used the body force propeller method (i.e. virtual disk method) rather than modelling the rotating propeller. Therefore, a concern can be raised with regards to the modelling the hull and propeller interaction.

2.8. Literature gap identification

Up until this point, a broad literature review has been made. During this literature review, the following research gaps were identified to the best of the author's knowledge.

- Granville's similarity law scaling has been widely used to predict the roughness effect on ship resistance and it is generally considered as a valid approach. However, there exists no specific study validating Granville's method against a ship model towing test. Therefore, an experimental validation is still needed to demonstrate the suitability of Granville's method for 3D hulls.
- Recently, there have been active efforts devoted to modelling the roughness effects in CFD simulations. However, the validations were merely performed against flat plates with zero pressure gradient. That is to say, these demonstrations are only valid for the frictional resistance, and it cannot guarantee the validity for other resistance components originating from the curved hulls. Therefore, the validity of the CFD approach for 3D hulls is still to be demonstrated.
- There have been relatively few studies investigating the effect of biofouling on full-scale ship resistance. These studies were mainly focussing on the effect of hull fouling on ship resistance and effective power. However, the investigation could be extended for better understanding. For example, investigations into the roughness effect on the form factor, nominal wake and the flow

characteristics around the hull (e.g. pressure field, boundary layer thickness) can be useful.

- CFD simulations can be effectively used to predict the effect of propeller fouling, as it can predict the roughness effect on the pressure field around the propeller. However, there is no CFD study investigating the effect of biofouling on a full-scale marine propeller. Therefore, the CFD method can be extended to examine the effect of biofouling on full-scale marine propeller performances.
- No study has been devoted to investigating the effect of hull and/or propeller fouling on the propulsion efficiency of a self-propelled ship. Therefore, the CFD method can be effectively used to investigate the effect of hull and propeller fouling on ship self-propulsion performance.
- In the conventional studies, the hull surfaces have been treated as uniform rough surfaces while the real ships' hulls are exposed to heterogeneous fouling accumulation. Therefore, it is worthwhile to conduct an experimental study to investigate the effect of heterogeneous distributions of hull roughness on ship resistance.
- To the best of the author's knowledge, there exists no specific study investigating the roughness effect on ship resistance of different hull forms with different scales and speeds. Therefore, it is worth performing CFD

simulations of different ships to examine the different roughness effects on different ships.

These research gaps are addressed throughout this PhD thesis.

2.9. Chapter summary and conclusion

A comprehensive literature survey has been conducted and the research gaps have been identified in this chapter.

3. Methodology

3.1. Introduction

This chapter presents the general methodology used throughout this PhD thesis, while each chapter presents the specific details of its own methodology.

3.2. Methodology

Figure 3.1 illustrates the methodology used in this PhD study. As shown in the figure, the thesis consists of three distinct parts. The chapters in Part I provide experimental validations by means of tank testing to demonstrate the suitability of the methods for the added resistance prediction due to hull roughness: Granville's similarity law scaling method (Chapter 4) and the CFD method involving modified wall-functions (Chapter 5). The chapters in Part II present the full-scale applications of the CFD approach to predict the effect of biofouling on the full-scale ship hydrodynamic problems, including ship resistance (Chapter 6), propeller performance (Chapter 7) and ship self-propulsion performance (Chapter 8). Finally, extended investigations are presented in Part III. Chapter 9 presents the investigations into the effect of heterogeneous distributions of hull roughness on ship resistance, while Chapter 10 is involved with the differences in the effect of hull fouling with the variations of hull forms, ship lengths (scales) and speeds.

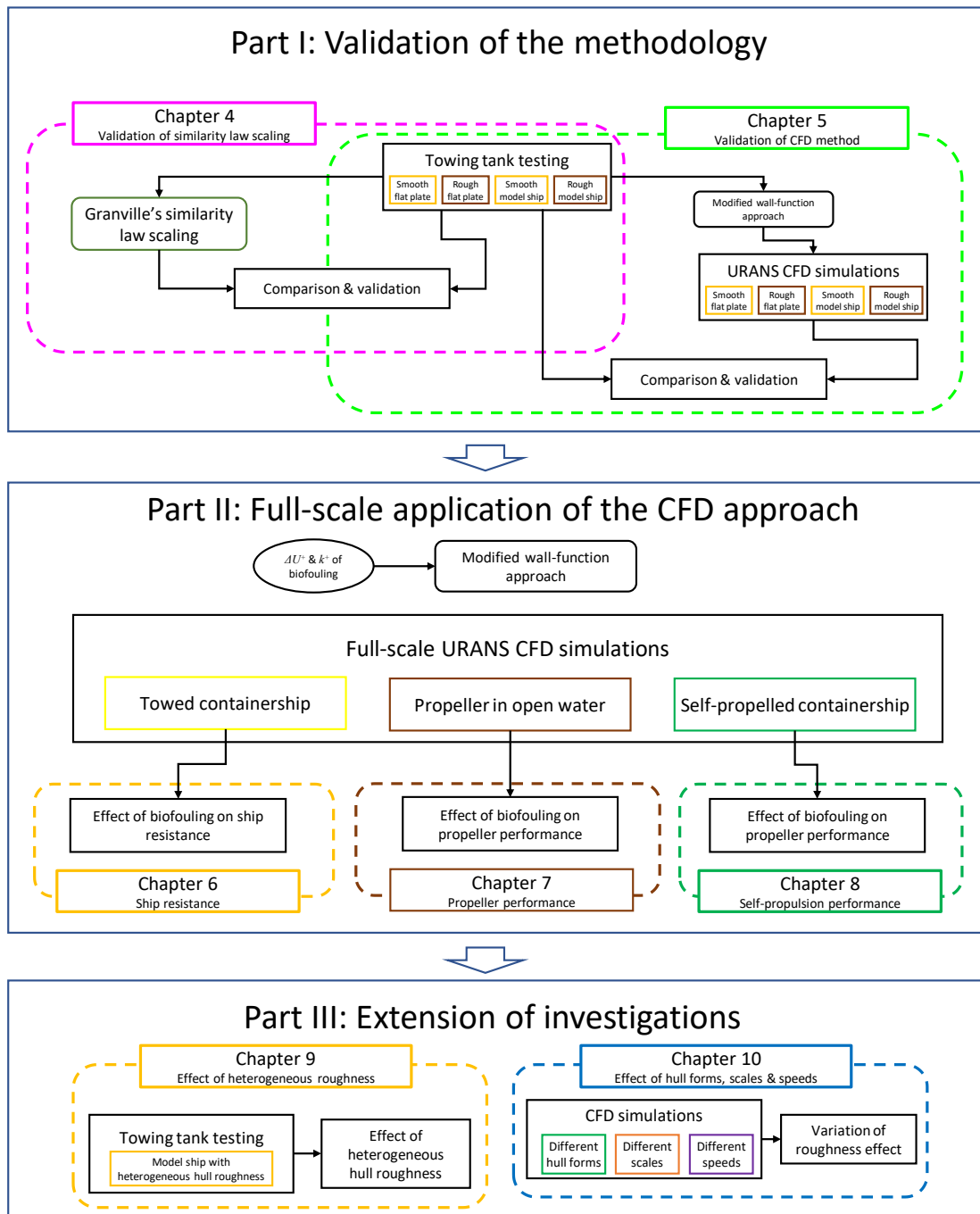


Figure 3.1 Methodology followed in the thesis

Chapter 4 presents an experimental investigation into the effect of hull roughness on ship resistance and provides a validation of the similarity law scaling, by using tank testing of a flat plate and a KRISO Container Ship (KCS) model. Both the plate and model ship were tested in smooth and rough (sand-grain) surface conditions. The roughness functions of the rough surface were derived by using the results of the flat plate towing tests. Using the obtained roughness function, the frictional resistance was extrapolated to the length of the model ship following the similarity law scaling procedure. The total resistance of the rough ship model was then predicted using the extrapolated frictional resistance and the result of the smooth ship model, and then compared with the results from the rough ship model.

Validation of the CFD approach for modelling the roughness effect on ship resistance is presented in Chapter 5. CFD models of the towed flat plate and the KCS model were developed, and the results were compared with the towing test results obtained in Chapter 4. To represent the effect of hull roughness, the roughness function of the sand-grain surface, which was determined in Chapter 4, was employed in the wall-function of the CFD model (i.e. modified wall-function approach). The result of the CFD simulations was compared with the experimental result, to demonstrate the validity of the roughness modelling in CFD on the total resistance of the 3D hull.

Full-scale applications of the CFD approach are presented in Chapter 6-8. In Chapter 6, the roughness function of barnacles (Demirel et al., 2017a) was employed in the wall-function of the CFD model to represent the surface roughness of barnacle fouling with varying barnacle sizes and coverage densities. For validation of the modified wall-function approach with the roughness function of barnacles, towed-flat plate simulations were carried out and compared against the experimental data Demirel et al. (2017a). The modified-wall function approach was then applied to full-scale ship hydrodynamic problems: towed KCS, KP505 propeller (i.e. the propeller of KCS) in open water, and self-propelled KCS. From the full-scale KCS simulations in Chapter 6, the effect of barnacle fouling was examined on the ship resistance components, form factors and wake fractions as well as the flow characteristics around the hull. From the full-scale KP505 propeller simulations in Chapter 7, the effect of barnacles on the propeller open water performance was predicted with the advance coefficients ranging

from 0.2 to 0.8. In Chapter 8, the full-scale KCS self-propulsion simulations were conducted in various configurations of the hull and/or propeller fouling. The effects of barnacle fouling were investigated on the ship resistance, delivered power and other propulsion efficiencies.

Chapter 9 involves towing tests of a model ship of the Wigley hull with heterogeneous hull roughness. The model ship was towed with different hull conditions such as smooth, $\frac{1}{4}$ -bow-rough, $\frac{1}{4}$ -aft-rough, $\frac{1}{2}$ -bow-rough, $\frac{1}{2}$ -aft-rough, and full-rough conditions. The differences in the added resistance between the heterogeneous hull roughness conditions were discussed. Also, a new prediction method was proposed to predict the added resistance due to the heterogeneous hull roughness based on Granville's similarity law scaling and the predictions were compared with the experimental result.

Chapter 10 presents the extension of the CFD approach for better understanding of the fouling effect on ship resistance performance. Using the same CFD approach as in Chapter 6-8, ship resistance simulations were conducted using two different hull forms, KRISO Containership (KCS) and KRISO Tanker (KVLCC2). Each hull form was modelled in three different scales (i.e. model-scale, moderate-scale and full-scale) with a range of Froude numbers. From the simulations, the effect of hull fouling on ship hydrodynamic characteristics were investigated for the different ships, scales and speeds were investigated.

3.3. Chapter summary

The general methodology used in the thesis has been presented in this chapter.

4. Experimental and theoretical investigation into the roughness effect on ship resistance

4.1. Introduction

The boundary layer similarity law analysis, which was proposed by Granville (1958; 1978), can be used to extrapolate the roughness effect on skin friction. The merit of using this method is that once the roughness function, ΔU^+ , of the surface is known, the full-scale roughness effect on an arbitrary length of the body with the same roughness can be predicted.

Although Granville's similarity law scaling was derived based on reasonable assumptions and shows a good agreement with full-scale ship trial results (Schultz, 2007), Granville's similarity law analysis is still limited by the assumptions of flat plate, uniform distribution of roughness Reynolds number and the roughness function (Demirel et al., 2017b).

Great effort has been made to assess the roughness effect on skin friction, however, there is little research applied to a ship model experimentally. Kiosidou et al. (2017) performed tank testing of a flat plate and a model ship, both in smooth and rough conditions, where the rough surface was created by applying sandpapers. From the flat plate test, they obtained the roughness function of the sandpaper surfaces, and extrapolated the frictional resistance to a 180 m ship using Granville's similarity law scaling procedure. They scaled the rough ship results to the same 180 m ship using the resistance formula of Schlichting (2017). The results obtained by the above-mentioned two methods were compared against each other. The comparison suggested the two results do not agree with each other well. However, they did not directly compare the extrapolated result with the experimental results for the model-scale rough ship, and hence could not provide a reasonable validation of Granville's similarity law analysis.

As reviewed in Chapter 2, Granville's scaling method is still the most widely used method to predict the roughness effect on ship resistance, owing to its merit that this method can predict the roughness effect on the frictional resistance for ships of arbitrary lengths and speeds. Also, the recent CFD studies show good agreement with the results obtained by Granville's extrapolation (Demirel et al., 2017b). Considering the computational cost for the CFD studies, as well as the fact that the simulations can only be conducted for one ship length at once, Granville's similarity law scaling is still a computationally economic and robust method.

As mentioned earlier, however, this method can only predict the frictional resistance of a flat plate of the given length. Recent studies claim that the other resistance components for a ship-shape body, such as viscous pressure resistance and wave making resistance, are also affected by the roughness effect (Demirel et al., 2017b). Therefore, it is worthwhile to conduct an experiment using a ship model with a rough surface, and compare the results with those predicted using Granville's extrapolation to check the validity of this scaling method for predicting the roughness effect on ship resistance.

To the best of the author's knowledge, there exists no specific study comparing the ship resistance predicted following Granville's scaling procedure with the resistance measured directly from a rough model ship tank test. Therefore, the aim of this chapter is to fill this gap by conducting towing tests using a flat plate and a model ship, both in smooth and rough conditions.

This chapter is organised as follows: The methodology used in this chapter is explained in Section 4.2.1, while Section 4.2.2 discuss the details of the roughness function determination method. The details of the Granville's boundary layer similarity law scaling is discussed in Section 4.2.4. The uncertainties of the towing tests are estimated in Section 4.2.5 based on the ITTC recommendations. Section 4.3.1 and 4.3.2 discuss the results of the towing tests. Based on the roughness function of the rough surface determined in Section 4.3.3, the frictional resistance of the rough model ship is predicted using the similarity law scaling in Section 4.3.4. Section 4.3.5 compares the

predicted total resistance of the rough model ship against the results of the towing test. Finally, the chapter summary and conclusions are presented in Section 4.4.

4.2. Methodology

4.2.1. Approach

Figure 4.1 schematically illustrates the methodology used in this chapter. The first step is conducting four different towing tests using a flat plate and a model ship, both in smooth and rough surface conditions. In order to roughen the surfaces, the same sand grit (aluminium oxide abrasive powder) was applied to the surfaces of the plate and the model ship. The second step is the determination of the roughness functions. The roughness functions for the given surface roughness were calculated using the indirect method for flat plates, presented by Granville (1987). The third step is extrapolating the rough frictional resistance ($C_{F,r}$) from the plate length (1.5 m) to the model ship length (3.0 m), following the boundary layer similarity law scaling procedure, presented by Granville (1958; 1978). The final step is predicting the total resistance of the rough model ship ($C_{T,r}$) using the extrapolated flat plate frictional resistance and the smooth ship results. The predicted rough ship resistance is then compared with the measured rough ship resistance ($C_{T,r}$). Both *2D method* and *3D method* are adopted in the prediction of the rough ship resistance, where the *2D method* only considers the roughness effect on the frictional resistance while the *3D method* considers the effect on the viscous pressure resistance as well.

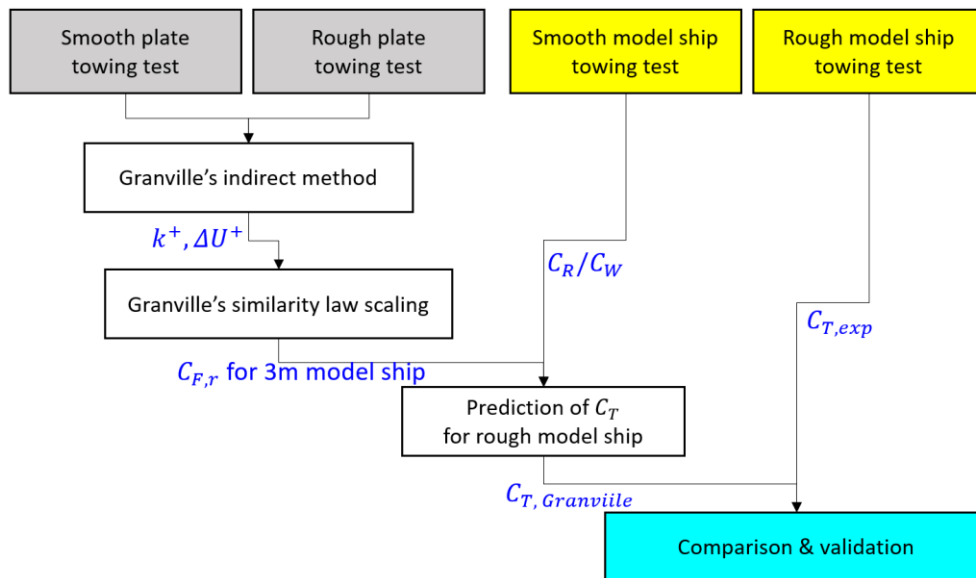


Figure 4.1 Schematic illustration of the methodology in Chapter 4

4.2.2. Experimental setup

4.2.2.1. Towing tank

The towing tests were conducted in the Kelvin Hydrodynamics Laboratory (KHL) of the University of Strathclyde. The tank has a dimension of 76.0 m (L) × 4.6 m (W) × 2.5 m (D). The tank is equipped with a digitally controlled towing carriage, a state-of-the-art absorbing wave maker, and a highly effective sloping beach. The carriage has a velocity range of 0-5 m/s. Fresh water was used in the experiments, wherein the water temperature was monitored during the tests. Figure 4.2 shows the towing carriage in the KHL.



Figure 4.2 The towing carriage of the Kelvin Hydrodynamics Laboratory

4.2.2.2. Flat plate towing test

The flat plate used in this study was manufactured from 304 stainless steel grade sheet stock. Figure 4.3 illustrates the experimental setup used for the flat plate towing test. The plate has a thickness of 5 mm, and the leading edge of the plate was shaped to a radius of 2.5 mm while the trailing edge was kept sharp, which is the same as the plate used by Demirel et al. (2017a). The flatness of the plates, as well as their dimensions were checked using a CNC (Computer Numerical Control) machine. After being smoothed and polished, the plate was installed on a custom-built test rig on the towing carriage, and it was carefully aligned with the centreline of the tank in order to minimise side forces.

The flat plate was towed in smooth condition first, at the speed range of 1.5 – 4.5 m/s. After finishing the smooth plate test, the same plate was coated with Clarke Aluminium Oxide Abrasive Powder, 60-80 grit, to create a rough surface. Then towing tests in the rough condition were carried out at the same speed range. Figure 4.4 shows the smooth flat plate and the same plate coated with the sand grit (aluminium oxide abrasive powder). The details of the measurement of the surface roughness and the choice of the representative roughness height, k , can be found in section 4.3.3.

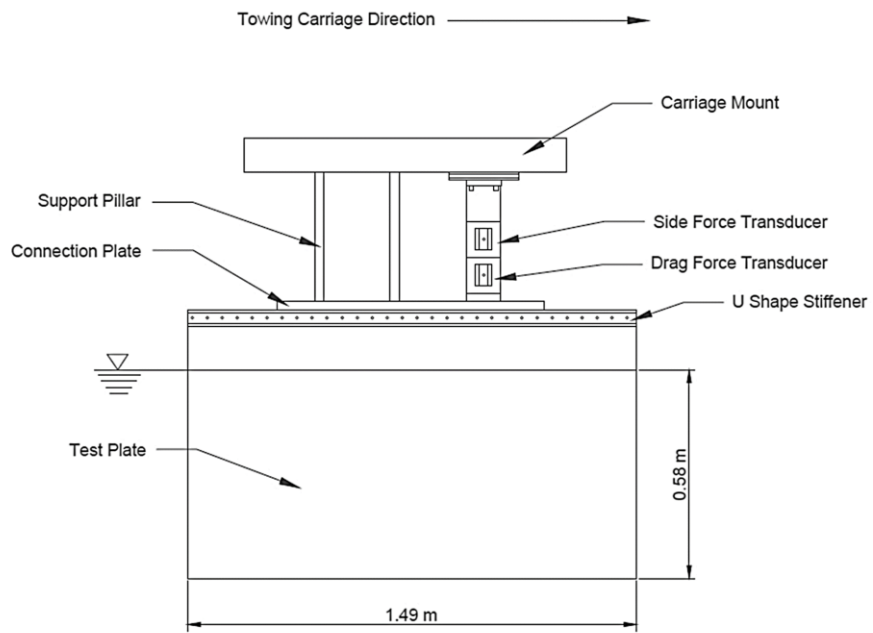


Figure 4.3 Experimental setup for flat plate towing test



(a) Flat plate in smooth condition



(b) Flat plate in rough condition

Figure 4.4 Flat plate used in this study, (a) smooth condition, (b) rough condition

4.2.2.3. Model ship towing test

In this study, a model of the KRISO Container Ship (KCS) was used for the model ship towing tests. The principal particulars of the KCS are given in Table 4.1. The model was built at a scale factor of 75 and towed without a rudder or appendages. Figure 4.5 illustrates the experimental setup used for the towing tests. During the test, the model was free to trim and sink. Two Linear Variable Differential Transducers (LVDT) were used to measure the sinkage at the midship point and the stern, then using the sinkage values at the two points, the trim angle was calculated using trigonometry. A load cell was attached at the tow point to measure the total resistance of the model ship.

As with the flat plate towing test, the model ship was first towed in smooth condition (at the speed range of 1.04-1.54 m/s). After the smooth towing test, the model ship was coated with the same sand grit (aluminium oxide abrasive powder) as applied to the flat plate. Then the rough model ship was towed at the same speed range. Figure 4.6 shows the smooth model ship and the same model ship in the rough condition.

Table 4.1 Principal particulars of the KCS in full-scale adapted from Kim et al. (2001) and Larsson et al. (2013).

Parameters		Full-scale	Model-scale
Scale factor	λ	1	75
Length between the perpendiculars	L_{PP} (m)	230	3.0667
Length of waterline	L_{WL} (m)	232.5	3.1
Beam at waterline	B_{WL} (m)	32.2	0.4293
Depth	D (m)	19.0	0.2533
Design draft	T (m)	10.8	0.144
Wetted surface area w/o rudder	S (m ²)	9424	1.6753
Displacement	∇ (m ³)	52030	693.733
Block coefficient	C_B	0.6505	0.6505
Design speed	V (knot, m/s)	24	1.426
Froude number	F_n	0.26	0.6505
Centre of gravity	KG (m)	7.28	0.0971
Metacentric height	GM (m)	0.6	0.008

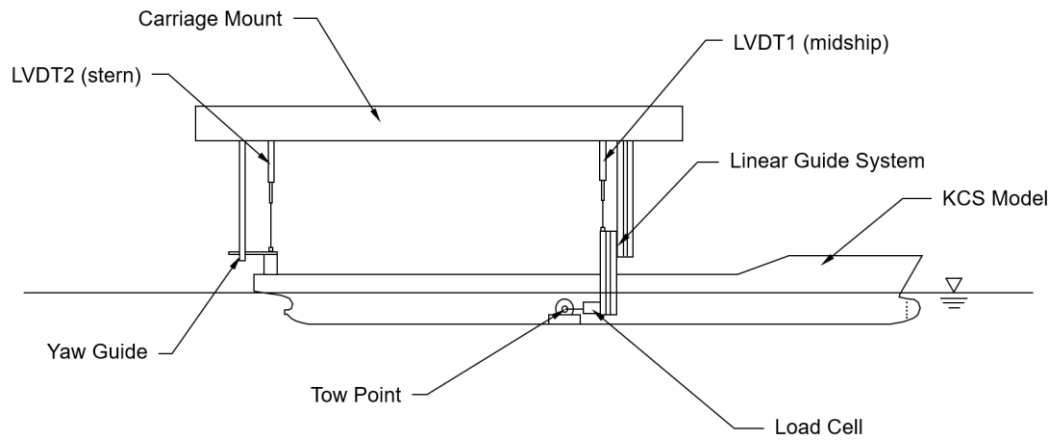


Figure 4.5 Experimental set up for model ship towing test



(a) KCS model in smooth condition



(b) KCS model in rough condition

Figure 4.6 KCS model used in this study (a) smooth condition, (b) rough condition

4.2.3. Roughness function determination

The roughness function for the given surface roughness was obtained using the results from the flat plate tests. To separate the frictional resistance coefficient, C_F , of the towed plates from the total resistance coefficient, C_T , the following assumptions were made: i) The total resistance values of the flat plates consist of the frictional resistance, C_F , and the residuary resistance coefficient, C_R ; ii) the frictional resistance of the smooth plate, C_F , follows the Kármán-Schoenherr friction line (Schoenherr, 1932), as

$$\frac{0.242}{\sqrt{C_F}} = \log (Re_L C_F) \quad (4.1)$$

where, Re_L is the Reynolds number based on the length of the plate; iii) the residuary resistance values, C_R , are functions of the Froude number, F_n , and the roughness effect on C_R is negligible.

Using the above assumptions, the frictional resistance for the rough flat plate can be determined as

$$C_{R,s} = C_{T,s} - C_{F,s} \quad (4.2)$$

$$C_{R,r} = C_{R,s} \quad (4.3)$$

$$C_{F,r} = C_{T,r} - C_{R,s} \quad (4.4)$$

where, the second subscript 's' and 'r' indicate the smooth and rough surface conditions, respectively. It is of note that this calculation is only valid for the C_F values obtained at the same Froude number, F_n , and hence the same towing speed in this study.

Using the obtained frictional resistance values for the rough plate, $C_{F,r}$, the roughness functions, ΔU^+ , and the corresponding roughness Reynolds number, k^+ , were calculated following the indirect roughness determination procedure for towed plates, also known as the *overall method*, which was proposed by Granville (1958; 1987). In this method, the k^+ and ΔU^+ values can be determined as follows.

$$\Delta U^+ = \sqrt{\frac{2}{C_{F,s}}} - \sqrt{\frac{2}{C_{F,r}}} - 19.7 \left(\sqrt{\frac{C_{F,s}}{2}} - \sqrt{\frac{C_{F,r}}{2}} \right) - \frac{1}{\kappa} \Delta U^{+'} \sqrt{\frac{C_{F,r}}{2}} \quad (4.5)$$

$$k^+ = \left(\frac{k}{L} \right) \left(\frac{Re_L C_F}{2} \right) \sqrt{\frac{2}{C_{F,r}}} \left[1 - \frac{1}{\kappa} \sqrt{\frac{2}{C_{F,r}}} + \frac{1}{\kappa} \left(\frac{3}{2\kappa} - \Delta U^{+'} \right) \frac{C_{F,r}}{2} \right] \quad (4.6)$$

where, κ is the von Kàrmàn constant (=0.41) and ΔU^{+} is the slope of the roughness function as a function of $\ln k^{+}$, and k is the representative roughness height.

4.2.4. Granville's boundary layer similarity law scaling

In order to scale the frictional resistance coefficient of the 1.5 m rough plate to the 3 m model ship, the similarity law scaling procedure of Granville (1958; 1978) was used with the $C_{F,r}$, ΔU^{+} , and k^{+} values obtained from the flat plate towing tests.

Figure 4.7 schematically illustrates the scaling procedure used in this study following Granville's similarity law analysis. The first step is drawing a smooth friction coefficient line, $C_{F,s}$, against $\log Re_L$. In this study, the Kàrmàn-Schoenherr friction line was used (Equation 4.1). The second step is shifting the smooth friction line by $\Delta U^{+}\kappa/\ln(10)$ in the $\log Re_L$ direction, in order to represent the rough friction coefficient, $C_{F,r}$. The third step is plotting the line of the constant L_{plate}^{+} value satisfying the following equation.

$$Re_L = \frac{L_{plate}^{+}}{\sqrt{\frac{C_F}{2} \left(1 - \frac{1}{\kappa} \sqrt{\frac{C_F}{2}} \right)}} \quad (4.7)$$

where L_{plate}^{+} is a non-dimensional length of the plate defined by

$$L_{plate}^{+} = \frac{L_{plate} U_{\tau}}{\nu} \quad (4.8)$$

The fourth step is shifting the line of constant L_{plate}^{+} by $\log(L_{model\ ship}/L_{plate})$ in the $\log Re_L$ direction. This line is termed as $L_{model\ ship}^{+}$. The final step is finding the intersection of the $C_{F,r}$ line and the $L_{model\ ship}^{+}$ line. The $C_{F,r}$ and Re_L values at the

intersection represent the frictional resistance of the KCS model, and the corresponding Reynolds number, respectively.

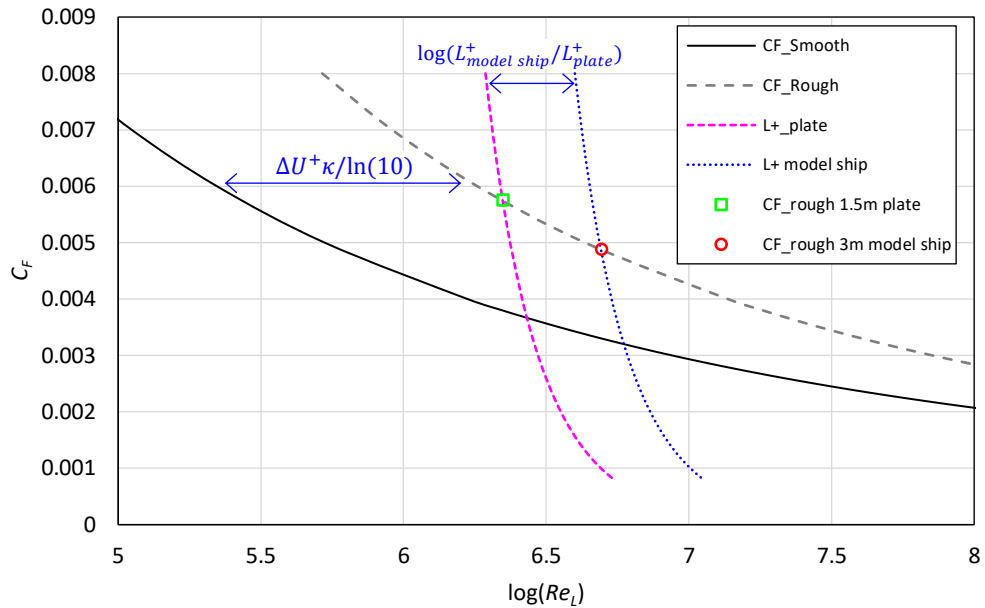


Figure 4.7 Schematic of Granville's similarity law scaling procedure

4.2.5. Uncertainty analysis

Uncertainty analysis was conducted to estimate the uncertainties of the measurements in the tests, following the ITTC recommended procedures (ITTC, 2014). The precision limits were determined through repeatability test at the lowest and highest towing speeds, while the bias limits were calculated considering the uncertainties associated with calibration, data acquisition, data reduction and conceptual bias.

Table 4.2 shows the absolute and relative overall uncertainties of the measurements at the lowest speed and the highest speed. As shown in the table, the overall 95% confidence limits for the frictional resistance for the rough plate, $C_{F,r}$, were $\pm 2.2\%$ and $\pm 0.9\%$ at the lowest and highest speeds, respectively. And the overall uncertainties for the roughness functions, ΔU^+ , were $\pm 5.5\%$ and $\pm 0.5\%$, at the lowest and highest

speeds, respectively, while the uncertainties for the total resistance of the rough model ship, $C_{T,r}$, were $\pm 2.1\%$ and $\pm 1.7\%$, respectively.

Table 4.2 Overall uncertainties of the measurements with 95% confidence level, where τ and σ are trim and sinkage, respectively

	Parameter	Lowest speed		Highest speed	
		Overall Uncertainty	%	Overall Uncertainty	%
Flat plate	$C_{T,s}$	$\pm 9.07E-05$	$\pm 2.1\%$	$\pm 3.21E-05$	$\pm 0.9\%$
	$C_{F,s}$	$\pm 6.92E-06$	$\pm 0.2\%$	$\pm 6.24E-07$	$\pm 0.02\%$
	$C_{T,r}$	$\pm 9.10E-05$	$\pm 1.4\%$	$\pm 4.36E-05$	$\pm 0.7\%$
	$C_{F,r}$	$\pm 1.29E-04$	$\pm 2.2\%$	$\pm 5.41E-05$	$\pm 0.9\%$
	ΔU^+	$\pm 2.76E-01$	$\pm 5.5\%$	$\pm 3.72E-02$	$\pm 0.5\%$
Model ship	$C_{T,s}$	$\pm 6.09E-05$	$\pm 1.4\%$	$\pm 4.95E-05$	$\pm 1.0\%$
	τ_s (°)	$\pm 1.09E-01$	$\pm 10.8\%$	$\pm 2.00E-01$	$\pm 8.9\%$
	σ_s (mm)	$\pm 2.65E-01$	$\pm 8.0\%$	$\pm 4.25E-01$	$\pm 4.4\%$
	$C_{T,r}$	$\pm 1.20E-04$	$\pm 2.1\%$	$\pm 1.16E-04$	$\pm 1.7\%$
	τ_r (°)	$\pm 1.02E-01$	$\pm 11.3\%$	$\pm 1.84E-01$	$\pm 10.5\%$
	σ_r (mm)	$\pm 2.39E-01$	$\pm 7.8\%$	$\pm 4.28E-01$	$\pm 5.3\%$

4.3. Results

4.3.1. Flat plate towing test

Figure 4.8 compares the total resistance coefficients and the frictional resistance coefficients for the smooth and rough plates obtained from the towing tests. As mentioned earlier (Equation 4.1- 4.4), the difference between the smooth C_T obtained from the towing test and the theoretical C_F was defined as the residuary resistance, C_R . Then the frictional resistance for the rough plate was determined as the difference between the total resistance and the residuary resistance at the same speed ($C_{F,r} = C_{T,r} - C_R$).

As shown in Figure 4.8, the frictional resistance of the rough plate first increases with increasing Reynolds number and tends to converge around $Re_L = 3.5 \times 10^6$ (i.e. $C_{F,r}$ is independent of Re_L), suggesting the fully rough regime is reached beyond this point, whereas the values below remain in the transitionally rough regime (Flack and Schultz, 2014).

The increases in C_F of the flat plates due to the roughness effect were observed to be 50% and 94% at the lowest and the highest speeds, respectively.

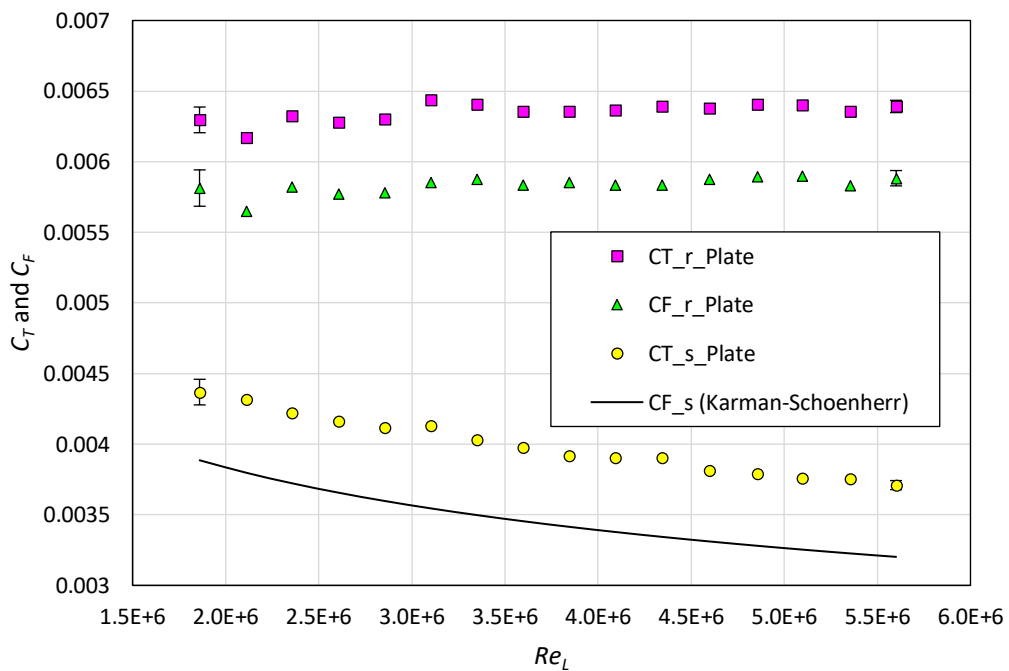


Figure 4.8 C_T and C_F values of the flat plate in smooth and rough conditions

4.3.2. Model ship towing test

Figure 4.9 shows the total resistance coefficient values, C_T , obtained from the towed model ship in the smooth and rough conditions. As can be seen, both the smooth and rough C_T show similar overall trends, while the magnitude of the rough C_T is

significantly higher than that of the smooth C_T . The increases in C_T values due to the roughness effect were observed to be 30 % and 32% at the lowest and highest speeds, respectively.

Figure 4.10 compares the trim, τ , of the smooth and rough model ships, as well as the sinkage, σ , measured at the midship point ($\sigma_{midship}$) and the stern of the model ship (σ_{stern}). As observed in this figure, the roughness effect on the τ and σ values are minor, but the effects increase with increasing speeds. The midship sinkage values, σ , for the rough hull were observed to be smaller than those of smooth hull, while the roughness effect on the stern sinkage was negligible. As a result, the trim angles, τ , show decreases due to the roughness effect.

This effect of the surface roughness on the trim and sinkage is thought to be related to the pressure distribution, that is, the surface roughness altered the pressure distribution along the hull compared with the smooth case.

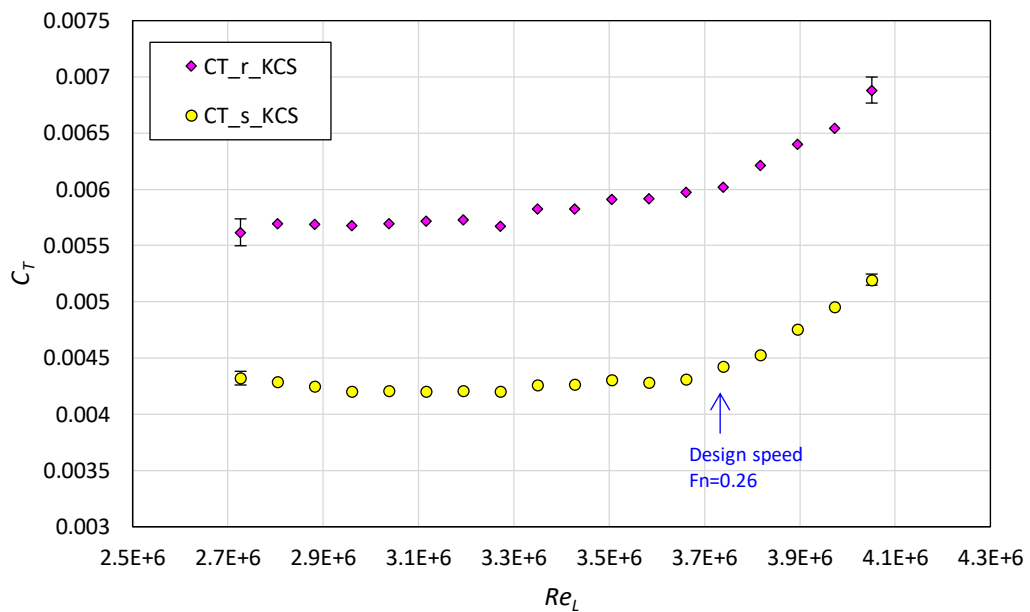


Figure 4.9 C_T values of the model ship in smooth and rough conditions

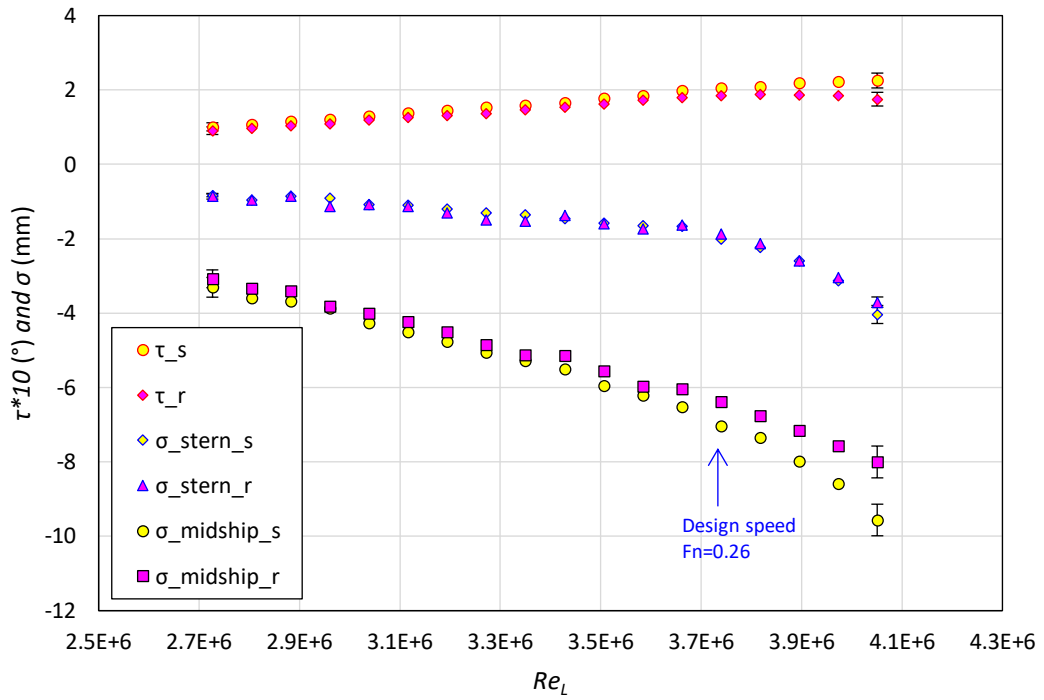


Figure 4.10 τ and σ values for the model ship in smooth and rough conditions

4.3.3. Roughness function determination

As explained in section 4.2.3, the results obtained from the flat plate towing tests were used to calculate the roughness function following the indirect method for towed plates (*overall method*), presented by Granville (1987). The surface roughness of the flat plate was measured using a *TQC Sheen B.V.* © Hull Roughness Gauge, which measures the maximum peak to trough roughness height over a 50 mm interval, Rt_{50} , (TQC, 2019). The average Rt_{50} value of the plate was measured to be 353 μm .

Figure 4.11 compares the Colebrook type roughness function of Grigson (1992), the analytical fit of Cebeci and Bradshaw (1977) based on the sand grain roughness functions of Nikuradse (1933), and the roughness functions from the current study, based on the different choices of the representative roughness heights, k .

As shown in the figure, when the representative roughness height is chosen as $k = Rt_{50}$, the roughness functions lie between Colebrook-type and Nikuradse-type roughness functions. When k is set to $1.73Rt_{50}$, the roughness function shows excellent agreement with the Nikuradse roughness function. On the other hand, when $k = 0.4Rt_{50}$ is used, the roughness function showed deviations with the Colebrook-type roughness function at low k^+ regions. This can be mostly attributed to the fact that the current rough surfaces showed behaviours of the transitionally rough regime (Figure 8), resulting in inflectional behaviour in the roughness function. Therefore, a better agreement was achieved with the inflectional Nikuradse-type roughness function than the monotonic Colebrook type roughness function. For comparison, the results were also plotted using $k = 0.75Rt_{50}$, which was suggested by Schultz and Flack (2003), for sandpaper roughness.

It is worthwhile to mention that in the current study the choice of the representative roughness height, k , does not affect the roughness function values, ΔU^+ , but only changes the roughness Reynolds number, k^+ . Therefore, the choice of the representative roughness height does not affect any results of this study.

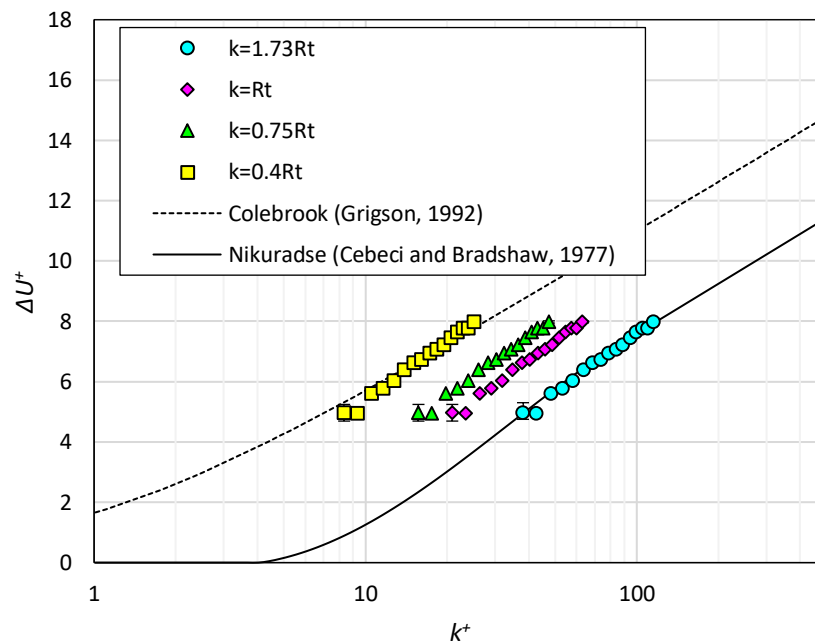


Figure 4.11 Roughness functions, based on the different choices of the representative roughness height

4.3.4. Extrapolation of the frictional resistance

As explained in section 4.2.4, the frictional resistance of the 1.5 m rough plate, $C_{F,r}$, was extrapolated to the length of the model ship (3.0 m) using the boundary layer similarity law analysis, proposed by Granville (1958; 1978). The extrapolated $C_{F,r}$ values for the 3.0 m flat plate was assumed to be equal to that of the model ship in the rough condition. In the extrapolation procedure the Nikuradse type roughness function model of Cebeci and Bradshaw (1977) was used (with the use of $k = 1.73Rt_{50}$), rather than using the discrete ΔU^+ values, to ensure that the extrapolated speed range covers the towing speeds of the model ship. Figure 4.12 compares the frictional resistance for the rough flat plate obtained from the towing test and the extrapolated $C_{F,r}$ values for the model ship.

Shown for comparison in Figure 4.13 is the extrapolated frictional resistance, $C_{F,r,Granville}$ for the model ship, smooth frictional resistance, $C_{F,s}$, obtained from the Kármán-Schoenherr friction line, and the total resistance coefficients, $C_{T,s}$ and $C_{T,r}$ measured from the towing tests. It is of note that the increases in the frictional resistance for the model ship were 33% and 46% at the lowest and highest towing speeds of the model ship, respectively.

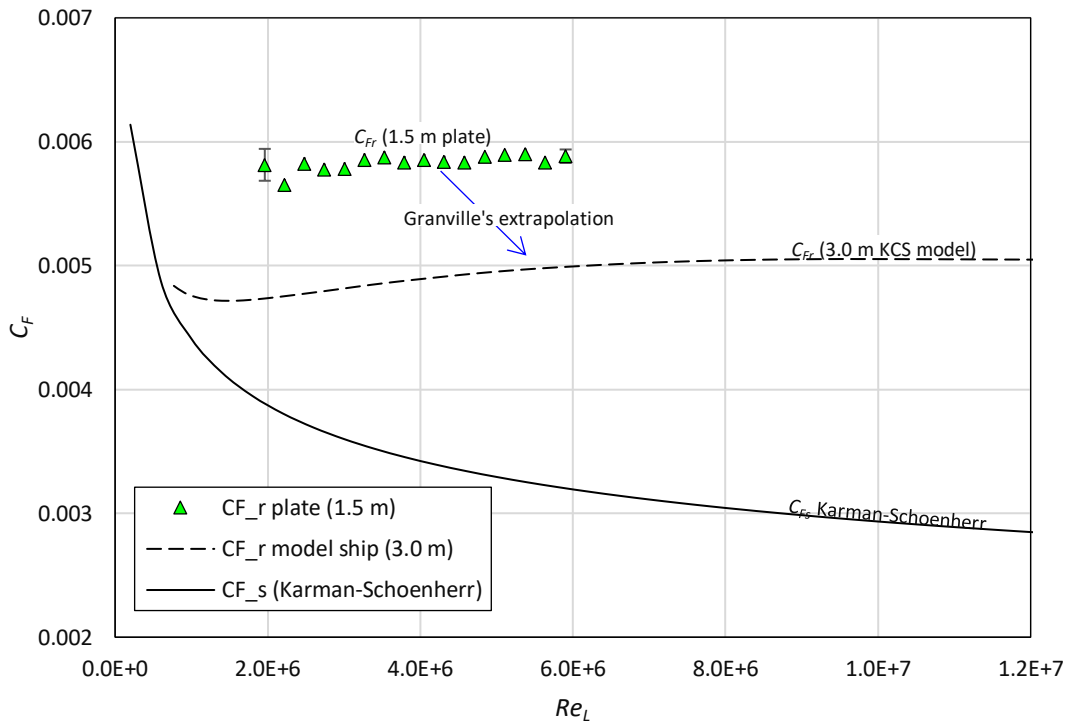


Figure 4.12 $C_{F,r}$ values for the rough plate and the extrapolated $C_{F,r}$ for the rough KCS model using Granville's similarity law scaling

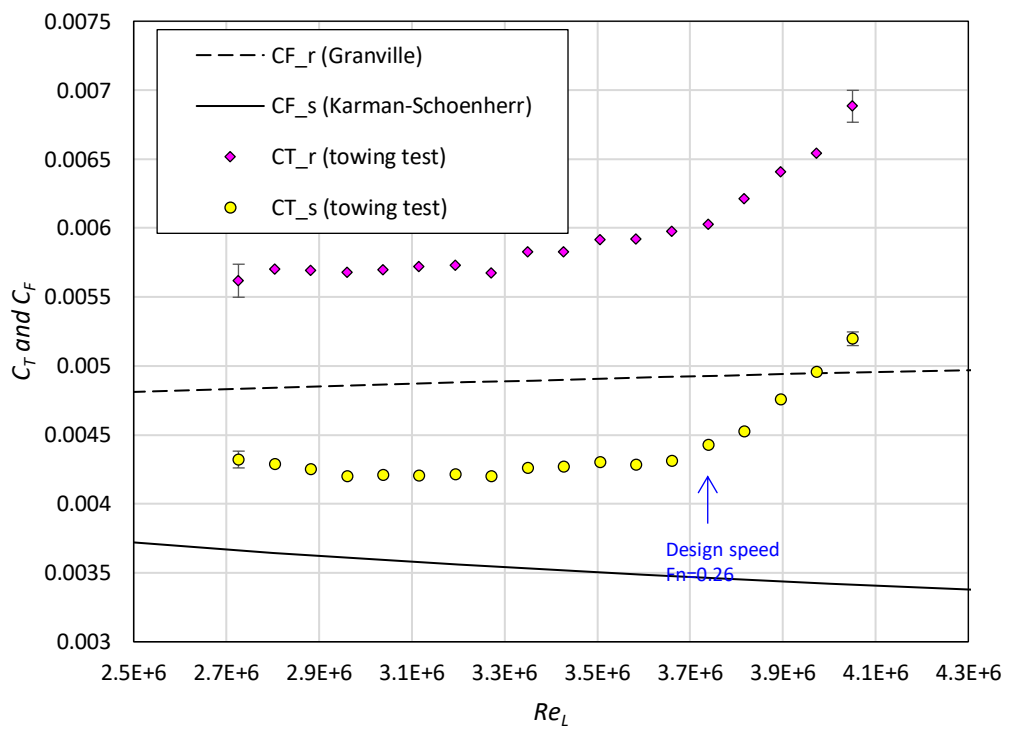


Figure 4.13 C_T and C_F values for the model ship in smooth and rough conditions

4.3.5. Prediction of the total resistance and comparison with the experimental data

Using the extrapolated frictional resistance values for the rough model ship ($C_{F,r,Granville}$), the total resistance coefficient in the rough condition, $C_{T,r}$, was predicted and compared with the experimental results obtained from the model ship towing test in the rough condition. Two different methods were used for the prediction, namely the *2D method* and the *3D method*.

In the *2D method*, i.e. Froude's method, which considers the roughness effect on the frictional resistance only, the ship total resistance was considered to consist of the sum of the frictional resistance and the residuary resistance ($C_T = C_F + C_R$). The residuary resistance is assumed to be independent of the surface roughness. Then the total resistance for the rough model ship, $C_{T,r,2D}$, is determined by

$$C_{R,s} = C_{T,s} - C_{F,s} \quad (4.7)$$

$$C_{R,r} = C_{R,s} \quad (4.8)$$

$$C_{T,r,2D} = C_{F,r,Granville} + C_{R,r} \quad (4.9)$$

Equation 4.9 can be written alternatively as

$$C_{T,r,2D} = C_{T,s} + \Delta C_F \quad (4.10)$$

where, ΔC_F is the added resistance due to the surface roughness ($\Delta C_F = C_{F,r,Granville} - C_{F,s}$).

In the *3D method*, i.e. Hughes method, which considers the roughness effect on the frictional resistance and the viscous pressure resistance, the ship total resistance was considered to consist of the frictional resistance, the viscous pressure resistance and the wave making resistance ($C_T = C_F + C_{VP} + C_W$, or $C_T = (1 + k)C_F + C_W$), where

$1 + k$ is the form factor. The wave making resistance and the form factor were assumed to be independent of the surface roughness. Then the total resistance for the rough model ship, $C_{T,r,3D}$, is determined by

$$C_{W,s} = C_{T,s} - (1 + k)C_{F,s} \quad (4.11)$$

$$C_{W,r} = C_{W,s} \quad (4.12)$$

$$C_{T,r,3D} = (1 + k)C_{F,r,Granville} + C_{W,r} \quad (4.13)$$

Equation 13 can be written alternatively as

$$C_{T,r,3D} = C_{T,s} + (1 + k)\Delta C_F \quad (4.14)$$

For the calculation, the experimental form factor value of KCS, $1 + k = 1.2$, was used (Van et al., 2011).

Figure 4.14 compares the total resistance coefficients for the rough model ship, predicted from *2D method* and *3D method*, and the experimental $C_{T,r}$ values measured from the towing test. As shown in the figure, a good agreement was achieved between the experimental $C_{T,r}$ values and the predicted $C_{T,r}$ values. This suggests that the use of Granville's similarity law scaling method is valid for the prediction of the roughness effect on ship resistance.

It can be seen from the figure that, the results predicted using *3D method* show better agreement with the experimental data compared to those of *2D method*. Therefore, it can be deduced that the surface roughness not only increases the frictional resistance but also increases the viscous pressure resistance. This effect on the viscous pressure resistance has been also observed from several CFD studies (e.g. Demirel et al. (2017b)) but has not been proven experimentally.

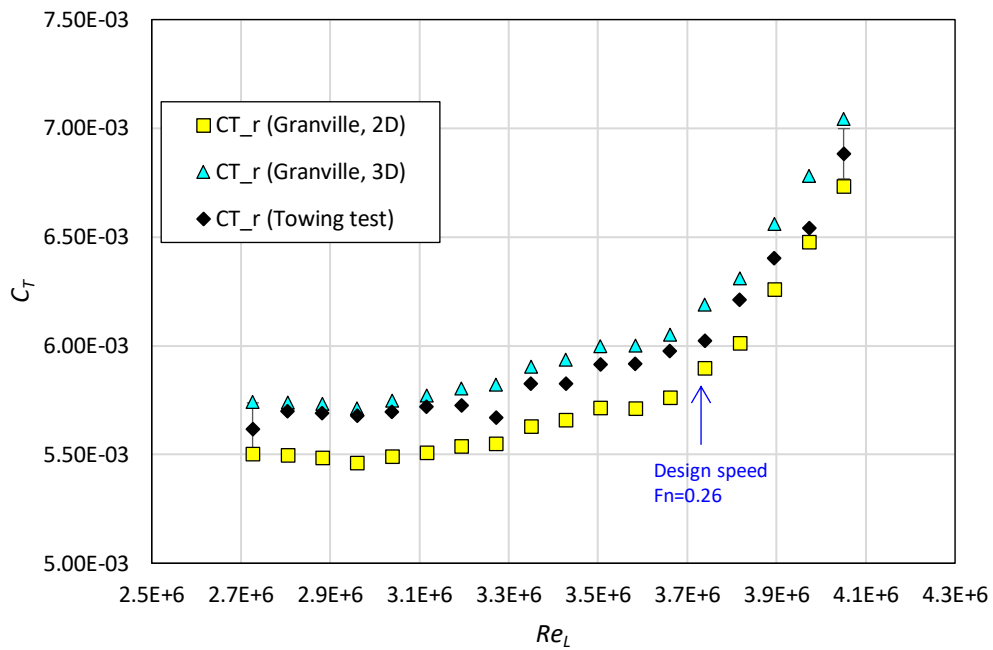


Figure 4.14 $C_{T,r}$ values predicted from the two different methods, and those measured from the model ship towing test

4.4. Chapter summary and conclusions

Towing tests involving a flat plate and a model ship were conducted in smooth and rough conditions for the investigation of the effect of roughness on ship resistance, as well as to validate the use of Granville’s similarity law scaling. In order to roughen the surfaces of the plate and model ship, sand grit (aluminium oxide abrasive powder) was applied.

The plate and the model ship were towed in smooth and rough conditions at a range of speeds. Significant increases in the frictional resistance of the towed plate (up to 94%) and the total resistance of the model ship (up to 32%), were observed due to the rough surfaces, while changes in the trim and sinkage of the model ship were also identified.

The results of the towing tests were used to calculate the roughness function for the rough surface. Using the flat plate towing test results as well as the roughness function,

the frictional resistance for the rough plate was extrapolated to the length of the model ship using Granville's similarity law scaling method.

Utilising the extrapolated result, the total resistance of the model ship in the rough condition was predicted. For the prediction, two different methods were used (*2D method* and *3D method*). The predicted total resistance coefficients from both the methods showed good agreement with the results of the towing tests, suggesting that the use of Granville's similarity law scaling is valid for the prediction of roughness effect on ship resistance. The results also imply that the roughness effect on the viscous pressure resistance should be also considered for better prediction.

This study not only presents the investigations of the roughness effect on ship resistance, but also provides the first experimental validation of the use of Granville's similarity law scaling procedure for ship-shape bodies.

5. Validation of the CFD method for predicting the roughness effect

5.1. Introduction

As reviewed in Chapter 2, recently, the use of Computational Fluid Dynamics (CFD) is considered as an effective alternative to predict the roughness effect on ship resistance (Atlar et al., 2018). The merit of using CFD is that the distribution of the local friction velocity, u_τ , is dynamically computed for each discretised cell, and therefore the dynamically varying roughness Reynolds number, k^+ , and corresponding roughness function, ΔU^+ , can be considered in the computation. The 3D effects can also be taken into account, and the simulations are free from the scale effects if they are modelled in full-scale.

Correspondingly, there have been an increasing number of studies utilising CFD modelling to predict the effect of surface roughness on ship resistance (Demirel et al., 2014; Demirel et al., 2017b; Farkas et al., 2018). These recent studies suggest that the hull roughness does not only increase the ship frictional resistance but also affects the viscous pressure resistance and the wave making resistance.

Although several studies validated their CFD approaches by comparing the simulation results with the experimental data, the validations were merely performed against the towing tests of flat plates, which have no pressure gradients. That is to say, these validations are only valid for the frictional resistance, and thus it cannot guarantee the validity of it for other resistance components originating from the 3D shape of the ship hulls. Therefore, the validity of the CFD approach for 3D hulls still remains to be demonstrated.

To the best of the author's knowledge, there is no specific study to validate the CFD modelling of hull roughness against ship model test. Therefore, the aim of this chapter

is to fill this gap by developing a CFD model to predict the effect of the hull roughness and performing a validation study by comparing with the experimental data of a model ship with a rough surface.

This chapter is organised as follows: The methodology used in this chapter is explained in Section 5.2.1, while Section 5.2.2 covers the mathematical formulations of the CFD model. Section 5.2.3 explains the modified wall-function approach. In Section 5.2.4, a new roughness function model is proposed to represent the roughness function of the sand-grain roughness determined in Chapter 4. The details of the geometry and boundary conditions of the CFD simulations are discussed in Section 5.2.5. The mesh generation is presented in Section 5.2.6. In Section 5.2.7, the numerical uncertainties of the simulations are estimated based on the GCI method. Section 5.3.1 includes the validation study of the CFD simulations by comparing the results against the experimental results obtained in Chapter 4. In Section 5.3.2, the investigation of the roughness effect is expanded by decomposing the resistance components, and Section 5.3.3 investigates the roughness effect on the flow characteristics. Finally, the chapter summary and conclusions are presented in Section 5.4.

5.2. Methodology

5.2.1. Approach

A schematic illustration of the current study is shown in Figure 5.1. In this study, CFD models were developed to simulate the towing tests of the flat plate and KCS model ship conducted in Chapter 4 (Figure 4.3 – 4.6). In order to represent the surface roughness of the sand-grain surface, a roughness function model was proposed and employed in the wall-function of the CFD model. The simulation results of the flat plate and model ship in the smooth and rough surface conditions were then compared with the experimental data to demonstrate the validity of the CFD approach for predicting the effect of hull roughness on the ship resistance.

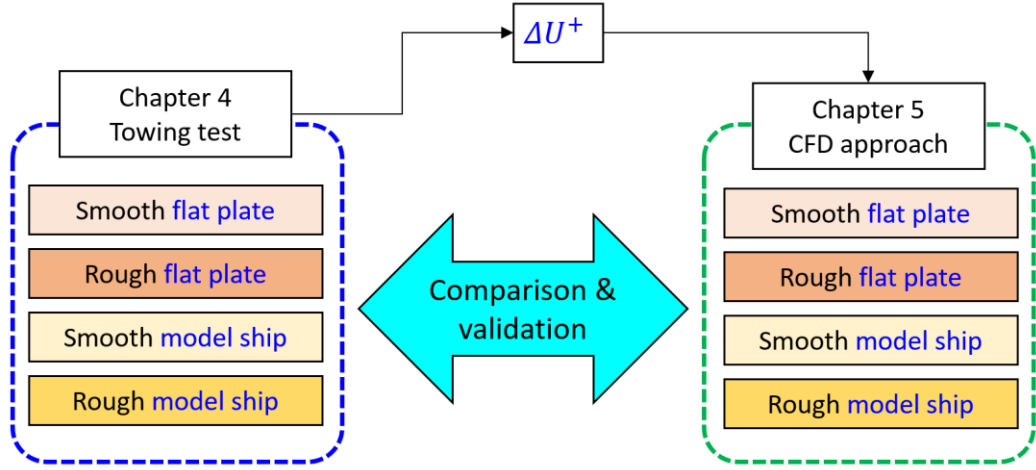


Figure 5.1 Schematic illustration of the methodology in Chapter 5

5.2.2. Mathematical formulations

The CFD models were developed based on the unsteady Reynolds-averaged Navier-Stokes (URANS) method using a commercial CFD software package, STAR-CCM+ (version 12.06).

The averaged continuity and momentum equations for incompressible flows may be given in tensor notation and Cartesian coordinates as in the following two equations (Ferziger and Peric, 2002).

$$\frac{\partial(\rho\bar{u}_i)}{\partial x_i} = 0 \quad (5.1)$$

$$\frac{\partial(\rho\bar{u}_i)}{\partial t} + \frac{\partial}{\partial x_j}(\rho\bar{u}_i\bar{u}_j + \rho\overline{u'_i u'_j}) = -\frac{\partial\bar{p}}{\partial x_i} + \frac{\partial\bar{\tau}_{ij}}{\partial x_j} \quad (5.2)$$

where, ρ is the density, \bar{u}_i is the averaged velocity vector, $\rho\overline{u'_i u'_j}$ is the Reynolds stress, \bar{p} is the averaged pressure, $\bar{\tau}_{ij}$ is the mean viscous stress tensor components. This viscous stress for a Newtonian fluid can be expressed as

$$\bar{\tau}_{ij} = \mu \left(\frac{\partial \bar{u}_i}{\partial x_j} + \frac{\partial \bar{u}_j}{\partial x_i} \right) \quad (5.3)$$

where, μ is the dynamic viscosity. Using the Boussinesq hypothesis, the Reynolds stress can be written as

$$-\rho \overline{u'_i u'_j} = \mu_t \left(\frac{\partial \bar{u}_i}{\partial x_j} + \frac{\partial \bar{u}_j}{\partial x_i} \right) - \frac{2}{3} \left(\rho k + \mu_t \frac{\partial \bar{u}_k}{\partial x_k} \right) \delta_{ij} \quad (5.4)$$

where, μ_t is the turbulent eddy viscosity, k is turbulent kinetic energy, and δ_{ij} is the Kronecker delta.

In the CFD solver, the computational domains were discretised and solved using a finite volume method. The second-order upwind convection scheme and a first-order temporal discretisation were used for the momentum equations. The overall solution procedure was based on a Semi-Implicit Method for Pressure-Linked Equations (SIMPLE) type algorithm.

The shear stress transport (SST) k - ω turbulence model (Menter, 1994) was used to predict the effects of turbulence, which combines the advantages of the k - ω and the k - ε turbulence model. This model uses a k - ω formulation in the inner parts of the boundary layer and a k - ε formulation in the free-stream for a more accurate near wall treatment with less sensitivity of inlet turbulence properties, which leads to a better prediction in adverse pressure gradients and separating flow. A second-order convection scheme was used for the equations of the turbulent model.

For the free surfaces, the Volume of Fluid (VOF) method was used with High Resolution Interface Capturing (HRIC).

5.2.3. Modified wall-function approach

As reviewed in Chapter 2, The generalised velocity profile in the log-law region for a rough surface is then given as

$$U^+ = \frac{1}{\kappa} \log y^+ + B - \Delta U^+ \quad (5.5)$$

The roughness function, ΔU^+ can be expressed as a function of the roughness Reynolds number, k^+ , defined as

$$k^+ = \frac{kU_\tau}{\nu} \quad (5.6)$$

where, k is the roughness height. It is of note that ΔU^+ simply vanishes in the case of a smooth condition. Once the roughness function, $\Delta U^+ = f(k^+)$, of the given roughness surface is known, it can be employed in the wall-function in the CFD model as in Equation 5.5. Then the surface boundary condition can represent the roughness effect on the velocity profile in the turbulent boundary layer.

5.2.4. Roughness function model

For the representation of the sand-grain rough surface of the flat plate and KCS model (Figure 4.4 and 4.6), the roughness function determined in Chapter 4 was used in the CFD model (Figure 4.11). In order to employ the roughness function in the wall-function of the CFD model, a roughness function model was proposed as,

$$\Delta U^+ = \begin{cases} 0 & \rightarrow k^+ < 3 \\ \frac{1}{\kappa} \ln \left(0.49k^+ - 3 \left(\frac{k^+ - 3}{25 - 3} \right) \right)^{\sin \left[\frac{\pi \log(k^+/3)}{2 \log(25/3)} \right]} & \rightarrow 3 \leq k^+ < 25 \\ \frac{1}{\kappa} \ln(0.49k^+ - 3) & \rightarrow 25 \leq k^+ \end{cases} \quad (5.7)$$

in which, κ is the von-Karman constant ($\kappa = 0.42$). It is of note that this roughness function model is based on the use of the maximum peak to trough roughness height over a 50 mm interval, Rt_{50} , as the reference roughness height ($k = Rt_{50} = 353 \mu\text{m}$) that was measured in Section 4.3.3 (Figure 4.11).

As shown in Figure 5.2, an excellent agreement was achieved between the proposed roughness function model and the experimental roughness function determined in Section 4.3.3.

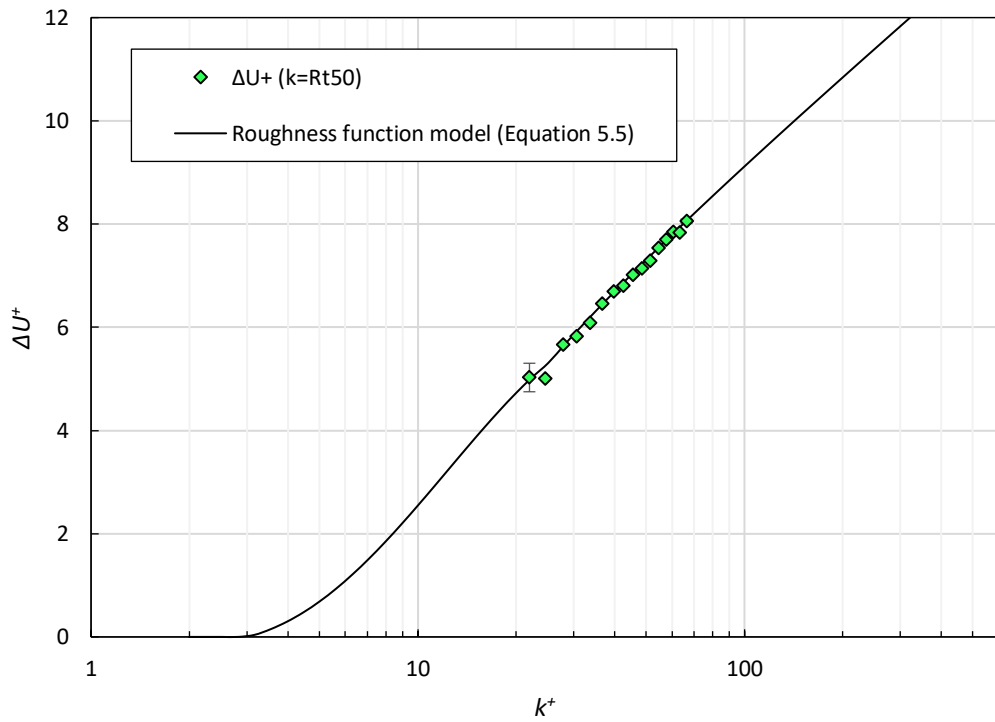


Figure 5.2 Experimental roughness function of the sand-grain surface and the proposed roughness function model

5.2.5. Geometry and boundary conditions

5.2.5.1. Flat plate simulation

Figure 5.3 shows the dimensions and the boundary conditions used for the flat plate simulations. The size of the computational domain was selected to represent the towing test in Chapter 4. For the two opposite faces at the x –direction, a velocity inlet boundary condition was applied for the inlet free-stream boundary condition, and a pressure outlet was chosen for the outlet boundary condition and the distances of these boundaries from the plate were chosen as used by Demirel et al (2014). The bottom and the side walls of the tank were selected as slip-walls and to represent the towing tank in the Kelvin Hydrodynamics Laboratory, where the towing tests were conducted. In order to save the computational time, a symmetry boundary condition was applied on the vertical centre plane ($y = 0$), so that only a half of the plate and the control volume were taken into account.

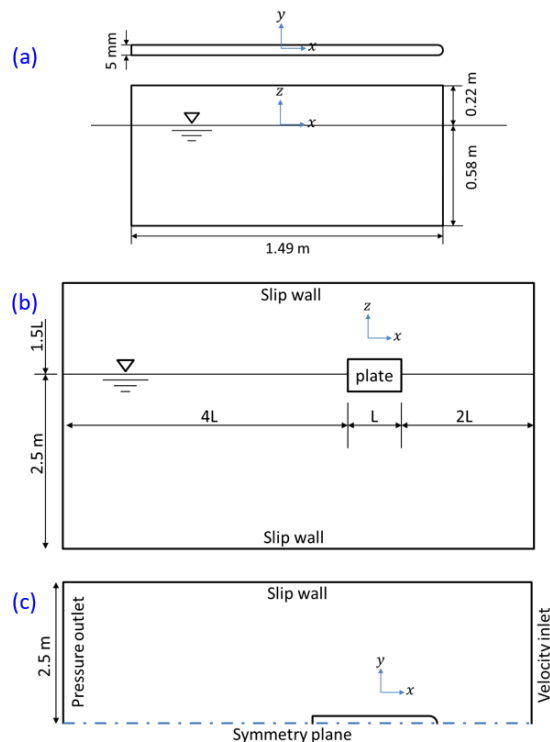


Figure 5.3 The dimensions and boundary conditions for the flat plate simulation model, (a) the flat plate, (b) profile view, (c) top view

2.1.1.1. KCS model ship simulation

Table 5.1 shows the principal particulars of the KCS. The CFD simulation of the KCS model was modelled, using the scale factor of 75 as used for the model ship in Chapter 4. As shown in Figure 5.4, two different computational domain types were used, namely double-body and free-surface simulations, for the purpose of decomposing the resistance components. In the double-body simulation, the free surface is replaced by the symmetry boundary condition such that there is no wave-making behaviour and hence there exist only the viscous resistance (i.e. $R_T = R_V = R_F + R_{VP}$). On the other hand, the free-surface simulations have the free surface and hence consider the wave-making behaviours such that the wave making resistance is included in the total ship resistance (i.e. $R_T = R_F + R_{VP} + R_W$).

The boundary conditions used for the free-surface and double-body simulations are shown in Figure 5.4. It is of note that the model ship was free to sink and trim in the simulations.

Table 5.1 Principal particulars of the KCS in full-scale and model-scale, adapted from Kim et al. (2001) and Larsson et al. (2013)

Parameters		Full-scale	Model-scale
Scale factor	λ	1	75
Length between the perpendiculars	L_{PP} (m)	230	3.0667
Length of waterline	L_{WL} (m)	232.5	3.1
Beam at waterline	B_{WL} (m)	32.2	0.4293
Depth	D (m)	19.0	0.2533
Design draft	T (m)	10.8	0.144
Wetted surface area w/o rudder	S (m ²)	9424	1.6753
Displacement	∇ (m ³)	52030	693.733
Block coefficient	C_B	0.6505	0.6505
Design speed	V (knot, m/s)	24	1.426
Froude number	F_n	0.26	0.6505
Centre of gravity	KG (m)	7.28	0.0971
Metacentric height	GM (m)	0.6	0.008

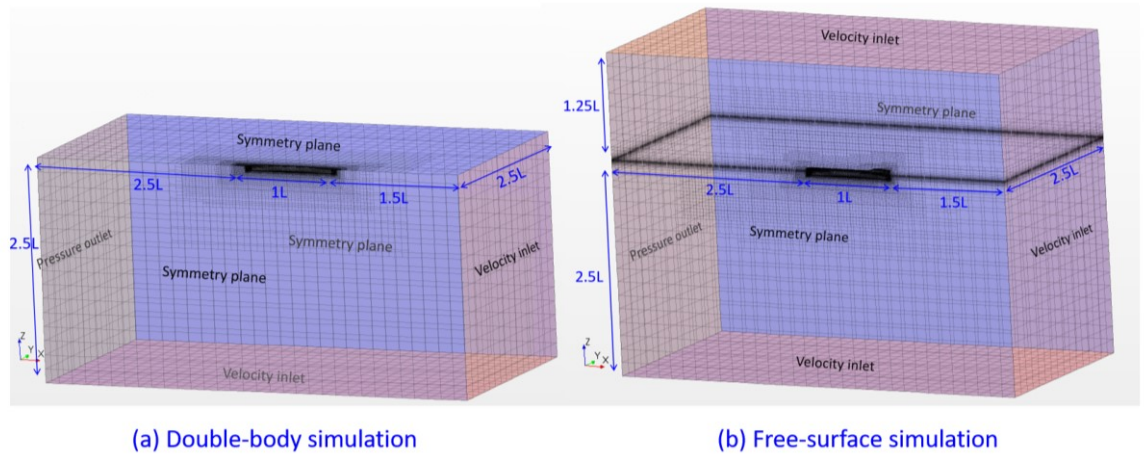


Figure 5.4 Computational domain and boundary conditions of the KCS model ship simulation, (a) double-body simulation, (b) free-surface simulation

5.2.6. Mesh generation

Mesh generation was performed using the built-in automated meshing tool of STAR-CCM+. Trimmed hexahedral meshes were used. Local refinements were made for finer grids in the critical regions, such as the regions near the free surface, leading and trailing edges of the flat plate and the bulbous bow of the KCS hull. The prism layer meshes were generated for near-wall refinement. The first layer cell thicknesses on the surfaces of the plate and the model ship were chosen such that the y^+ values are always higher than 30, and also higher than the roughness Reynolds number values, k^+ , as suggested by Demirel et al. (2017b). Fig. 5.5 and Fig. 5.6 show the volume meshes of the flat plate and KCS model ship simulations.

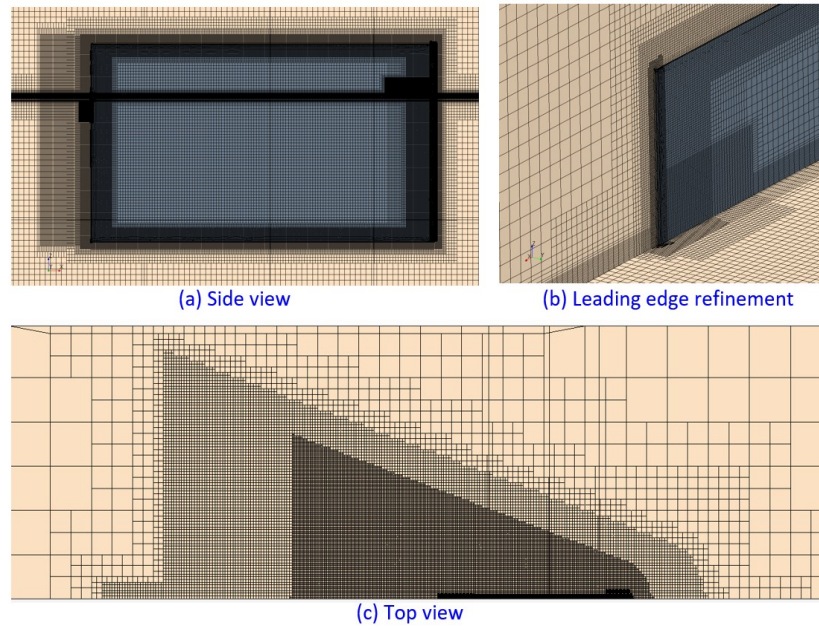


Figure 5.5 Volume mesh of the flat plate simulation

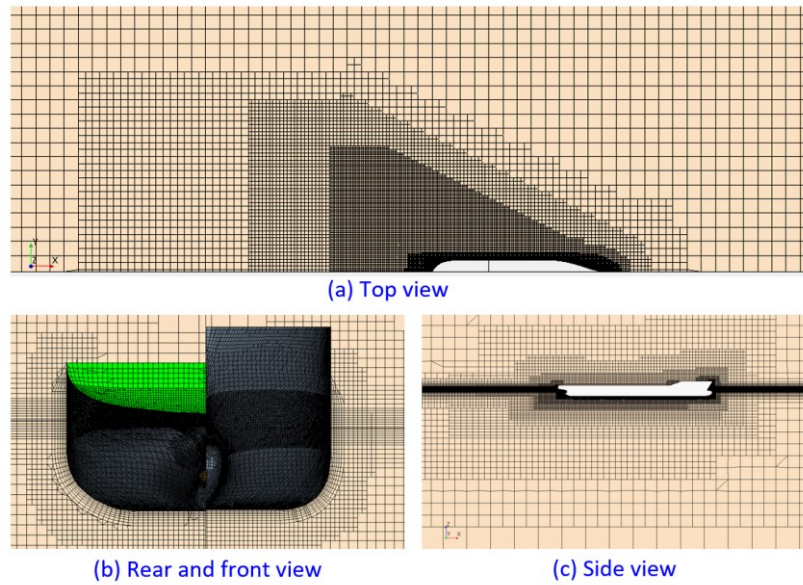


Figure 5.6 Volume mesh of the KCS model ship simulation

5.2.7. Uncertainty analysis

Convergence studies were carried out to assess the spatial and temporal uncertainties of the simulations. The Grid Convergence Index (GCI) method based on Richardson's extrapolation (Richardson, 1910) was used to estimate the numerical uncertainties. It

is of note that, although the GCI method was first proposed for spatial convergence studies, it can also be used for a temporal convergence study, as similarly used by Tezdogan et al. (2015) and Terziev et al. (2018).

According to Celik et al. (2008) the apparent order of the method, p_a , is determined by

$$p_a = \frac{1}{\ln(r_{21})} \left| \ln \left| \frac{\varepsilon_{32}}{\varepsilon_{21}} \right| + q(p_a) \right| \quad (5.8)$$

$$q(p_a) = \ln \left(\frac{r_{21}^{p_a} - s}{r_{32}^{p_a} - s} \right) \quad (5.9)$$

$$s = \text{sign} \left(\frac{\varepsilon_{32}}{\varepsilon_{21}} \right) \quad (5.10)$$

where, r_{21} and r_{32} are refinement factors given by $r_{21} = \sqrt[3]{N_1/N_2}$ for a spatial convergence study of a 3D model, or $r_{21} = \Delta t_1/\Delta t_2$ for a temporal convergence study. N and Δt are the cell number and time step, respectively. $\varepsilon_{32} = \phi_3 - \phi_2$, $\varepsilon_{21} = \phi_2 - \phi_1$, and ϕ_k denotes the key variables, i.e. C_T and n in this study.

The extrapolated value is calculated by

$$\phi_{ext}^{21} = \frac{r_{21}^p \phi_1 - \phi_2}{r_{21}^p - 1} \quad (5.11)$$

The approximate relative error, e_a^{21} , and extrapolated relative error, e_{ext}^{21} , are then obtained by

$$e_a^{21} = \left| \frac{\phi_1 - \phi_2}{\phi_1} \right| \quad (5.12)$$

$$e_{ext}^{21} = \left| \frac{\phi_{ext}^{21} - \phi_1}{\phi_{ext}^{21}} \right| \quad (5.13)$$

Finally, the fine-grid convergence index is found by

$$GCI_{fine}^{21} = \frac{1.25e_a^{21}}{r_{21}^p - 1} \quad (5.14)$$

2.1.1.2. Spatial convergence study

For the spatial convergence study, three different sets of mesh configurations were generated based on different resolutions, which are referred to as fine, medium and coarse meshes corresponding the cell numbers of N_1 , N_2 , and N_3 . Table 5.2 depicts the required parameters for the calculation of the spatial discretisation error. The simulations were conducted in the smooth surface condition, with the inlet speeds of 4.5 m/s ($Re_L = 5.6 \times 10^6$) and 1.426 m/s ($Fn = 0.26$, $Re_L = 3.7 \times 10^6$), for the flat plate and the KCS model (free-surface) simulations respectively. The total resistance coefficients, C_T , were used as the key variables.

As indicated in the table, the numerical uncertainties of the fine meshes (GCI_{fine}^{21}) for the flat plate and KCS hull simulations are 0.79% and 0.10% respectively. For accurate predictions, the fine meshes were used for further simulations in this study.

Table 5.2 Parameters used for the discretisation error for the spatial convergence study, key variable: C_T

	Flat plate simulation	KCS model simulation
N_1	451,271	601,355
N_2	913,737	887,428
N_3	2,258,814	1,306,433
r_{21}	1.57	1.21
r_{32}	1.42	1.21
ϕ_1	3.710E-03	4.471E-03
ϕ_2	3.753E-03	4.461E-03
ϕ_3	3.836E-03	4.494E-03
ε_{32}	8.34E-05	3.23E-05
ε_{21}	4.30E-05	-9.08E-06
s	1	-1
e_a^{21}	1.16%	0.20%
q	3.82E-01	-6.14E-03
p_a	2.31E+00	6.53E+00
ϕ_{ext}^{21}	3.686E-03	4.474E-03
e_{ext}^{21}	0.63%	-0.08%
GCI_{fine}^{21}	0.79%	0.10%

2.1.1.3. Temporal convergence study

For the temporal convergence study, three different time steps, namely Δt_1 , Δt_2 , and Δt_3 , were used for the simulations using the fine meshes. Table 5.3 shows the required parameters for the calculation of the temporal discretisation error. The simulations were conducted in the smooth surface condition, with the inlet speeds of 4.5 m/s ($Re_L = 5.6 \times 10^6$) and 1.426 m/s ($Fn = 0.26$, $Re_L = 3.7 \times 10^6$), for the flat plate and KCS model (free-surface) simulations respectively. The total resistance coefficients, C_T , were used as the key variables.

As indicated in the table, the numerical uncertainties ($GCI_{\Delta t_1}^{21}$) of the flat plate and the KCS hull simulations are 0.57% and 0.27% respectively when the smallest time steps are used (Δt_1). For accurate predictions, the smallest time steps (Δt_1) were used for further simulations in this study. For all the simulations, 10 inner iterations were used at each time step.

Table 5.3 Parameters used for the discretisation error for the temporal convergence study, key variable: C_T

	Flat plate simulation	KCS model simulation
Δt_1	0.02s	0.01s
Δt_2	0.04s	0.02s
Δt_3	0.08s	0.04s
r_{21}, r_{32}	2	2
ϕ_1	3.710E-03	4.471E-03
ϕ_2	3.709E-03	4.528E-03
ϕ_3	3.708E-03	4.539E-03
ε_{32}	-7.00E-07	1.09E-05
ε_{21}	-7.30E-07	5.78E-05
e_a^{21}	0.02%	1.29%
p_a	6.05E-02	2.41E+00
ϕ_{ext}^{21}	3.727E-03	4.457E-03
e_{ext}^{21}	-0.46%	0.30%
$GCI_{\Delta t_1}^{21}$	0.57%	0.37%

5.3. Results

5.3.1. Validation against experiment

5.3.1.1. Flat plate simulation

Figure 5.7 compares the total resistance coefficient, C_T , values in the smooth and rough surface conditions predicted from the current CFD simulations and the result of the flat plate towing tests in Chapter 4. The CFD simulations were conducted at the speed range of 1.5 – 4.5 m/s with 1.0 m/s interval, with the corresponding Reynolds numbers of $Re_L = 1.9 - 5.6 \times 10^6$.

As shown in the figure, the C_T values of the smooth flat plate predicted from the CFD simulations show an excellent agreement with the experimental data. Similarly, a good agreement was achieved between the CFD and EFD results for the C_T of the rough flat plate apart from the under-prediction of the C_T value at the lowest speed (1.5 m/s, $Re_L = 1.9 \times 10^6$). Considering the uncertainty of the experimental C_T values and the roughness function (Figure 5.2) as well as the numerical uncertainty of the simulation, this slight under-prediction is believed to be acceptable.

This agreement suggests the validity of the use of the current CFD approach (modified wall-function approach) to predict the increased skin friction due to the surface roughness, as similarly shown by Demirel et al. (2017b).

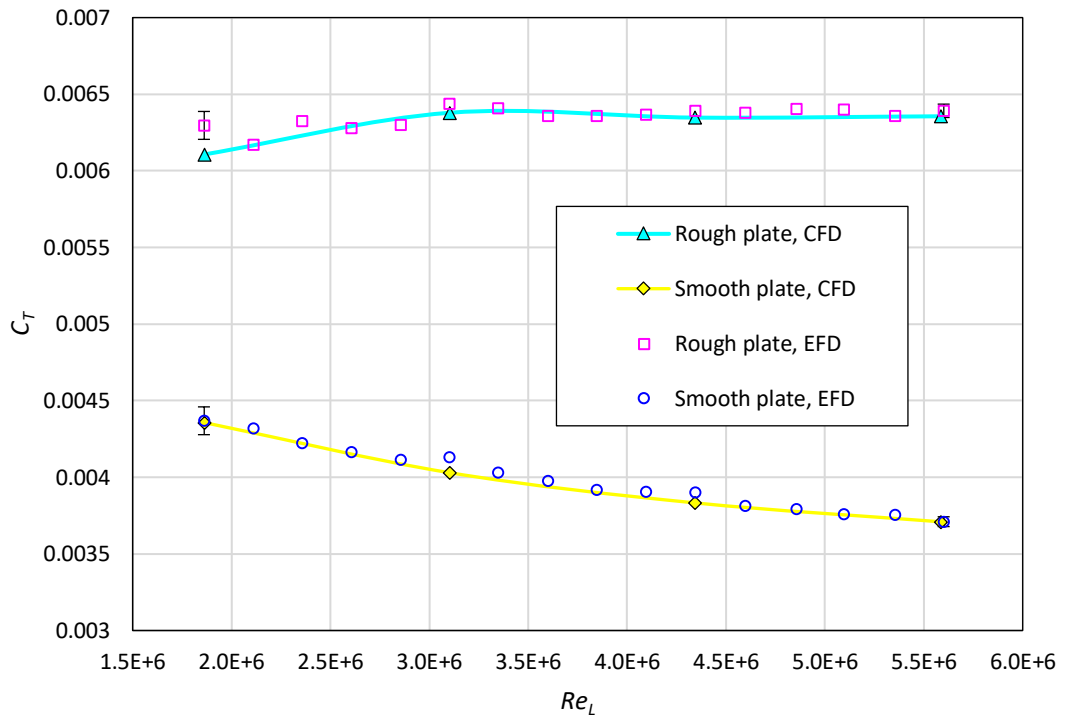


Figure 5.7 Total resistance coefficient, C_T , of the towed flat plate in the smooth and rough surface conditions, predicted from the current CFD simulations and the results of the towing test in Chapter 4

2.1.1.4. KCS model simulation (free-surface)

Although the use of the modified wall-function approach is validated against the flat plate towing tests, this does not necessarily guarantee the validity of using this method to predict the roughness effect on the ship resistance of a 3D hull. Therefore, this subsection presents the comparison between the CFD approach and the experimental result of the towing test of the KCS model ship in the smooth and rough surface conditions in Chapter 4.

Figure 5.8 shows a comparison of the C_T values of the KCS model ship predicted from the current CFD simulations and the experimental results. The CFD simulations were conducted at the speed range of 1.07 – 1.54 m/s, which correspond to the full-scale speed range 18 – 26 knots with 2 knots interval. The corresponding Reynolds numbers are $Re_L = 2.8 - 4.1 \times 10^6$, while the Froude numbers are $Fn = 0.195 -$

0.282. In both the smooth and rough surface conditions, the C_T values predicted from the CFD simulations agrees well with the experimental C_T values. Therefore, it suggests that the modified wall-function approach can accurately predict the effect of hull roughness on the total ship resistance, which includes the 3D effects. To the best of the author's knowledge this is the first validation of the CFD modelling of hull roughness against ship model test.

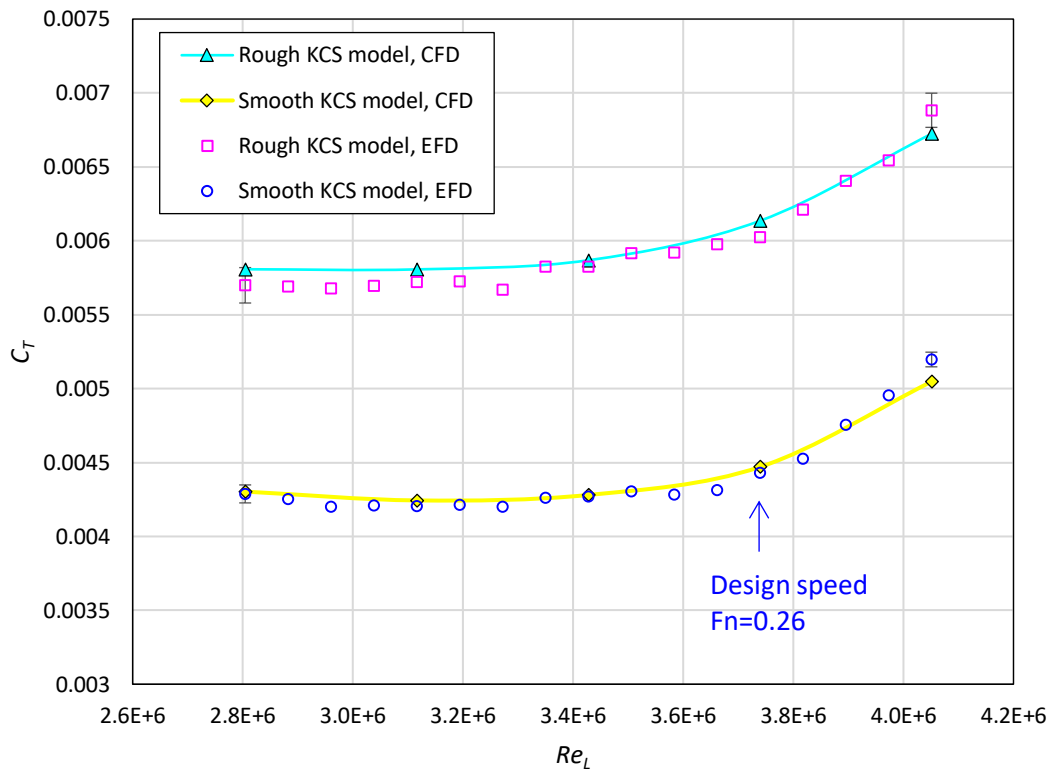


Figure 5.8 Total resistance coefficient, C_T , of the KCS model ship in the smooth and rough surface conditions, predicted from the current CFD simulations and the results of the towing test in Chapter 4

5.3.2. Effect of hull roughness on the ship resistance components

In the previous sub-section, the validity of the modified wall-function approach was demonstrated for predicting the effect of hull roughness on the ship total resistance. Therefore, it is worth utilising the benefits of using CFD for better understanding the roughness effect on the individual ship resistance components. Decompositions of the ship total resistance into the different resistance components are presented in this section.

Before investigating the effect of hull roughness on the resistance components, it would be timely to restate these components in detail. The resistance coefficients can be obtained by dividing the drag, R , with the dynamic pressure, $\frac{1}{2}\rho V^2$, and the wetted surface area of the ship hull, S , as

$$C = \frac{R}{\frac{1}{2}\rho S V^2} \quad (5.15)$$

The total ship resistance coefficient, C_T , can be decomposed into the two main components; the frictional resistance coefficient, C_F , and the residuary resistance coefficient, C_R , given by

$$C_T = C_F + C_R \quad (5.16)$$

The residuary resistance is can be further divided into the viscous pressure resistance coefficient, C_{VP} , and the wave making resistance coefficient, C_W , given by

$$C_R = C_{VP} + C_W \quad (5.17)$$

$$C_T = C_F + C_{VP} + C_W \quad (5.18)$$

The viscous pressure or also known as form drag is broadly assumed to be proportional to the frictional resistance (Lewis, 1988), with the use of form factor, k , as given

$$C_{VP} = kC_F \quad (5.19)$$

$$C_T = (1 + k)C_F + C_W \quad (5.20)$$

The sum of frictional resistance and the viscous pressure resistance is also referred to as viscous resistance, C_V , as

$$C_V = C_F + C_{VP} = (1 + k)C_F \quad (5.21)$$

2.1.1.5. Frictional resistance and residuary resistance

The total resistance coefficients, C_T , were divided into the frictional resistance coefficient, C_F , and the residuary resistance coefficient, C_R , by simply decomposing the total drag acting on the ship into the shear and pressure force components from the free-surface simulations.

The C_F and C_R values of the KCS model in the smooth and the rough conditions are shown in Figure 5.9. The C_F values for the rough KCS model remain rather consistent with the Reynolds numbers, while the smooth C_F values show a decreasing trend. This can be explained by the fact that C_F tends to lose its dependency to the Reynolds number when it approaches the fully rough regime (Nikuradse, 1933), as similarly observed by other studies (e.g. Demirel et al., 2017b)

On the other hand, the rough case shows larger C_R values than the smooth case, but the differences become smaller as the Reynolds number increases (which can be more clearly seen in Figure 5.10). To fine the rationale behind this observation, further investigation was carried out by decomposing the C_R into the C_{VP} and C_W .

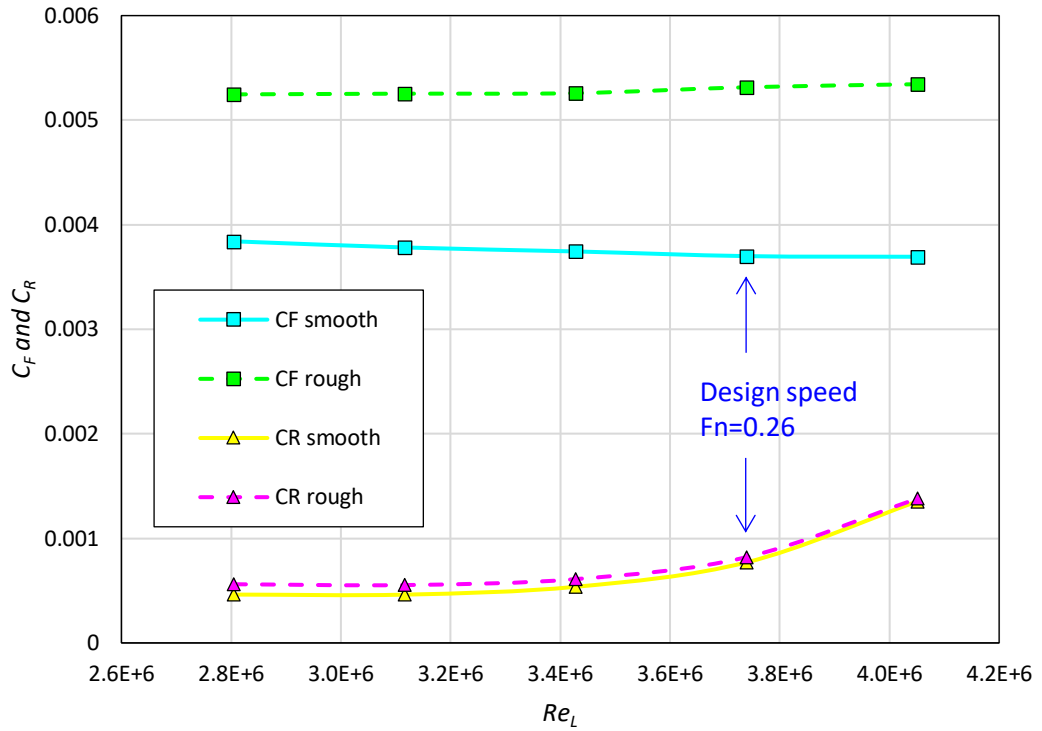


Figure 5.9 C_F and C_R values of the KCS model in the smooth and rough surface conditions

2.1.1.6. Viscous pressure and wave making resistance

In order to decompose the C_R into the C_{VP} and C_W , the form factor values were used with Equation 5.17. The form factor values were calculated from the double-body simulations as

$$k = \frac{C_{V,db}}{C_{F,db}} - 1 \quad (5.22)$$

where $C_{V,db}$ and $C_{F,db}$ denote the viscous resistance and frictional resistance obtained from the double-body flow simulations. Table 5.4 shows the form factor values for the smooth and rough KCS models for the given speeds. The form factor values showed decreases due to the hull roughness.

Table 5.4 C_V , C_{VP} and k values obtained from the double-body simulations

Speed (m/s)	Smooth			Rough		
	$C_{V,db}$	$C_{F,db}$	k	$C_{V,db}$	$C_{F,db}$	k
1.0692	4.049E-03	3.721E-03	8.813E-02	5.539E-03	5.102E-03	8.578E-02
1.1880	3.967E-03	3.646E-03	8.802E-02	5.525E-03	5.087E-03	8.618E-02
1.3068	3.899E-03	3.583E-03	8.792E-02	5.477E-03	5.041E-03	8.652E-02
1.4255	3.839E-03	3.529E-03	8.783E-02	5.513E-03	5.077E-03	8.597E-02
1.5443	3.787E-03	3.482E-03	8.776E-02	5.532E-03	5.095E-03	8.582E-02

Using the form factor values, k , C_{VP} and C_W were calculated as

$$C_{VP} = kC_F \quad (5.23)$$

$$C_W = C_R - C_{VP} \quad (5.24)$$

Figure 5.10 compares the C_R , C_{VP} and C_W values of the KCS model in the smooth and rough surface conditions. As expected, the rough KCS model has larger C_{VP} values than the smooth KCS model, but the contributions of C_{VP} values in C_R show decreasing trends with increasing speeds (thus, the Reynolds number). On the other hand, the wave making resistance, C_W , values for both the smooth and rough cases increase with the speed. The discrepancy between smooth and rough C_W is small at low speeds, but smooth C_W becomes larger than rough C_W as the speed increases.

Subsequently, the differences between the smooth and rough C_R become smaller at higher Reynolds numbers as the roughness effects on the C_{VP} and C_R cancel each other.

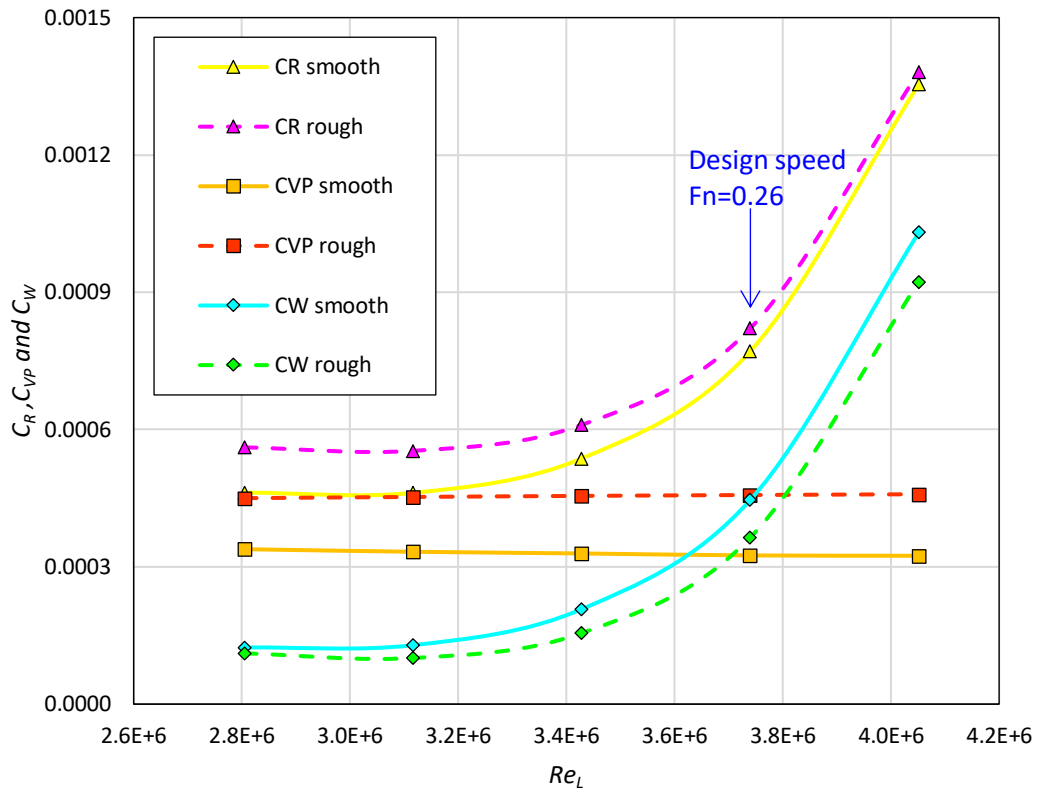


Figure 5.10 C_R , C_{VP} and C_W values of the KCS model in the smooth and rough surface conditions

5.3.3. Effect of hull roughness on the flow characteristics

This section compares the flow characteristics around the KCS model in the smooth and rough surface conditions at its design speed ($V_{model} = 1.43$ m/s, $Fn = 0.26$, $Re_L = 3.7 \times 10^6$).

2.1.1.7. Velocity field

Figure 5.11 and 5.12 compare the mean axial velocity contours around the stern of the KCS model ship in both the surface conditions. The mean axial velocity was normalised by dividing the velocity with the advance speed of the ship. As shown in

the figures, the hull roughness resulted in the decelerated flow around the stern and it enlarged the wake field. This enlarged wake region can be closely related to the distribution of the surface pressure at the stern (Figure 5.15), which leads to the increase in the viscous pressure resistance.

Another notable feature is the increased boundary layer thickness due to the hull roughness as shown in Figure 5.11. It can be more clearly seen in Figure 5.13, where the boundary layer is represented by the slices of axial velocity contours limited to $V_x/V_{model} = 0.9$. This increased boundary layer thickness results in increased momentum loss and hence the frictional resistance, as shown in Figure 5.9. This roughness effect on the boundary layer thickness leads to increased momentum loss and thus leads to increased skin friction. This observation is in correspondence with the experimental and numerical studies of other researchers (e.g. Schultz and Flack, 2005, 2007; Demirel et al, 2017a).

As the enlarged wake field due to the hull roughness was observed in Figure 5.12, the nominal wake fractions of the smooth and rough KCS model were calculated. Figure 5.14 illustrates the distribution of the local wake fraction, $w'_n = 1 - V_x/V_{model}$, at the propeller plane ($x = 0.0175L_{pp}$). The inner and outer circles denote the hub diameter and the propeller diameter, respectively. From the figure, it is evident that the hull roughness increases the local wake fraction significantly, and it led to a 35% increase in the mean nominal wake fraction, w_n (0.31 to 0.42).

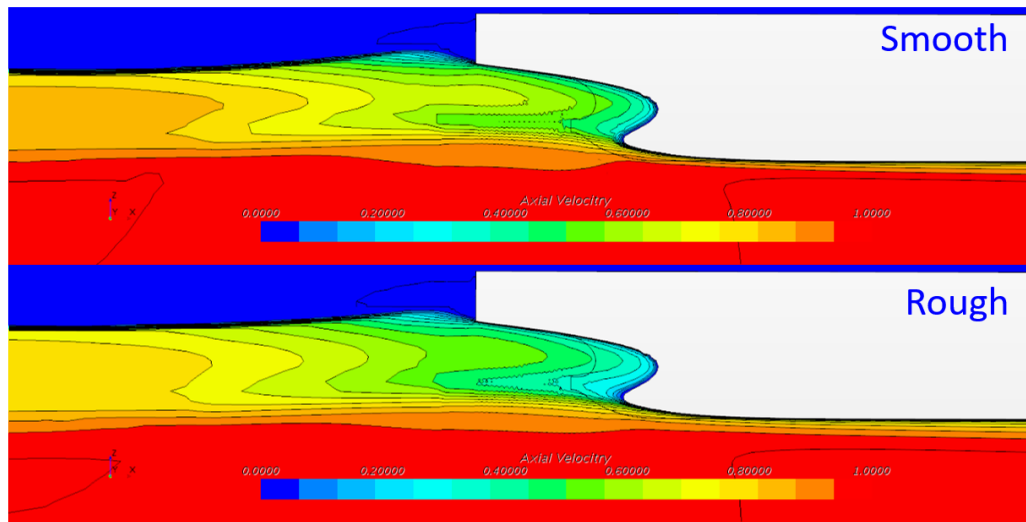


Figure 5.11 Mean axial velocity contours at $y = 0.006L_{pp}$

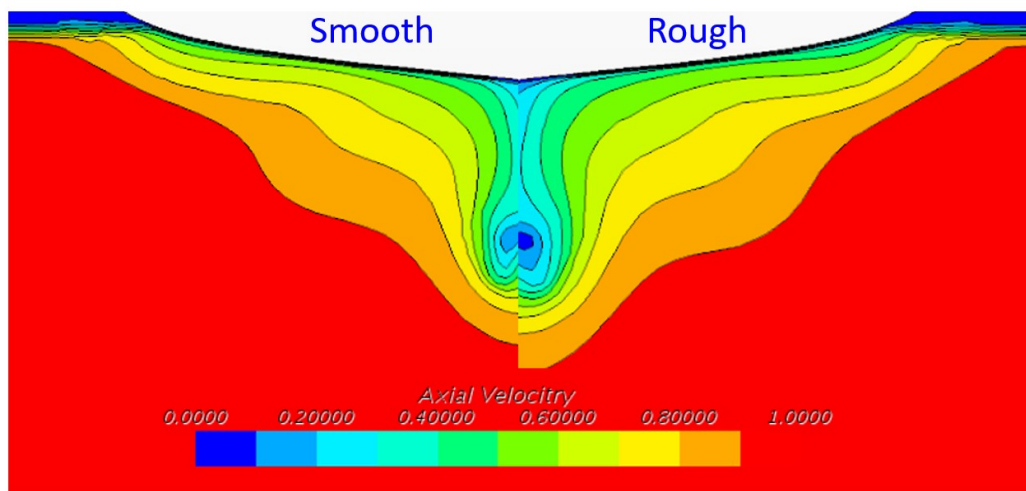


Figure 5.12 Mean axial velocity contours at $x = 0.0175L_{pp}$

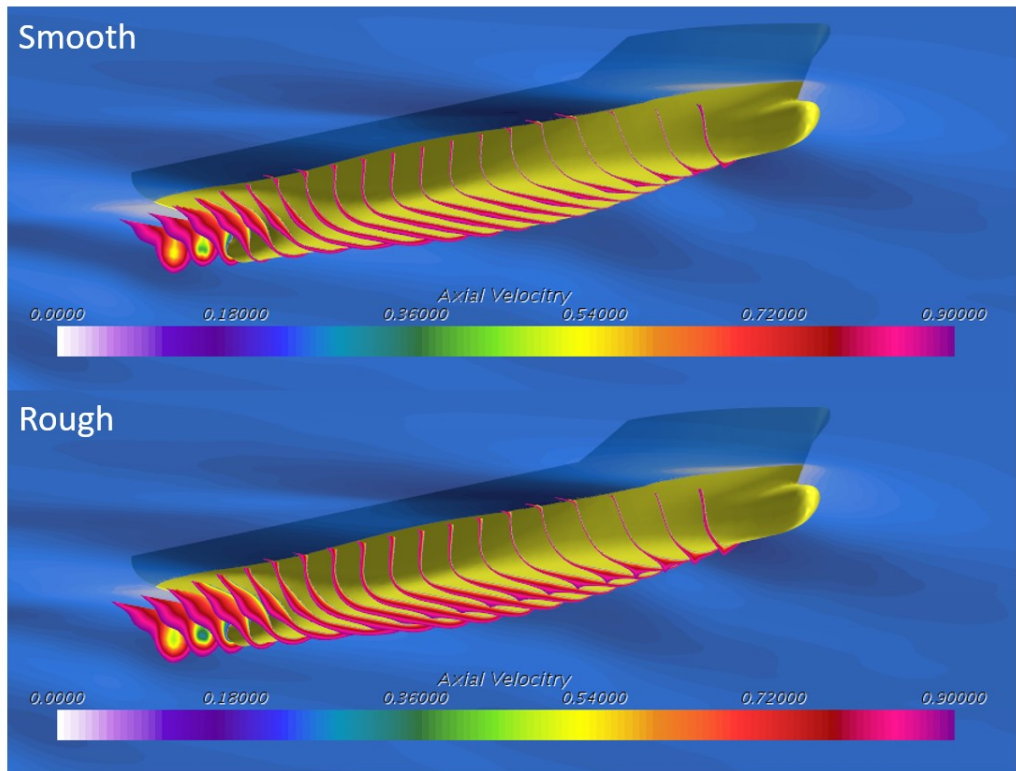


Figure 5.13 Boundary layer representation by slices limited to axial velocity ($V_x/V_{model} = 0.9$)

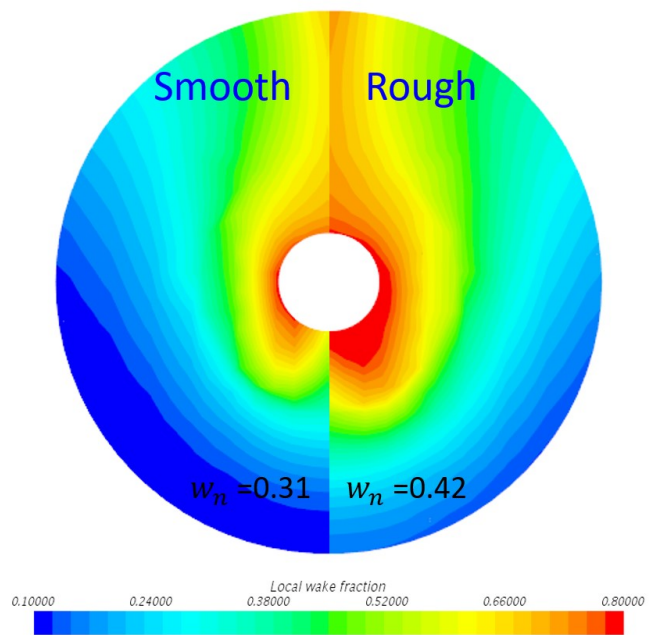


Figure 5.14 Local wake fraction, w_n' , at the propeller plane

2.1.1.8. Pressure field

Figure 5.15 illustrates the distribution of the dynamic pressure coefficient along the hull in the smooth and rough surface conditions. It can be seen from the figure that the rough case has smaller pressure magnitudes at the stern (i.e. reduced pressure recovery). This smaller surface pressure at the stern due to the hull roughness can be related to the increased viscous pressure resistance, C_{VP} , in Figure 5.10.

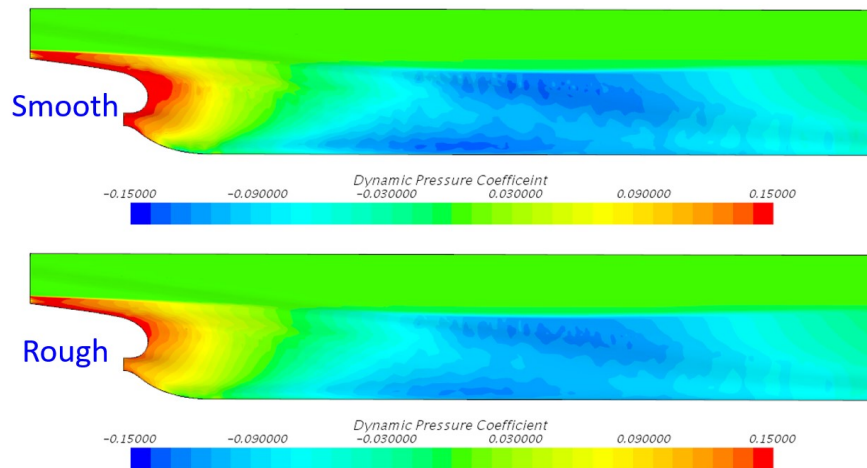


Figure 5.15 Pressure distribution on the KCS model ship

2.1.1.9. Wave profile

Figure 5.16 compares the wave patterns around the KCS model in the smooth and rough surface conditions. It is seen from the figure that the wave elevations around the hull are reduced by the hull roughness. This roughness effect on the wave pattern can be also seen in Fig. 18, which compares the wave elevation along the line with constant $y = 0.1509L_{pp}$. This roughness effect on the wave profile is in accordance with the reduced C_W values due to the hull roughness as shown in Figure 5.10. This observation also agrees with the finding of Demirel et al. (2017b).

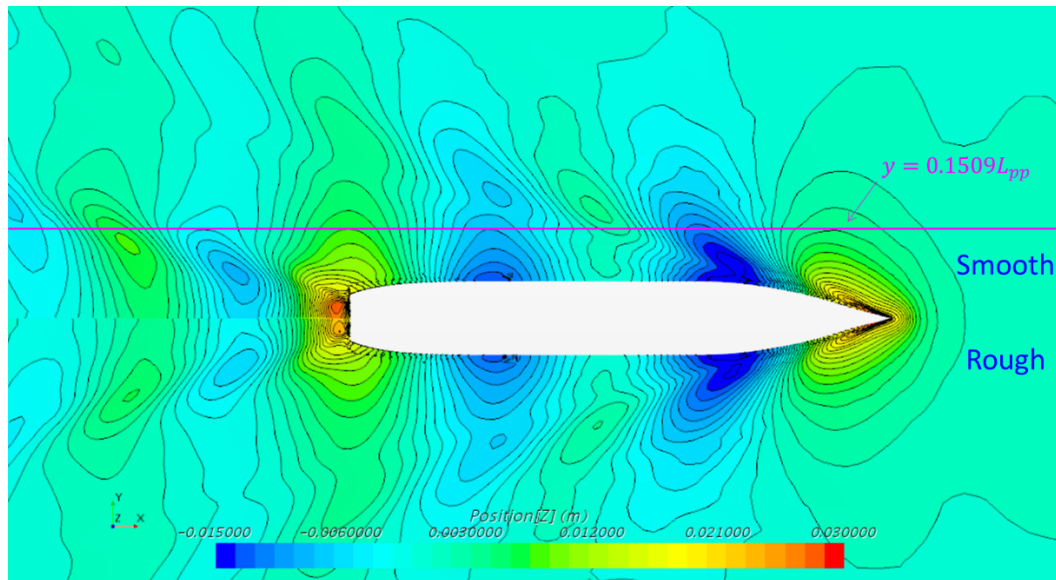


Figure 5.16 Wave pattern around the KCS model

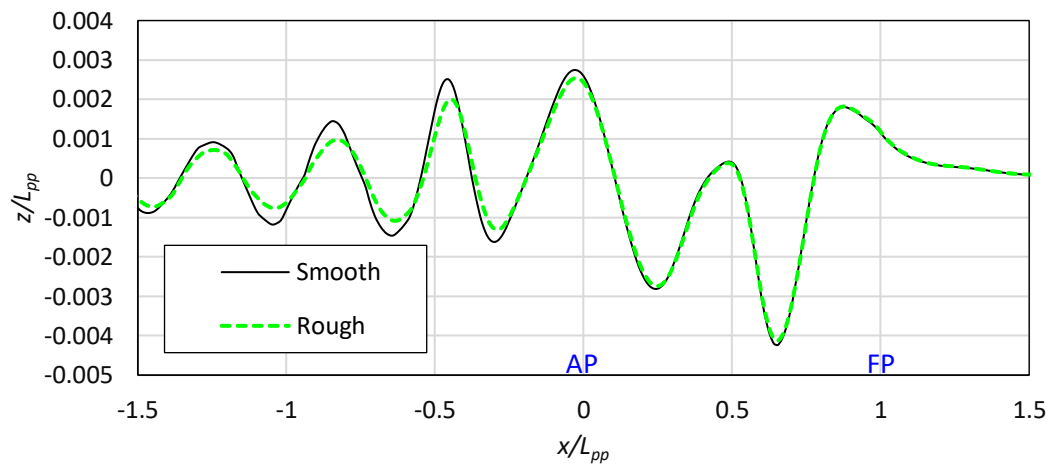


Figure 5.17 Wave elevation along a line with constant $y = 0.1509L_{pp}$

5.4. Chapter summary and conclusions

In this study, the CFD approach to predict the effect of hull roughness on the ship resistance was validated against the experiment of a towed flat plate and a model ship in the smooth and rough surface conditions. In order to simulate the effect of the surface roughness, a roughness function model was proposed based on the roughness function, which was determined in Chapter 4, and employed in the wall-function of the CFD model.

Spatial and temporal convergence studies were performed using the Grid convergence Index (GCI) method, to estimate the numerical uncertainties of the proposed CFD models and to determine sufficient grid-spacings and time steps.

Fully nonlinear unsteady RANS simulations of the flat plate and the KCS model ship were conducted in the smooth and rough surface conditions. The simulation results showed excellent agreement with the towing test result (Chapter 4) in both the smooth and rough surface conditions. This result suggests that the CFD approach (i.e. modified wall-function approach) can accurately predict not only the roughness effect on the skin friction, but also the total resistance of a 3D hull.

The total ship resistance predicted from the CFD simulations in the smooth and rough conditions were decomposed into individual resistance components. Significant increases in the frictional resistance, C_F , due to the hull roughness were found. Increases in the viscous pressure resistance, C_{VP} , and decreases in the wave making resistance, C_W , were also observed due to the hull roughness.

The effect of hull roughness on the flow characteristics around the hull was also examined. By comparing the velocity field around the KCS model in the smooth and rough conditions, a decelerated flow and enlarged wake field were observed downstream of the stern, as well as the increased boundary layer thickness. It was found that the hull roughness reduces the pressure recovery at the stern, which leads to increased viscous pressure resistance. Smaller wave elevation due to the hull

roughness was also noted, which is closely related to the smaller wave making resistance for the rough case.

6. CFD prediction of the effect of biofouling on full-scale ship resistance

6.1. Introduction

As reviewed in Chapter 2, predicting the effect of biofouling on full-scale ship performance is important. However, there have been relatively few studies conducted to investigate the effect of biofouling on full-scale ship resistance (Demirel et al., 2017b; Farkas et al. 2018; 2019). The investigations should be extended to increase the understandings of the effect of roughness on ship hydrodynamic performance.

To the best of the author's knowledge, there exists no specific study to predict the effect of barnacles of varying sizes and coverages on the ship resistance components. Therefore, the aim of this chapter is to fill this gap by developing a CFD model to simulate a realistic surface roughness through employing a roughness function model representing barnacle fouling and performing a comprehensive investigation on the roughness effect of barnacle fouling on ship hydrodynamic characteristics using the CFD approach.

This chapter is organised as follows: The methodology used in this chapter is explained in Section 6.2.1. The modified wall-function approach as the roughness function of barnacles are discussed in Section 6.2.2. In Section 6.2.3. the details of the numerical modelling are covered including the mathematical formulations, geometry and boundary conditions of the simulations as well as mesh generation. Section 6.3 covers the verification and validation studies of the CFD simulations. The effect of barnacles on ship resistance components are presented in Section 6.4.1 to 6.4.4, while the roughness effect on the flow characteristics are covered in Section 6.4.5 to 6.4.8. Finally, chapter summary and conclusions are discussed in Section 6.5.

6.2. Methodology

6.2.1. Approach

A schematic illustration of the current study is shown in Figure 6.1. The first step is employing the roughness function of the barnacle fouling into the wall-function in the CFD model (i.e. modified wall-function approach) so that the wall boundary condition can represent the rough surface due to barnacles. The roughness function and the corresponding roughness heights obtained by Demirel et al. (2017a) was selected and employed in the wall-function of the CFD model. The second step is the validation of the modified wall-function approach for barnacle fouling. Towed flat plate simulations were conducted and compared with the experimental result of Demirel et al. (2017a). The third step is conducting full-scale CFD simulations using the modified wall-function approach to predict the effect of barnacle fouling on the ship resistance components. The frictional resistance coefficients were predicted for the KCS 3D hull and compared with the results obtained from the full-scale flat plate simulation of the same ship using CFD as well as the results for the same ship based on Granville's similarity law scaling procedure. The roughness effect on the different resistance components was also examined using the results of KCS hull simulations. Finally, the roughness effect on the wave profile, pressure distribution along the hull, velocity distribution and boundary layer development around the hull, and on the wake flow were examined.

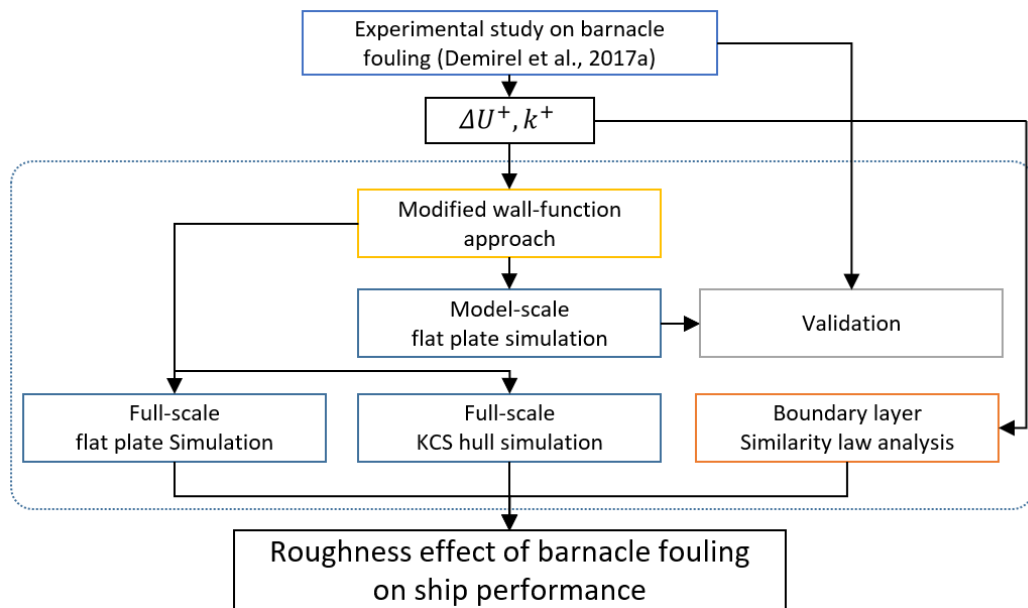


Figure 6.1 Schematic illustration of the methodology in Chapter 6

6.2.2. Roughness function of barnacles

In this study, the modified wall-function approach was used to represent the surface conditions of barnacle fouling, using the roughness function of Demirel et al. (2017a). Further details on the modified wall-function approach can be found in Section 5.2.3.

Demirel et al. (2017a) used an experimental approach to find the roughness function of barnacle fouling. The study was based on an extensive series of towing test of flat plates covered with artificial barnacle patches. Different sizes of real barnacles, categorised as small, medium and big regarding their size, were digitised using 3D scanning technology and 3D printed into artificial barnacle tiles. The barnacle tiles were glued onto the surfaces of flat plates by differing the coverage area and the plates were towed at a range of speeds. From the analyses of the experimental results, they showed that the roughness functions of the barnacle fouling follow the Colebrook type roughness functions of Grigson (1992), given by

$$\Delta U^+ = \frac{1}{\kappa} \ln(1 + k^+) \quad (6.1)$$

Table 6.1 compares the roughness length scales of barnacle fouling obtained by the experiment and Figure 6.2 shows the roughness functions for the different barnacle fouling conditions, obtained by Demirel et al. (2017a).

Table 6.1 Roughness length scales of the barnacle fouling conditions, adapted from Demirel et al. (2017a)

Test surface	Barnacle type	Surface coverage (%)	Barnacle height h (mm)	Representative roughness height k_G (μm)
B10%	Big	10 %	5	174
B20%	Big	20 %	5	489
M10%	Medium	10 %	2.5	84
M20%	Medium	20 %	2.5	165
M40%	Medium	40 %	2.5	388
M50%	Medium	50 %	2.5	460
S10%	Small	10 %	1.25	24
S20%	Small	20 %	1.25	63
S40%	Small	40 %	1.25	149
S50%	Small	50 %	1.25	194

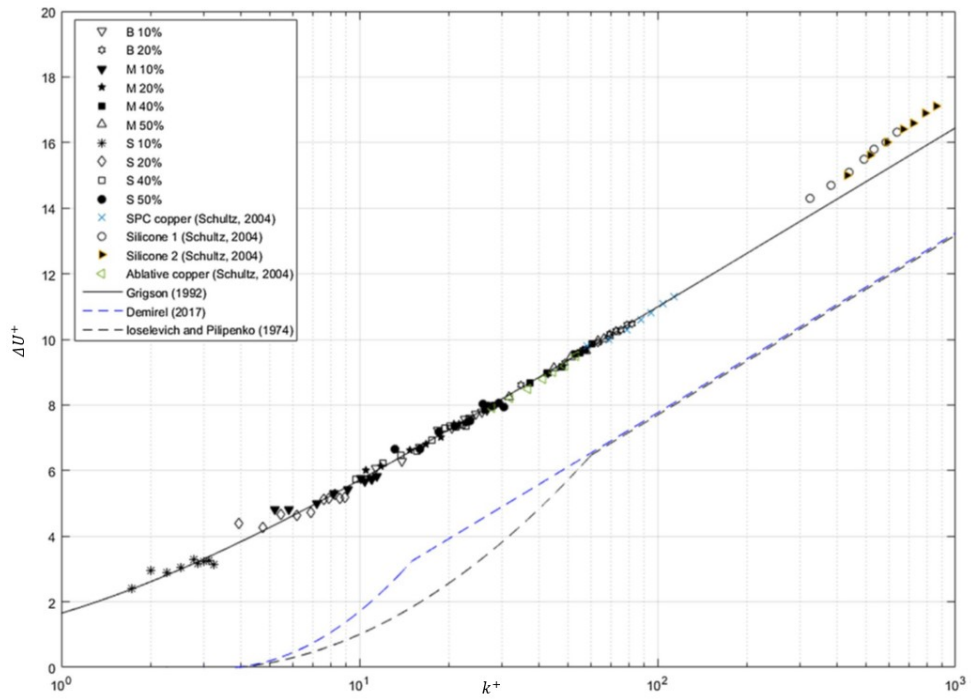


Figure 6.2 Roughness functions for the test surfaces, adapted from Demirel et al. (2017a)

6.2.3. Numerical modelling

2.1.1.10. Mathematical formulations

The CFD models were developed based on the unsteady Reynolds-averaged Navier-Stokes (URANS) method using a commercial CFD software package, STAR-CCM+ (version 12.06). The mathematical formulations are identical to those used in Chapter 5. The details can be found in Section 5.2.2.

2.1.1.11. Geometry and boundary conditions

In the study, three different CFD models were developed to study the effect of the barnacle fouling, and these include: (i) Model-scale flat plate simulations for the validation; (ii) Full-scale flat plate representation of the KCS hull ; (iii) Full-scale 3D simulations of the KCS hull appended with a rudder.

The geometry and boundary conditions for the model-scale flat plate simulations are identical to those used in Chapter 5. The details can be found in Section 5.2.5.1.

Figure 6.2 shows the dimensions and the boundary conditions used for the full-scale flat plate simulation. The length of the full-scale flat plate was chosen to represent the length of the KCS so that the roughness effect at the same Reynolds number of the KCS at its design speed (24 knots) and slow streaming speed (19 knots) can be examined. The full-scale plate simulation was modelled as fully submerged by defining the boundary conditions of horizontal and vertical centre planes ($z = 0$ and $y = 0$, respectively) as the symmetry planes. As a consequence, only a quarter of the plate and the fluid domain was taken into account in order to save the computational time.

The full-scale KCS simulations were conducted using the same geometry and boundary conditions used for the model-scale towed KCS simulations in Chapter 5 (Figure 5.4). The only difference to mention is that the simulations in this chapter were conducted in full-scale with a fixed condition while those in Chapter 5 was conducted in the model-scale with free sinkage and trim. The principal particulars of the KCS in full-scale can be found in Table 5.1 in Section 5.2.5.2.

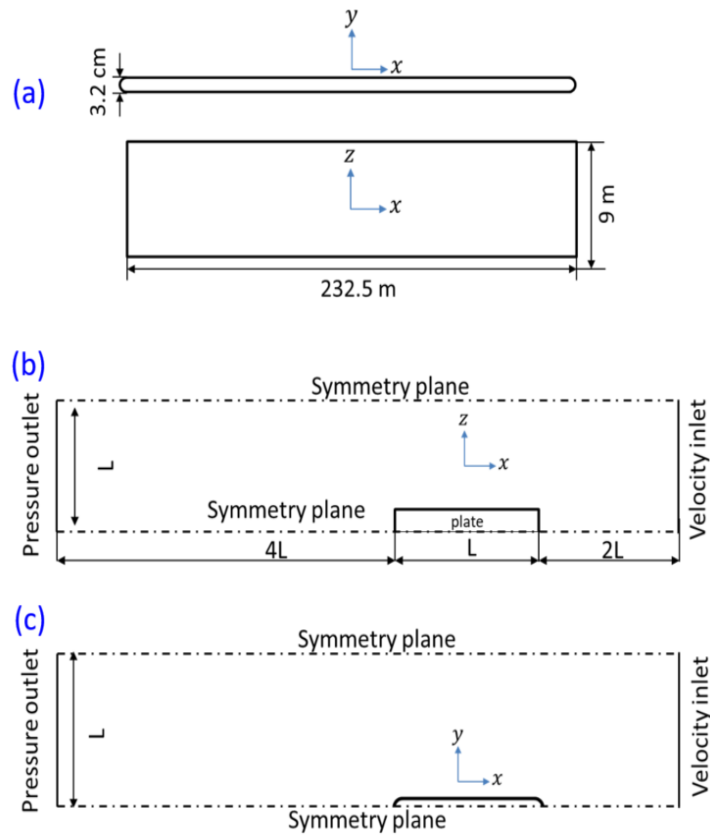


Figure 6.3 The dimensions and boundary conditions for the full-scale flat plate simulation model, (a) the plate, (b) profile view of the computational domain, (c) top view of the computational domain.

6.2.4. Mesh generation

Mesh generation was performed using the built-in automated meshing tool of STAR-CCM+. The same techniques used for the mesh generation as used in Chapter 5. Further details can be found in Section 5.2.6. Figure 6.3 shows the grid structure of the full-scale KCS simulation used in this chapter.

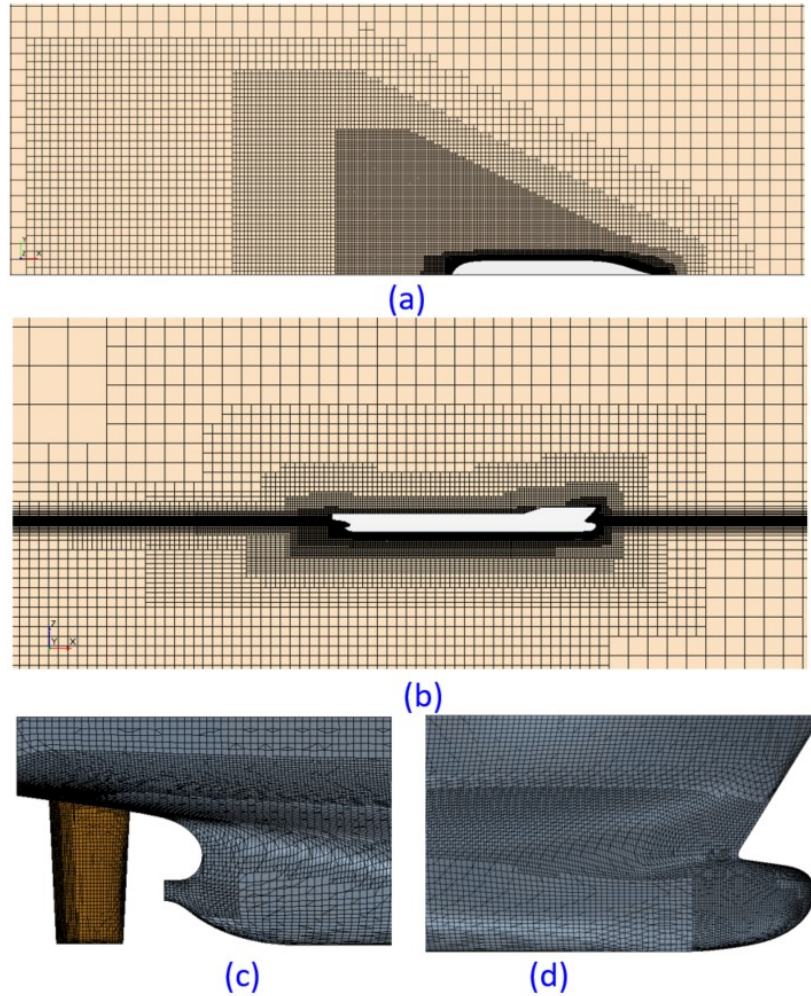


Figure 6.4 Volume mesh of full-scale KCS hull simulation model, (a) top view, (b) profile view, (c) stern refinement, (d) bow refinement

6.3. Verification and validation

6.3.1. Verification study

Verification studies were conducted to estimate the spatial and temporal uncertainties of the simulations. The Grid Convergence Index (GCI) method based on Richardson's extrapolation (1910) was used to estimate the numerical uncertainties, as used in Chapter 5. The details of the GCI method can be found in Section 5.2.7.

6.3.1.1. Spatial convergence study

For spatial convergence study, three different resolution of meshes were generated, which are referred to as fine, medium, and coarse meshes corresponding the cell numbers of N_1 , N_2 , and N_3 . Table 3 shows the required parameters for the calculation of the spatial discretization error. The total resistance coefficient values, C_T , of smooth cases were used as the key variables. The inlet velocity for the model-scale flat plate simulation was set to $V = 2.435 \text{ m/s}$ which is one of the towing speeds of Demirel et al. (2017a), while the inlet velocity of 24 knots was used for the simulations of full-scale flat plate and KCS hull. As indicated in the table, the numerical uncertainty of fine meshes (GCI_{fine}^{21}) for the model-scale flat plate, full-scale flat plate and KCS hull CFD models are 0.77%, 0.11% and 0.96% respectively. For accurate prediction of the roughness effect of barnacle fouling, the fine mesh of each case was used in this study.

Table 6.2 Parameters used for the calculation of the discretization error for the spatial convergence study, key variable: C_T

	Model-scale flat plate	Full-scale flat plate	Full-scale KCS hull
N_1	2,300,000	1,200,000	2,000,000
N_2	930,000	850,000	1,300,000
N_3	460,000	610,000	630,000
r_{21}	1.35	1.12	1.26
r_{32}	1.26	1.12	1.42
ϕ_1	3.981E-03	1.357E-03	2.095E-03
ϕ_2	4.021E-03	1.355E-03	2.103E-03
ϕ_3	4.092E-03	1.347E-03	2.126E-03
ε_{32}	7.16E-05	-7.94E-06	2.27E-05
ε_{21}	3.98E-05	-2.62E-06	8.67E-06
s	1	1	1
e_a^{21}	1.00%	0.19%	0.41%
q	3.74E-01	6.50E-02	-5.34E-01
p_a	3.19E+00	1.02E+01	1.86E+00
ϕ_{ext}^{21}	3.956E-03	1.358E-03	2.078E-03
e_{ext}^{21}	0.62%	-0.09%	0.78%
GCI_{fine}^{21}	0.77%	0.11%	0.96%

2.1.1.1. Temporal convergence study

For the temporal convergence study, three different time steps, namely Δt_1 , Δt_2 , and Δt_3 , were applied to the simulations using fine meshes. Table 6.3 shows the required parameters for the calculation of the temporal discretization error. The total resistance coefficient values, C_T , of smooth cases were used as the key variable. The inlet velocity for the model-scale flat plate simulation was set to $V = 2.435 \text{ m/s}$ which is one of the towing speeds of Demirel et al. (2017a), while the inlet velocity of 24 knots was used for full-scale flat plate and the KCS hull simulations. As indicated in the table, the numerical uncertainties of the smallest time steps ($GCI_{\Delta t_1}^{21}$) of the model-scale flat plate, full-scale flat plate, and KCS hull CFD models are 0.01%, 0.002% and 0.65% respectively. For accurate prediction of the roughness effect of barnacle fouling on ship resistance, the smallest time step, Δt_1 , of each model was used in this study. It is of note that the recommended time step by ITTC (2011b) is $0.005 \sim 0.01L/V$, and the time steps used in this study were within this range or even smaller.

Table 6.3 Parameters of the calculation of the discretization error for the temporal convergence study, key variable: C_T

	Model-scale flat plate	Full-scale flat plate	Full-scale KCS hull
Δt_1	0.01s	0.16s	0.02s
Δt_2	0.02s	0.32s	0.04s
Δt_3	0.04s	0.64s	0.08s
r_{21}, r_{32}	2	2	2
ϕ_1	3.981E-03	1.357E-03	2.095E-03
ϕ_2	3.980E-03	1.357E-03	2.108E-03
ϕ_3	3.978E-03	1.360E-03	2.136E-03
ε_{32}	-2.58E-06	2.77E-06	2.88E-05
ε_{21}	-8.80E-07	2.50E-07	1.31E-05
e_a^{21}	0.02%	0.018%	0.62%
p_a	1.55E+00	3.47E+00	1.14E+00
ϕ_{ext}^{21}	3.982E-03	1.357E-03	2.084E-03
e_{ext}^{21}	-0.01%	0.0018%	0.52%
$GCI_{\Delta t_1}^{21}$	0.01%	0.0023%	0.65%

6.3.2. Validation study

6.3.2.1. Validation of the modified wall-function approach

Figure 6.4 compares the C_T values of model-scale flat plates in different fouling conditions computed from the CFD simulations with the experimental data of Demirel et al. (2017a). The horizontal axes of the figures indicate the corresponding representative roughness heights of the barnacle fouling conditions given in Table 6.1. It is evident from the figure that a good agreement is achieved between the current CFD model and the experiment of Demirel et al. (2017a). This suggests that the modified wall-function approach can accurately represent the surface roughness of barnacle fouling. Therefore, this CFD approach can be used to investigate the effect of biofouling on the hydrodynamic characteristics of ships.

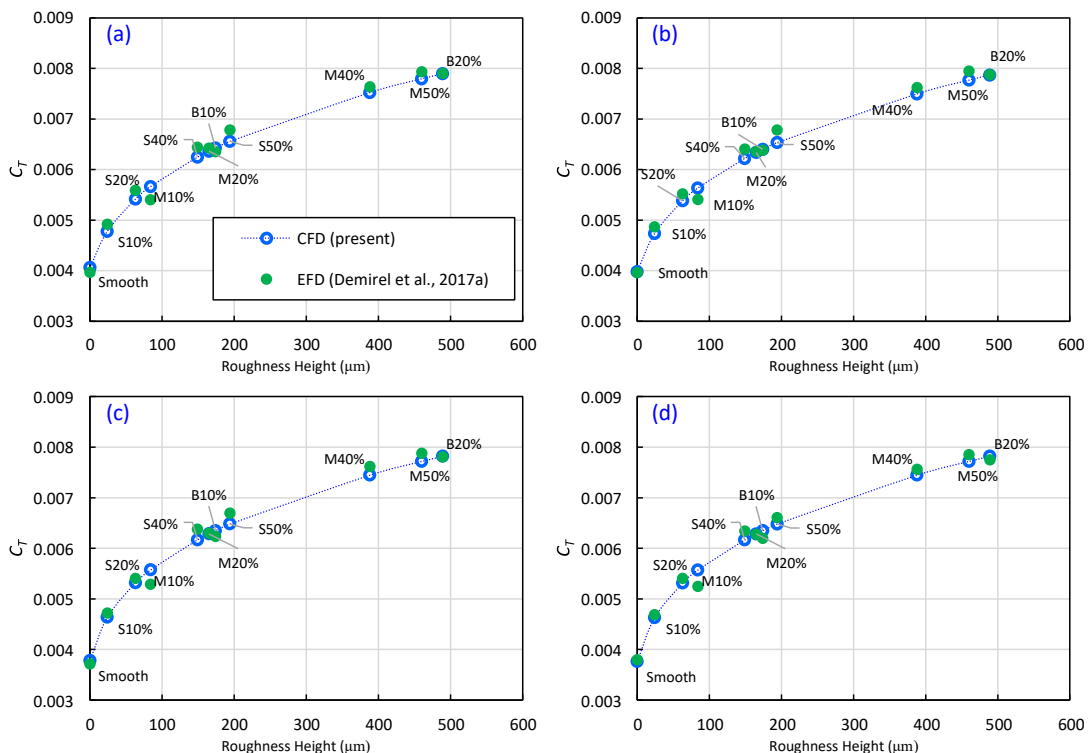


Figure 6.5 C_T values of flat plates towed with different fouling conditions obtained from the simulations and the experiments by Demirel et al. (2017a), (a) $Rn=2.79E+06$, (b) $Rn=3.19E+06$, (c) $Rn=4.51E+06$, (d) $Rn=4.70E+06$

6.3.2.2. Validation of the CFD models in smooth condition

To validate the CFD models in smooth condition, the C_T values obtained using the CFD simulations were compared with the experimental data of Demirel et al. (2017a) and the extrapolated result using the experimental data of Kim et al. (2001). The inlet velocity of model-scale flat plate simulation was set to $V = 2.435 \text{ m/s}$ ($Rn = 2.8 \times 10^6$), which is one of the towing speeds of Demirel et al. (2017a), while the design speed of the KCS was used for the full-scale KCS hull simulation. The full-scale C_T value used for the comparison were extrapolated following the ITTC 1957 method (i.e. Froude's method) using the frictional resistance coefficient, C_F , obtained from ITTC 1957 friction line (ITTC, 2011) and the residuary resistance, C_R , obtained by Kim et al. (2001). As can be seen in Table 6.4, the model-scale flat plate and full-scale KCS hull simulation results show good agreement with the experimental results, showing relative errors of 0.38% and 0.54% respectively.

Table 6.4 C_T values obtained from the CFD simulations and the experiments (Demirel et al., 2017a; Kim et al., 2011)

	Reynolds number	C_T , CFD	C_T , EFD	Relative error
Model-scale flat plate	2.8×10^6	3.981×10^{-3}	^a 3.397×10^{-3}	0.38%
Full-scale KCS hull	2.7×10^9	2.095×10^{-3}	^b 2.083×10^{-3}	0.54%

^a experimental data of Demirel et al. (2017a), ^b extrapolated result using the experimental data of Kim et al. (2001) based on the ITTC 1957 method

6.4. Results

6.4.1. Total resistance and effective power

The total resistance coefficients, C_T , were obtained from the full-scale KCS hull simulations in the surface conditions of varying sizes and coverage of barnacle fouling. As indicated in Table 6 the C_T values show a significant increase due to the barnacle fouling. The increase in total resistance and the effective power of the ship was observed to be higher at 19 knots than 24 knots (by 73% and 60%, respectively). It can be attributed to the fact that the contribution of the frictional resistance becomes more dominant at lower speeds, and it is believed that the surface roughness mainly affects the frictional resistance rather than other resistance components. For these reasons, it appears that the effect of surface roughness on ship total resistance is more dominant at lower speeds. Therefore, it is worth investigating the effect of barnacle fouling on different resistance components.

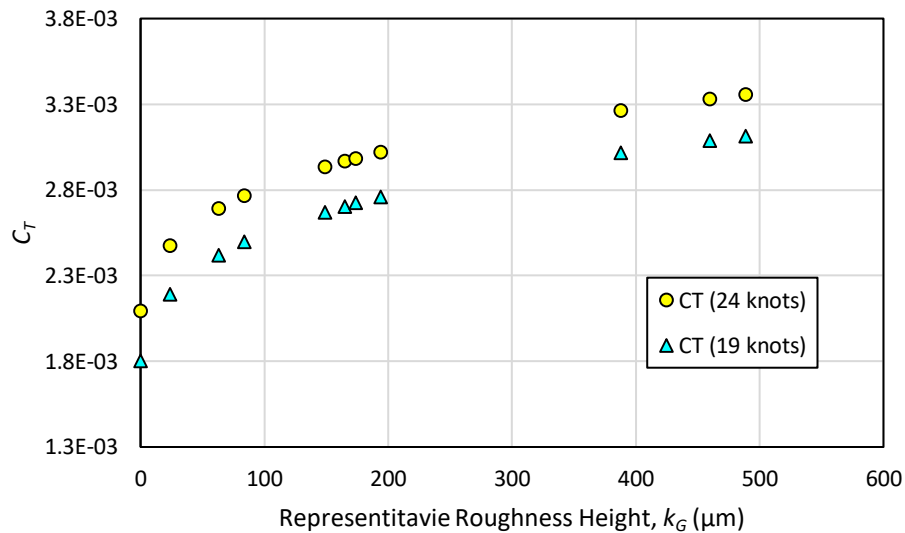


Figure 6.6 C_T values obtained by the full-scale CFD simulations

Table 6.5 C_T values obtained from full-scale KCS hull simulation

Test Surface	k_G (μm)	24 knots		19 knots	
		C_T	$\Delta C_T, \Delta P_E$	C_T	$\Delta C_T, \Delta P_E$
Smooth	0	2.095E-03	0%	1.803E-03	0%
S10%	24	2.475E-03	18%	2.192E-03	22%
S20%	63	2.691E-03	28%	2.419E-03	34%
M10%	84	2.767E-03	32%	2.498E-03	39%
S40%	149	2.936E-03	40%	2.670E-03	48%
M20%	165	2.968E-03	42%	2.704E-03	50%
B10%	174	2.985E-03	42%	2.724E-03	51%
S50%	194	3.020E-03	44%	2.760E-03	53%
M40%	388	3.265E-03	56%	3.018E-03	67%
M50%	460	3.333E-03	59%	3.088E-03	71%
B20%	489	3.358E-03	60%	3.114E-03	73%

6.4.2. Frictional resistance and residuary resistance

The frictional resistance coefficients and residuary resistance coefficients were directly computed from the full-scale KCS hull simulations and flat plate simulation. Additionally, the simulation results were compared with the C_F values of flat plates with the same length as the KCS, extrapolated using Granville's boundary layer similarity law scaling method (Granville, 1958; 1987).

Figure 6.6 shows the frictional resistance coefficients, C_F , obtained from the two full-scale simulations and similarity law analysis at the design speed of 24 knots and slow steaming speed of 19 knots. In the figure, the C_F values are plotted against the representative roughness heights, k_G , of the corresponding fouling conditions. As can be seen in the figure, the frictional resistance coefficients obtained using the three different methods show excellent agreement in trends and with close values in magnitudes at both speeds. It appears that due to the three-dimensional effect, the C_F

values of the 3D KCS hull simulations are always higher than those of flat plate simulations.

Table 6.6 compares the frictional resistance coefficients, the percentage of added resistance ($\% \Delta C_F$) and the residuary resistance coefficients, C_R , obtained from the 3D full-scale KCS hull simulations with different fouling conditions at 24 knots and 19 knots. The increases in the C_F values of KCS due to the fouling conditions were predicted to be up to 93% and 88% in the most severe fouled conditions (B20% case) at the design speed and slow streaming speed, respectively. It is notable that only with 10% coverage of small barnacle (S10% case) fouling can result in a nearly 30% increase in the frictional resistance of KCS at the design speed.

It is also not surprising that the C_F values of the fouled cases (except S10%) remain rather consistent with the increasing speed (from 19 knots to 24 knots) while the smooth C_F is decreasing, as C_F starts to lose its dependency on the Reynolds number when it approaches the fully rough regime (Moody, 1944). For the same reason, $\% \Delta C_F$ values appear higher at 24 knots than 19 knots, as only C_F in the smooth case decreases with the increase of Reynolds number while C_F of rough surfaces remain relatively consistent.

On the other hand, interesting features were observed in residuary resistance, C_R , between the two speeds. As can be seen in Figure 6.7, the C_R values of the KCS at 24 knots showed a decreasing trend with increasing fouling rate, while it tended to decrease as the roughness height increases at 19 knots. It appears that this difference arises from the different portions of viscous pressure resistance, C_{VP} , and wave-making resistance, C_W , at different speeds as firstly found in Demirel et al. (2017b).

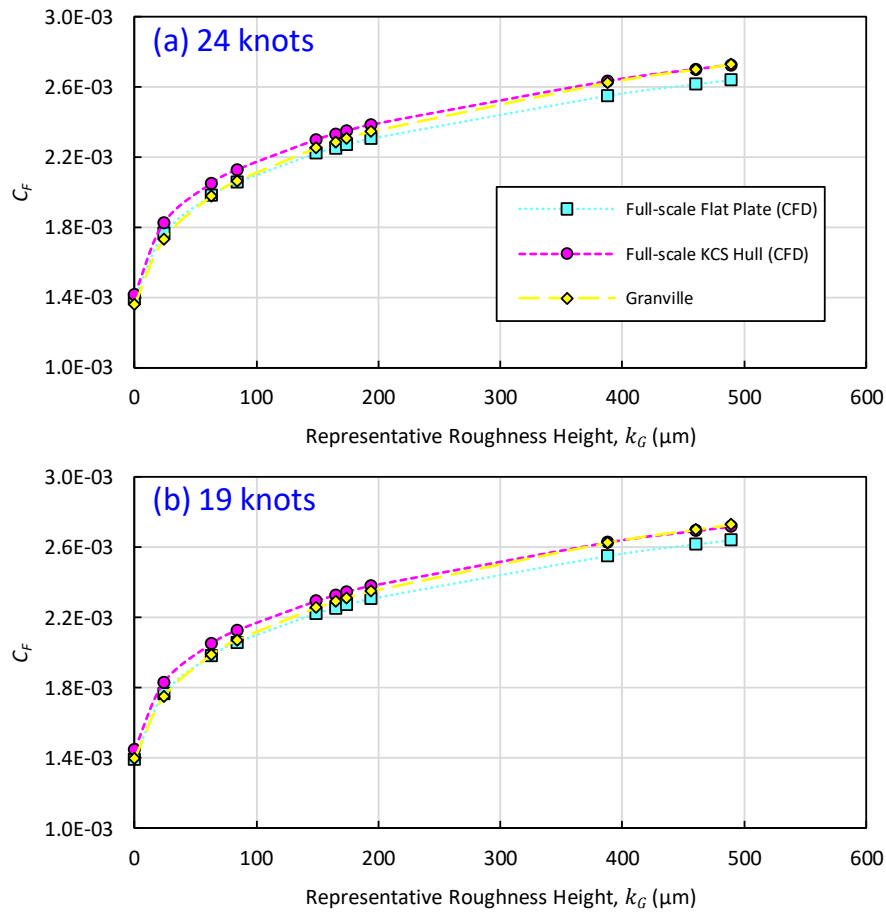


Figure 6.7 C_F values obtained by the full-scale CFD simulations and Granville's similarity law extrapolation at (a) 24 knots and (b) 19 knots

Table 6.6 Comparison of the frictional resistance coefficients and the residuary resistance coefficients computed from the full-scale KCS hull simulations at 24 knots and 19 knots

Surface condition	k_G (μm)	24 knots				19 knots			
		C_F	$\% \Delta C_F$	C_R	ΔC_R	C_F	$\% \Delta C_F$	C_R	ΔC_R
Smooth	0	1.415E-03	0%	6.792E-04	0.0%	1.446E-03	0%	3.565E-04	0.0%
S10%	24	1.826E-03	29%	6.489E-04	-4.5%	1.829E-03	26%	3.632E-04	1.9%
S20%	63	2.050E-03	45%	6.409E-04	-5.6%	2.049E-03	42%	3.697E-04	3.7%
M10%	84	2.128E-03	50%	6.395E-04	-5.8%	2.126E-03	47%	3.716E-04	4.2%
S40%	149	2.299E-03	62%	6.371E-04	-6.2%	2.294E-03	59%	3.766E-04	5.6%
M20%	165	2.331E-03	65%	6.365E-04	-6.3%	2.326E-03	61%	3.779E-04	6.0%
B10%	174	2.348E-03	66%	6.363E-04	-6.3%	2.345E-03	62%	3.791E-04	6.3%
S50%	194	2.384E-03	68%	6.357E-04	-6.4%	2.380E-03	65%	3.799E-04	6.6%
M40%	388	2.632E-03	86%	6.334E-04	-6.7%	2.628E-03	82%	3.906E-04	9.6%
M50%	460	2.700E-03	91%	6.331E-04	-6.8%	2.693E-03	86%	3.943E-04	10.6%
B20%	489	2.725E-03	93%	6.335E-04	-6.7%	2.718E-03	88%	3.956E-04	11.0%

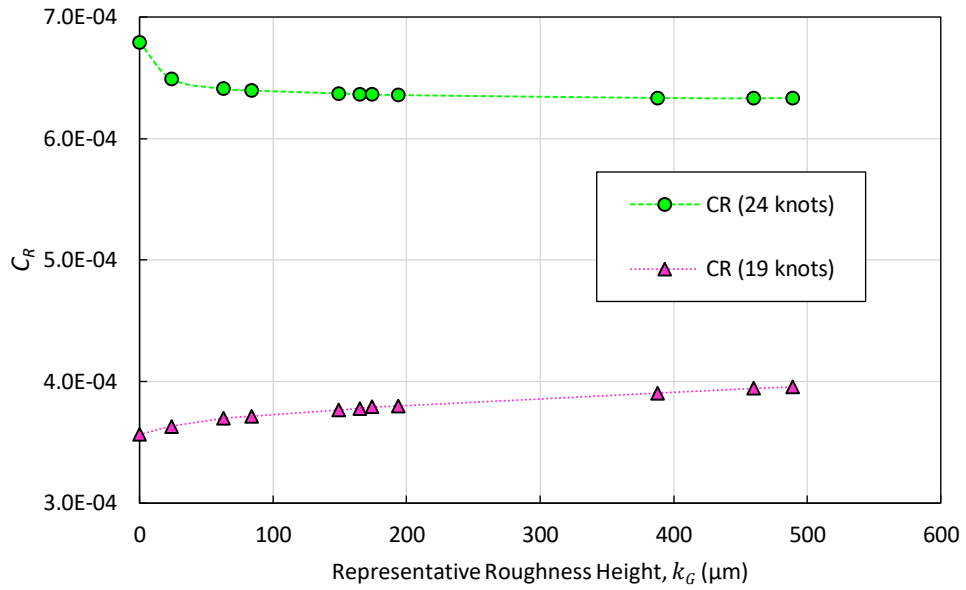


Figure 6.8 Residuary resistance coefficients versus roughness heights, obtained from full-scale KCS hull simulations at 24 knots and 19 knots

6.4.3. Viscous pressure and wave-making resistance

To investigate the rationale behind the different trend of the residuary resistance at different speeds, the residuary resistance coefficients were divided into the viscous pressure resistance coefficients, C_{VP} , and wave-making resistance coefficients, C_W . To find the equivalent form factors, k , double-body flow calculations were conducted, as similarly done in Chapter 5. Table 6.7 shows the form factors, k , of the KCS obtained from the double-body simulations at the design speed (24 knots) and slow steaming speed (19 knots). As can be seen from the table, the k values were observed to decrease as the surface roughness increases. Therefore the increase of C_{VP} due to the surface roughness is not proportional to C_F , which disagrees with the assumptions of Lewis (1988) and Demirel et al. (2017b).

Figure 6.8 shows the C_R , C_{VP} and C_W values varying with the fouling rate. It is apparent that the wave-making resistance, C_W , of the KCS decreases as the level of

hull fouling increases, whilst the viscous pressure resistance, C_{VP} , increases with the increasing fouling rate, as similarly observed in Chapter 5. Since C_R is sum of C_{VP} and C_W , C_R can increase or decrease depending on the dominance of C_{VP} and C_W . Therefore, the full-scale C_R values at 24 knots show a decreasing trend with increasing surface fouling due to the dominance of C_W while they show an increasing trend at 19 knots due to the relatively small portion of C_W .

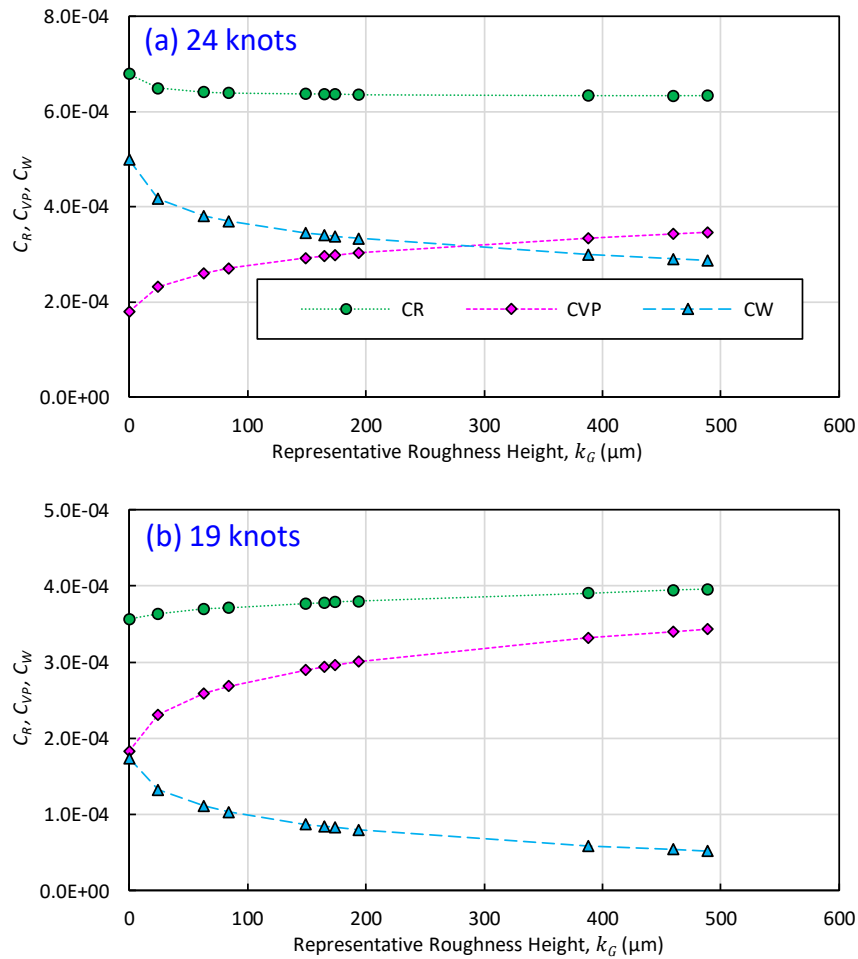


Figure 6.9 Comparison of the residuary resistance, viscous pressure resistance and wave-making resistance versus the representative roughness height of the fouling conditions, (a) 24 knots, (b) 19 knots

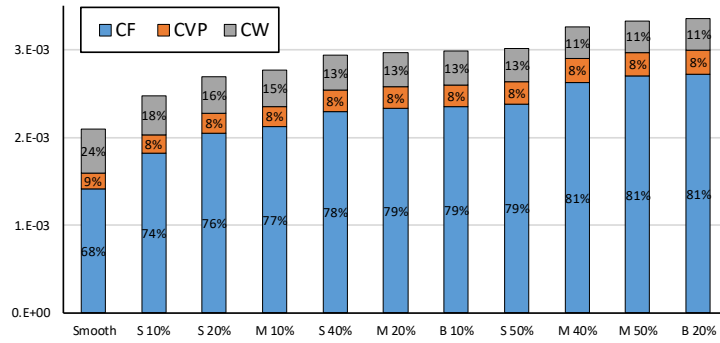
Table 6.7 Form factor calculation from the double-body simulations

Surface condition	k_G (μm)	24 knots				19 knots			
		$C_{V,db}$	$C_{F,db}$	k	Δk	$C_{V,db}$	$C_{F,db}$	k	Δk
Smooth	0	1.511E-03	1.341E-03	0.1268	0%	1.547E-03	1.374E-03	0.1259	0%
S10%	24	1.959E-03	1.759E-03	0.1137	-10%	1.965E-03	1.765E-03	0.1133	-10%
S20%	63	2.194E-03	1.978E-03	0.1092	-14%	2.198E-03	1.981E-03	0.1095	-13%
M10%	84	2.275E-03	2.054E-03	0.1076	-15%	2.278E-03	2.056E-03	0.1080	-14%
S40%	149	2.452E-03	2.218E-03	0.1055	-17%	2.454E-03	2.220E-03	0.1054	-16%
M20%	165	2.486E-03	2.250E-03	0.1049	-17%	2.488E-03	2.251E-03	0.1053	-16%
B10%	174	2.504E-03	2.266E-03	0.1050	-17%	2.506E-03	2.268E-03	0.1049	-17%
S50%	194	2.541E-03	2.301E-03	0.1043	-18%	2.543E-03	2.302E-03	0.1047	-17%
M40%	388	2.800E-03	2.541E-03	0.1019	-20%	2.802E-03	2.542E-03	0.1023	-19%
M50%	460	2.869E-03	2.605E-03	0.1013	-20%	2.871E-03	2.606E-03	0.1017	-19%
B20%	489	2.895E-03	2.629E-03	0.1012	-20%	2.897E-03	2.630E-03	0.1015	-19%

6.4.4. Contribution of resistance components

Since it was found in the previous sections that the effect of surface roughness varies in each resistance component, it is worth investigating the change in the portions of resistance components due to barnacle fouling. Figure 6.9 compares the percentages of the resistance components in different surface conditions at the two speeds. The portions of C_F values increase from 68% to 81% at 24 knots and from 80% to 87% at and 19 knots. On the other hand, the percentage of C_{VP} in total resistance tends to remain rather stable for both speeds, while the percentage of C_W rapidly decrease from 24% to 11% at 24 knots, and from 10% to 4% at 19 knots. As discussed in section 4.3.1 the frictional resistance coefficients are more dominant at 19 knots, and result in larger increases in total resistance as the surface roughness increases.

(a) 24 knots



(b) 19 knots

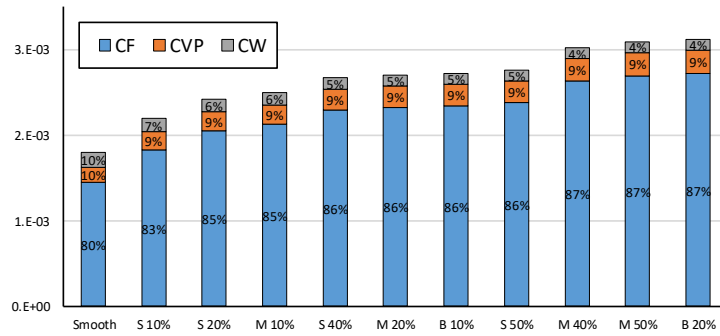


Figure 6.10 Percentage bar diagram of the resistance components, at (a) 24 knots, (b) 19 knots

6.4.5. Wave profile

As it was found that the surface roughness of the KCS affects the wave-making resistance, it is worth examining the roughness effect on wave profiles of the KCS. Figure 6.10 compares the wave profile along a line with $y = 0.1509L_{pp}$ of the KCS in the smooth case and the rough case (B20%). The wave profiles obtained from model-scale simulations ($\lambda=31.6$) was included in the figure for comparison. In both the scales, the wave profiles of the smooth and rough cases collapse on top of each other for $x > -0.25L_{pp}$ and then deviate from each other in the region downstream of the ship. This observation suggests that the roughness effect on the ship wave is minor with the exception of the wake region where the viscous effects become important (Castro et al., 2011). The reduced wave elevation observed in the wake region by the

roughness effect is in accordance with the finding of decreasing trend of C_W with increasing fouling rate observed in Figure 6.7.

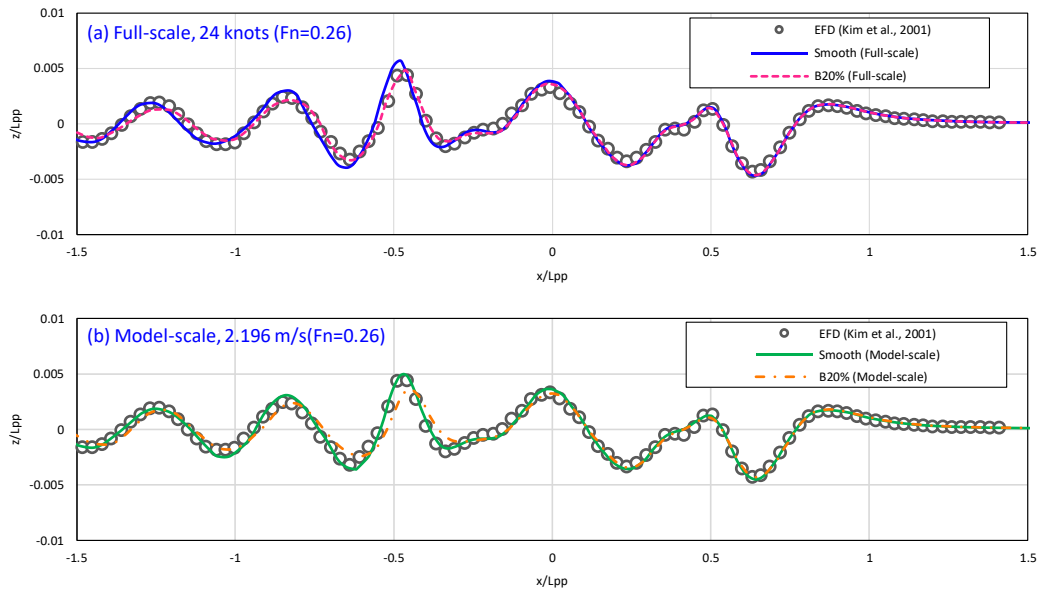


Figure 6.11 Wave profile along a line with constant $y = 0.1509L_{pp}$ for smooth and fouled (B20%) cases, (a) full-scale, (b) model-scale

6.4.6. Pressure distribution

Figure 6.11 shows the pressure distribution along the KCS hull in the smooth and fouled (B20%) surface condition. The surface roughness reduces the pressure recovery at the stern significantly, which increases the viscous pressure resistance, C_{VP} as observed from the previous section. It has been also observed that the surface roughness increases the pressure at the forepart of the rudder, which is believed to be due to the reduced flow velocity after the stern that can be seen in the following subsection. It is also notable that the pressure distributions of different surface conditions were similar from the bow to the middle of the ship. This finding denotes that the pressure distribution is not significantly affected by the surface roughness unless an adverse pressure gradient occurs, and hence it supports the assumption that the residuary resistance of the flat plates, which has zero pressure gradient, is not affected by the surface roughness (Schultz, 2007; Demirel et al., 2017a).

Figure 6.12 shows the pressure contours at $y = 0.006L_{pp}$, downstream to the KCS in the smooth and fouled case (B20%) surface condition. It can be seen from the figure that the surface roughness decreases the magnitude of the pressure downstream to the hull. The significantly decreased pressure below the free surface behind the hull is in accordance with the reduce wave elevation after the stern in the rough case as observed in Figure 6.10.

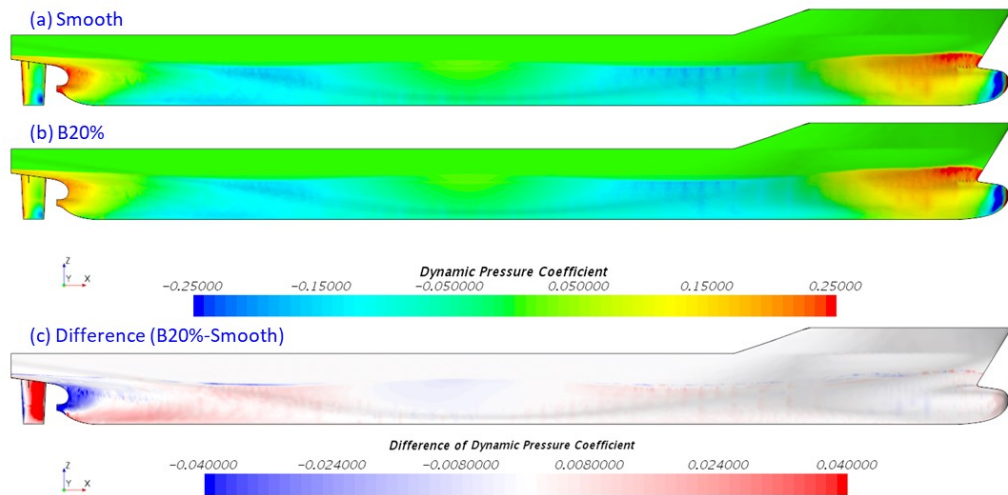


Figure 6.12 Pressure distribution on the KCS hull, (a) smooth case, (b) fouled case (B20%), (c) difference (rough-smooth), at 24 knots

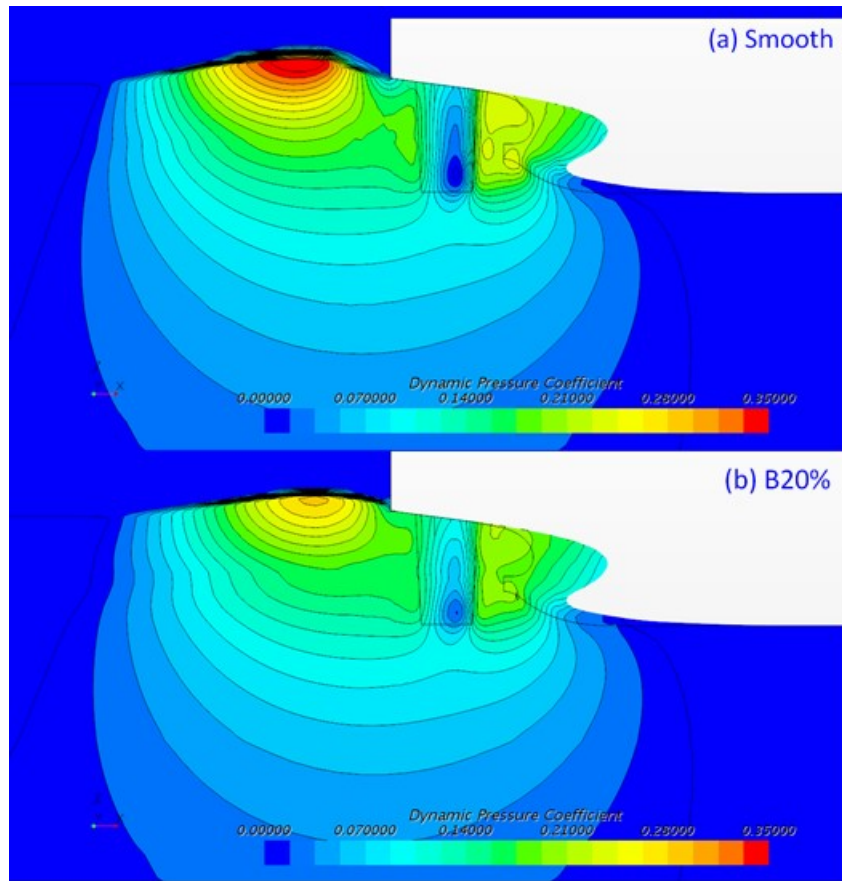


Figure 6.13 Pressure distribution on the plane with constant $y = 0.006L_{pp}$, (a) smooth case, (b) fouled case (B20%), at 24 knots

6.4.7. Velocity field

Figure 6.13 illustrates the boundary layer represented by the slices of axial velocity contours limited to $V_x/V_{ship} = 0.9$ for smooth and rough cases. It can be seen that the surface roughness results in the increased boundary layer thickness along the hull, and thus increase in the skin friction. This finding is consistent with the observation from the model-scale simulation in Chapter 5.

Figure 6.14 compares the mean axial velocity contours around the stern of KCS for both smooth and rough cases at 24 knots. The mean axial velocity was non-dimensionalized by dividing the velocity by the advance velocity of the ship. The surface roughness decelerates the flow velocity around the ship stern and hence

enlarges the wakefield. It is believed that this enlarged wake region interacts with the pressure distribution at the stern and brings an increase in the viscous pressure resistance. Another notable point is that the surface roughness decreases the velocity below the free surface behind the hull, and hence it is likely seen that this deceleration of the water particles causes the reduced wave elevation after the stern in rough cases as observed in Figure 6.11.

The wake (velocity) contour plots at a plane with constant $x = 0.0175L_{pp}$ at 24 knots are shown in Figure 6.15 for the smooth and rough hull surfaces on the port and starboard half, respectively. It can be seen that the wake contours are strongly affected by the surface roughness. The rough case, B20%, has slowed down the wake velocities and hence enlarged the wake region due to the surface roughness. The decelerated flow around the hull can affect not only the ship resistance but also the propulsion performance of the ship as it affects the wake fraction at the propeller section.

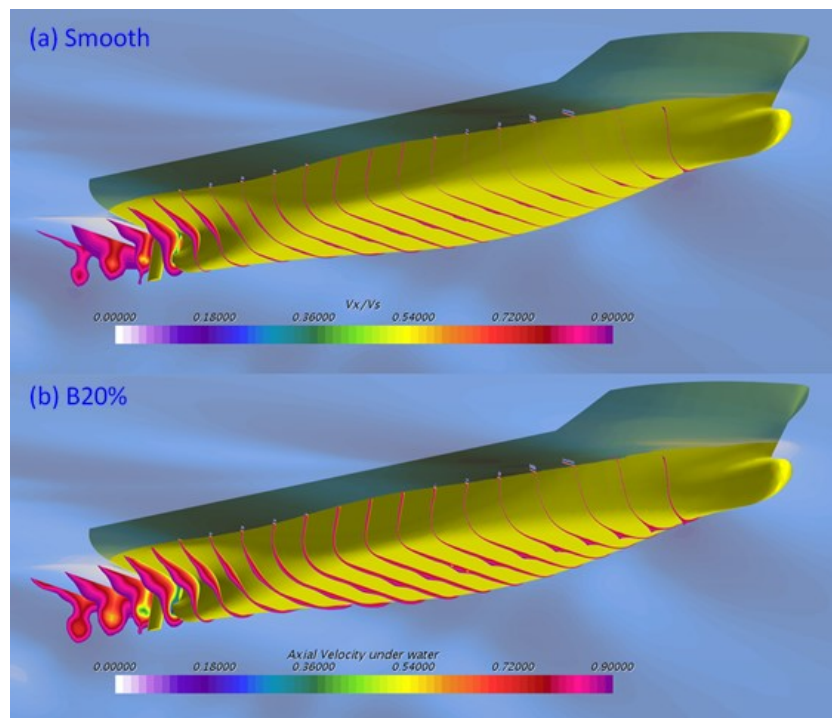


Figure 6.14 Boundary layer represented by slices limited to $V_x/V_{ship} = 0.9$, (a) smooth case, (b) fouled case (B20%)

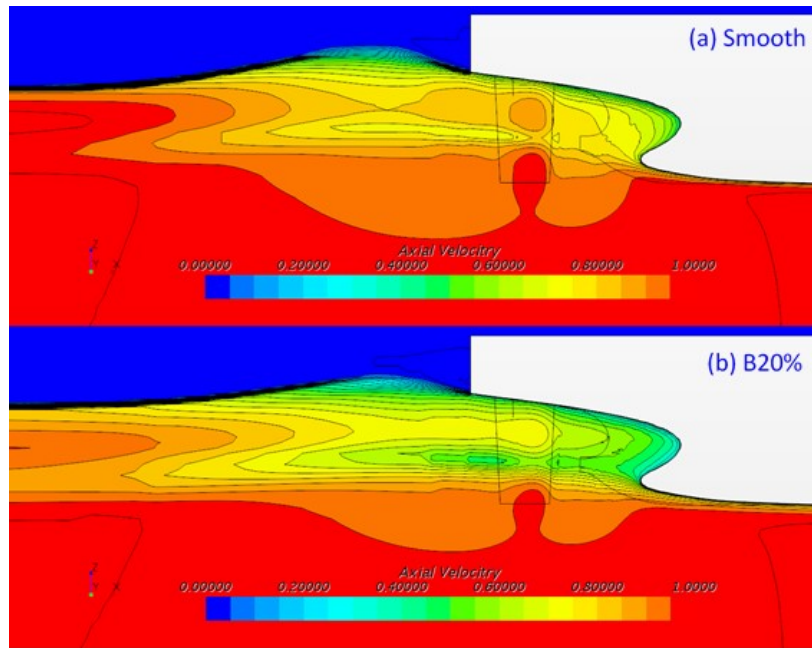


Figure 6.15 Contours of mean axial velocity at $y = 0.006L_{pp}$, (a) smooth case, (b) fouled case, at 24 knots

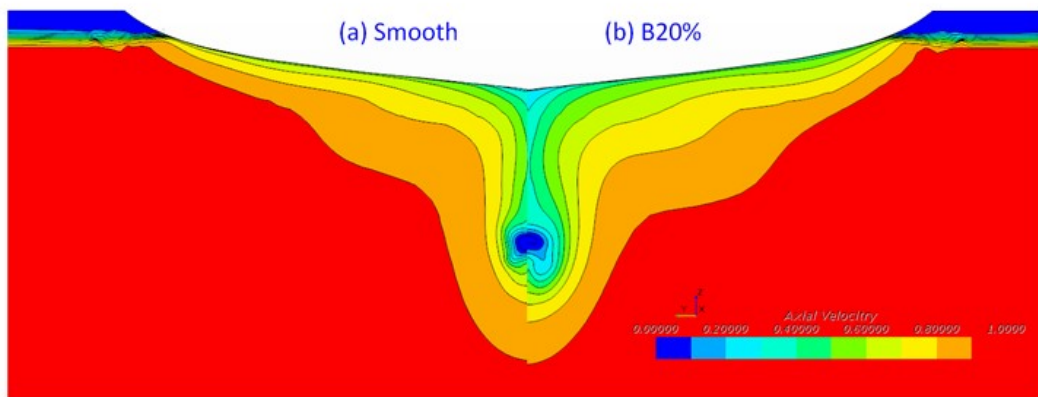


Figure 6.16 Contours of mean axial velocity at $x = 0.0175L_{pp}$, (a) smooth case, (b) fouled case, at 24 knots

6.4.8. Nominal wake

The analysis of the wake flow velocity at the stern region indicated that the surface roughness increases the wake flow which can be best represented by the classical nominal wake fraction parameter. Figure 6.16 compares the distribution of the local wake fraction, $w_x' = 1 - V_x/V_{ship}$, and the transverse velocity vector, V_{xy} , at the propeller plane $x = 0.0175L_{pp}$ at 24knots. The inner and outer circles denote the hub diameter, D_H , and the propeller diameter, D_P , respectively. As shown in the figure, it is evident that the surface roughness of the hull increases the local wake fraction significantly. It was also observed that the surface roughness affects the direction and magnitude of the transverse flow at the propeller section.

Table 6.8 compares the mean nominal wake fraction, w_n , of the KCS in different surface conditions. The mean nominal wake fraction, w_n , was calculated integrating the local wake fraction, w_x' , over the propeller disc. As indicated in the table, the increase in mean nominal wake fraction due to the barnacle fouling can be up to 47% and 44% at 24 knots and 19 knots respectively. From this result, one may expect that the increase in wake fraction may compensate the negative effect of hull fouling in the resistance of the ship by increasing the hull efficiency, η_H . However, the decelerated inflow at the propeller section also affects the propeller efficiency, η_P , by altering the propeller advance coefficient, J . Further investigations into the effect of hull and propeller roughness on ship propulsion performance can be found in Chapter 8.

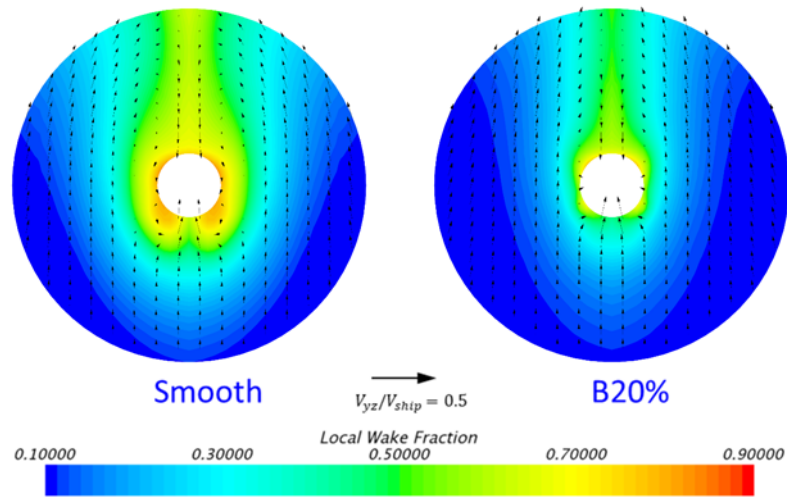


Figure 6.17 Nominal wake distribution, w_x' , and transverse velocity vector, V_{xy} , at the propeller plane in smooth and fouled cases, at 24 knots

Table 6.8 Mean nominal wake fractions computed from the simulations

Surface condition	k_G (μm)	24 knots		19 knots	
		w_n	Δw_n	w_n	Δw_n
Smooth	0	0.1962	0%	0.2015	0%
S 10%	24	0.2350	20%	0.2265	12%
S 20%	63	0.2390	22%	0.2419	20%
M 10%	84	0.2444	25%	0.2474	23%
S 40%	149	0.2565	31%	0.2595	29%
M 20%	165	0.2588	32%	0.2619	30%
B 10%	174	0.2601	33%	0.2632	31%
S 50%	194	0.2627	34%	0.2659	32%
M 40%	388	0.2811	43%	0.2842	41%
M 50%	460	0.2862	46%	0.2892	44%
B 20%	489	0.2880	47%	0.2910	44%

6.5. Chapter summary and conclusions

CFD models for the prediction of the effect of barnacle fouling on ship hydrodynamics have been proposed. To represent the surface roughness of barnacle fouling in the simulation, the roughness function of barnacles obtained by Demirel et al. (2017a) was adopted and embedded into the wall-function of the CFD software so that the surface boundary condition of the hull can represent the barnacle fouling.

A verification study was also conducted to assess the numerical uncertainties of the proposed CFD models and to determine sufficient grid-spacings and time steps. Spatial and temporal convergence studies were performed using the Grid Convergence Index (GCI) method. For the validation of the modified wall-function approach, model-scale flat plate simulations representing different levels of barnacle fouling were modelled using the proposed approach. The simulation results showed excellent agreement with the experimental results of Demirel et al. (2017a).

Fully nonlinear unsteady RANS simulations of the full-scale flat plate representation of the KCS hull and the 3D representation of the same hull with rudder were performed to predict the effect of barnacle fouling on the resistance of this ship. The resulting frictional resistance coefficients were compared with each other, and also compared with the frictional resistance calculated by boundary layer similarity law scaling analysis and they all showed very good agreement in trends and magnitudes. It was observed that up to 93% and 88% of the frictional resistance increase at the design speed and the slow streaming speed can be experienced due to the barnacle fouling.

An interesting finding is that the residuary resistance values of the full-scale KCS show a decreasing trend with increasing fouling rate at 24 knots whereas they show an opposite trend at 19 knots. The residuary resistance coefficients were separated into the viscous pressure resistance and wave-making resistance coefficients, and it was observed that the wave-making resistance decreases with increasing surface roughness while the viscous pressure resistance increases with the increasing fouling rate for both speeds. Therefore, it can be concluded that the residuary resistance can increase or

decrease depending on the dominance of the wave-making resistance and the viscous pressure resistance.

Another interesting finding is that the form factor values decrease as the surface roughness increases. This finding reveals that the increase in the viscous pressure resistance due to the surface roughness is not proportional to the increase in the frictional resistance, which disagrees with the assumptions of Lewis (1988) and Demirel et al. (2017b).

The roughness effect on the wave profile of the KCS was also examined by comparing those of smooth and rough simulations. As expected from the behaviour of the wave-making resistance coefficient, it has been found that the surface roughness results in smaller wave amplitude in the wake region.

By comparing the pressure distributions along the KCS hull in smooth and rough cases, it was found that the surface roughness reduces the pressure recovery at the stern, which results in increased viscous pressure resistance. It is notable that the pressure distributions were observed to be similar from the bow to the middle of the hull. This finding shows that the surface roughness does not affect the residuary resistance unless an adverse pressure gradient occurs, which supports the assumptions made by Schultz (2007) and Demirel et al. (2017a).

The effect of surface roughness on velocity distribution around the hull has also been explored. And it was observed that the surface roughness increases boundary layer thickness and enlarges wake region.

Another important finding is that the stern wake of the ship is significantly affected by the surface roughness. It was found that up to 47% increase in nominal wake fraction can occur due to the hull fouling, which is likely to affect the propulsion performance of the ship.

7. CFD prediction of the effect of biofouling on full-scale propeller performance

7.1. Introduction

As reviewed in Chapter 2, the prediction methods for the roughness effect on the full-scale propeller performance is not well established yet. Atlar et al. (2002) conducted numerical calculations to determine the roughness effect on the propeller open water characteristics, by using a lifting surface based propeller model combined with an empirical skin friction correction. They used a propeller roughness comparator to represent the blade roughness after several years in service. The increment of the blade section drag coefficient due to the roughness was calculated utilising the early work of Mosaad (1986) and used in the numerical computation. The result indicated that the loss of the propeller efficiency could be as high as 12 % with the increase in torque and decrease in thrust due to the surface roughness of the blades.

Similarly to Atlar et al. (2002), Seo et al. (2016) also used a lifting surface based propeller model with enhanced empirical correction for the skin friction for the numerical predictions of full-scale propeller efficiency loss due to surface fouling on the blades. The increased drag coefficient of the blade section due to the surface fouling were predicted based on the boundary layer similarity law analysis. Utilising the drag coefficients of different fouling conditions, they estimated a 14.6% loss in propeller efficiency with small calcareous fouling condition.

However, these studies are still limited by the fact that the roughness effect on the propeller is only considered by using increased blade section drag coefficients rather than imitating the roughness effect on the fluid field around the propeller, which is closely related to the surface pressure distribution on the blades. In consequence, they could not observe a considerable roughness effect on thrust, while significant increases in the torque were observed from the calculation results.

Recently, as asserted by Atlar et al. (2018), the use of Computational Fluid Dynamics (CFD) is seen as an effective alternative to overcome the above-mentioned limitations of the boundary layer similarity law analysis. In CFD simulations, the roughness effect on the pressure field around the propeller can be predicted as well as other hydrodynamic characteristics. Owen et al. (2018) investigated the roughness effect of biofouling on propeller characteristics using a CFD software (STAR-CCM+). A roughness function model representing different fouling conditions was employed in the wall-function of the CFD software. The simulation results indicated that severe calcareous fouling could result in 30.3% of efficiency loss compared to the smooth case. However, as the simulations were conducted in the model-scale only, it is still questionable if the simulation results can realistically represent the full-scale effect of biofouling on real marine propellers.

To the best of the author's knowledge, there exists no specific study to predict the effect of biofouling on the full-scale marine propeller characteristics using CFD. Therefore, the aim of this chapter is to fill this gap by developing a CFD model to predict the effect of biofouling on the open water performance of a full-scale marine propeller.

This chapter is organised as follows: Section 7.2.1 explains the methodology used in this chapter, while Section 7.2.2 covers the modified wall-function approach for barnacle fouling. The details of the numerical modelling are discussed in Section 7.2.3, including the mathematical formulations, geometry and boundary conditions of the simulations as well as the mesh generation. The verification and validation studies are presented in Section 7.3. The roughness effect on the open water performance of the propeller is presented in Section 7.4.1 while the effect on the flow characteristics is discussed in Section 7.4.2. Finally, chapter summary and conclusions are discussed in Section 7.5.

7.2. Methodology

7.2.1. Approach

A schematic illustration of the current study is shown in Figure 7.1. As used in Chapter 6, the same modified wall-function approach was applied to full-scale KP505 propeller simulations to predict the effect of barnacles on the open water performance. A validation study was performed by comparing the smooth open water curves obtained from the CFD simulations with the experimental results of Fujisawa et al. (2000). The CFD simulations then conducted under different fouling conditions. The changes in the open water performance of the propeller due to the barnacles were examined. Finally, the roughness effects on the flow characteristics around the propeller were investigated.

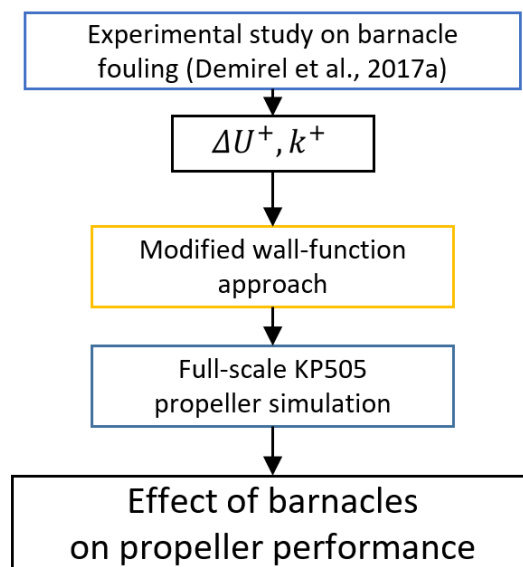


Figure 7.1 Schematic illustration of the methodology in Chapter 7

7.2.2. Modified wall-function approach for barnacle fouling

As mentioned earlier, the same modified wall-function approach with the roughness function of barnacles (Demirel et al., 2017a) was used as in Chapter 6. Further details regarding the modified wall-function approach and the roughness function of the barnacle surfaces can be found in Section 5.2.3 and Section 6.2.2, respectively.

7.2.3. Numerical modelling

7.2.3.1. Mathematical formulations

The CFD models were developed based on the unsteady Reynolds-averaged Navier-Stokes (URANS) method using a commercial CFD software package, STAR-CCM+ (version 12.06). The mathematical formulations are identical to those used in Chapter 5. The details can be found in Section 5.2.2.

7.2.3.2. Geometry and boundary conditions

In this study, a full-scale CFD model of KP505 propeller was developed to examine the effect of biofouling on propeller performance. The KP505 propeller was designed by Korea Research Institute of Ships and Ocean Engineering (KRISO) to be used for the KRISO Container Ship (KCS). Table 7.1 and Figure 7.2 show the principal particulars and geometry of the KP505 propeller.

Table 7.1 Principal particulars of KP505 propeller

Propeller Type	FPP
No. of Blades	5
Diameter (m)	7.9
P/D (mean)	0.950
Ae/Ao	0.800
Rotation	Right Hand
Hub ratio	0.18
Section	NACA66

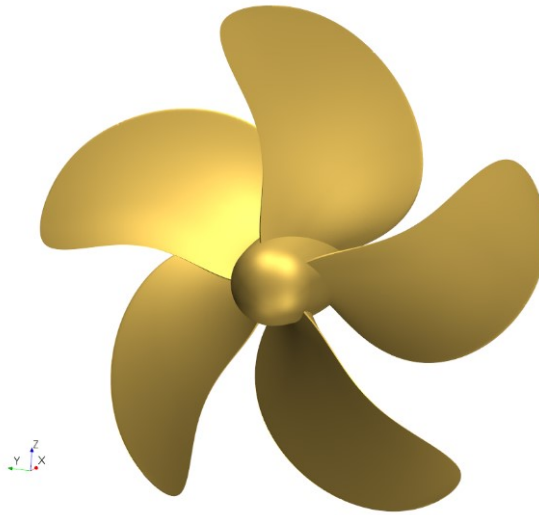


Figure 7.2 KP505 propeller

Figure 7.3 depicts an overview of the computational domain with the selected boundary conditions in the CFD simulations. The boundary conditions of the simulations were selected to represent the propeller which is completely submerged in an infinite ocean. The computational domain consists of a stationary region (outer zone) and a rotating region (inner zone).

For the opposite faces at the x –direction, a velocity inlet boundary condition was applied for the inlet free-stream boundary condition, and a pressure outlet was chosen for the outlet boundary condition while the far-field boundaries were defined as symmetry planes. The inlet, outlet and far-field boundaries were placed at $5D$, $13D$ and $3.5D$ distance from the propeller to avoid any reflections downstream of the propeller and to ensure uniform incoming flow upstream of the propeller, as similarly used by Owen et al. (2018).

The surface boundary condition of the propeller was defined as the no-slip condition. For smooth cases, the smooth type wall-function was used (i.e. Equation 5.5 without ΔU^+) while the fouled cases used the rough type wall-function containing the roughness function model, corresponding Equation 5.5 and 6.1. It is of note that for the fouled propeller simulations, the rough surface conditions were applied to both the propeller hub and blades.

In this study, the Moving Reference Frame (MRF) approach was used to simulate the rotating propeller (Luo et al., 1994). The MRF approach, also known as ‘Multiple Reference Frame’ or ‘Frozen Rotor Approach’, is a steady-state approximation. In this approach, individual cell zones can be assigned different translational and/or rotational motions and solved using the corresponding equations of the reference frames, e.g. the inner zone (yellow cylinder in Figure 7.3) using a rotating frame and the outer zone associated with a stationary frame in this study. Since the MRF approach does not require complicated mesh motion and uses a steady-state solver for the flow field, it is simpler and computationally cheaper compared to other unsteady approaches (e.g. the Sliding Mesh). As shown by other studies (Owen et al., 2018; Mizzi et al., 2017), the author believes that the MRF method does not bring any significant difference in the results compared to other unsteady methods.

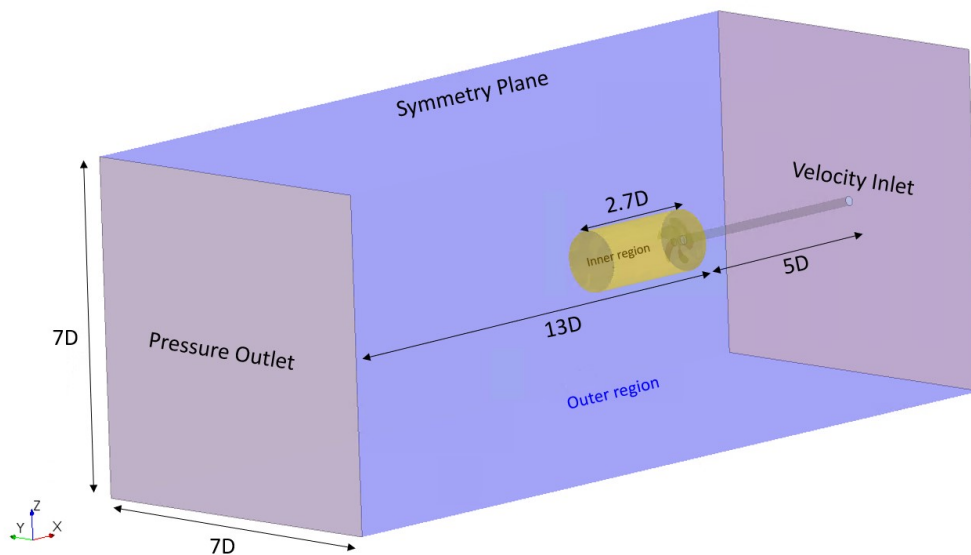
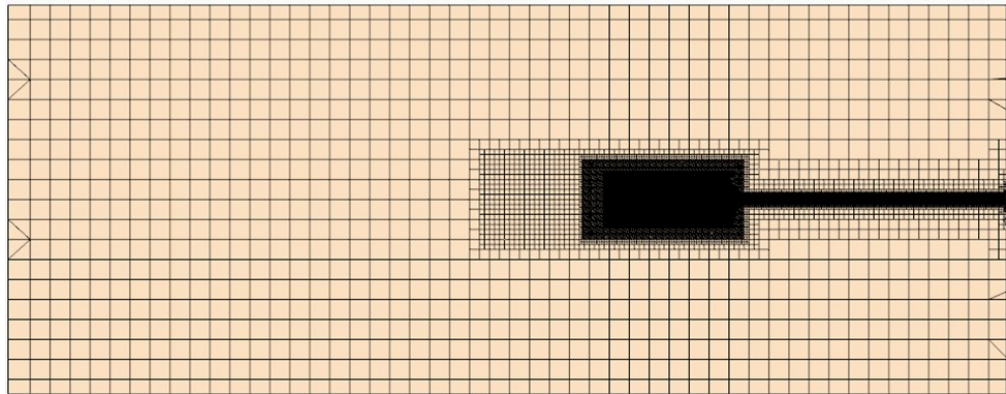


Figure 7.3 Computational domain and boundary conditions of the simulation model

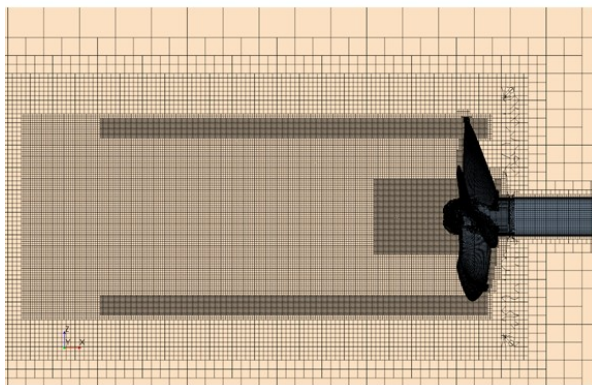
7.2.4. Mesh generation

Mesh generation was performed using the built-in automated meshing tool of STAR-CCM+. Trimmed hexahedral meshes were used for the high-quality grid for the complex domains. Local refinements were made for finer grids in the critical regions,

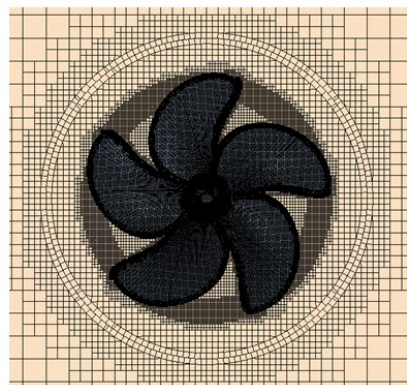
such as blade edges and areas where the tip and hub vortices are expected to occur as shown in Figure 7.4. The prism layer meshes were used for near-wall refinement, and the thickness of the first layer cell on the surface was chosen such that the y^+ value is always higher than 30 and k^+ , as suggested by Demirel et al. (2017a) and CD-Adapco (2017).



(a) Side view



(b) Grid refinement for vortices



(c) Suction side

Figure 7.4 Grid system of KP505 simulation

7.3. Verification and validation

7.3.1. Verification study

Verification studies were conducted to estimate the spatial uncertainties of the simulations. The Grid Convergence Index (GCI) method based on Richardson's extrapolation (1910) was used to estimate the numerical uncertainties, as used in Chapter 5. Further details regarding the GCI method can be found in Section 5.2.7.

It is of note that the simulations were conducted using a steady solver, only the spatial convergence study was carried out.

7.3.1.1. Spatial convergence study

For the grid convergence study, grid structures with three different resolutions were generated, which are referred to as fine, medium, and coarse meshes corresponding to cell numbers of N_1 , N_2 , and N_3 . Table 7.2 shows the required parameters for the calculation of the spatial discretization error. The propeller open water characteristics, K_T , K_Q and η_O , of the smooth case at the advance coefficient of $J = 0.7$ were used as the key variables. As indicated in the table, the GCI values of K_T , K_Q and η_O using the fine mesh is 0.0002%, 0.38%, and 0.89%, respectively. For accurate prediction, the fine mesh was used to simulate the roughness effect of barnacle fouling on the propeller performance.

Table 7.2 Parameters used for the calculation of the discretization error for the spatial convergence study, key variable: K_T , $10K_Q$, and η_o

	K_T	$10K_Q$	η_o
N_1	6,009,483	6,009,483	6,009,483
N_2	2,253,645	2,253,645	2,253,645
N_3	1,250,127	1,250,127	1,250,127
r_{21}	1.63	1.63	1.63
r_{32}	1.34	1.34	1.34
ϕ_1 (Fine)	1.7980E-01	2.978E-01	6.73E-01
ϕ_2 (Medium)	1.7978E-01	2.988E-01	6.70E-01
ϕ_3 (Course)	1.7960E-01	2.990E-01	6.69E-01
ε_{32}	-1.78E-04	2.41E-04	-1.00E-03
ε_{21}	-1.61E-05	9.79E-04	-3.00E-03
s	1	1	1
e_a^{21}	0.01%	0.33%	0.45%
q	1.72E+00	6.70E-01	6.13E-01
p_a	8.40E+00	1.49E+00	9.91E-01
ϕ_{ext}^{21}	1.798E-01	2.969E-01	6.778E-01
e_{ext}^{21}	-0.0001%	0.3053%	-0.7074%
GCI_{fine}^{21}	0.0002%	0.38%	0.89%

7.3.2. Validation study

The propeller open water curves computed in the full-scale CFD simulations were compared with the model-scale Experimental Fluid Dynamics (EFD) of Fujisawa et al. (2000).

As presented in Figure 7.5, a good agreement was achieved between the CFD and EFD results. There is a slight overestimation of K_T and K_Q at low J values and conversely, a slight underestimation of them at high J values as similarly observed from the full-scale KP505 simulations by Castro et al. (2011). It is of note that the propeller Reynolds numbers, based on chord length at 0.7R and the relative flow velocity ($V_R = \sqrt{V_A^2 + (0.7\pi nD)^2}$) of the current full-scale CFD were $5.6 - 5.8 \times 10^7$, at $J = 0.2 - 0.8$, while these for the model-scale EFD were $6.5 - 6.9 \times 10^5$.

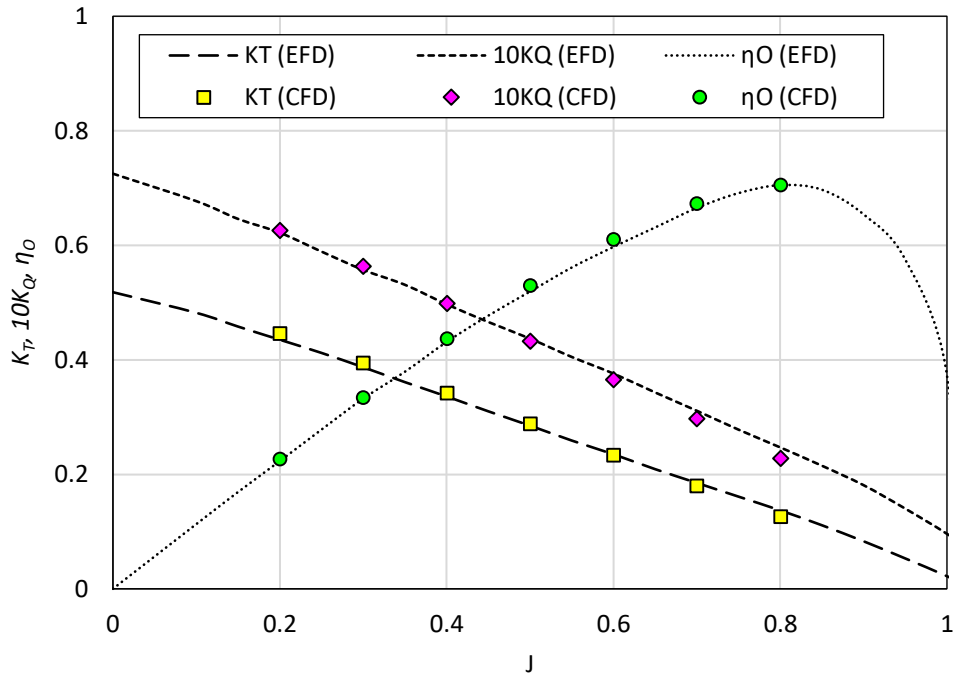


Figure 7.5 Comparison of the propeller open water curves obtained from the current CFD and EFD (Fujisawa et al., 2000)

7.4. Results

7.4.1. Roughness effect on the open water coefficients

For the investigation into the effect of barnacle fouling on the propeller performance characteristics, full-scale simulations of the propeller performance in open water were conducted in the different fouling conditions. The simulations were conducted at the advance coefficients, J , ranging from 0.2 to 0.8, where the corresponding propeller Reynolds numbers are 5.6×10^7 to 5.8×10^7 .

Figures 7.6-7.8 compare the propeller open water characteristics computed from the CFD simulations in the different surface conditions of barnacle fouling. In the figure, the K_T , $10K_Q$ and η_O values are plotted against the representative roughness heights of the corresponding fouling conditions (Table 6.1).

As shown in Figure 7.6, the thrust coefficients, K_T , were observed to decrease with increasing fouling severity. The relative differences in K_T between the smooth case and the most severe fouling case (B20%) were -3.7% at $J=0.2$ to -11.1% at $J=0.8$. It is of note that while the absolute differences between the smooth and rough cases remain similar among the different advance coefficients, the relative differences were observed to be larger at higher advance coefficients due to the smaller smooth K_T values at high advance coefficients.

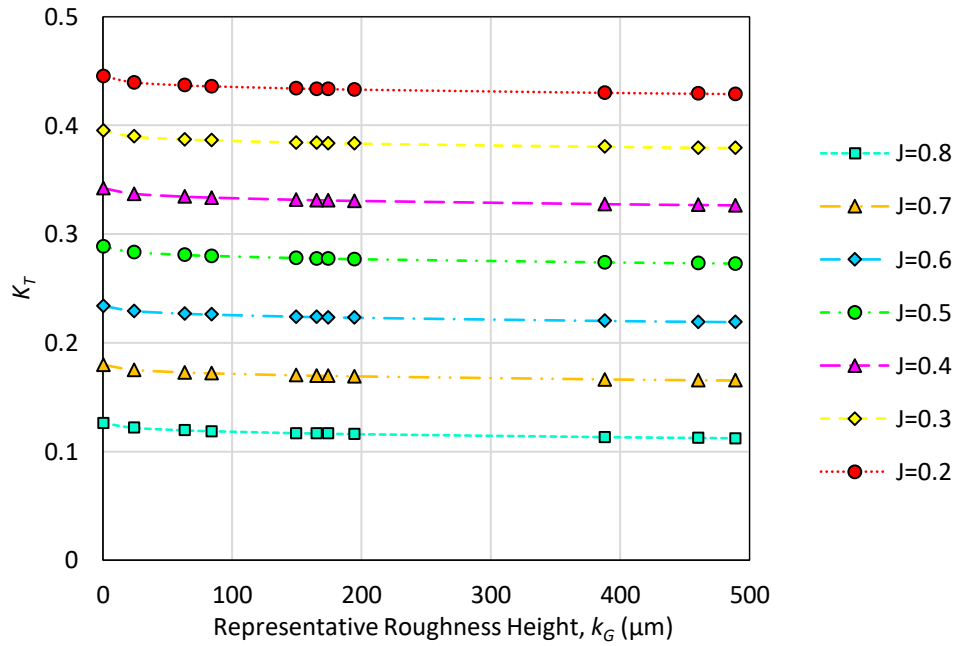


Figure 7.6 Thrust coefficients decreasing with the level of surface fouling

Figure 7.7 compares the torque coefficients, $10K_Q$, values against the representative roughness heights. Contrary to the case of K_T , there is a tendency for the $10K_Q$ values to increase with the increasing level of fouling. The relative differences in $10K_Q$ between the smooth case and the most severe fouling case (B20%) were 2.6% at $J=0.2$ to 10.2% at $J=0.8$. Similarly, to the thrust coefficients, the relative differences were larger at high advance coefficients while the absolute differences remained similar.

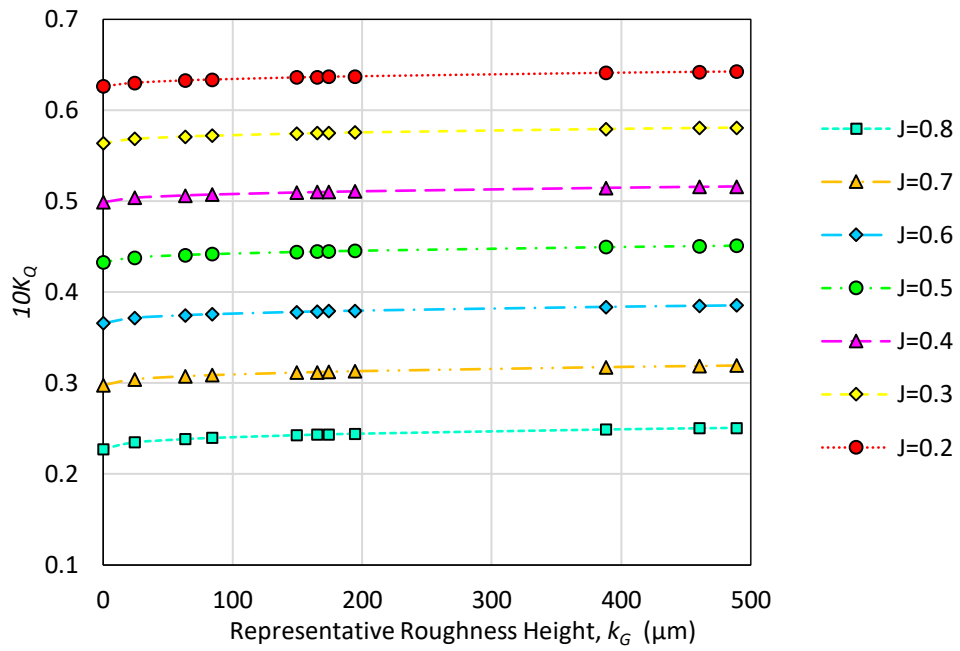


Figure 7.7 Torque coefficients increasing with the level of surface fouling

The decrease in thrust coefficients and the increase in torque coefficients result in a reduction of propeller open water efficiencies, η_o , as shown in Figure 7.8. The relative differences in η_o between the smooth case and the most severe fouling case (B20%) were -6.2% at $J=0.2$ to -19.3% at $J=0.8$. Unlike the cases of K_T and $10K_Q$, both of the absolute and relative differences of η_o between the smooth and rough cases were observed to be larger at high advance coefficients, due to the fact that η_o indicates the ratio of K_T and $10K_Q$.

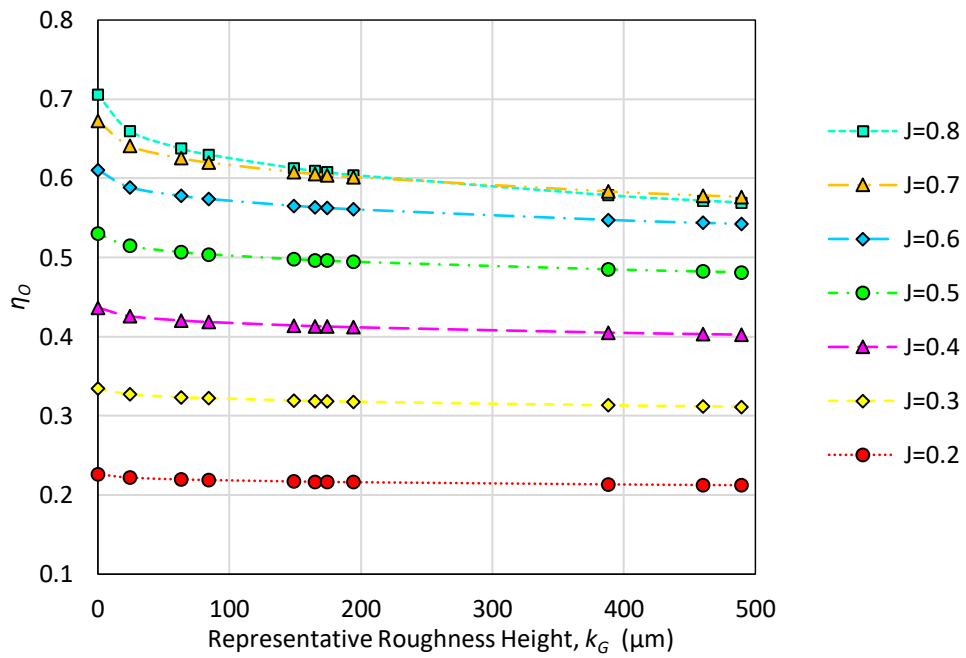


Figure 7.8 Propeller efficiency decreasing with the level of surface fouling

It is interesting to note that, as shown in Figure 7.6-7.8, the rate of the change in K_T , K_Q , and, η_0 become smaller as the fouling severity increases, which is in agreement with the behaviour of the full-scale measurements as discussed by Atlar et al. (2002).

Figure 7.9 compares the overall propeller open water curves computed in the smooth condition and the most severe fouling condition (B20%). The consistent decreases in K_T and the increases in K_Q along with the advance coefficients can be seen in the figure. An interesting feature from the figure is that the optimum J point where the maximum efficiency is found was moved with the presence of surface fouling (i.e. the smooth case shows the maximum η_0 at $J=0.8$, while that of the rough case is found around $J=0.7$).

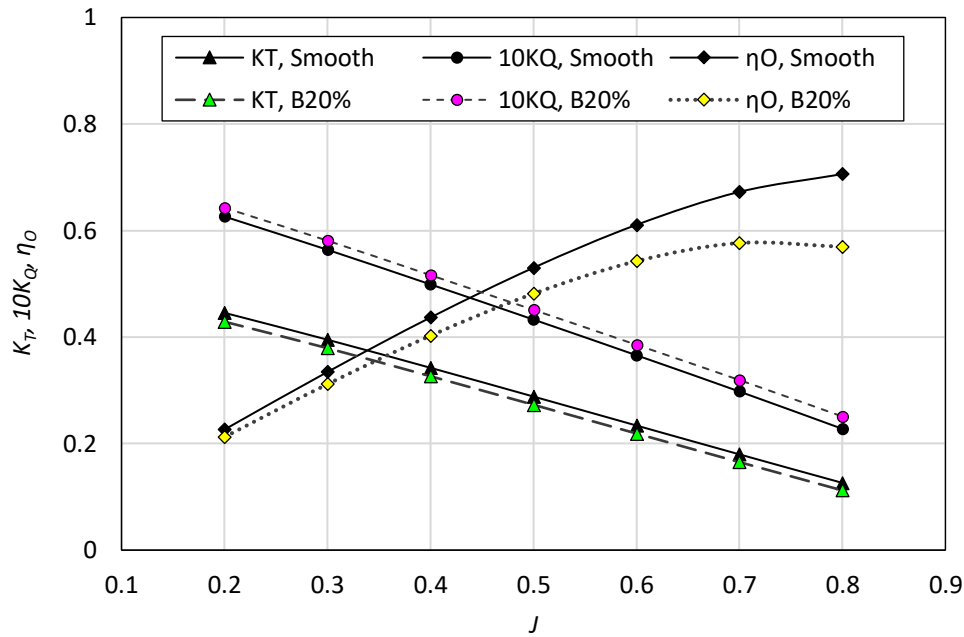


Figure 7.9 Comparison of the Propeller open water curves in smooth and rough (B20%) conditions

Figure 7.10 and 7.11 illustrate the contributions of the pressure and shear (frictional) components in the thrust and torque coefficients (i.e. $T_{total} = T_{shear} + T_{pressure}$ and $Q_{total} = Q_{shear} + Q_{pressure}$) at $J=0.7$. The surface conditions were arranged in the order of increasing fouling severity (i.e. representative roughness height, k_G , from Table 1).

As can be seen in Figure 7.10, the shear components of the thrust always act in the negative direction and increase with the level of surface fouling (by 154%), while the pressure components decrease with the increased surface roughness (by -8.1 %). Accordingly, the total thrust coefficient decreases with the presence of surface fouling.

On the other hand, an interesting feature was observed in the torque coefficients. As can be seen in Figure 7.11, the pressure torque components decrease with increasing surface fouling (by -5.1%), which is desirable for propeller efficiency. However, the rate of increase in frictional torque component is much higher (by 168%) than that of

pressure torque such that the overall torque coefficients show an increasing trend with the level of surface fouling. It is of note that the decrease in the pressure torque can be related to the decreased pressure thrust as shown in Figure 7.10.

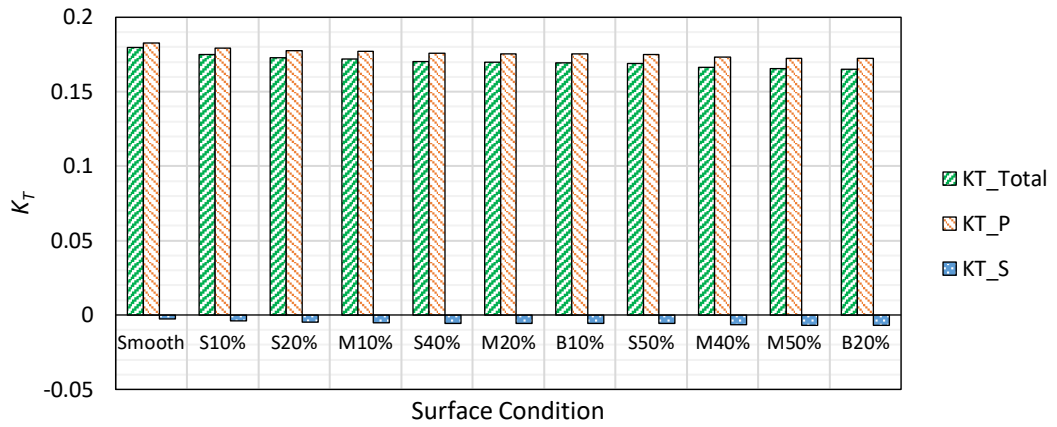


Figure 7.10 Contribution of the thrust coefficient components, at J=0.7

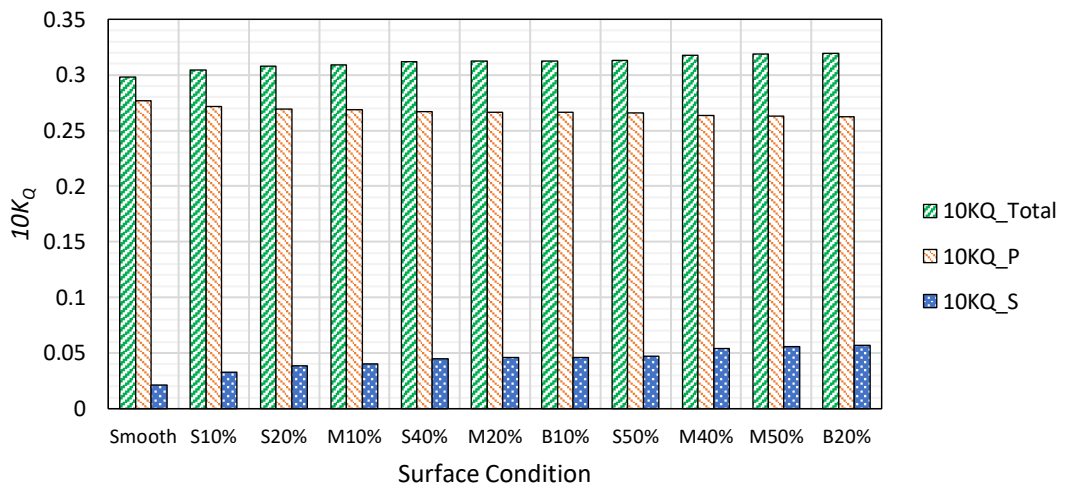


Figure 7.11 Contribution of the torque coefficient components, at J=0.7

7.4.2. Roughness effect on flow characteristics

7.4.2.1. Pressure distribution

Figure 7.12 compares the pressure fields on the $y = 0$ plane in the smooth and fouled (B20%) surface conditions. The pressure was non-dimensionalised by dividing it by the dynamic pressure, $1/2\rho V^2$. It can be seen from the figure that the fouled case has a less vivid colour map of the pressure distribution, which results in a smaller pressure difference between the pressure and suction sides of the propeller, as depicted in Figure 7.13. This observation is in accordance with the decreased pressure components in the thrust and torque due to the surface fouling observed in the previous section.

Interestingly a remarkable reduction was observed in the pressure drop downstream of the propeller hub by the fouled surface. This can be seen as a positive effect of the surface roughness as opposed to its unfavourable effect on the propeller blades. The change in pressure distribution can be explained by the reduced strength of the hub vortex, which can be found in Figure 7.17 and 7.18.

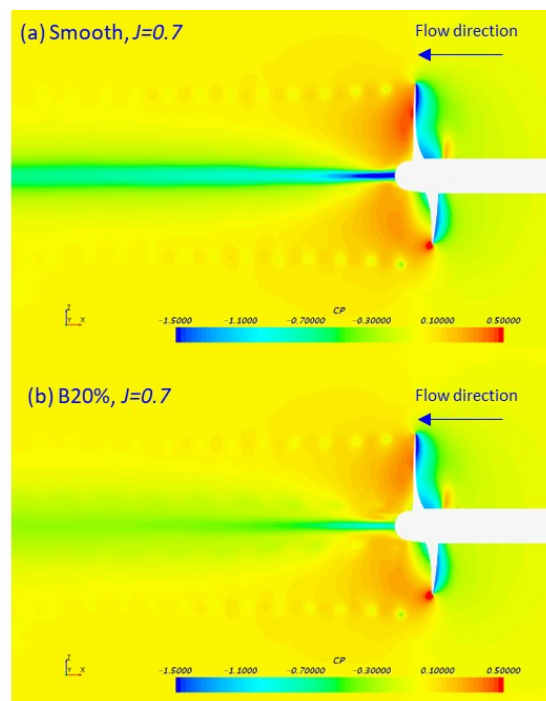


Figure 7.12 Pressure distribution on $y = 0$ plane, at $J=0.7$

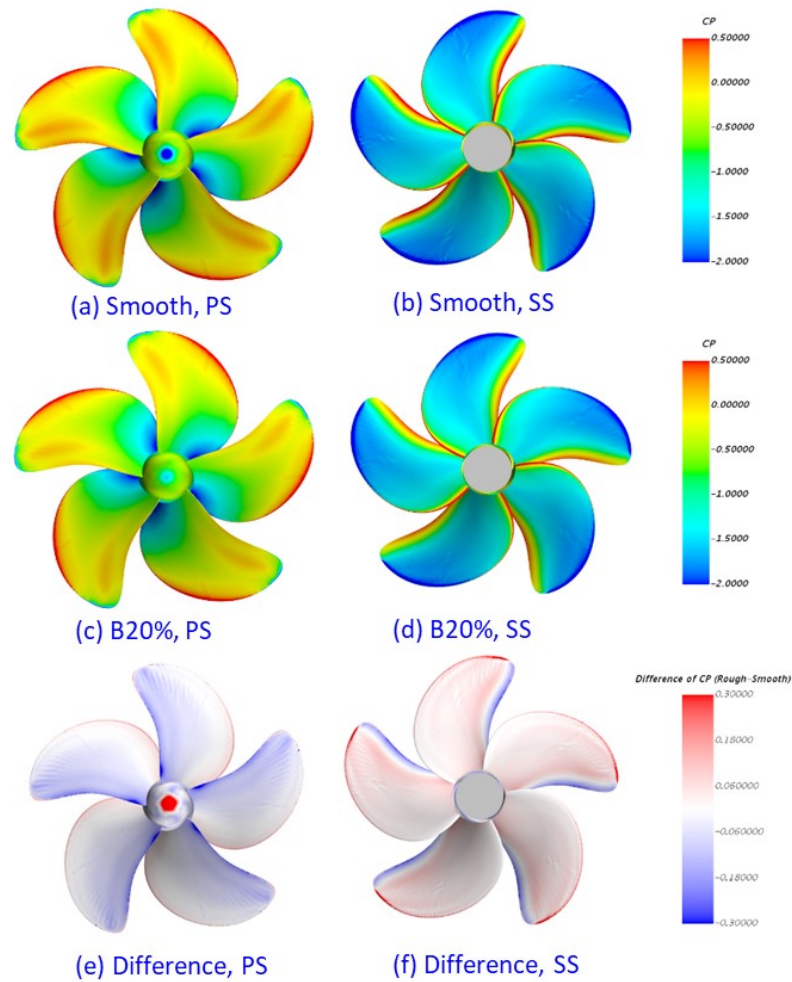


Figure 7.13 Pressure distribution on the propeller surface, at $J=0.7$

7.4.2.2. Wall shear stress distribution

Figure 7.14 illustrates the non-dimensional wall shear stress magnitude on the propeller surface in the smooth and fouled (B20%) surface conditions at $J=0.7$. The wall shear stress was non-dimensionalised by dividing it by the dynamic pressure, $1/2\rho V^2$. As can be seen in the figure, the wall shear stress values increased significantly due to the increased surface roughness. This observation is in agreement with the increased shear torque components observed in the previous section.

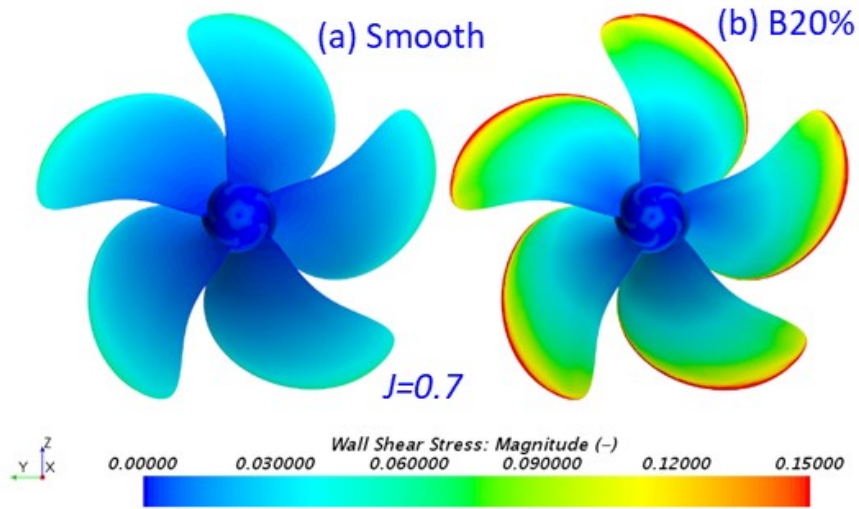


Figure 7.14 Wall Shear stress coefficients, at $J=0.7$

7.4.2.3. Velocity distribution

Figure 7.15 and 7.16 illustrate the axial and transverse velocity on the $y = 0$ plane in the smooth and fouled (B20%) surface conditions at $J=0.7$. As shown in Figure 7.15, the fouled case shows more scattered velocity distributions compared to the smooth case, which is believed to be linked to the pressure distribution resulting in thrust loss.

As shown in Figure 7.16, increases in boundary layer thickness due to the surface fouling on the blades were observed, which can be related to the increased wall stress observed in Figure 7.14. From this observation, it can also be deduced that the increased boundary layer thickness increases the amount of fluid rotating with the propeller. Therefore, the transverse velocity distribution at the downstream becomes more fluctuating and complicated as can be seen in Figure 7.16b.

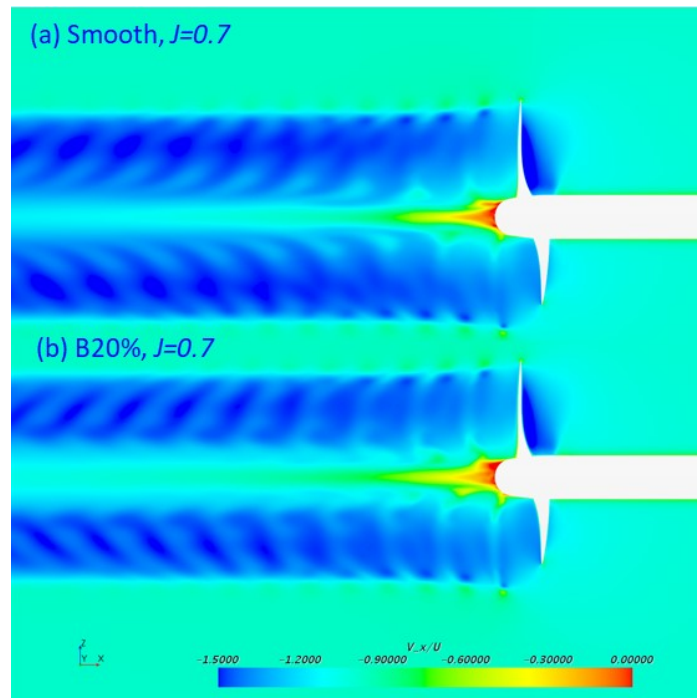


Figure 7.15 Axial velocity on $y = 0$ plane, at $J=0.7$

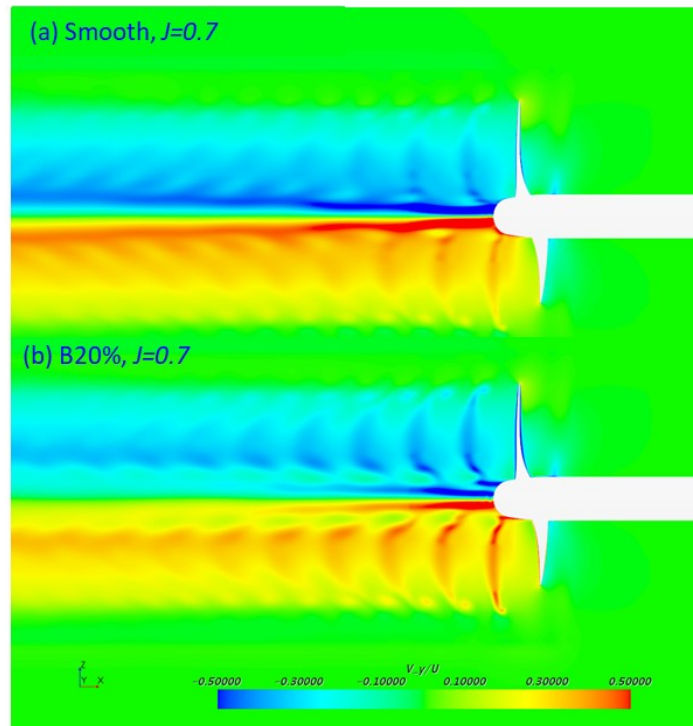


Figure 7.16 Transverse velocity on $y = 0$ plane, at $J=0.7$

7.4.2.4. Propeller vortices

To examine the effect of barnacle fouling on the propeller vortices, the vorticity magnitudes on the $y = 0$ plane for the smooth and fouled (B20%) surface conditions are illustrated in Figure 7.17. Similar to the features of the pressure and velocity fields observed in the previous sections, the vorticity of the fouled case shows a more dispersed distribution compared to the smooth case. The strengths of tip and hub vortices were observed to be reduced due to the surface roughness and thus dissipate earlier, while the vorticity in between tip and hub vortices increases.

This can be seen more clearly using the second invariant of the velocity gradient tensor, Q-Criterion. Figure 7.18 illustrates the iso-surface of Q-Criterion ($Q = 10s^{-2}$) coloured with relative helicity. The tip and hub vortices of the fouled propeller dissipate earlier than those of the smooth propeller, and stronger vortices formed in between the tip and hub vortices can also be found in the figure. It can be inferred that the reduced the hub vortex is related to the reduced pressure drop downstream of the propeller hub as shown in Figure 7.13.

This finding is significant since it suggests the possibility that the surface roughness can be used to control the propeller vortices and resolve the problems associated with the propeller vortices, e.g. propeller cavitation. However, this will require a fine compromise between the two conflicting consequences, i.e. the efficiency loss of the blades and mitigation of hub vortex cavitation.

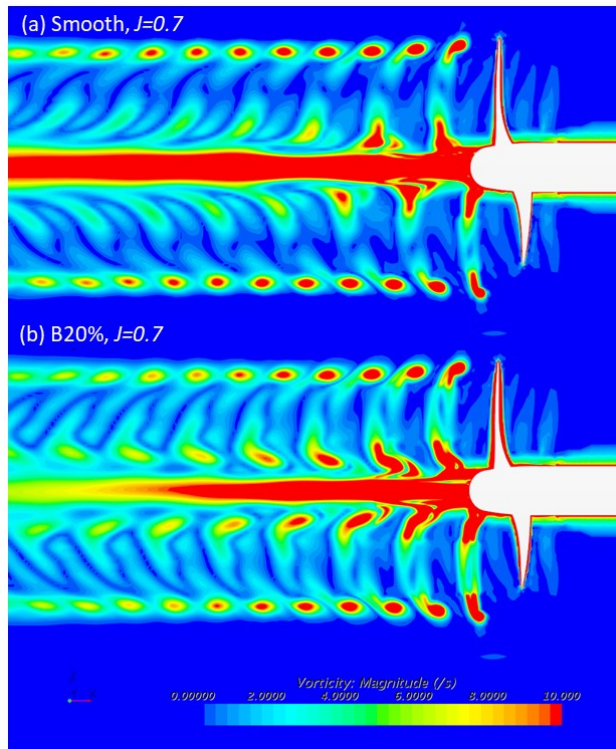


Figure 7.17 Vorticity magnitude on $y = 0$ plane, at $J=0.7$

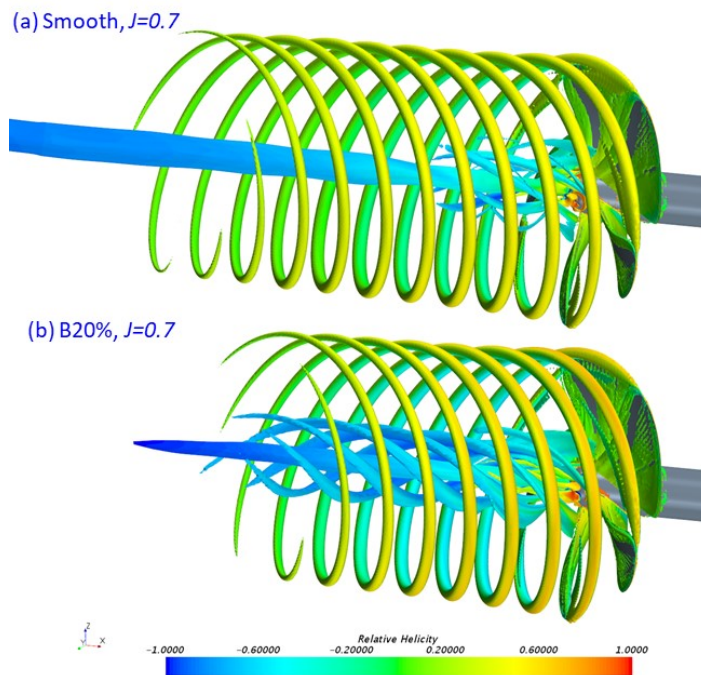


Figure 7.18 Isosurface of Q-criterion, at $J=0.7$

7.5. Chapter summary and conclusions

A CFD model has been proposed to investigate the effect of barnacle fouling on the performance of the KP505 propeller. To predict the effect of barnacles on the propeller surface, the same modified wall-function approach was applied to full-scale KP505 propeller simulations as used in Chapter 6.

A verification study was conducted to assess the numerical uncertainties of the proposed CFD model and to determine sufficient grid-spacings. The propeller open water coefficients obtained from the CFD simulations were compared with the experimental data of Fujisawa et al. (2000) and showed a good agreement.

Fully nonlinear RANS simulations of the full-scale KP505 propeller were performed in different surface conditions to investigate the effect of barnacle fouling on the propeller open water performance. Decreases in the thrust coefficient were observed with the presence of surface fouling while the torque coefficient increases. This leads to a loss in propeller open water efficiency up to 19.3% with the most severe fouling condition (B20%).

The roughness effect on the fluid field downstream of the propeller was also examined. More dispersed distributions of the pressure field were observed when the propeller is fouled, which leads to the decreased pressure differences on the pressure side and suction side of the propeller. Interestingly, the pressure drop behind the propeller cap is remarkably reduced due to the fouled surface, which can be interpreted as a positive consequence (e.g. to mitigate/reduce hub vortex cavitation), apart from its unfavourable effect on the blades.

The axial and transverse velocity distributions in the smooth and rough surface conditions were also compared. The axial velocities of the fouled case showed more scattered distribution than the smooth case as similarly observed in the pressure field.

From the transverse velocity distribution, increased boundary layer thickness on the propeller blades was found, which can be related to the increased wall shear stress.

Another interesting finding is that the surface roughness reduces the strength of the propeller hub and tip vortices, which is believed to be one of the reasons for the reduced pressure drop downstream of the propeller hub. This suggests the possibility that the surface roughness can be used to control the propeller vortex and the associated problems.

This study has provided several important findings such as the roughness effect on the propeller open water characteristics, pressure and velocity distributions, and propeller vortices. However, since this study was only conducted in open water condition, i.e. a uniform inflow, it may not well represent a real case of a marine propeller which is operating in the wake of a ship hull. Therefore, to fill this gap, an investigation into the effect of hull and propeller fouling on ship self-propulsion performance is presented in Chapter 8.

8. CFD prediction of the effect of biofouling on ship self-propulsion performance

8.1. Introduction

As reviewed in Chapter 2, there have been active efforts devoted to investigating the critical impact of biofouling on ship resistance and powering, as well as the effect on propeller performance. Although these studies enable us to better understand the effect of biofouling on full-scale ship resistance and propeller characteristics, it is still worth investigating the effect of biofouling on ship self-propulsion characteristics to precisely predict the effect on the delivered power of the ship with the presence of the hull-rudder-propeller interaction. The prediction of the impact of the hull and/or propeller fouling can be used as a cost-benefit analysis, to schedule the hull and/or propeller cleaning, by comparing the cost associated with the dry-docking and cleaning against the economic penalty of the increased fuel consumption.

To the best of the author's knowledge, there exists no specific study to predict the effect of biofouling on the full-scale ship self-propulsion characteristics using CFD. Therefore, the main aim of this chapter is to fill this gap by developing a CFD model to investigate the effect of barnacles on ship self-propulsion characteristics and perform a systematic analysis on the effects of both the hull fouling and propeller fouling.

This chapter is organised as follows: Section 8.2.1 explains the methodology used in this chapter, and Section 8.2.2 covers the modified wall-function approach for barnacle fouling. The details of the numerical modelling are discussed in Section 8.2.3, including the mathematical formulations, geometry and boundary conditions of the simulations as well as the mesh generation. Section 8.2.4 explains the fouling scenarios used in this study, while Section 8.2.5 presents the propeller speed controller used to find the self-propulsion point. The verification and validation study is presented in

Section 8.3. The simulation results are presented in Chapter 8.4, and the effect of the hull and/or propeller fouling on ship self-propulsion characteristics are discussed. Finally, the roughness effect on the flow characteristics around the hull and propeller is discussed in Chapter 8.5.

8.2. Methodology

8.2.1. Approach

A schematic illustration of the current study is shown in Figure 8.1. As used in Chapter 6 and 7, the same modified wall-function approach was applied to full-scale KCS self-propulsion simulations to predict the effect of biofouling on ship self-propulsion performances. A verification study was performed to examine the numerical uncertainties arising from the spatial and temporal discretisation. A validation study for the self-propulsion model with a smooth surface was performed by comparing a model-scale simulation with experimental data and investigating the effect of scale and the presence of the rudder. The CFD simulations were conducted in different configurations of fouling severities (barnacle sizes and coverages) and fouling scenarios (namely; *fouled-hull/clean-propeller*, *clean-hull/fouled-propeller*, and *fouled-hull/fouled-propeller*). Finally, the effect of biofouling on the self-propulsion characteristics have been studied.

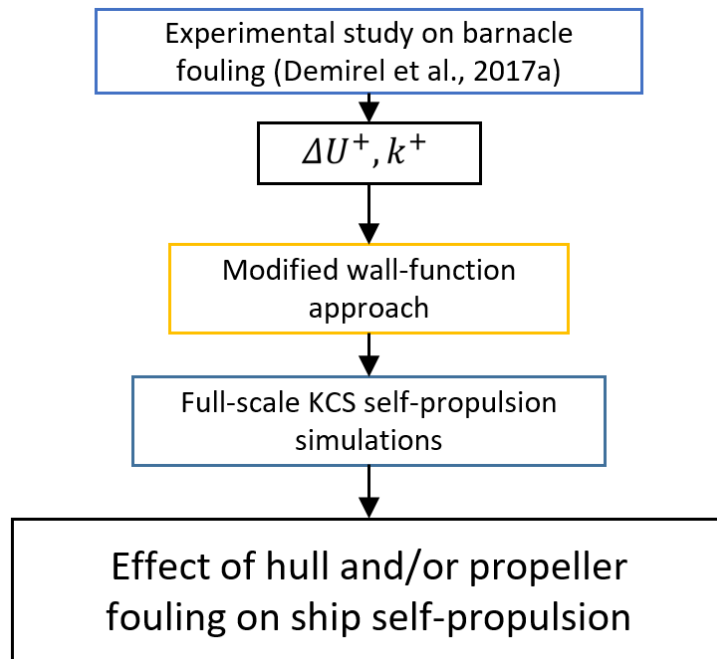


Figure 8.1 Schematic illustration of the methodology in Chapter 8

8.2.2. Modified wall-function approach for barnacle fouling

As mentioned earlier, the same modified wall-function approach with the roughness function of barnacles (Demirel et al., 2017a) was used as in Chapter 6 and 7. Further details regarding the modified wall-function approach and the roughness function of the barnacle surfaces can be found in Section 5.2.3 and Section 6.2.2, respectively.

8.2.3. Numerical modelling

8.2.3.1. Mathematical formulations

The CFD models were developed based on the unsteady Reynolds-averaged Navier-Stokes (URANS) method using a commercial CFD software package, STAR-CCM+ (version 12.06). The mathematical formulations are identical to those used in Chapter 5. The details can be found in Section 5.2.2.

8.2.3.2. Geometry and boundary conditions

A full-scale model of the KRISO container ship (KCS) with rudder and propeller (KP505) was used in this study. The geometry of the KCS with KP505 rudder is presented in Figure 8.2. The principal particulars of KCS can be found in Table 5.1, while the principal particulars of KP505 propeller can be found in Table 7.1.



Figure 8.2 Geometry of the KCS with rudder and propeller

Figure 8.3 depicts an overview of the computational domain with the selected boundary conditions in the CFD simulations. The computational domain consists of a stationary region and a rotating region, where the propeller is located (cylinder in the magnifier window in Figure 8.3). In order to simulate the rotating propeller behind the hull, a sliding mesh method was used whereas the MRF method was used for the propeller open water simulation in Chapter 7, as the free surface is present in the self-propulsion simulations. For the opposite faces in the x – direction, velocity inlet boundary and pressure outlet boundary conditions were applied. On the other hand, the far-field boundaries (bottom, top and side walls) were defined as velocity inlets for the representation of deep water and infinite air conditions. The inlet, outlet, sidewall and bottom boundaries were located at a $2.5L_{PP}$ distance from the aft perpendicular of the ship, while the top boundary was located at a $1.25L_{PP}$ distance, as similarly used by Demirel et al. (2017b). The surface boundary conditions for the hull, rudder and propeller were defined as no-slip walls. For clean hull and clean propeller cases, the smooth type wall-function was used, whereas the rough type wall-functions, containing the roughness functions of barnacles, were used for the rough surfaces of fouled hull and propeller. It is of note that the simulations were conducted in fixed conditions, such that the ship was not allowed to sink or trim.

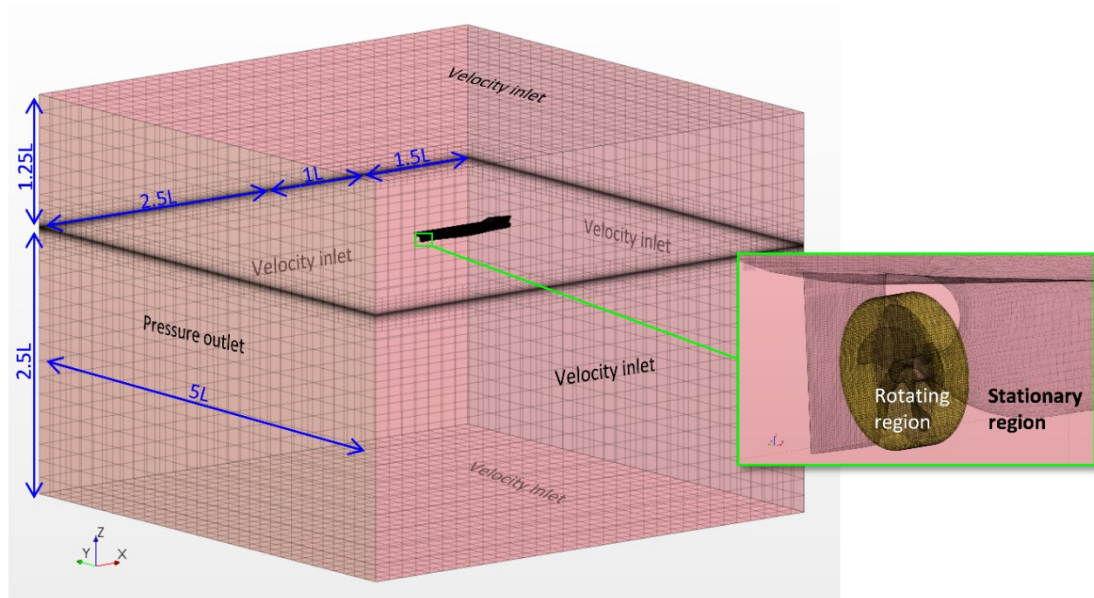


Figure 8.3 Computational domain and boundary conditions used in Chapter 8

8.2.3.3. Mesh generation

Mesh generation was performed using the built-in automated meshing tool of STAR-CCM+. Trimmed hexahedral meshes were used. Local refinements were made for finer grids in the critical regions, such as the area around the propeller, near the free surface, the rudder and bulbous bow of the hull as shown in Figure 8.4. The prism layer meshes were used for near-wall refinement, and the thickness of the first layer cell on the surface was chosen such that the y^+ values are always higher than 30, and, also higher than the k^+ values, as suggested by Demirel et al. (2017b), and CD-Adapco (2017). It is of note that the same mesh was used for all the smooth and rough surface conditions, including the near-wall refinement.

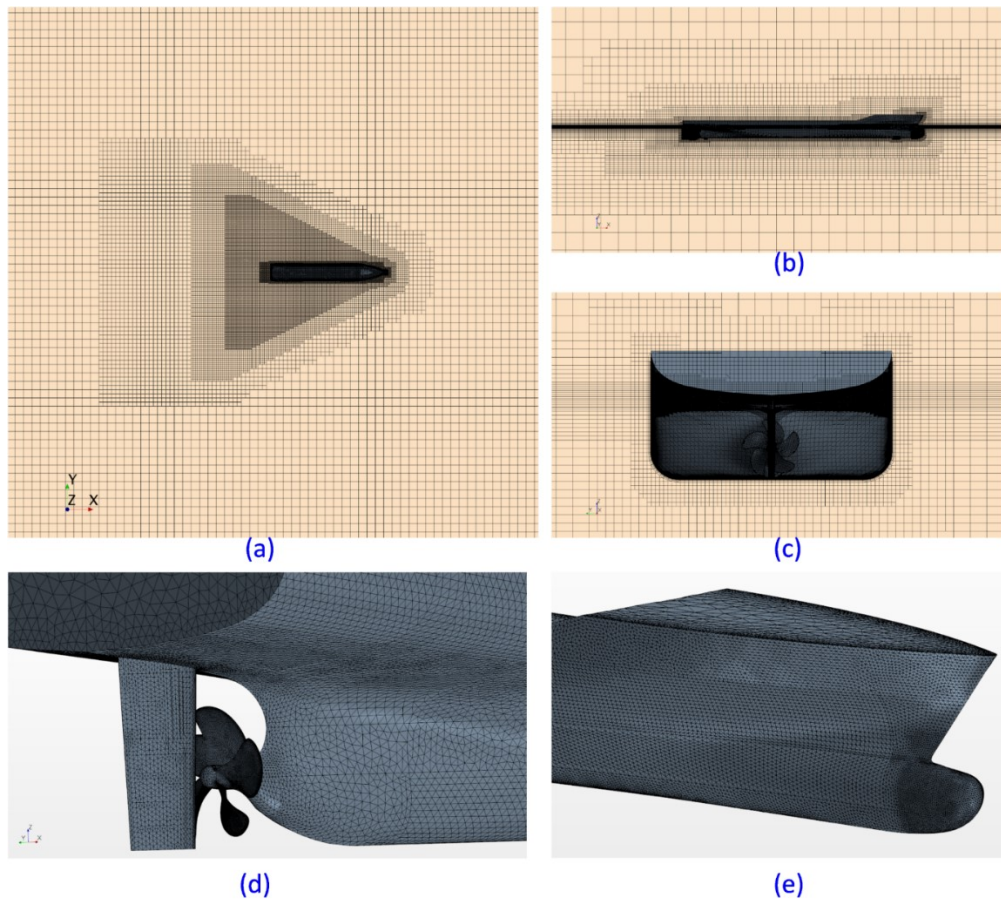


Figure 8.4 Volume mesh and surface of the simulation model (a) two view, (b) profile view, (c) rear view, (d) stern, (e) bow

8.2.4. Fouling conditions

The simulations were conducted under combinations of different fouling scenarios and surface conditions (fouling severities). Table 8.1 shows the different fouling conditions applied to the simulations. The fouling scenarios consist of three fouling configurations namely; ‘*fouled-hull/clean-propeller*’, ‘*clean-hull/fouled-propeller*’, and ‘*fouled-hull/fouled-propeller*’ as well as ‘*clean-hull/clean-propeller*’ condition as a reference case.

Ten different surface conditions, which can be found in Table 1, were then applied for the three fouling scenarios except for *clean-hull/clean-propeller* condition. Therefore,

a total of 31 different simulations were carried out in this study (1 smooth and 3×10 fouled conditions).

Table 8.1 Fouling conditions of different fouling scenarios and surface conditions

Fouling scenario	Hull and rudder fouling	Propeller fouling	Surface (fouling severity) condition
<i>Clean-hull/clean-propeller</i>	No	No	Smooth
<i>Fouled-hull/clean-propeller</i>	Yes	No	S10%, S20%, S40%, S50% M10%, M20%, M40%, M50% B10%, B20%
<i>Clean-hull/fouled-propeller</i>	No	Yes	S10%, S20%, S40%, S50% M10%, M20%, M40%, M50% B10%, B20%
<i>Fouled-hull/fouled-propeller</i>	Yes	Yes	S10%, S20%, S40%, S50% M10%, M20%, M40%, M50% B10%, B20%

8.2.5. Propeller controller

In order to find the self-propulsion point, a proportional-integral (PI) controller was embedded in the simulations, which controls the propeller rotational speed, n . The error, e , is defined as the difference between the total drag, R_T , and the thrust of the propeller, T , given by

$$e = R_T - T \quad (8.1)$$

Then the rotational speed of the propeller, n , is determined as

$$n = n_0 \left(1 + K_P e + K_I \int_{t_0}^t e \, dt \right) \quad (8.2)$$

where n_0 is the initial rotational speed of the propeller. t is time, and t_0 is the time when the PI controller is turned on. K_P and K_I are the proportional and integral gains of the controller, respectively. The K_P and K_I values were chosen such that $K_P e$ and $K_I \int_{t_0}^t e \, dt$ are nondimensional, given as

$$K_P = \frac{\alpha}{\rho L_{pp}^2 V^2} \quad (8.3)$$

$$K_I = \frac{\beta}{\rho L_{pp}^3 V^2} \quad (8.4)$$

It is worth noting that the choice of α and β values does not need to be optimal, but it can be beneficial to find proper values to reduce the computational cost. In this study, these values were selected as $\alpha = 100$ and $\beta = 1000$ after several trial and errors, and the same α and β values were used for the model-scale and full-scale simulations (and also for all surface conditions).

Figure 8.5 gives an example of the propeller revolution, n , controlled by the PI controller. The figure illustrates that the n values for the two simulations (*clean-hull/clean-propeller* and *fouled-hull/fouled-propeller, B20%*) remained to n_0 (in this case, 1.7 rps) until the PI controller is activated at $t = t_0$ (in this case, 1,210 s). Then the n values are altered such that the self-propulsion points are achieved.

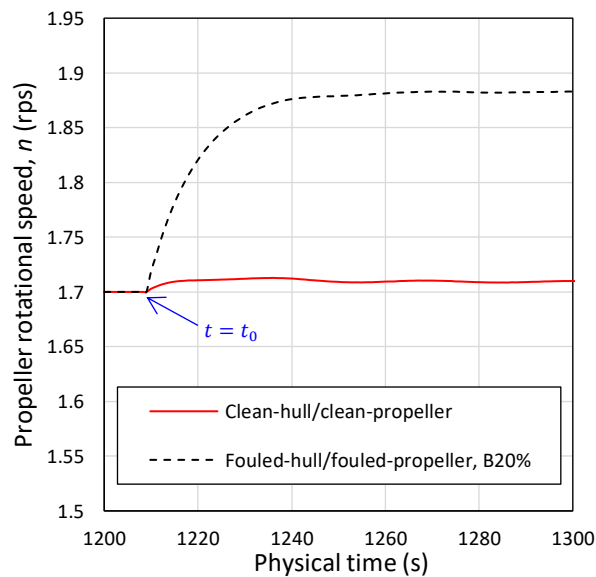


Figure 8.5 Rotational speed of the propeller controlled by the PI controller

8.3. Verification and validation study

8.3.1. Verification study

Verification studies were conducted to estimate the spatial and temporal uncertainties of the simulations. The Grid Convergence Index (GCI) method based on Richardson's extrapolation (1910) was used to estimate the numerical uncertainties, as used in Chapter 5, 6, and 7. The details of the GCI method can be found in Section 5.2.6.

8.3.1.1. Spatial convergence study

For spatial convergence study, three different resolutions of meshes were generated, which are referred to as fine, medium, and coarse meshes corresponding the cell numbers of N_1 , N_2 , and N_3 . Table 8.2 shows the required parameters for the calculation of the spatial discretisation error. The total resistance coefficient, C_T , and the propeller rotational speed, n , of *clean-hull/clean-propeller* case were used as the key variables. The simulations were conducted at the design speed (24 knots) with the Reynolds number of 2.39×10^9 . As indicated in the table, the numerical uncertainties of C_T and n values for the fine mesh (GCI_{fine}^{21}) are 0.06% and 0.02% respectively. For accurate predictions, the fine mesh was used for the simulations.

Table 8.2 Parameters used for the calculation of the discretisation error for the spatial convergence study

	C_T	n
N_1	3,742,239	3,742,239
N_2	2,017,894	2,017,894
N_3	1,135,263	1,135,263
r_{21}	1.36	1.36
r_{32}	1.33	1.33
ϕ_1	2.675E-03	1.70279
ϕ_2	2.684E-03	1.70452
ϕ_3	2.736E-03	1.71433
ε_{32}	5.21E-05	9.81E-03
ε_{21}	8.49E-06	1.73E-03
s	1	1
e_a^{21}	0.32%	0.10%
q	1.59E-01	1.55E-01
p_a	6.39E+00	6.12E+00
ϕ_{ext}^{21}	2.674E-03	1.702E+00
e_{ext}^{21}	0.05%	0.02%
GCI_{fine}^{21}	0.06%	0.02%

8.3.1.2. Temporal convergence study

For the temporal convergence study, three different time steps, namely Δt_1 , Δt_2 , and Δt_3 , were applied to the simulations using fine meshes. Table 8.3 shows the required parameters for the calculation of the temporal discretisation error. The total resistance coefficient, C_T , and the propeller rotational speed, n , of *clean-hull/clean-propeller* case were used as the key variables. The simulations were conducted at the design speed (24 knots) with the Reynolds number of 2.39×10^9 . As indicated in the table, the numerical uncertainties of C_T and n values for the smallest time steps ($GCI_{\Delta t_1}^{21}$) are 0.031% and 0.017% respectively. For accurate predictions, the smallest time step $\Delta t_1 = 0.0025s$ was used for the simulations. It is of note that ITTC recommends selecting the time steps such that the propeller rotates $0.5-2^\circ$ per time step (ITTC, 2011), and all the simulation cases in this study were conducted within this range.

Table 8.3 Parameters used for the calculation of the discretisation error for the temporal convergence study

	C_T	n
Δt_1	0.0025s	0.0025s
Δt_2	0.0050s	0.0050s
Δt_3	0.0100s	0.0100s
r_{21}, r_{32}	2	2
ϕ_1	2.675E-03	1.70279
ϕ_2	2.678E-03	1.70380
ϕ_3	2.696E-03	1.70930
ε_{32}	1.77E-05	5.50E-03
ε_{21}	3.11E-06	1.01E-03
e_a^{21}	0.12%	0.06%
p_a	2.50E+00	2.44E+00
ϕ_{ext}^{21}	2.675E-03	1.703E+00
e_{ext}^{21}	0.025%	0.013%
$GCI_{\Delta t_1}^{21}$	0.031%	0.017%

8.3.2. Validation study

The simulations for the prediction of the effect of barnacles were conducted in full-scale with propellers and rudders. However, the reference experiment was conducted in model-scale without a rudder (Hino, 2005), and therefore, they cannot be directly compared due to the scale effect and the interaction arising from the rudder. To handle it properly, four different simulations were modelled for the validation, namely; ‘*model-scale/with-rudder*’, ‘*model-scale/without-rudder*’, ‘*full-scale/with-rudder*’, and ‘*full-scale/without-rudder*’.

Figure 8.6 schematically illustrates the validation process used in this study. As the self-propulsion experiment of Hino (2005) was conducted in model-scale without a rudder, this cannot be directly compared with the current full-scale KCS model with the rudder. Therefore, the validation process consists of two steps. First, a model-scale KCS simulation ($\lambda = 31.6$) was carried out without the rudder to be compared with the experimental data (validation 1). And then the results from the four different

simulations were compared to examine the scale effect and the effect of the presence of rudder.

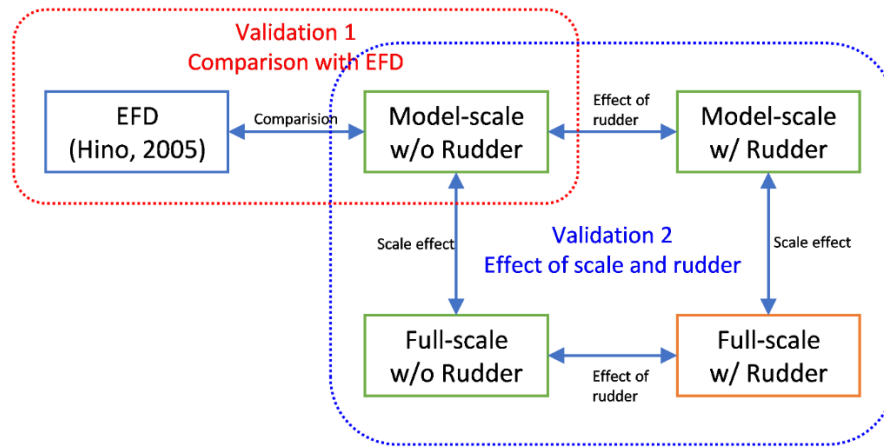


Figure 8.6 Schematic diagram of the process of the validation study

8.3.2.1. Validation 1: comparison with EFD

As mentioned earlier, the simulation of a model-scale self-propelled KCS ($\lambda = 31.6$) was modelled without a rudder to be compared with the experimental data of Hino (2005). The simulation was conducted at the design speed ($R_n = 1.40 \times 10^7$). The experiment was conducted at the ship point using a skin friction correlation force, SFC . In this study, the skin friction correlation force, SFC , was calculated as

$$SFC = \frac{1}{2} \rho_M S_M V_M^2 (1 + k) [C_{F0M} - (C_{F0S} + \Delta C_F)] \quad (8.5)$$

where, ρ_M , S_M and V_M are the water density, wetted surface area, and speed of the model ship. C_{F0M} and C_{F0S} are the frictional resistance coefficients at the model-scale and full-scale design speed, respectively. The C_{F0} values were calculated using the ITTC 1957 friction line ($C_{F0} = 0.075 / (\log_{10} R_n - 2)^2$). ΔC_F is roughness allowance, and k is the form factor. $\Delta C_F = 0.00027$ and $1 + k = 1.1$ were used as per the suggestion of Carrica et al. (2010).

Figures 8.7-8.10 compare the self-propulsion parameters obtained from the current CFD simulation (model-scale without a rudder) with the experimental data of Hino (2005), together with the CFD results from Tokyo 2015 CFD workshop, which is available at <https://t2015.nmri.go.jp/>.

As shown in the figures, generally, the simulation result shows good agreement with the experimental data and the average values of the Tokyo 2015 CFD results. The relative differences between the current CFD and experiment for the C_T , n , K_T , and K_Q are 1.07%, 0.58%, 0.54%, and 5.49%, respectively. The current simulation over-estimate the torque coefficient, K_Q , compared to the experiment, but it shows a good agreement with the average of the other CFD results.

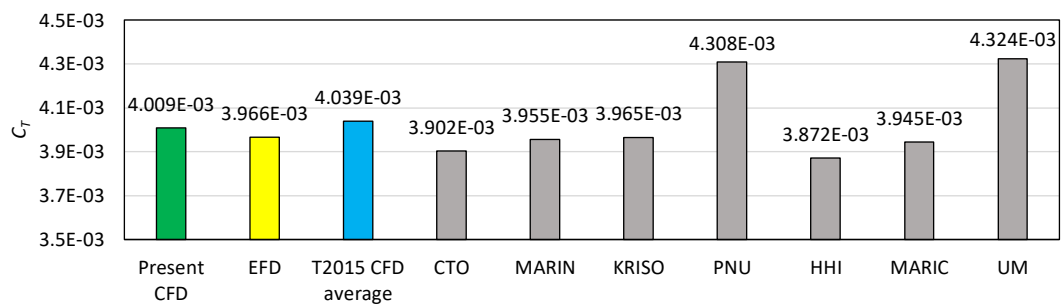


Figure 8.7 Total resistance coefficient, C_T , values obtained from the present CFD simulation (model-scale without a rudder), and EFD (Hino, 2005), and other CFD results from the CFD workshop Tokyo 2015

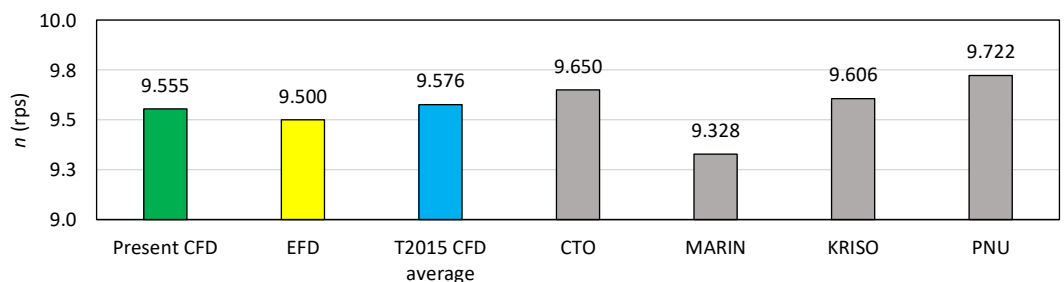


Figure 8.8 Propeller rotational speed, n , values obtained from the present CFD simulation (model-scale without a rudder), and EFD (Hino, 2005), and other CFD results from the CFD workshop Tokyo 2015

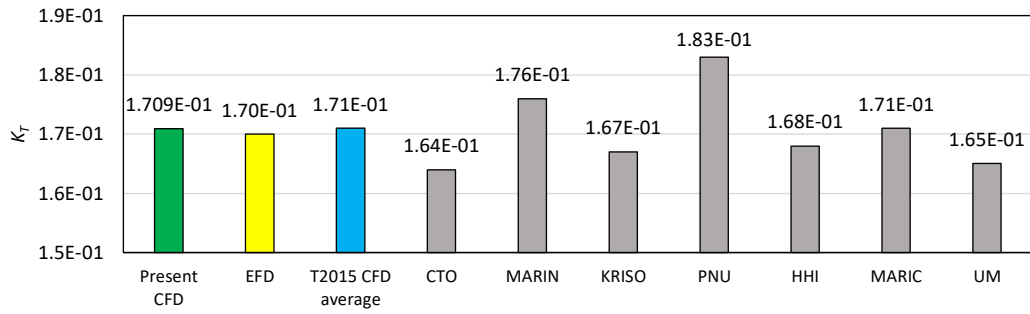


Figure 8.9 Thrust coefficient, K_T , values obtained from the present CFD simulation (model-scale without a rudder), and EFD (Hino, 2005), and other CFD results from the CFD workshop Tokyo 2015

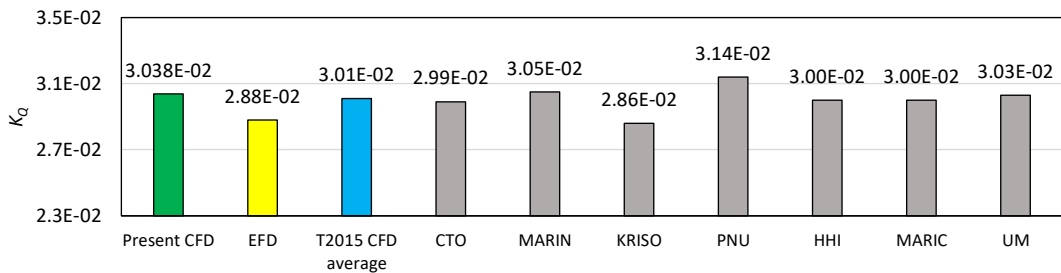


Figure 8.10 Torque coefficient, K_Q , values obtained from the present CFD simulation (model-scale without a rudder), and EFD (Hino, 2005), and other CFD results from the CFD workshop Tokyo 2015

8.3.2.2. Validation 2: effect of scale and interaction with rudder

As mentioned earlier, in order to assess the scale effect and the interaction due to the presence of rudder, two model-scale simulations with and without a rudder, and two full-scale simulations with and without rudder were conducted. Figure 8.11 compares the geometries of the KCS models with and without a rudder.

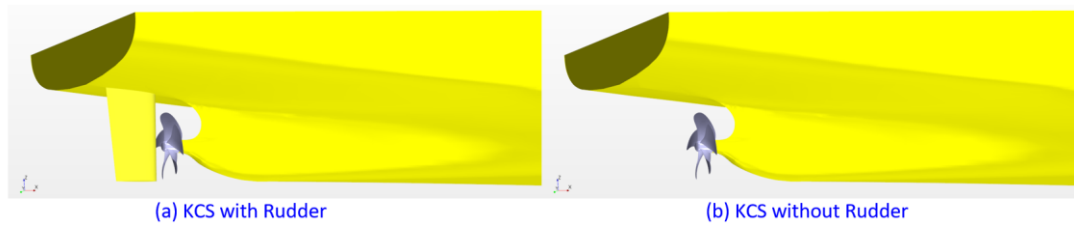


Figure 8.11 Geometries representing (a) KCS with a rudder and (b) and without a rudder

Table 8.4 shows the self-propulsion parameters obtained from the four different simulations. The relative differences, D , were calculated as $D = (woR - wR)/wR$, where wR and woR denote the self-propulsion parameters of *with-rudder* and *without-rudder* cases, respectively. For the model-scale simulations, the advance coefficients at the self-propulsion points were calculated using the open water curve of the KP505 propeller, obtained by Fujisawa et al. (2000), while the full-scale open water curve obtained from the CFD simulation in Chapter 7 was used for the full-scale advance coefficients.

As shown in the table, and visually illustrated in Figure 8.12 and 8.13, the differences between the *with-rudder* cases and *without-rudder* cases were consistent in both the scales. Interestingly, in both scales, although the *without-rudder* cases have smaller C_T values, the self-propulsion points for these simulations were achieved at higher propeller revolutions, n , compared to the *with-rudder* cases. This can be attributed to the smaller $1 - w_T$ values (i.e. higher wake fractions, w_T) of *with-rudder* cases. The *with-rudder* cases have smaller $1 - t$ values (i.e. higher thrust deduction factors, t). However, the effect of the rudder on the wake fraction was found to be larger than the effect on thrust deduction factor; hence the hull efficiencies, η_H , of *with-rudder* cases were observed to be larger than the *without-rudder* cases. The effects of the rudder on the behind-hull propeller efficiency, η_B , were also negative. Finally, the overall propulsive efficiency, $\eta_D = \eta_H \eta_B$, were observed to decrease in the absence of rudder in both the scales, resulting in the increased shaft powers, SP .

It is of note that, the experimental study of Reichel (2009), which investigates the hull-rudder-propeller interaction, shows very similar results, although the result showed strong dependences on the ship speed.

Table 8.4 Self-propulsion parameters obtained from the model-scale and full-scale simulations with and without a rudder

	Model-scale			Full-scale		
	w/ Rudder	w/o Rudder	D (%)	w/ Rudder	w/o Rudder	D (%)
C_T	0.004089	0.004009	-1.96%	0.002676	0.002583	-3.45%
n (rps)	9.3750	9.5548	1.92%	1.7028	1.7368	2.00%
$n' = nL_{pp}/V$	31.073	31.669	1.92%	31.723	32.356	2.00%
K_T	0.1850	0.1709	-7.60%	0.1720	0.1579	-8.19%
K_Q	0.0315	0.0304	-3.70%	0.0276	0.0263	-4.60%
$1 - t$	0.8164	0.8401	2.90%	0.7840	0.8109	3.44%
J	0.7001	0.7293	4.18%	0.7144	0.7409	3.71%
$1 - w_T$	0.7472	0.7933	6.18%	0.7784	0.8234	5.78%
η_o	0.6650	0.6803	2.29%	0.6815	0.6863	0.70%
η_H	1.0926	1.0589	-3.09%	1.0072	0.9849	-2.22%
η_R	0.9856	0.9599	-2.61%	1.0446	1.0233	-2.04%
η_B	0.6555	0.6530	-0.38%	0.7119	0.7023	-1.35%
η_D	0.7162	0.6914	-3.46%	0.7170	0.6917	-3.54%
SP (kW)	1.594E-01	1.625E-01	1.95%	2.700E+04	2.733E+04	1.22%

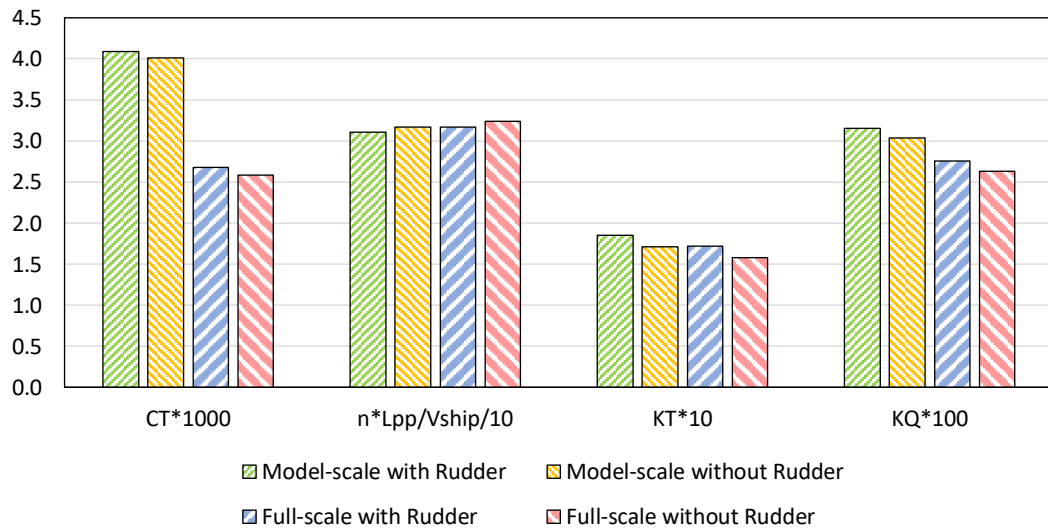


Figure 8.12 C_T , n , K_T and K_Q values at self-propulsion points obtained from the model-scale and full-scale simulations with and without a rudder

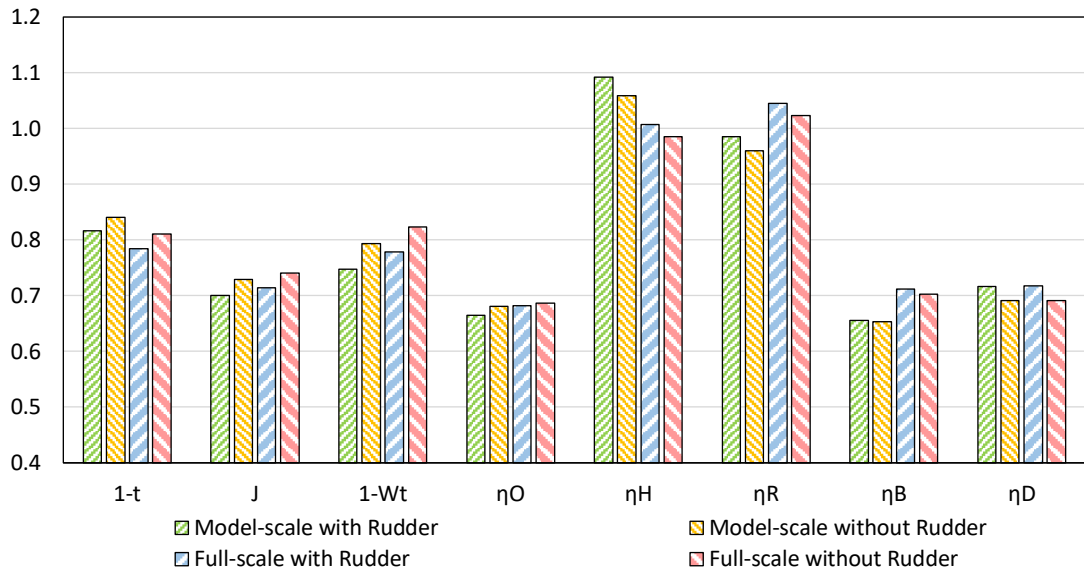


Figure 8.13 Self-propulsion parameters and propeller efficiencies at self-propulsion points obtained from the model-scale and full-scale simulations with and without a rudder

8.4. The effect of biofouling on ship self-propulsion characteristics

Full-scale self-propulsion simulations were conducted under 31 different conditions as indicated in Table 8.1. The self-propulsion parameters obtained from the simulations can be found in Table 8.5-8.7. The thrust deduction factors, $1 - t$, for the *fouled-hull* cases were calculated using the corresponding C_T values obtained from the full-scale towed KCS simulations in Chapter 6, while the advance coefficients, J , for the *fouled-propeller* cases were calculated using the corresponding open water curves obtained from the full-scale KP505 simulations in Chapter 7.

Table 8.5 Self-propulsion parameters under 'fouled-hull/clean-propeller' conditions

Test Surface	$C_T \cdot 10^3$	$C_P \cdot 10^3$	$C_R \cdot 10^3$	$K_T \cdot 10$	$K_Q \cdot 10^2$	n (rps)	$1-t$	J	$1-w_T$	η_O	η_H	η_R	η_B	η_D	SP (MW)
Smooth	2.675	1.441	1.234	1.720	2.757	1.7028	0.7840	0.7144	0.7784	0.6815	1.0072	1.0446	0.7119	0.7170	27.00
S 10%	3.079	1.843	1.236	1.886	2.980	1.7445	0.8044	0.6837	0.7632	0.6625	1.0540	1.0365	0.6867	0.7238	31.39
S 20%	3.318	2.070	1.248	1.978	3.101	1.7686	0.8118	0.6669	0.7547	0.6521	1.0757	1.0330	0.6736	0.7246	34.03
M 10%	3.401	2.148	1.253	2.009	3.142	1.7768	0.8144	0.6611	0.7517	0.6486	1.0834	1.0319	0.6692	0.7250	34.97
S 40%	3.586	2.320	1.267	2.076	3.231	1.7950	0.8193	0.6488	0.7452	0.6409	1.0994	1.0297	0.6600	0.7256	37.06
M 20%	3.622	2.352	1.270	2.088	3.247	1.7984	0.8200	0.6464	0.7439	0.6395	1.1023	1.0294	0.6582	0.7256	37.47
B 10%	3.642	2.370	1.272	2.095	3.256	1.8004	0.8202	0.6452	0.7433	0.6387	1.1034	1.0292	0.6573	0.7253	37.70
S 50%	3.682	2.406	1.276	2.109	3.275	1.8042	0.8208	0.6426	0.7419	0.6371	1.1064	1.0287	0.6554	0.7251	38.15
M 40%	3.963	2.658	1.305	2.204	3.399	1.8311	0.8247	0.6251	0.7324	0.6263	1.1259	1.0260	0.6426	0.7235	41.40
M 50%	4.040	2.726	1.314	2.229	3.433	1.8384	0.8255	0.6205	0.7299	0.6234	1.1310	1.0254	0.6392	0.7230	42.31
B 20%	4.067	2.751	1.316	2.238	3.444	1.8409	0.8263	0.6188	0.7290	0.6224	1.1335	1.0252	0.6380	0.7232	42.62

Table 8.6 Self-propulsion parameters under 'clean-hull/fouled-propeller' conditions

Test Surface	$C_T \cdot 10^3$	$C_P \cdot 10^3$	$C_R \cdot 10^3$	$K_T \cdot 10$	$K_Q \cdot 10^2$	n (rps)	$1-t$	J	$1-w_T$	η_O	η_H	η_R	η_B	η_D	SP (MW)
Smooth	2.675	1.441	1.234	1.720	2.757	1.7028	0.7840	0.7144	0.7784	0.6815	1.0072	1.0446	0.7119	0.7170	27.00
S 10%	2.676	1.441	1.234	1.699	2.869	1.7133	0.7842	0.7097	0.7781	0.6462	1.0078	1.0379	0.6707	0.6759	28.62
S 20%	2.678	1.442	1.236	1.689	2.923	1.7192	0.7834	0.7071	0.7779	0.6289	1.0071	1.0361	0.6516	0.6562	29.46
M 10%	2.678	1.442	1.236	1.685	2.942	1.7211	0.7834	0.7063	0.7778	0.6229	1.0072	1.0356	0.6451	0.6497	29.75
S 40%	2.679	1.442	1.237	1.676	2.983	1.7256	0.7833	0.7045	0.7779	0.6098	1.0069	1.0346	0.6309	0.6353	30.41
M 20%	2.679	1.442	1.237	1.675	2.991	1.7264	0.7834	0.7042	0.7779	0.6073	1.0070	1.0344	0.6282	0.6326	30.53
B 10%	2.679	1.442	1.237	1.674	2.996	1.7270	0.7832	0.7039	0.7779	0.6060	1.0068	1.0343	0.6268	0.6310	30.61
S 50%	2.677	1.442	1.235	1.672	3.004	1.7275	0.7838	0.7037	0.7779	0.6032	1.0076	1.0342	0.6238	0.6286	30.73
M 40%	2.678	1.442	1.236	1.659	3.070	1.7346	0.7834	0.7009	0.7779	0.5838	1.0071	1.0329	0.6030	0.6072	31.78
M 50%	2.677	1.442	1.235	1.655	3.087	1.7363	0.7836	0.7001	0.7779	0.5785	1.0073	1.0326	0.5974	0.6017	32.06
B 20%	2.678	1.442	1.236	1.654	3.094	1.7371	0.7834	0.6998	0.7779	0.5766	1.0071	1.0325	0.5953	0.5995	32.18

Table 8.7 Self-propulsion parameters under 'fouled-hull/fouled-propeller' conditions

Test Surface	$C_T \cdot 10^3$	$C_P \cdot 10^3$	$C_R \cdot 10^3$	$K_T \cdot 10$	$K_Q \cdot 10^2$	n (rps)	$1-t$	J	$1-w_T$	η_O	η_H	η_R	η_B	η_D	SP (MW)
Smooth	2.675	1.441	1.234	1.720	2.757	1.7028	0.7840	0.7144	0.7784	0.6815	1.0072	1.0446	0.7119	0.7170	27.00
S 10%	3.080	1.844	1.236	1.865	3.089	1.7548	0.8043	0.6790	0.7624	0.6302	1.0549	1.0308	0.6496	0.6852	33.11
S 20%	3.320	2.070	1.250	1.944	3.260	1.7844	0.8113	0.6599	0.7535	0.6064	1.0768	1.0263	0.6224	0.6701	36.74
M 10%	3.404	2.149	1.255	1.970	3.317	1.7947	0.8137	0.6534	0.7504	0.5986	1.0844	1.0250	0.6136	0.6654	38.04
S 40%	3.590	2.320	1.270	2.027	3.443	1.8171	0.8185	0.6395	0.7436	0.5822	1.1008	1.0224	0.5952	0.6552	40.98
M 20%	3.626	2.353	1.273	2.038	3.467	1.8214	0.8193	0.6369	0.7423	0.5791	1.1038	1.0220	0.5918	0.6533	41.56
B 10%	3.645	2.371	1.275	2.043	3.480	1.8239	0.8195	0.6354	0.7416	0.5775	1.1050	1.0217	0.5900	0.6520	41.88
S 50%	3.685	2.407	1.278	2.055	3.506	1.8286	0.8201	0.6325	0.7401	0.5742	1.1081	1.0213	0.5864	0.6497	42.53
M 40%	3.969	2.660	1.310	2.133	3.688	1.8627	0.8234	0.6126	0.7302	0.5521	1.1276	1.0184	0.5622	0.6339	47.27
M 50%	4.047	2.728	1.319	2.154	3.736	1.8719	0.8242	0.6073	0.7275	0.5464	1.1329	1.0177	0.5561	0.6300	48.61
B 20%	4.075	2.753	1.322	2.161	3.754	1.8752	0.8247	0.6054	0.7264	0.5443	1.1352	1.0175	0.5538	0.6287	49.10

8.4.1. Effect on total resistance coefficient

Figure 8.14 illustrates the total resistance coefficient values, C_T , obtained from the simulations under the different fouling conditions. In the figure, the C_T values are plotted against the representative roughness height, k_G , of the given surface conditions, which can be found in Table 6.1. It should be borne in mind that the C_T values with zero representative roughness height, k_G , represent *clean-hull/clean-propeller* case. In the figure, the C_T values for *clean-hull/fouled-propeller* case remained rather constant, whereas those of the *fouled-hull* conditions show significant increases. From this, it can be deduced that the propeller fouling does not affect the resistance of the ship, as expected.

When they are compared with the C_T values obtained from the full-scale towed KCS in Chapter 6, the C_T values from the self-propulsion simulations are higher than those of the towed ship simulations, but the trends are similar. This can be explained by the propeller-hull interaction, which is generally referred as ‘thrust deduction’, where the pressure at the stern is reduced by the propeller accelerating the flow, and the ship resistance is increased due to the reduction of the stern pressure.

It was observed that this thrust deduction mostly appears in the form of the increase in the residuary resistance coefficient, C_R , rather than frictional resistance coefficient, C_F . As shown in Figure 8.16, the C_R values of the self-propulsion simulations are significantly higher than those of the towed ship simulation obtained in Chapter 6, while the differences between them are relatively minor in the frictional resistance coefficient, C_F , as can be seen in Figure 8.15.

Interestingly, unlike the decreasing C_R values with the surface fouling severity of the towed ship simulations, the C_R values from the self-propulsion simulations under the *fouled-hull* conditions show rather increasing trends. This can be mostly attributed to the increased propeller rotational speeds, n , under those fouling conditions, which causes a higher thrust deduction. The details of the effect of biofouling on the propeller rotational speed, n , can be found in the following section.

The increase in C_T , C_F , and C_R with B20% surface condition were 52.0%, 90.8% and 91.0%, respectively, for *fouled-hull/clean-propeller* case, and 52.3%, 6.7%, and 7.2%, respectively for *fouled-hull/fouled-propeller* case.

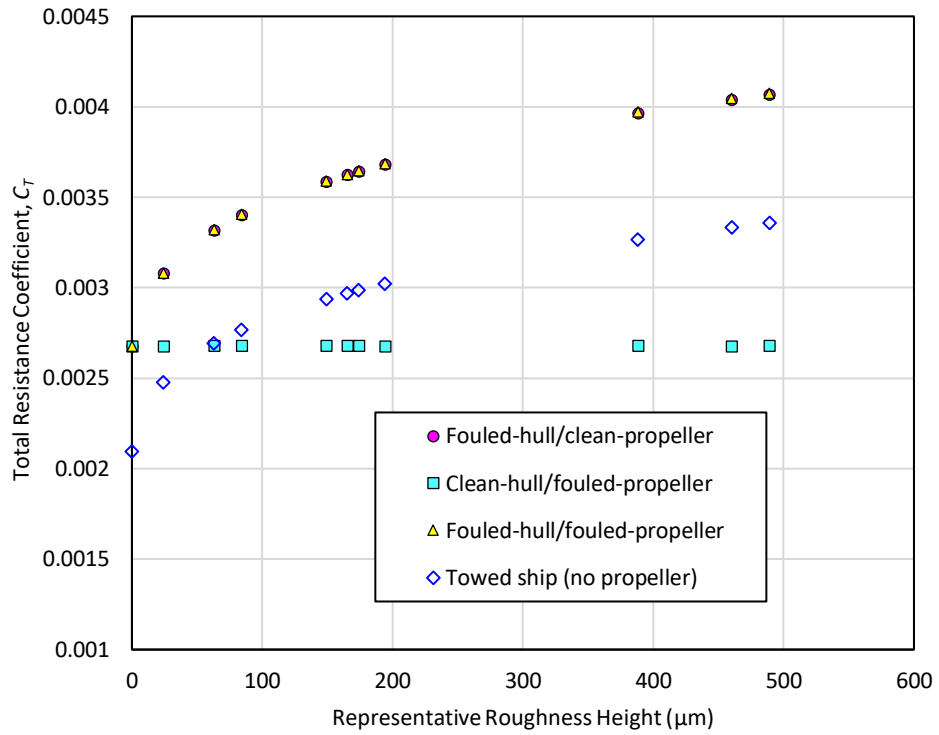


Figure 8.14 Total resistance coefficient, C_T , at self-propulsion point under the given fouling conditions, plotted against the representative roughness heights of the surface fouling conditions in Table 6.1

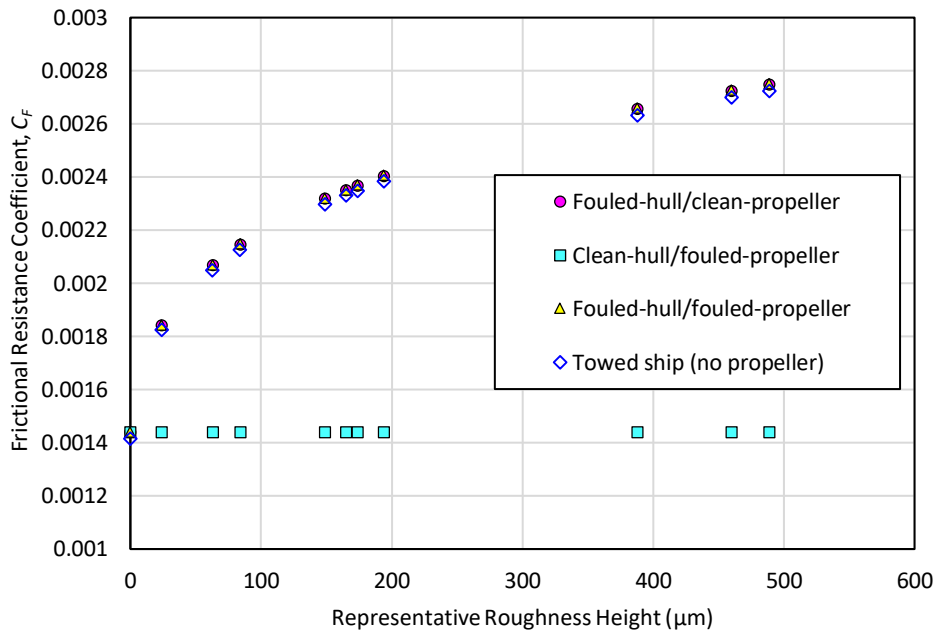


Figure 8.15 Frictional resistance coefficient, C_F , at self-propulsion point under the given fouling conditions, plotted against the representative roughness heights of the surface fouling conditions in Table 6.1

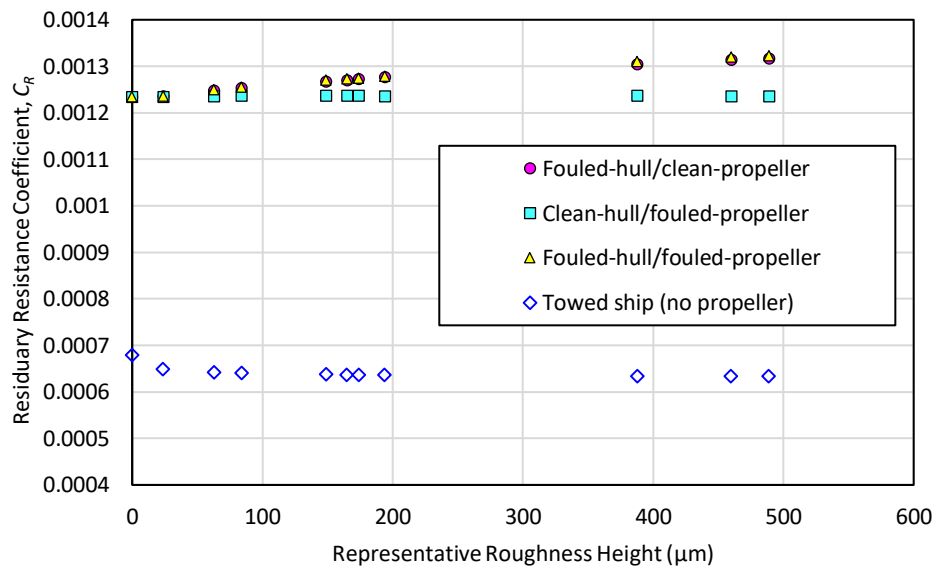


Figure 8.16 Residuary resistance coefficient, C_R , at self-propulsion point under the given fouling conditions, plotted against the representative roughness heights of the surface fouling conditions in Table 6.1

8.4.2. Effect on propeller rotational speed

Figure 8.17 compares the rotational speed of the propeller, n , at the self-propulsion point under the different fouling conditions. The result suggests that hull fouling and propeller fouling both increase the n values at the self-propulsion point, but the impact of hull fouling is much severe than that of propeller fouling. The reason for the increase in n values under *fouled-hull* conditions can be ascribed to the increased C_T values which were found in Figure 8.14, while the increase in n values under *fouled-propeller* conditions can be explained by the decreased thrust at the same advance coefficient, J , due to the propeller fouling as previously observed in Figure 7.6. It means, for a *fouled-propeller* case a higher n value is required to achieve the same thrust, T .

The increases in n values under *fouled-hull/clean-propeller*, *clean-hull/fouled-propeller*, and *fouled-hull/fouled-propeller* conditions at the most severe surface fouling condition (B20%) were observed to be 8.1%, 2.0%, and 10.1%, respectively.

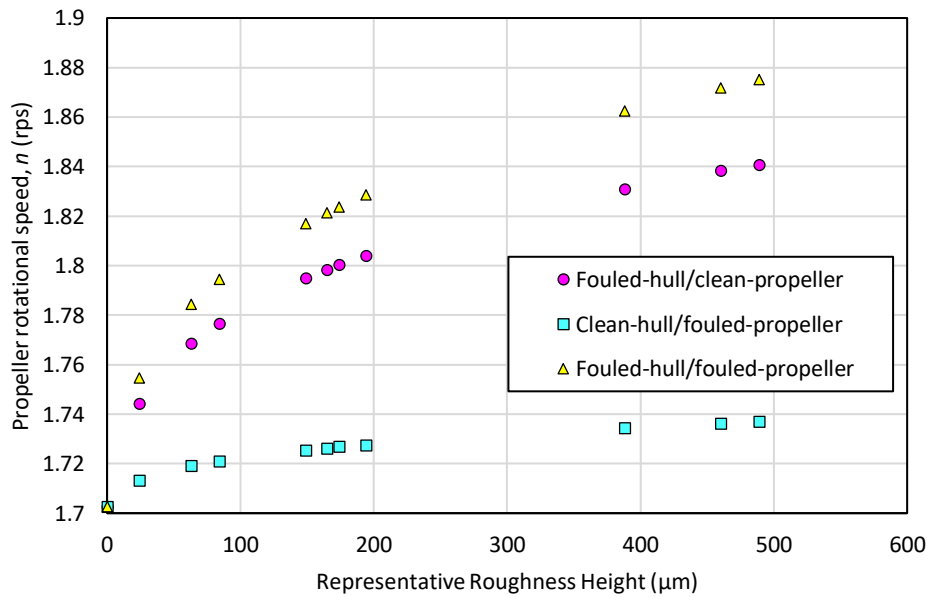


Figure 8.17 Propeller rotational speed, n , at self-propulsion point under the given fouling conditions, plotted against the representative roughness heights of the surface conditions in Table 6.1

8.4.3. Effect on thrust and torque coefficients

Figure 8.18 shows the thrust coefficients, K_T , at the self-propulsion points under the given fouling conditions. As expected, *fouled-hull* cases show an increasing trend of K_T values with increasing fouling severities. Interestingly, *clean-hull/fouled-propeller* case shows decreasing K_T values due to the propeller fouling. This can be explained by the fact that the required thrust, T , remains rather constant in this condition due to the constant total resistance as shown in Figure 8.14. But, the rotational speed of the propeller, n , increases due to the propeller fouling as shown in Figure 8.17. As a result, the $K_T = T / (\rho n^2 D^4)$ values decrease with increasing level of surface fouling. For a similar reason, *fouled-hull/fouled-propeller* case shows smaller K_T values compared to those of *fouled-hull/clean-propeller* case.

The increases and decrease in K_T values under *fouled-hull/clean-propeller*, *clean-hull/fouled-propeller*, and *fouled-hull/fouled-propeller* conditions at the most severe surface fouling condition (B20%) were observed to be 30.1%, -3.8%, and 25.7%, respectively.

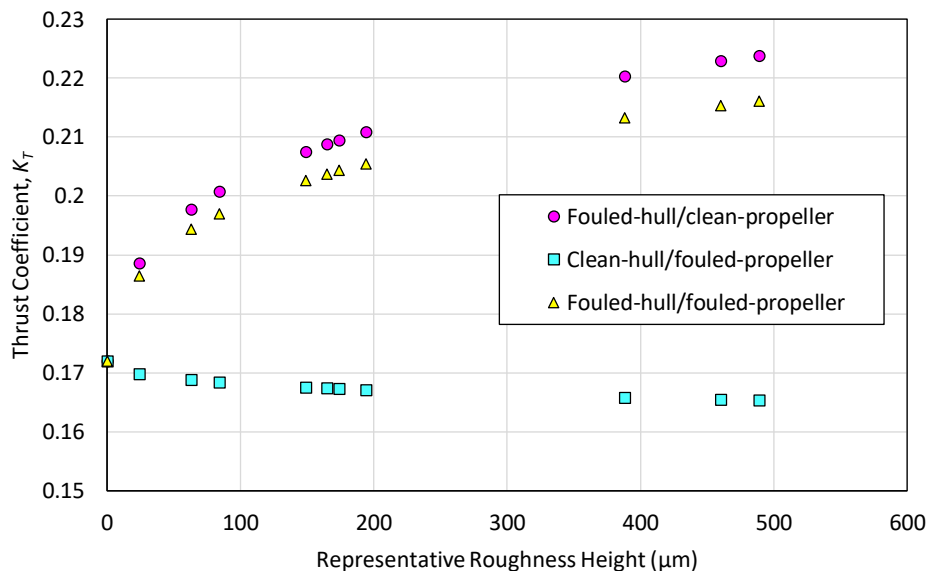


Figure 8.18 Thrust coefficient, K_T , at self-propulsion point under the given fouling conditions, plotted against the representative roughness heights of the surface conditions in Table 6.1

Figure 8.19 shows the torque coefficients, K_Q , at the self-propulsion points under the different fouling conditions. Similarly, to the trend of n values, it was shown that the K_Q values are affected by both of hull fouling and propeller fouling. The increase in K_Q values can be explained by the increase in the propeller rotational speeds, n , which results in reduced advance coefficients, J . Therefore, the K_Q values increase due to the reduced advance coefficients as well as the increased torques, Q , for *fouled-propeller* cases, as shown in Figure 7.6.

The increases in K_Q values for *fouled-hull/clean-propeller*, *clean-hull/fouled-propeller*, and *fouled-hull/fouled-propeller* conditions at the most severe surface fouling condition (B20%) were observed to be 24.9%, 12.2%, and 36.2%, respectively.

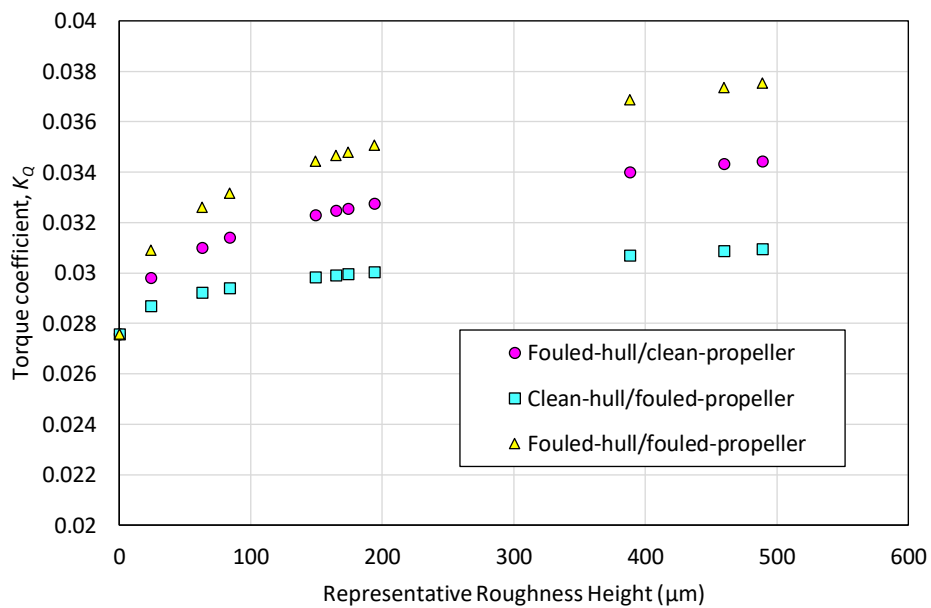


Figure 8.19 Torque coefficient, K_Q , at self-propulsion point under the given fouling conditions, plotted against the representative roughness heights of the surface conditions in Table 6.1

8.4.4. Effect on advance coefficient

Figure 8.20 shows the advance coefficients, J , at the self-propulsion points under the given fouling conditions. The J values were obtained by the thrust identity method using the open water curve for the fouled propellers obtained in Chapter 7 (Figure 7.6-7.9). The decrease in the advance coefficient values ($J = V_A/nD$) can mostly be attributed to the increases in the n values which is shown in Figure 18. Another reason for the decrease in J values can be the enlarged wakefield for the *fouled-hull* cases and hence decelerated flow velocity upstream of the propeller, V_A , as previously observed in Chapter 6 (Figure 6.12 and 6.13).

The decreases in J values for *fouled-hull/clean-propeller*, *clean-hull/fouled-propeller*, and *fouled-hull/fouled-propeller* conditions at the most severe surface fouling condition (B20%) were observed to be -13.4%, -2%, and -13.3%, respectively.

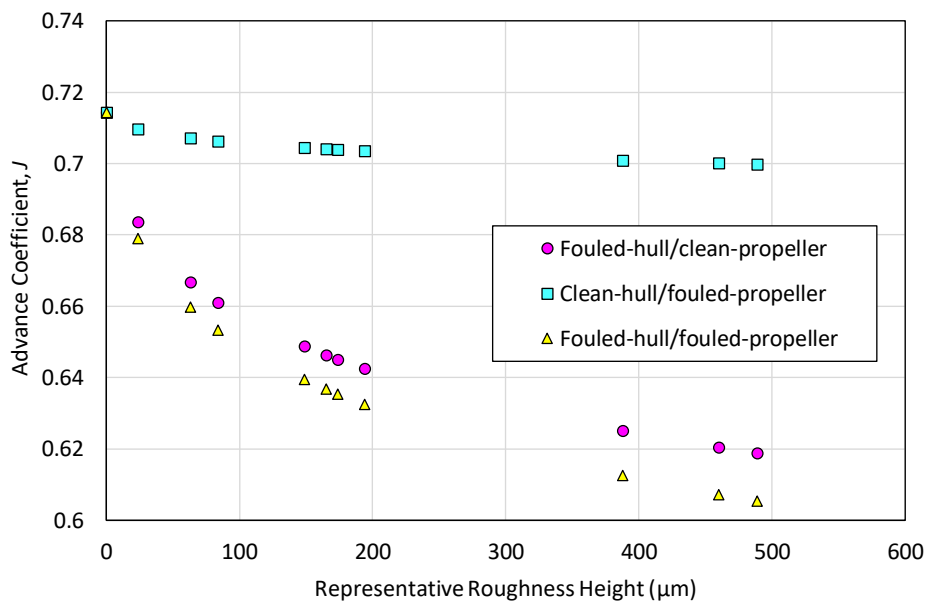


Figure 8.20 Advance coefficient, J , at self-propulsion point under the given fouling conditions, plotted against the representative roughness heights of the surface conditions in Table 6.1

8.4.5. Effect on thrust deduction factor

Figure 8.21 shows the thrust deduction factor, $1 - t$, at the self-propulsion points under the given fouling conditions. Interestingly, $1 - t$ values were revealed to increase (i.e. decreased thrust deduction factor, t) due to the hull fouling, which can result in improved hull efficiencies, η_H . While *fouled-hull* cases show increased $1 - t$ values, *clean-hull/fouled-propeller* case showed slightly decreased $1 - t$ values. For a similar reason, *fouled-hull/clean-propeller* case showed slightly larger $1 - t$ values than *fouled-hull/fouled-propeller* case.

It should be borne in mind that although the thrust deduction factors, t , showed decreases due to hull-fouling, it does not necessarily mean that the effect of thrust deduction is reduced. It only means, the 'ratio' between the required thrust, T , in self-propulsion condition and the towed ship total resistance, R_T , is reduced. That is to say, while the thrust deduction factor reduced, the absolute value of the drag owing to the thrust deduction can increase with increasing level of surface fouling, as shown in Figure 8.16.

The increases and decrease in $1 - t$ values under *fouled-hull/clean-propeller*, *clean-hull/fouled-propeller*, and *fouled-hull/fouled-propeller* conditions at the most severe surface fouling condition (B20%) were observed to be 5.4%, -0.1%, and 5.2%, respectively.

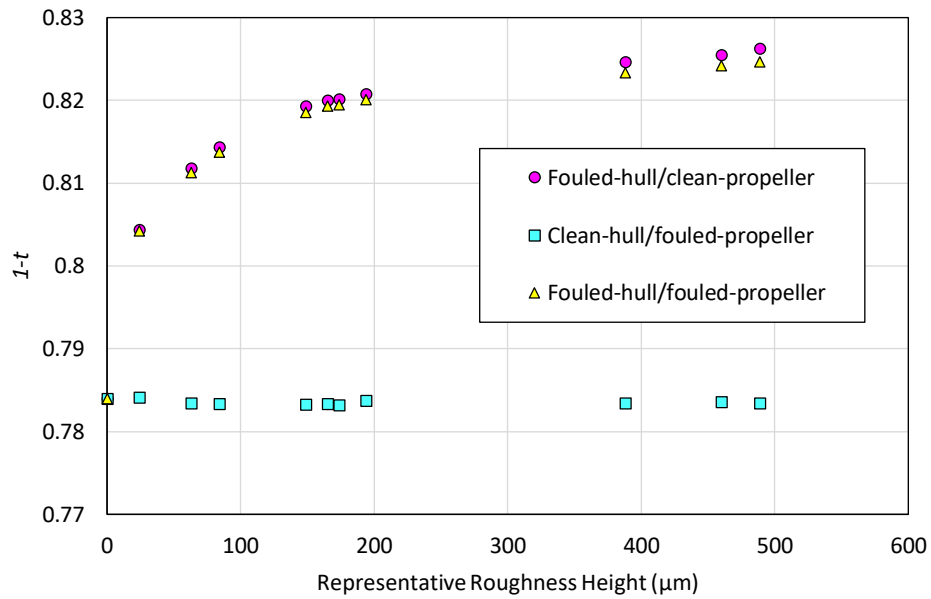


Figure 8.21 Thrust deduction factor, $1 - t$, at self-propulsion point under the given fouling conditions, plotted against the representative roughness heights of the surface fouling conditions in Table 6.1

8.4.6. Effect on wake fraction

Figure 8.22 shows the wake fractions, $1 - w_T$, at the self-propulsion points under the given fouling conditions. As can be seen in the figure, the $1 - w_T$ values of the *fouled-hull* cases showed decreases (i.e. increased wake fraction, w_T), which is desirable for hull efficiency, η_H . This increase in wake fraction, w_T , is consistent with the increased stern wakefield and nominal wake fraction, w_n , which was previously observed in Chapter 6 (Figure 6.14 and Table 6.8).

As expected, the effect of propeller fouling on the $1 - w_T$ values was minor. But, *fouled-hull/fouled-propeller* case showed slightly larger decreases than those of *fouled-hull/clean-propeller* case as can be seen in the figure.

The decreases in $1 - w_T$ values under *fouled-hull/clean-propeller*, *clean-hull/fouled-propeller*, and *fouled-hull/fouled-propeller* conditions at the most severe surface fouling condition (B20%) were revealed to be -6.4%, -0.1%, and -6.7%, respectively.

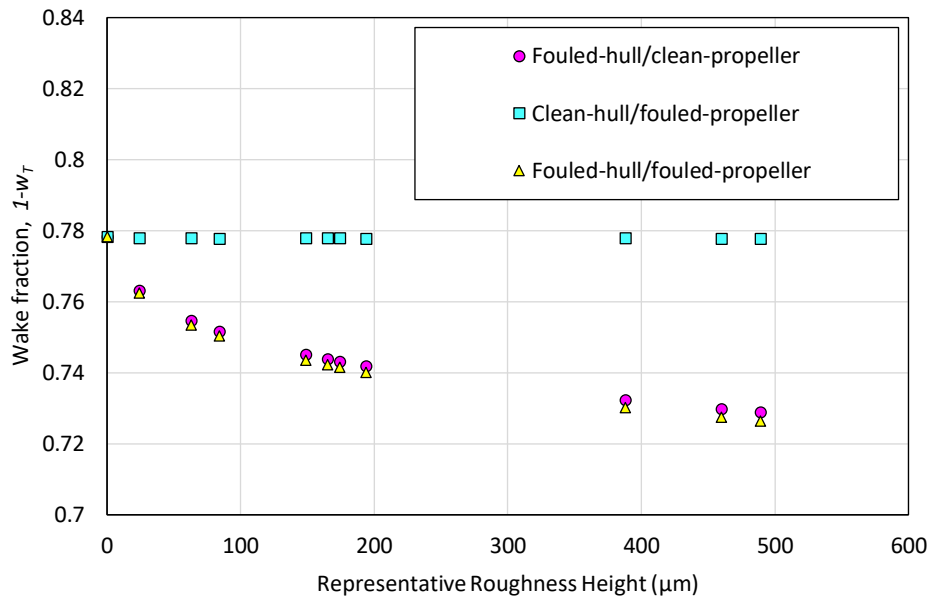


Figure 8.22 Wake fraction, $1 - w_T$, at self-propulsion point under the given fouling conditions, plotted against the representative roughness heights of the surface fouling conditions in Table 6.1

8.4.7. Effect on relative rotative efficiency and open water efficiency

Figure 8.23 shows the relative rotative efficiencies, η_R , and propeller open water efficiencies, η_O , at the self-propulsion points under the given fouling conditions. As can be seen in the figure, the η_R values showed decreasing trends with both of the hull fouling and propeller fouling, but the magnitude of the decrease is smaller than that for open water efficiencies, η_O . The decrease in η_O values can be related to the decreased advance coefficient values, J , which is shown in Figure 8.20. However, unlike the J values, *clean-hull/fouled-propeller* case showed larger decreases in η_O values than *fouled-hull/clean-propeller*, due to that fact that the open water curves for the fouled propellers have smaller η_O than those for the clean propeller.

The decreases in η_R values under *fouled-hull/clean-propeller*, *clean-hull/fouled-propeller*, and *fouled-hull/fouled-propeller* conditions at the most severe surface

fouling condition (B20%) were observed to be -1.9%, -1.2%, and -2.6%, respectively. And the decreases in η_O for those fouling conditions were observed to be -8.7%, -15.4% and -20.1%, respectively.

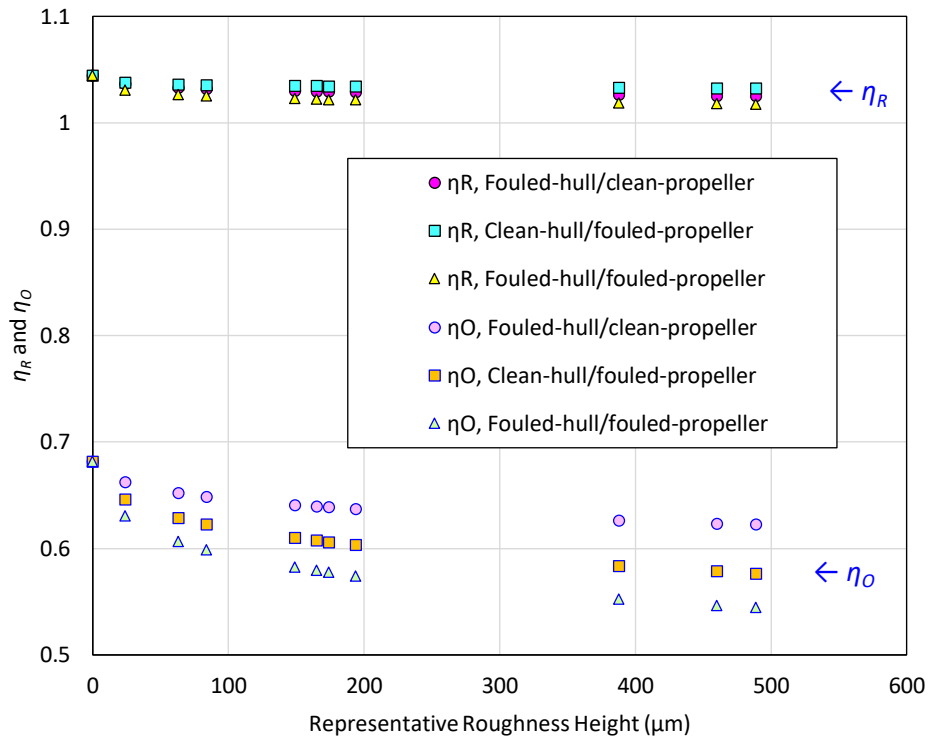


Figure 8.23 Relative rotative efficiency, η_R , and propeller open water efficiency, η_O , at self-propulsion point under the given fouling conditions, plotted against the representative roughness heights of the surface fouling conditions in Table 6.1

8.4.8. Effect on hull efficiency and behind-hull efficiency

Figure 8.24 compares the hull efficiencies, η_H , and behind-hull propeller efficiencies, η_B , at the self-propulsion points under the given fouling conditions. As the effect of propeller fouling on $1 - t$ and $1 - w_T$ were found to be minor, the η_H values ($\eta_H = 1 - t / 1 - w_T$) for *clean-hull/fouled-propeller* remained rather constant. For this reason, the η_H values for the *fouled-hull* cases collapsed on each other. As expected in

previous sections, the *fouled-hull* cases showed increasing trends of the η_H values with increasing level of surface fouling.

When it comes to the behind-hull efficiencies, η_B , they showed decreases due to both of the hull and propeller fouling. As the impact of them was larger for the η_O than η_R , the decreases in η_B values ($\eta_B = \eta_R \eta_O$) for the fouling conditions were found to follow the same order of the decrease in η_O .

The increases in η_H values under *fouled-hull/clean-propeller*, *clean-hull/fouled-propeller*, and *fouled-hull/fouled-propeller* conditions at the most severe surface fouling condition (B20%) were observed to be 12.5%, 0%, and -12.7%, respectively. And the decreases in η_B for those fouling conditions were -10.4%, -16.4% and -22.2%, respectively.

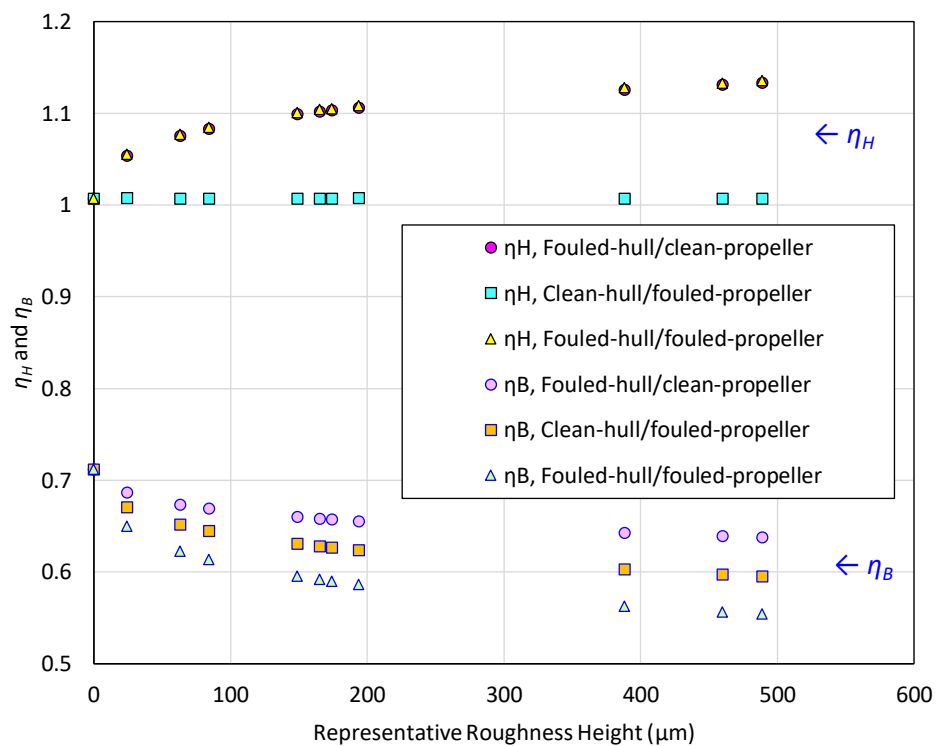


Figure 8.24 Hull efficiency, η_H , and behind-hull propeller efficiency, η_B , at self-propulsion point under the given fouling conditions, plotted against the representative roughness heights of the surface fouling conditions in Table 6.1

8.4.9. Effect on propulsive efficiency

Figure 8.25 shows the propulsive efficiencies, η_D , at the self-propulsion points under the given fouling conditions. As it was found in the previous sections that the hull efficiencies, η_H , are increased by hull fouling, while the behind-hull propeller efficiencies, η_B , are decreased by both of hull and propeller fouling, the propulsive efficiencies, $\eta_D = \eta_H \eta_B$, showed an interesting result.

In terms of *fouled-hull/clean-propeller* case, the magnitudes of the increases in η_H are larger than those of the decreases in η_B , as can be seen in Figure 8.24. As a result, the η_D values for this case showed increases.

The largest reductions in η_D values were observed for *clean-hull/fouled-propeller* case, as the η_H values were constant but η_B values were decreased due to the propeller fouling. On the other hand, *fouled-hull/fouled-propeller* case shows relatively smaller decreases in η_D values owing to the increased η_H values.

The increases and decrease in η_D values under *fouled-hull/clean-propeller*, *clean-hull/fouled-propeller*, and *fouled-hull/fouled-propeller* conditions at the most severe surface fouling condition (B20%) were observed to be 0.9%, -16.4%, and -12.3%, respectively.

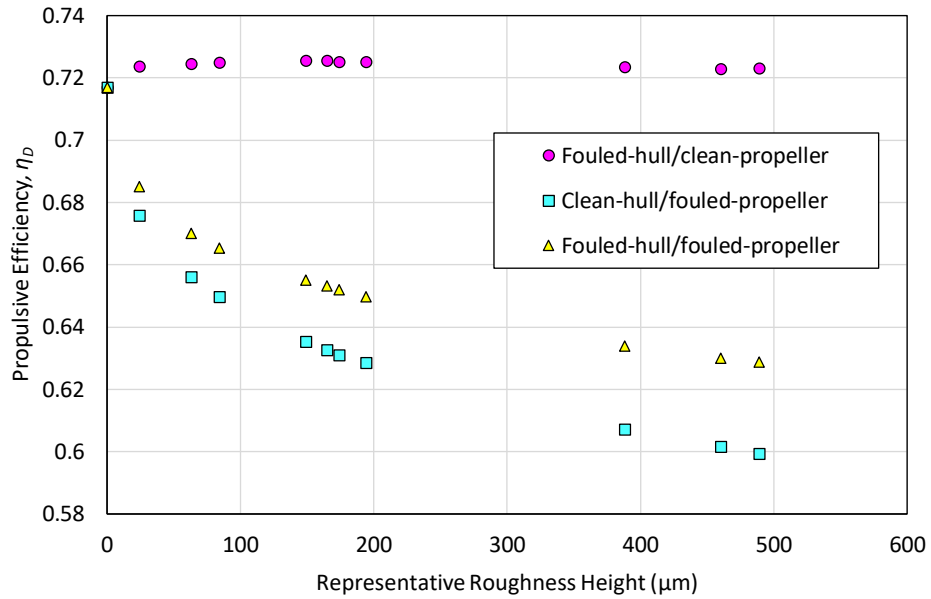


Figure 8.25 Propulsive efficiency, η_D , at self-propulsion point under the given fouling conditions, plotted against the representative roughness heights of the surface fouling conditions in Table 6.1

8.4.10. Power penalty

Using the simulation results, the increases in required shaft power, SP , under the given fouling conditions were calculated. The required shaft power can be calculated as

$$SP = 2\pi\rho K_Q n^3 D^5 \quad (8.5)$$

The required shaft power, SP , were calculated with the K_Q and n values obtained from the self-propulsion simulations under the given fouling conditions.

For comparison purposes, the required shaft powers, SP , for the given fouling conditions were calculated from two different methods: *self-propulsion* method, using the K_Q and n values directly obtained from the current self-propulsion simulations with Equation 8.5, and *towing/open-water* method using the corresponding K_Q and n values obtained from the towed ship and propeller open water simulations in Chapter 6 and 7.

In *towing/open-water* method the required shaft power, SP , was determined as follows:

- i) The required thrust, T , for the given conditions are calculated as $T = R_T/(1 - t)$, where R_T is the total resistance under the corresponding hull fouling obtained in Chapter 6 and $1 - t$ is the thrust deduction factor of Hino (2005);
- ii) then the advance coefficients, J , of the propeller open water curves, obtained in Chapter 7, are converted into the propeller revolutions, $n = V_s(1 - w_n)/(JD)$, where $1 - w_n$ is wake fraction for the hull fouling, obtained in Chapter 6, and V_s is the ship speed;
- iii) the thrust coefficients, K_T , of the open water curves are converted to thrust values as, $T = \rho n^2 D^4$, and then a n vs T curve is obtained;
- iv) from the n vs T curve, corresponding n is determined, such that the required thrust is achieved;
- v) K_Q value at the corresponding n (and hence J) is read from the open water curves obtained in Chapter 7;
- vi) finally, the required shaft power, SP , is determined using Equation 18, with the obtained n and K_Q values.

Figure 8.26 compares the required shaft powers, SP , at the self-propulsion points under the given fouling conditions, which were obtained using *self-propulsion* method and *towing/open-water* method. As can be seen in the figure, the SP values obtained from two different methods show a fair agreement in the trend, but *towing/open-water* method relatively under-predicted the SP values compared to those obtained from *self-propulsion* method.

It was observed that the SP values for *fouled-hull/clean-propeller* case show better agreement than other cases. Considering that *fouled-hull/clean-propeller* case showed the smallest roughness effect on the propulsive efficiency, η_D , it can be deduced that the differences between the two methods arise from the fact that *towing/open-water* method does not properly consider the roughness effect on the propulsive efficiency, η_D . That is to say, this method could not consider the roughness effect on the thrust deduction factor, $1 - t$, and the relative rotative efficiency, η_R . Also, the differences between $1 - w_n$ and $1 - w_T$ due to the hull-propeller interaction can be another reason for the disagreements.

However, considering the high computational cost required for the self-propulsion simulations, *towing/open-water* method can be considered as a reasonable alternative. It is of note that the CPU time required for *self-propulsion* method was 357,864 CPU-hours (11,544 hours \times 31 cases) and that for *towing/open-water* method was 16,115 CPU-hours (1,348 hours \times 11 cases + 117 hours \times 11 cases).

The increases in required shaft power SP values obtained from the simulations, under *fouled-hull/clean-propeller*, *clean-hull/fouled-propeller*, and *fouled-hull/fouled-propeller* conditions at the most severe surface fouling condition (B20%) were observed to be 57.8%, 19.2%, and 81.8%, respectively. And the increases calculated from *towing/open-water* method were 68.4%, 19.9% and 84.0%.

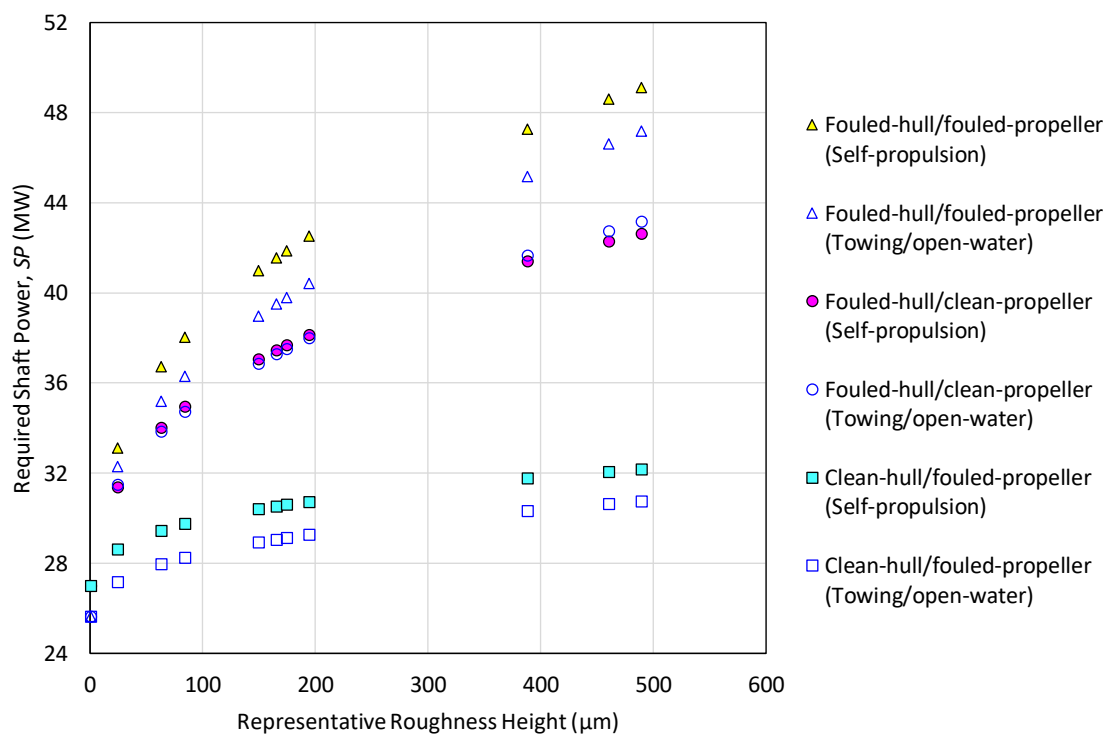


Figure 8.26 Required shaft power, SP , at self-propulsion point under the given fouling conditions, obtained from the current CFD and using the towed ship and propeller open water simulations (Chapter 6 and 7), plotted against the representative roughness heights of the surface fouling conditions in Table 6.1

8.5. The effect of biofouling on flow characteristics

8.5.1. Effect on velocity distribution

Figure 8.27 compares the velocity contours of V_{xz}/V_{ship} on the $y = 0.006L_{pp}$ plane, under the given fouling conditions, while Figure 8.28 illustrates the velocity contours of V_x/V_{ship} on the $x/L_{pp} = 0.0089$ plane (where $x/L_{pp} = 0$ means the after perpendicular plane). It can be seen from the figures that the velocity fields are strongly affected by the hull fouling while the effect of propeller fouling is relatively negligible. The higher velocities downstream to the propeller for the *fouled-hull* cases can be attributed to the higher rotational speeds, n , as shown in Figure 8.17.

Figure 8.27 shows the decelerated flow upstream to the propeller, and Figure 8.28 shows enlarged wake field for the *fouled-hull* cases, while the propeller fouling has almost no effect. This can be related to the effects on the wake fractions in Figure 8.22. Another notable point is that the *fouled-hull* cases have thicker boundary layers compared to the *clean-hull* cases, which is in correspondence with the increased C_T values in Figure 8.14.

The increased boundary layer thickness and enlarged wake field can be more clearly seen in Figure 8.29. In the figure, the boundary layer thickness of around the KCS hulls was represented by the contours of the turbulent kinetic energy ($TKE > 0.2 J/kg$). As similarly seen in the previous figures, Figure 8.29 illustrates increased boundary layer thicknesses and wake fields for *fouled-hull* cases, whereas no significant differences were found due to the propeller fouling. In a similar manner, the presence of the propeller does not result in significant differences, as can be seen when compared to the towed ship cases (e-f).

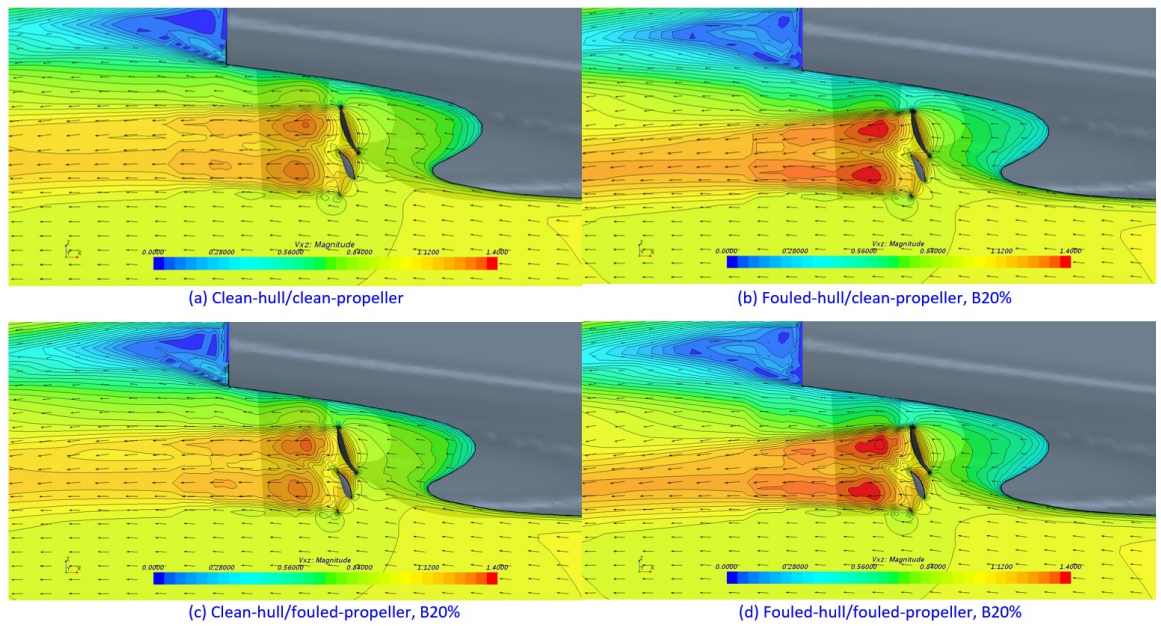


Figure 8.27 Velocity contour of V_{xz}/V_{ship} at $y = 0.006L_{pp}$, (a) clean-hull/clean-propeller, (b) fouled-hull/clean-propeller, B20%, (c) clean-hull/fouled-propeller, B20%, (d) fouled-hull/fouled-propeller, B20%

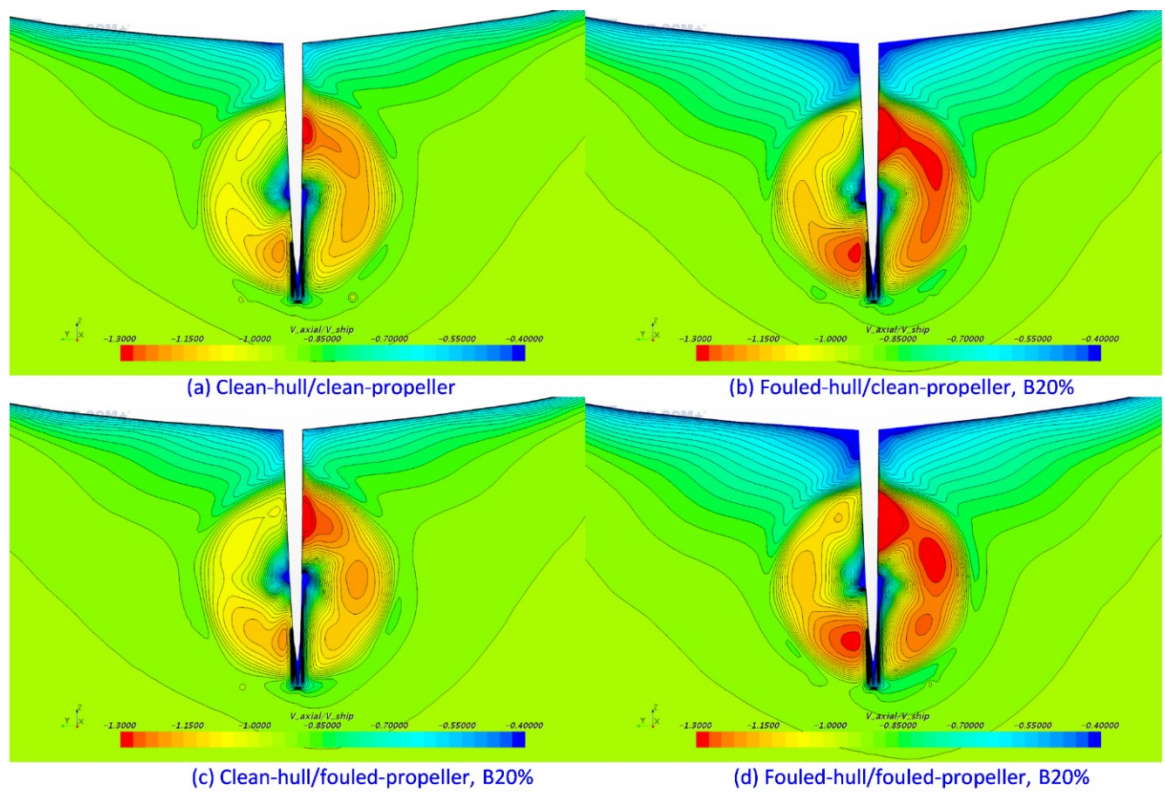


Figure 8.28 Axial velocity contour of V_x/V_{ship} at $x = 0.0089L_{pp}$, (a) clean-hull/clean-propeller, (b) fouled-hull/clean-propeller, B20%, (c) clean-hull/fouled-propeller, B20%, (d) fouled-hull/fouled-propeller, B20%

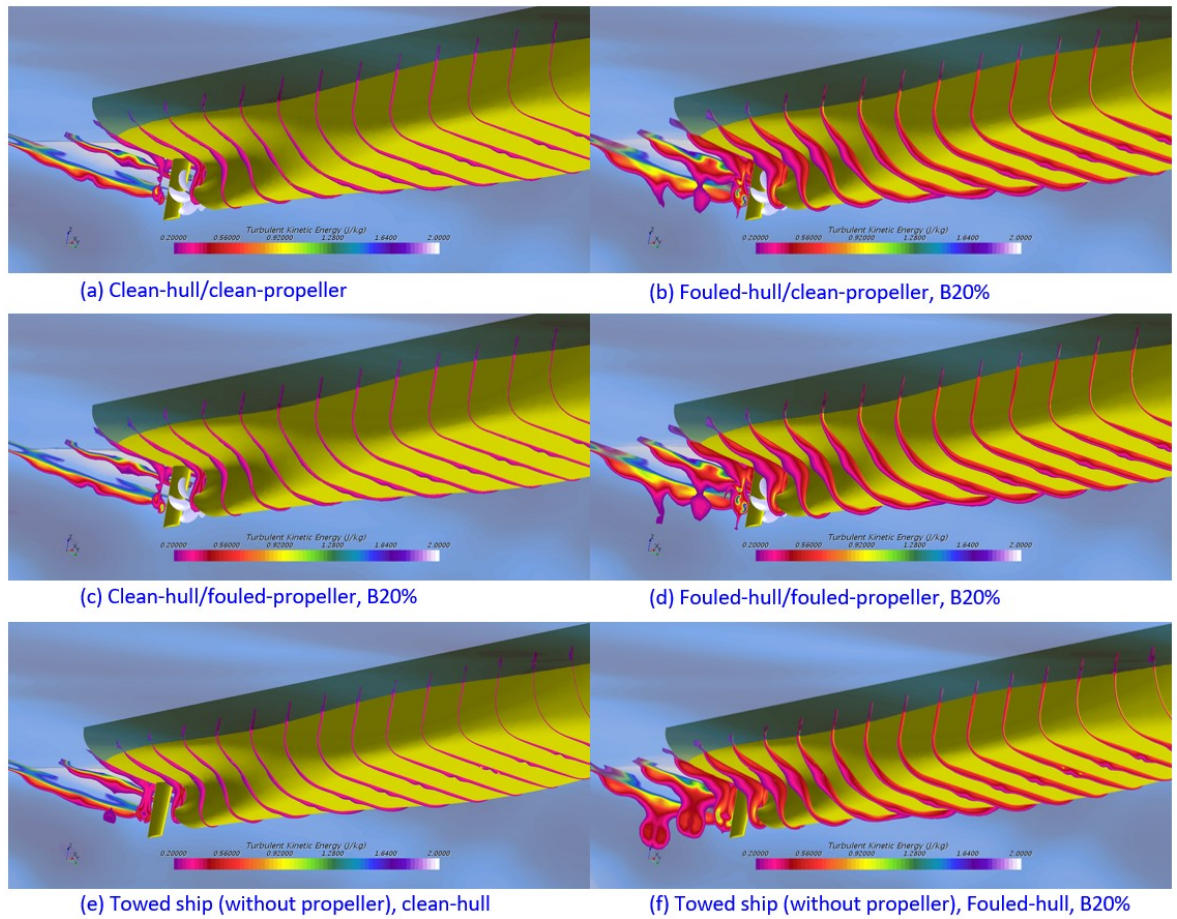


Figure 8.29 Boundary layer represented by slices limited to the turbulent kinetic energy, (a) clean-hull/clean-propeller, (b) fouled-hull/clean-propeller, B20%, (c) clean-hull/fouled-propeller, B20%, (d) fouled-hull/fouled-propeller, B20%, (e) towed ship, clean-hull, (f) towed ship, fouled-hull, B20%

8.5.2. Effect on surface pressure

Figure 8.30 compares the surface pressure at the stern of the ships under the different fouling conditions (a-d) and those computed under towing conditions in smooth and fouled (B20%) conditions (e-f). The pressure was non-dimensionalised by dividing it by the dynamic pressure, $1/2\rho V^2$. From the figure, it can be observed that the *fouled-hull* cases have lower surface pressure than *clean-hull* cases, which can result in larger viscous pressure resistance, as similarly observed in Chapter 6. Also, compared to the towed ship cases, the cases with propeller showed smaller surface pressures, which

causes thrust deduction and the increased residuary resistance, C_R , as shown in Figure 8.16.

It can also be observed from the figure that the effect of propeller fouling on the surface pressure of the hull and rudder is almost negligible. This finding can be related to the negligible effects of the propeller fouling on the residuary resistance coefficient, C_R , and the thrust deduction factor, $1 - t$, as shown in Figure 8.16 and Figure 8.21.

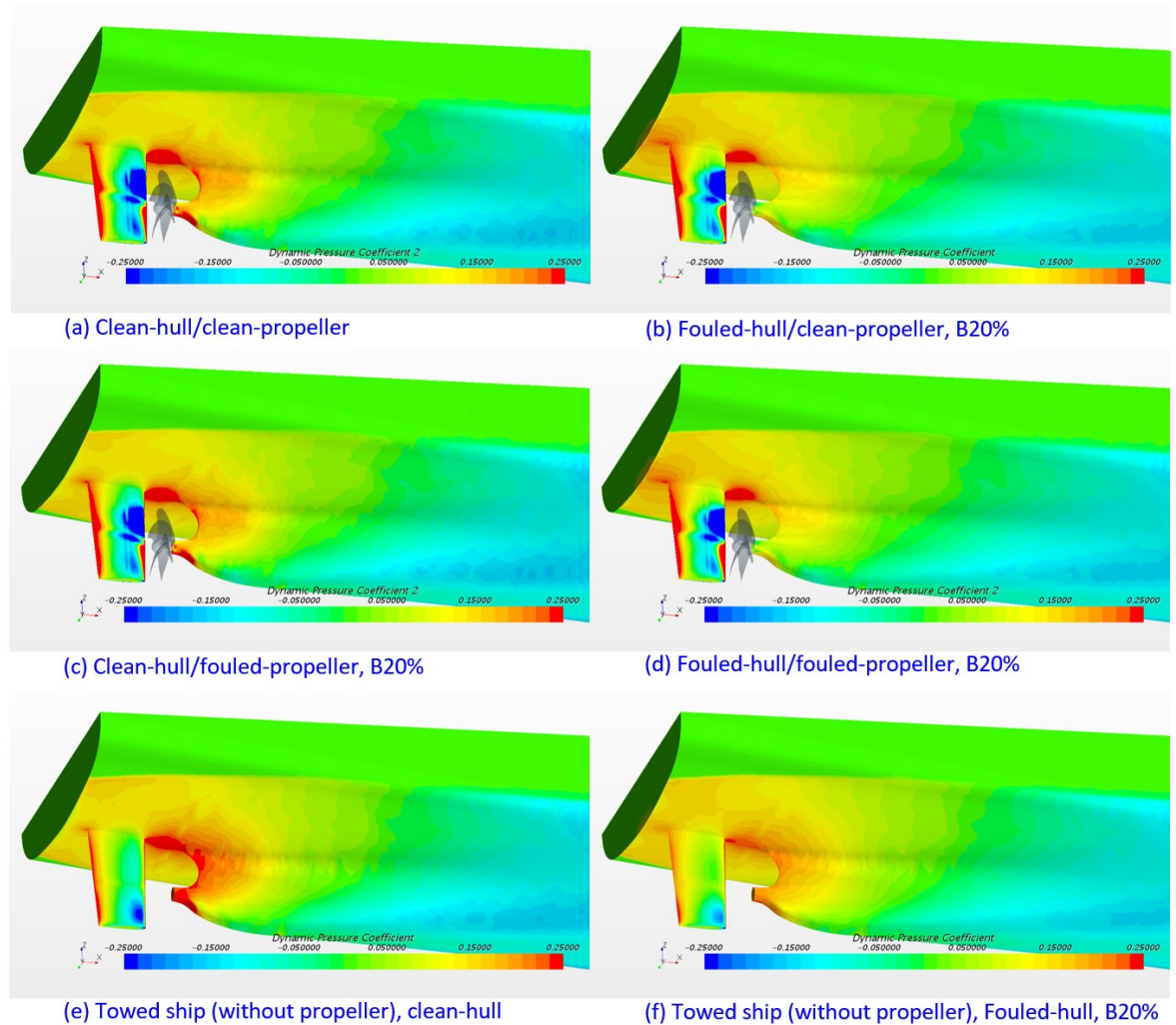


Figure 8.30 Surface pressure distribution at the stern (a) clean-hull/clean-propeller, (b) fouled-hull/clean-propeller, B20%, (c) clean-hull/fouled-propeller, B20%, (d) fouled-hull/fouled-propeller, B20%, (e) towed ship, clean-hull, (f) towed ship, fouled-hull, B20%

8.5.3. Effect on wave pattern

Figure 8.31 compares the wave patterns around the hull surface of the ships in different fouling conditions. It is seen from the comparison in the figure that the wave elevations around the hull are reduced by the hull fouling, but the effect of propeller fouling is almost negligible. It is of note that his finding is consistent with the findings of Demirel et al. (2017b) as well as the observations in Chapter 6.

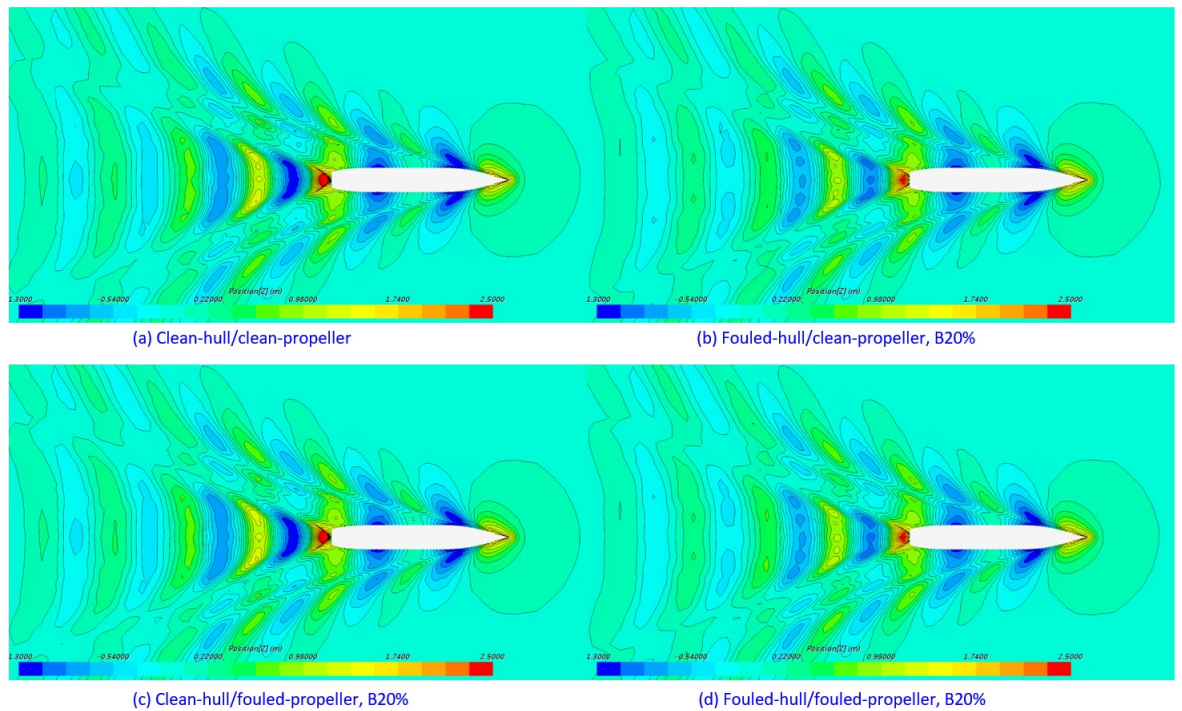


Figure 8.31 Wave pattern around the ship, (a) clean-hull/clean-propeller, (b) fouled-hull/clean-propeller, B20%, (c) clean-hull/fouled-propeller, B20%, (d) fouled-hull/fouled-propeller, B20%

8.5.4. Effect on vorticity field

An interesting feature was observed on the vorticity field downstream of the propeller. Figure 34 illustrates the vorticity magnitudes around the propeller at the self-propulsion points under the given surface conditions. As can be seen in the figure, the vorticity downstream to the propeller increased due to both of the hull fouling and propeller fouling. This can be seen as a consequence of the increased propeller revolutions, n , of those cases. Interestingly, however, when it comes to the vorticity on the leading edge of the rudders, the vorticity magnitudes for the *fouled-propeller* cases were observed to be reduced compared to the *clean-propeller* cases, although they have even higher propeller rotational speeds, n . This finding can be related to the observation in Chapter 7, i.e. the reduced propeller hub vortex under the fouled propeller cases (Figure 7.17 and 7.18). This can be seen as a positive feature with regard to the problems involving rudder-propeller interaction, such as cavitation and noise.

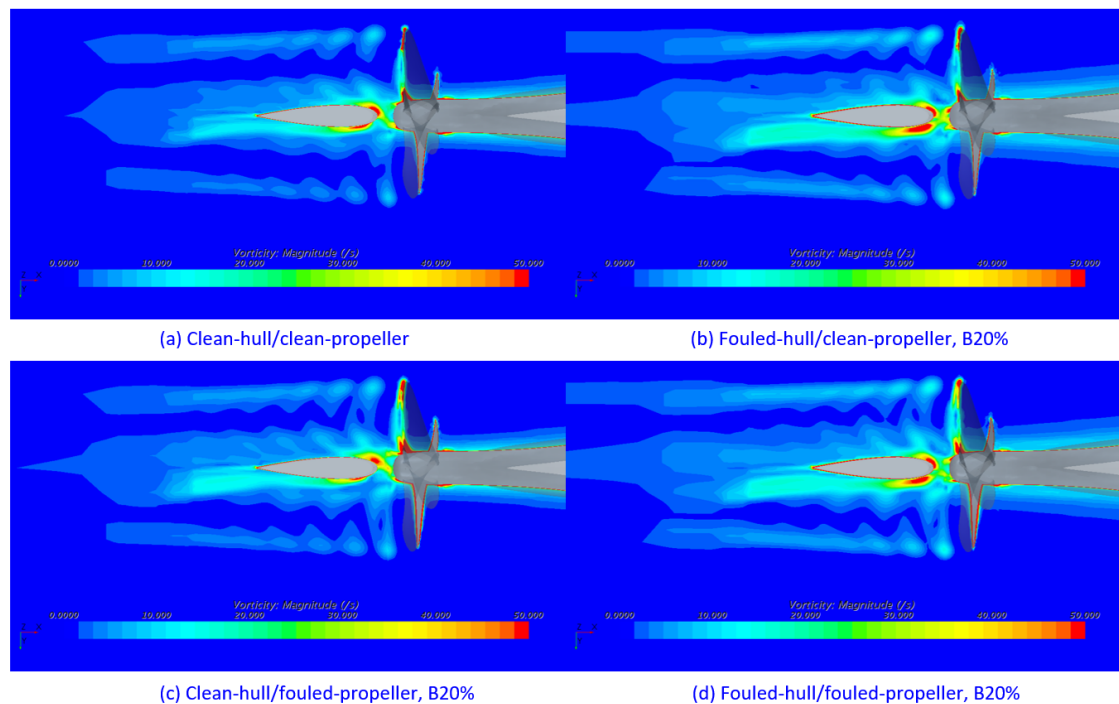


Figure 8.32 Vorticity contour around the propeller (bottom-up view), (a) clean-hull/clean-propeller, (b) fouled-hull/clean-propeller, B20%, (c) clean-hull/fouled-propeller, B20%, (d) fouled-hull/fouled-propeller, B20%

8.6. Chapter summary and conclusions

A CFD model for the prediction of the effect of biofouling on ship self-propulsion characteristics has been proposed. The same modified wall-function approach was applied, as used in Chapter 6 and 7, to represent the surface roughness of barnacles on the hull and propeller.

A verification study was carried out to assess the numerical uncertainties of the proposed CFD model and to determine sufficient grid-spacings and time steps. Spatial and temporal convergence studies were performed using the Grid Convergence Index (GCI) method.

For the validation of the current CFD model, four different simulations were conducted namely; ‘*model-scale/with-rudder*’, ‘*model-scale/without-rudder*’, ‘*full-scale/with-rudder*’, and ‘*full-scale/without-rudder*’. *Model-scale/without-rudder* simulation was compared with the experimental result and showed good agreement. The simulation results of the four different cases were compared to examine the scale effect and interactions with rudders.

Fully nonlinear URANS simulations of the full-scale KCS self-propulsion simulations were conducted in different configurations of fouling severities (barnacle sizes and coverage) and fouling scenarios (hull fouling, propeller fouling and both).

The result suggests that hull fouling increases total resistance coefficients, C_T , up to 52% with the most severe surface condition (B20%), whereas the effect of propeller fouling on the C_T values is negligible. The propeller rotational speed at the self-propulsion point, n , was observed to be increased due to both of hull fouling and propeller fouling. Interestingly, improved hull efficiencies, η_H were observed for the *fouled-hull* cases due to the increased stern wake, w_T , and reduced thrust deduction factor, t , while the effect of propeller fouling was minor. On the other hand, the behind-hull efficiencies, η_B , showed decreases due to the hull and propeller fouling. The overall propulsive efficiencies, η_D , for *fouled-hull/clean-propeller* case showed

increases whereas the other cases showed decreases. The impact on η_D values for *clean-hull/fouled-propeller* case was found to be most critical, which showed up to 22.2% decreases with the most severe surface condition.

Power penalties due to the given fouling conditions were also calculated using the self-propulsion simulation results as well as using the towed ship and propeller open water simulations, obtained from the previous chapters. The two different methods showed a fair agreement. The increases in the shaft power, SP , for *fouled-hull/fouled-propeller* case under the most severe surface condition, predicted from the *self-propulsion* method and *towing/open-water* method, were 81.8% and 84.0% increases, respectively.

The roughness effect on the flow characteristics was also examined. The velocity fields at the stern showed a strong dependency of the hull fouling whereas the effects of propeller fouling were relatively minor. As expected, *fouled-hull* cases showed thicker boundary layers on the hull. Decelerated flow upstream to the propeller and enlarged wake field due to the hull fouling was also observed, which is consistent with the increased wake fractions.

The surface pressures under different fouling conditions were also compared together with those of towed ship simulations without the propeller. Again, the effect of propeller fouling on the surface pressure on the hull and rudder was observed to be negligible while the effect of hull fouling was clearly seen.

An interesting finding is that the reduced vorticity on the leading edge of the rudders for *fouled-propeller* cases, even with the higher propeller revolutions due to the propeller fouling. This finding can be seen as positive, in terms of cavitation and noise, and could be related to the observation in Chapter 7, which showed reduced propeller hub vortex under the fouled propeller cases.

9. Effect of heterogeneous distribution of hull roughness on ship resistance

9.1. Introduction

As reviewed in Chapter 2, there has been extensive research carried out to predict the effect of hull roughness on ship resistance and powering, either using the similarity law scaling or Computational Fluid Dynamics (CFD). Also, this PhD thesis mainly uses these two methods. However, there has been a major simplification in the conventional studies. That is, the hull surfaces have been treated as uniformly rough, while the real ships' surfaces are not uniform as they are exposed to heterogeneous fouling accumulation. This difference can introduce uncertainties in the added resistance predictions, as claimed by Demirel et al. (2017a). Therefore, it is worthwhile to investigate whether the heterogeneous distribution of hull roughness brings different results compared to the case of homogeneous hull roughness (i.e. evenly distributed hull roughness).

To the best of the author's knowledge, there exists no specific study investigating the effect of heterogeneous distributions of hull roughness on ship resistance. Therefore, this study aims to fill this gap by conducting a model ship towing test with heterogeneous hull roughness.

In this study, towing tests were conducted using a Wigley hull model with heterogeneous hull roughness conditions (i.e. $\frac{1}{4}$ -bow-rough, $\frac{1}{4}$ -aft-rough, $\frac{1}{2}$ -bow-rough and $\frac{1}{2}$ -aft-rough conditions) as well as homogeneous conditions (i.e. smooth and full-rough conditions). In order to roughen the hull heterogeneously, the same sand grit used in Chapter 4 (aluminium oxide abrasive power) was used on parts of the hull surface. A new prediction method was proposed to predict the added resistance due to the heterogeneous hull roughness and the predictions were compared with the experimental result.

This chapter is organised as follows: Section 9.2.1 explains the methodology used in this chapter, and the experimental setup is presented in Section 9.2.2, including principal particulars of the model ship and the surface conditions. The uncertainties of the model test are estimated in Section 9.2.3. The test result of the Wigley hull with different surface conditions and discussions regarding the rationale of the effect of heterogeneous hull roughness on ship resistance are presented in Section 9.3. A new prediction method is proposed to predict the added resistance due to the heterogeneous hull roughness and the predictions are compared with the experimental result in Section 9.4. Finally, the chapter summary and conclusions are presented in Section 9.5.

9.2. Methodology

9.2.1. Approach

A schematic illustration of the current study is shown in Figure 9.1. The first half of the study is conducting towing tests of the Wigley hull model with different hull roughness conditions including the heterogeneous hull conditions (i.e. $\frac{1}{4}$ -bow-rough, $\frac{1}{4}$ -aft-rough, $\frac{1}{2}$ -bow-rough and $\frac{1}{2}$ -aft-rough conditions) as well as the homogeneous hull conditions (i.e. smooth and full-rough conditions). In order to roughen the hull surface heterogeneously, the same sand grit used in Chapter 4 was gradually applied on the different regions of the hull surface as shown in Figure 9.2. Because the Wigley hull has a symmetric hull shape to the midship, the same hull surfaces can be used for both the bow-rough and aft-rough conditions by towing the model in different directions. For example, the $\frac{1}{2}$ -rough hull surface in Figure 9.2 was used for both of the $\frac{1}{2}$ -bow-rough and $\frac{1}{2}$ -aft-rough conditions as shown in Figure 9.3.

The second half of the study is developing a new prediction method for predicting the effect of heterogeneous hull roughness on ship resistance. A new prediction method was proposed based on the similarity law scaling (Granville, 1958; 1978), considering the wetted surface areas of different hull regions with different hull roughness. The similarity law scaling was performed using the roughness function, ΔU^+ , of the sand

grit which was determined in Chapter 4, and the added resistance values of the Wigley model due to the heterogeneous hull roughness were predicted and compared with the results of the towing tests of the Wigley model.

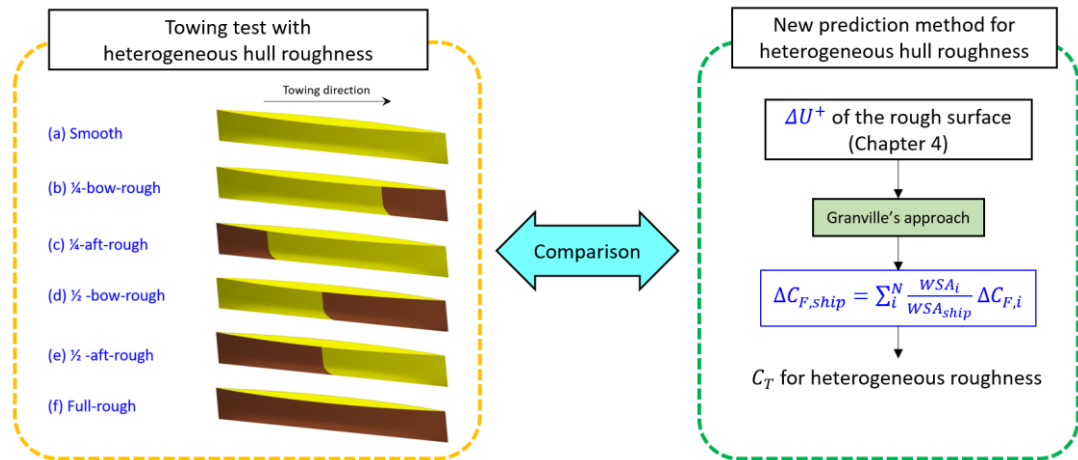


Figure 9.1 Schematic illustration of the methodology in Chapter 9

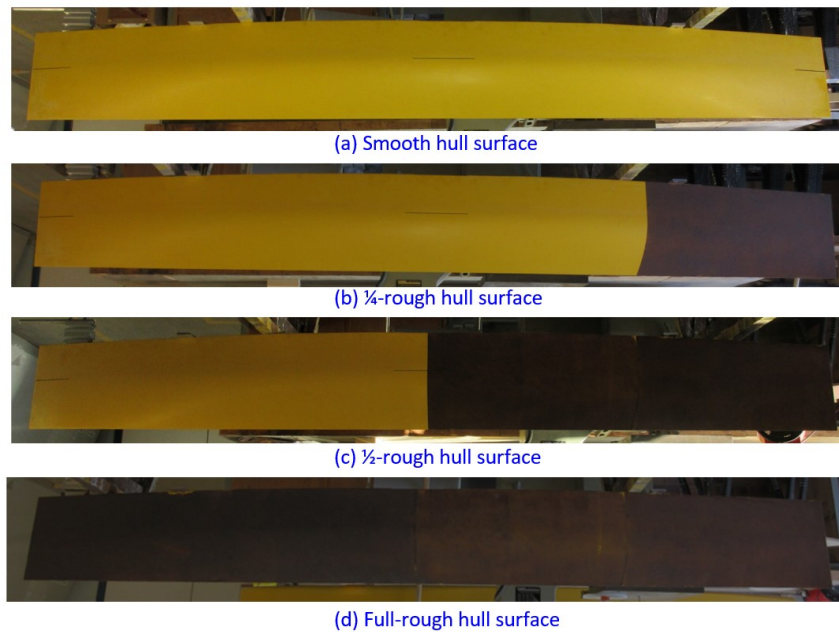


Figure 9.2 Wigley model with different surface conditions



Figure 9.3 The towing carriage of the Kelvin Hydrodynamics Laboratory and the Wigley model; (a) 1/2-bow-rough condition, (b) 1/2-aft-rough condition

9.2.2. Experimental setup

9.2.2.1. Towing tank

The towing tests of the Wigley hull model were carried out in the Kelvin Hydrodynamics Laboratory (KHL) of the University of Strathclyde. Further details of the towing tank and the carriage can be found in Section 4.2.2. Figure 9.3 shows the towing carriage in the KHL and the Wigley model.

9.2.2.2. Wigley hull model

In this study, a Wigley hull model with standard proportions was used. The Wigley hull is a parabolic hull form which can be represented by

$$y = \frac{B}{2} \left[1 - \left(\frac{2x}{L} \right)^2 \right] \left[1 + \left(\frac{z}{T} \right)^2 \right] \quad (9.1)$$

where, L , B and T are the length, waterline beam and the draft of the model. The principal particulars of the Wigley model can be found in Table 9.1. Figure 9.4 illustrates the experimental setup used for the towing test. During the test, the model was free to trim and sink. A load cell was attached at the tow point to measure the total resistance of the model ship. The model was towed with the speed range of 1.08 – 2.71

m/s, which corresponds to the Froude number, Fn , of 0.2 – 0.5. For roughening the surface, Clarke Aluminium Oxide Abrasive Powder, 60-80 grit ($Rt_{50}=353 \mu\text{m}$) was applied on the surface as used in Chapter 4.

Table 9.1 Principal particulars of the Wigley model and test conditions

Length	L (m)	3.00
Beam at waterline	B (m)	0.30
Draft	T (m)	0.1875
Beam/draft ratio	B/T	1.6
Total wetted surface area	WSA (m^2)	1.3383
Wetted surface area of first quarter	WSA_{Q1} (m^2)	0.3066
Wetted surface area of first half	WSA_{H1} (m^2)	0.6691
Displacement	∇ (m^3)	0.0750
Block coefficient	C_B	0.4444
Towing speed	V (m/s)	1.08 – 2.71
Froude number	Fn	0.2 – 0.5
Reynolds number	Re_L	$2.6 - 6.6 \times 10^6$
Water temperature	T_w ($^{\circ}\text{C}$)	12

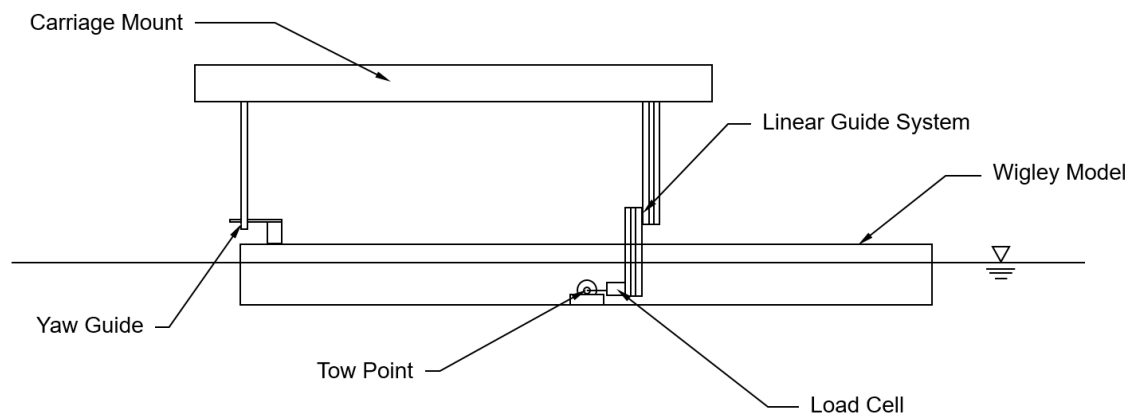


Figure 9.4 Experimental set up of the towing test

9.2.3. Uncertainty analysis

The uncertainties of the measurements in the tests were estimated following the ITTC recommended procedures (ITTC, 2014). The precision limits were determined through the repeatability test and the bias limits were calculated considering the uncertainties associated with the calibration, data acquisition, data reduction and conceptual bias. Due to the limited time, the repeatability tests of the bow rough conditions (e.g. ¼-bow-rough and ½-bow-rough) were conducted only at the highest speed while the repeatability tests of the aft rough conditions (e.g. ¼-aft-rough and ½-aft-rough) were conducted only at the lowest speed. Table 9.2 shows the absolute and relative overall uncertainties of the total resistance coefficient of the Wigley model.

Table 9.2 Overall uncertainties of C_T with 95% confidence level

Surface condition	Lowest speed		Highest speed	
	Overall Uncertainty	Percentage	Overall Uncertainty	Percentage
Smooth	±1.92E-04	±4.91%	±1.28E-04	±1.65%
¼-bow-rough	-	-	±1.25E-04	±1.44%
¼-aft-rough	±1.00E-04	±2.45%	-	-
½-bow-rough	-	-	±1.31E-04	±1.39%
½-aft-rough	±7.32E-05	±1.64%	-	-
Full-rough	±2.84E-04	±5.25%	±1.63E-04	±1.52%

9.3. Result

9.3.1. Verification of model symmetry

As mentioned earlier, the bow-rough and aft-rough conditions (e.g. $\frac{1}{2}$ -bow-rough and $\frac{1}{2}$ -aft-rough in Figure 9.1) were realised by towing the model in different directions while using the same hull surfaces (e.g. $\frac{1}{2}$ -rough surface in Figure 9.2) as shown in Figure 9.3. Therefore, it is necessary to verify the model symmetry before investigating the effect of heterogeneous hull roughness. Therefore, the towing test results of the homogeneous hull conditions (e.g. smooth and full-rough conditions) in different towing directions were compared for the verification of the model symmetry.

Figure 9.5 compares total resistance coefficient, C_T , of the Wigley model with the homogeneous hull conditions (e.g. smooth and full-rough conditions). As shown in the figures, the C_T values of the smooth condition were observed not to be significantly affected by the towing directions, showing the deviations within the uncertainty levels of the experiment. This suggests that the geometric accuracy of the model is within a satisfactory level. Therefore, the differences between the bow and aft rough conditions (i.e. difference between $\frac{1}{4}$ -bow-rough and $\frac{1}{4}$ -aft-rough conditions) can be purely attributed to the different locations of the hull roughness. Similarly, the C_T values of the full-rough conditions were almost identical regardless of the towing directions. This validates again the geometric symmetry of the model and also suggests that the potential imperfections of the sand grit application do not affect the result significantly.

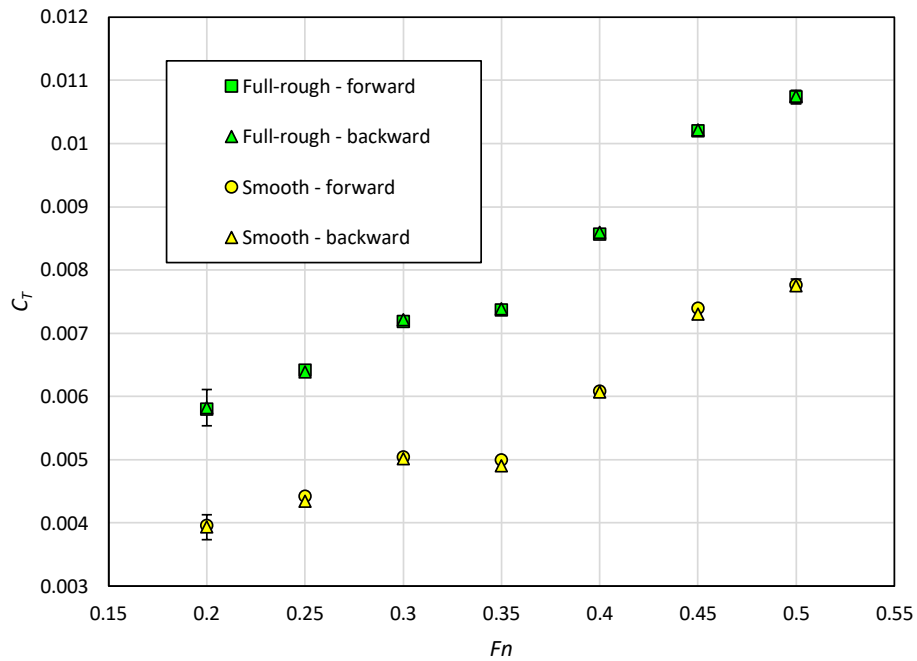


Figure 9.5 C_T values of smooth and full-rough conditions with different towing directions

9.3.2. Effect of heterogeneous hull roughness

As shown in Figure 9.6, the model with the $\frac{1}{4}$ -bow-rough condition showed larger C_T values compared to the C_T values of the $\frac{1}{4}$ -aft-rough condition. The percentage increases in C_T compared to the smooth condition, $\% \Delta C_T$, are 12 – 18% for the $\frac{1}{4}$ -bow-rough condition, while these values are 8 – 10% for the $\frac{1}{4}$ -aft-rough condition. Similarly, the Wigley hull with the $\frac{1}{2}$ -bow-rough condition showed larger C_T values than the results of the $\frac{1}{2}$ -aft-rough condition as shown in Figure 9.7. The $\% \Delta C_T$ values with the $\frac{1}{2}$ -bow-rough condition are 21 – 30%, while these values are 16 – 22% for the $\frac{1}{2}$ -aft-rough condition.

These results imply that the hull roughness of the front part of the ship results in more added resistance than the roughness of the rear part.

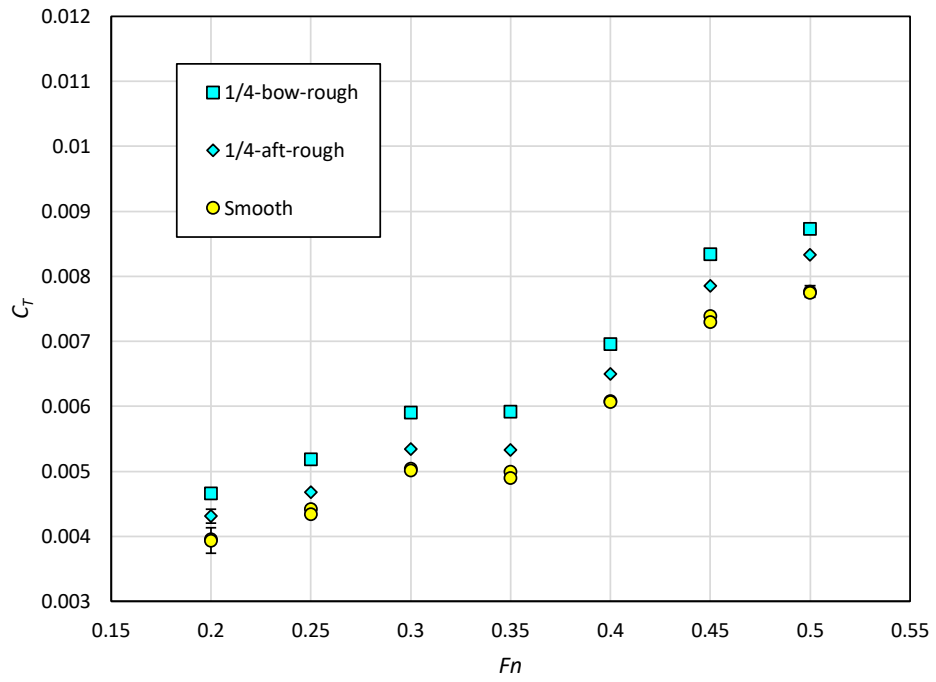


Figure 9.6 C_T values of Wigley model in smooth and $1/4$ -rough condition

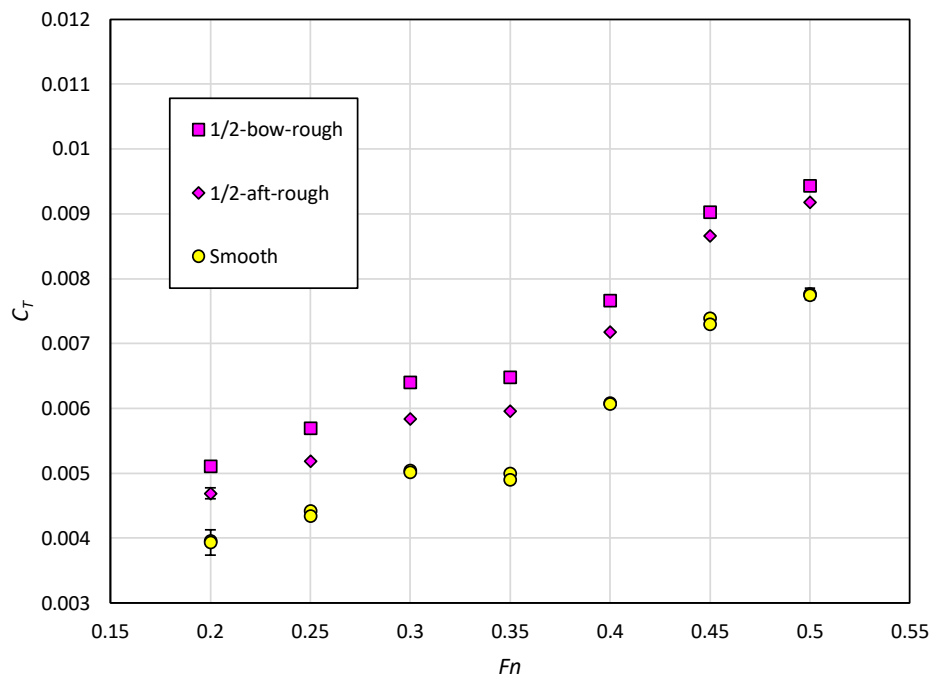


Figure 9.7 C_T values of Wigley model in smooth and $1/2$ -rough condition

9.3.3. Rationale of the differences

As differences in the roughness effect on the C_T were observed between the bow-rough and aft-rough conditions as shown in Figure 9.6 and 9.7, it is worthwhile to discuss the possible rationale behind this observation. One of the most likely reasons is the varying contributions of the local skin friction, C_f , to the total drag of the ship. It is a well-known fact that, regardless of the roughness effect, the C_f is larger near the leading edge due to the active transition behaviours and it decreases as the flow is developed along the hull (i.e. the bow region of the Wigley model has larger wall shear stress, τ_w). Accordingly, the roughness Reynolds numbers, $k^+ = kU_\tau/\nu$, in the bow region become larger and the roughness effect in this region becomes more evident.

Although the local skin friction on the Wigley model was not measured during the test, alternatively, this rationale could be supported by the CFD simulation of the 1.5m flat plate conducted in Chapter 5. Figure 9.8 compares the C_f values of the plate in the smooth and rough conditions along the line of $z = -2/T$, and the difference, ΔC_f , between the smooth and rough cases.

As shown in the figure, the smooth plate shows larger C_f near the leading edge and the values gradually reduce along the flat plate. The rough plate shows an even larger peak of the C_f near the leading edge. Accordingly, the ΔC_f is greater in the forward region and it reduces gradually along the plate, which is in correspondence with the k^+ values on the plate surface as shown in Figure 9.9.

From this observation, it can be deduced that the roughness effect on the skin friction (i.e. ΔC_f) is greater in the forward region of the flat plate and the same logic can be applied to ship hulls.

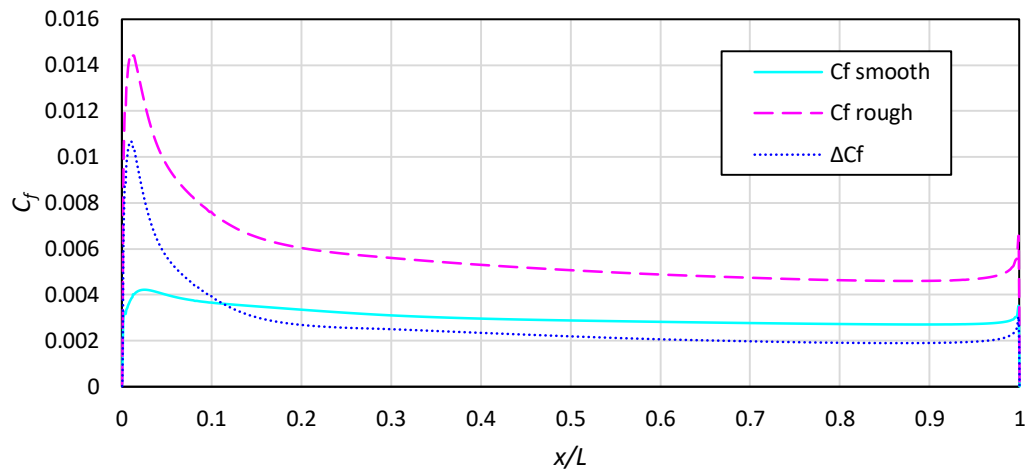


Figure 9.8 Local skin friction on the flat plate along the line of $z = -2/T$ in smooth and (homogeneously) rough condition with the towing speed of $V = 4.5$ m/s, obtained from the flat plate simulation in Chapter 5.

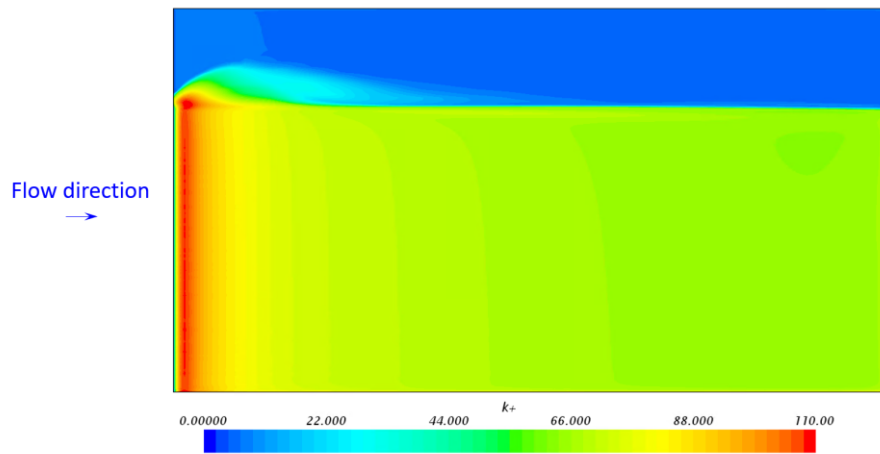


Figure 9.9 Roughness Reynolds number, k^+ , on the rough flat plate with the towing speed of $V = 4.5$ m/s, obtained from the flat plate simulation in Chapter 5.

9.4. New prediction method for heterogeneous hull roughness

In this study, a new prediction method was developed for the added resistance of a ship due to the heterogeneous hull roughness, based on the added resistance predictions obtained from the similarity law scaling of Granville (1958; 1978). This method considers the effect of different wetted surface areas of the individual regions with different hull roughness, while neglecting the effect of the different locations of the roughness.

The added frictional resistance of a ship, ΔC_F , with N different roughness regions is determined as

$$\Delta C_F = \sum_{i=1}^N \frac{WSA_i}{WSA_{ship}} \Delta C_{F,i} \quad (9.2)$$

where, WSA_i is the wetted surface area of the i^{th} region, WSA_{ship} is the total wetted surface area of the ship. $\Delta C_{F,i}$ is the added frictional resistance with the hull roughness in the i^{th} region obtained from the Granville's method, under the assumption of the homogeneous distribution of the given hull roughness. Details of Granville's similarity law scaling can be found in Chapter 4.2.4.

The frictional resistance of the ship with heterogeneous hull roughness, $C_{F,r}$, can be determined as

$$C_{F,r} = C_{F,s} + \Delta C_F \quad (9.3)$$

in which, $C_{F,s}$ is the frictional resistance coefficient of a smooth ship that can be obtained by using Kàrmàn-Schoenherr friction line (Schoenherr, 1932), as

$$\frac{0.242}{\sqrt{C_F}} = \log (Re_L C_F) \quad (9.4)$$

where, Re_L is the Reynolds number based on the length of the ship.

The obtained $C_{F,r}$ can be used to predict the total resistance coefficient, C_T , of a ship with heterogeneous hull roughness. In Chapter 4, it was concluded that the *3D method* predicts the total resistance more accurately than the *2D method*, since the hull roughness not only affects the skin friction but also increases the viscous pressure resistance, C_{VP} . Therefore, the *3D method* is used to predict the C_T of the Wigley model.

In the *3D method*, the total resistance for the rough model ship, $C_{T,r}$, is determined by

$$C_{T,r} = (1 + k)C_{F,r} + C_W \quad (9.5)$$

where, C_W is the wave-making resistance and k is the form factor of the ship.

9.4.1. Resistance prediction and comparison against EFD

Before predicting the frictional resistance of the Wigley model with different surface conditions using Equation 9.2, the frictional resistance of the sand grit surface was predicted first using the similarity law scaling. In Chapter 4, it was found that the sand grit surface (aluminium oxide abrasive powder) follow the Nikuradse-type roughness function model of Cebeci and Bradshaw (1977) when the reference roughness height, k , is set to $1.73Rt_{50}$, as shown in Figure 4.11. Therefore, the similarity law scaling was conducted using the roughness function model of Cebeci and Bradshaw (1977).

Figure 9.10 shows the C_F values of the Wigley hull with different surface conditions, predicted using the newly proposed method (Equation 9.2 and 9.3). In the figure, the

smooth type C_F values were calculated using the Kármán-Schoenherr friction line (Equation 9.4).

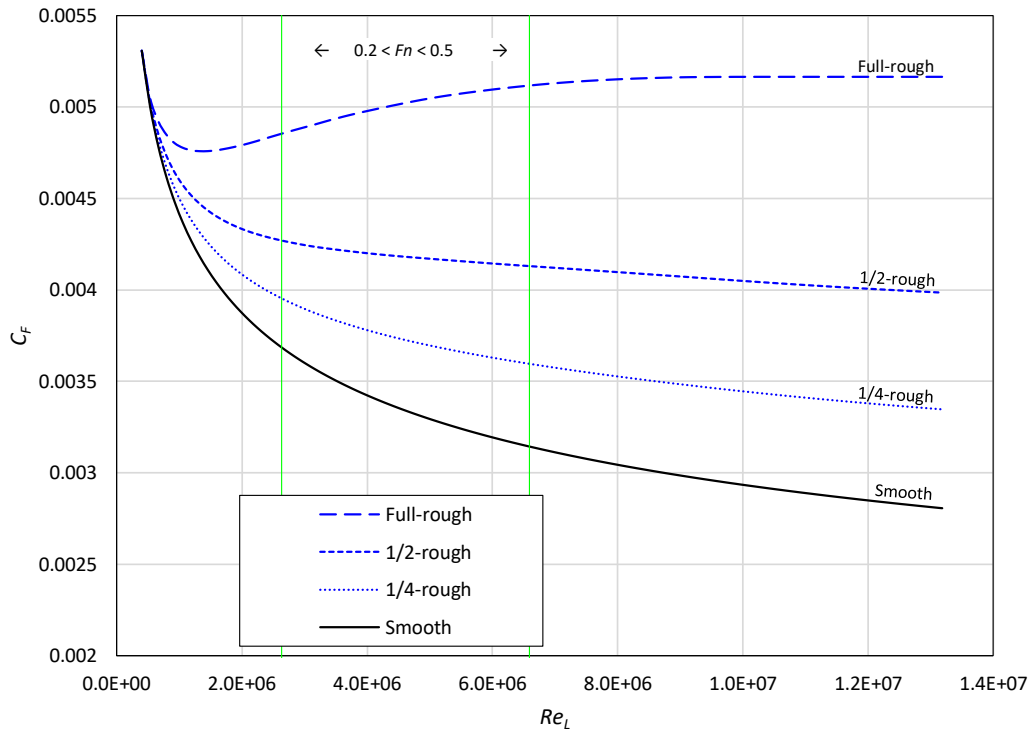


Figure 9.10 C_F predictions of the Wigley hull with different surface conditions

To calculate the C_T of the ship using the *3D method*, the form factor, k , and the wave-making resistance coefficient, C_W , values are needed (Equation 9.5). Unfortunately, the Prohaska's test could not be conducted in this study, as the result at low towing speed ($Fn < 0.2$) was unstable due to the absence of a turbulence stimulator. Alternatively, the form factor was obtained by reproducing the experimental data of Ju (1983), which used a similar length ($L=3.048$ m) of Wigley model with a similar water temperature (13 °C) as well as the same free trim and sinkage condition. As shown in Figure 9.11, the form factor value ($k=0.12$) was calculated using a regression line of the data at the low speed region ($Fn < 0.2$). Also, the potential-based C_W values for the Wigley hull with free trim and sinkage, determined by Chen et al. (2019), were used for the C_T prediction.

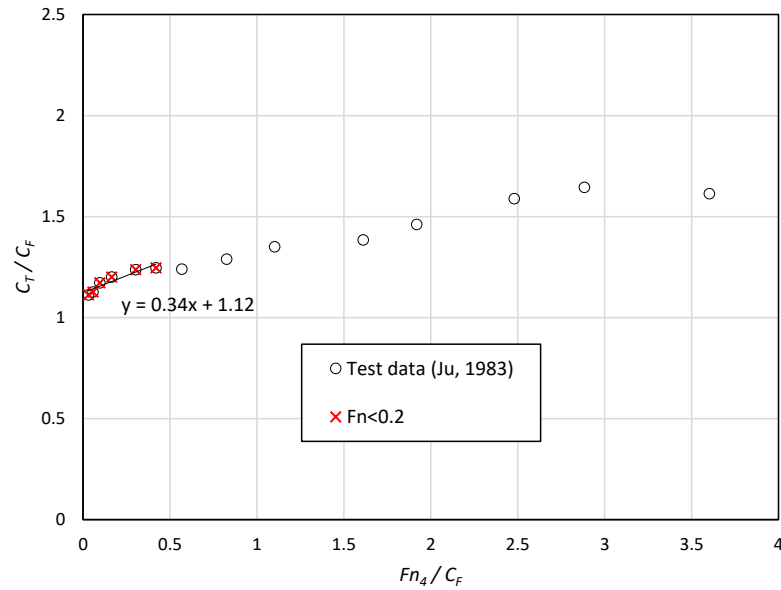


Figure 9.11 Form factor calculation based on the test data of Ju (1983)

Figure 9.12-9.14 show the C_T of the Wigley model obtained from the towing test and the predicted C_T values from the newly proposed method. The predicted C_T values show a reasonable agreement with the towing test results. As shown in Figure 9.12 and 9.13, the predicted C_T values of the heterogeneous hull conditions located mostly in between the bow-rough and aft-rough results of the experiment. This can be attributed to the fact that the newly proposed prediction method does not consider the effect of different locations of the hull roughness, while it considers the effect of the different wetted surface areas of the individual roughness regions. On the other hand, the prediction for the full-rough condition shows a fair agreement with the towing test as shown in Figure 9.14. It is of note that this new prediction method does not differ from the conventional Granville's approach for a homogeneously distributed hull roughness (e.g. full-rough condition in Figure 9.14).

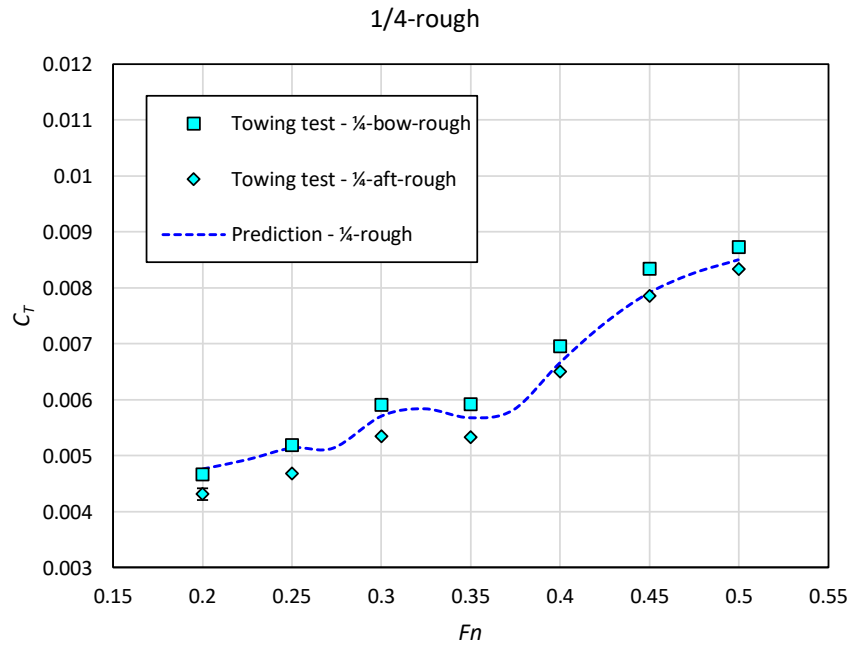


Figure 9.12 C_T values from the towing test and the predictions for the Wigley model with $1/4$ -rough condition

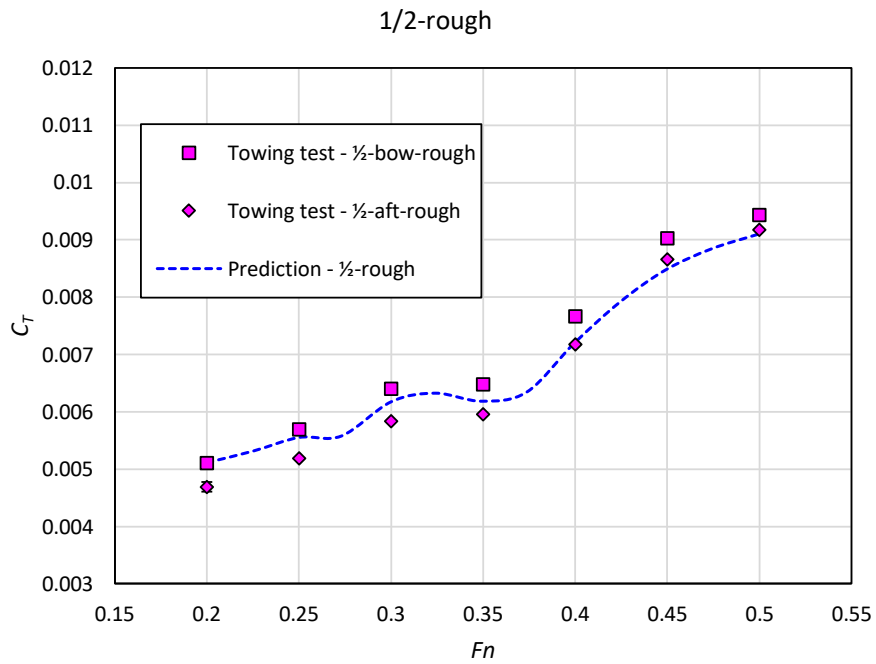


Figure 9.13 C_T values from the towing test and the predictions for the Wigley model with $1/2$ -rough condition

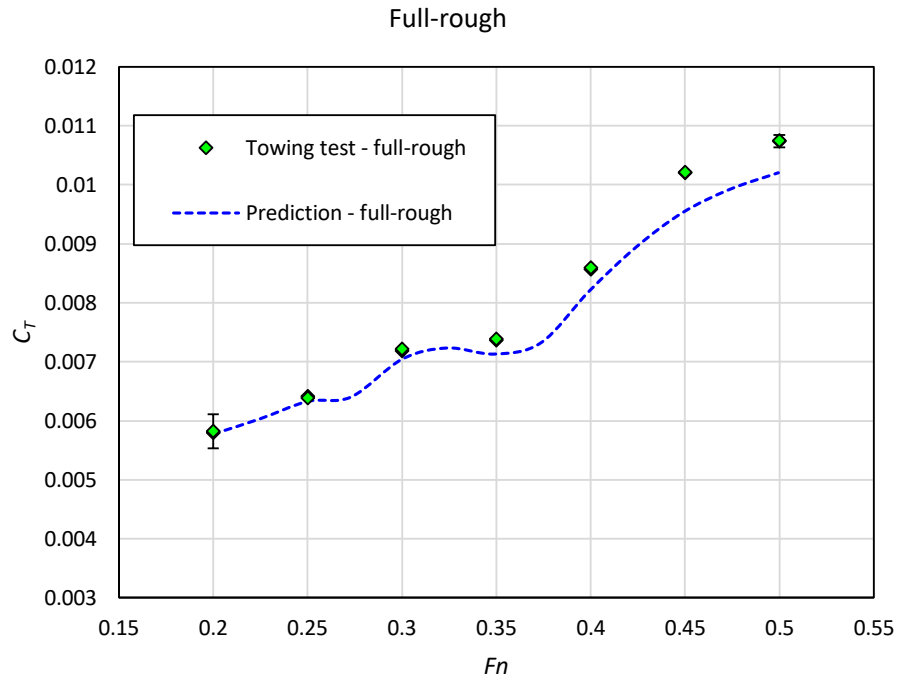


Figure 9.14 C_T values from the towing test and the predictions for the Wigley model with full-rough condition

9.5. Chapter summary and conclusions

In this chapter, towing tests were conducted involving a Wigley hull model with different hull roughness conditions, including the heterogeneous hull conditions (i.e. $\frac{1}{4}$ -bow-rough, $\frac{1}{4}$ -aft-rough, $\frac{1}{2}$ -bow-rough and $\frac{1}{2}$ -aft-rough conditions) and the homogeneous hull conditions (i.e. smooth and full-rough conditions). The bow-rough conditions (i.e. $\frac{1}{4}$ -bow-rough and $\frac{1}{2}$ -bow-rough) showed larger added resistance compared to the aft-rough conditions ($\frac{1}{4}$ -aft-rough and $\frac{1}{2}$ -aft-rough) with the same wetted surface area of the roughness region. This suggests that the hull roughness of the front part of the ship results in more added resistance than the hull roughness in other regions. The rationale behind this difference was discussed with an example of a CFD simulation conducted in our previous study.

A new method was proposed to predict the effect of heterogeneous hull roughness on ship resistance, based on the similarity law scaling. This method considers the different

wetted surface areas of the different roughness regions, while neglecting the location of the hull roughness. The results predicted using the newly proposed method showed a fair agreement with the towing test results. Considering that the heterogeneous roughness conditions used in this study are rather extreme (i.e. sudden changes in the hull roughness from a smooth surface to a remarkably rough surface), the newly proposed method could bring more reasonable predictions for real ship cases with milder heterogeneous distributions of hull roughness.

This study presents a useful investigation into the effect of heterogeneous hull roughness, suggesting that the hull roughness in different locations can bring different roughness effects on the ship resistance. For better understanding regarding this new observation, the study should be extended using CFD simulations, which will enable us to investigate the flow characteristics around the heterogeneous hull roughness. Another recommended future work is case studies to predict the added resistance due to heterogeneous hull roughness using CFD simulations and the newly proposed prediction method, to examine the agreement between these low and high-fidelity methods.

10. Fouling effect on resistance of different ship types

10.1. Introduction

In Chapter 6, the effect of hull fouling on the full-scale ship hydrodynamic characteristics has been investigated. A notable finding is that the hull roughness does not affect only the ship frictional resistance but also it affects the other resistance components, e.g. the viscous pressure resistance and wave making resistance. However, these findings cannot be generalised as the study was conducted only for a single type of hull form (KCS). Considering that the ship hydrodynamic behaviours vary with different ship types and dimensions, the roughness effect can also vary with different ships. In this context, it is worth examining the roughness effect on the resistance of different ships.

To the best of the author's knowledge, there exists no specific study investigating the roughness effect on the ship resistance of different hull forms with different scales and speeds. Therefore, the aim of this study is to fill this gap by performing a systematic series of CFD simulations of different hull forms in different scales and speeds. In this study, Unsteady Reynolds Averaged Navier-Stokes (URANS) based ship models of a container ship and a tanker were developed. Each vessel was modelled in three different scales, namely model-scale, moderate-scale and full-scale. The modified wall-function approach was used with the roughness function of barnacles as used in Chapter 6-8. The simulations of each vessel and each scale were performed with a range of speeds. Finally, the effect of biofouling on ship resistance components, form factor and flow characteristics around the hulls were investigated.

This chapter is organised as follows: The methodology used in this chapter is explained in Section 10.2.1 while Section 10.2.2 covers brief information regarding the modified wall-function approach for barnacle fouling. The details of the numerical modelling is

discussed in Section 10.2.3, including the mathematical formulations, geometry and boundary conditions as well as the mesh generation. The verification study and the numerical uncertainties are presented in Section 10.3.1, while the roughness effect on the resistance components are discussed in Section 10.3.2 and 10.3.3, based on the results of the double-body and free-surface simulations, respectively. The roughness effect on the flow characteristics around the KCS and KVLCC2 hulls in different scales are presented in Section 10.3.4. Finally, chapter summary and conclusions are presented in Section 10.4.

10.2. Methodology

10.2.1. Approach

A schematic illustration of the current study is shown in Figure 9.1. As used in Chapter 6 – 8, the same modified wall-function approach was used to represent the barnacles on the hulls. In order to investigate the differences due to the hull forms, the KRISO Containership (KCS) and the KRISO Tanker (KVLCC2) were modelled in three different scales (i.e. model-scale, moderate-scale, and full-scale). The CFD simulations of each vessel and each scale were performed with a range of speeds to investigate the differences in the fouling effect on the different hull forms, scales and speeds.

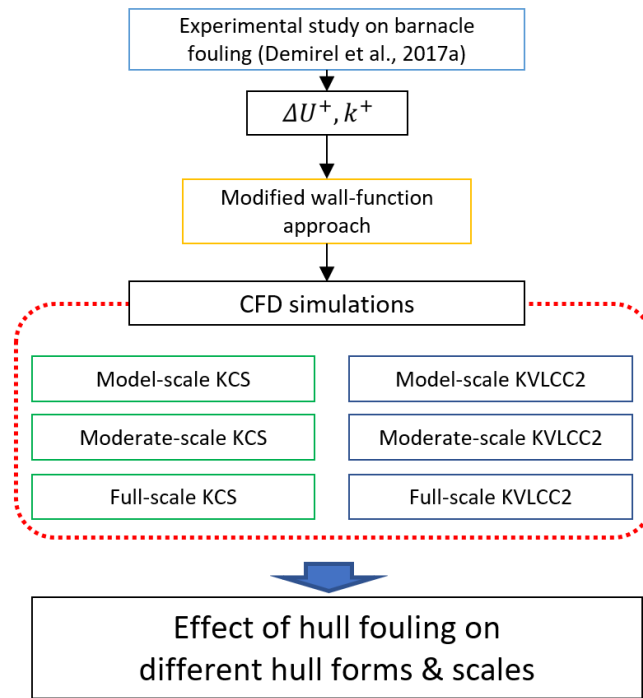


Figure 10.1 Schematic illustration of the methodology in Chapter 10

10.2.2. Modified wall-function approach for barnacle fouling

As mentioned earlier, the same modified wall-function approach with the roughness function of barnacles (Demirel et al., 2017a) was used as in Chapter 6 – 8. Further details regarding the modified wall-function approach and the roughness function of the barnacle surfaces can be found in Section 5.2.3 and Section 6.2.2, respectively.

10.2.3. Numerical modelling

10.2.3.1. Mathematical formulations

The CFD models were developed based on the unsteady Reynolds-averaged Navier-Stokes (URANS) method using a commercial CFD software package, STAR-CCM+ (version 13.06). The mathematical formulations are identical to those used in Chapter 5. The details can be found in Section 5.2.2.

10.2.3.2. Geometry and boundary conditions

In order to investigate the effect of biofouling on different ships, the benchmark ship hulls of a container ship (KCS) and a tanker (KVLCC2) were used for the CFD simulations. Figures 10.2 and 10.3 show the hull geometries of KCS and KVLCC2, respectively, while Tables 10.1 and 10.2 depict the principal particulars of these vessels. As shown in the figures and the tables, KCS represents a fast container ship with a sharp bow-shape, a slender hull form and a relatively shallow draught (i.e. $C_B=0.65$, $F_n=0.26$, $L_{PP}/T=21.30$), whereas KVLCC2 represents a slow tanker with a fuller bow-shape and hull form and a relatively deep draught (i.e. $C_B=0.81$, $F_n=0.14$, $L_{PP}/T=15.38$).

Table 10.3 shows the simulation cases used in this study. Each vessel was modelled in two different computational domain types, namely double-body and free-surface models, for the purpose of decomposing the resistance components. In a double-body simulation, the free surface is replaced by the symmetry boundary condition such that there is no wave-making behaviour and hence there exist only the viscous resistance (i.e. $R_T = R_V = R_F + R_{VP}$). On the other hand, the free-surface simulations have the free surface and hence consider the wave-making behaviours such that the wave making resistance is included in the total ship resistance (i.e. $R_T = R_F + R_{VP} + R_W$). The double-body simulations were modelled in three different scales (i.e. model-scale, moderate-scale, and full-scale) while the free-surface simulations were modelled only in the full-scales of the vessels, due to limited time and computational power. In order

to examine the effect of different ship speeds, the simulations were conducted at Froude number ranges of 0.130 – 0.282 for KCS and 0.083 – 0.156 for KVLCC2, at each scale.

Figures 10.4 and 10.5 illustrate the computational domain and the boundary conditions of the double-body and free-surface simulations of KCS and KVLCC2, respectively. In terms of the free-surface simulations, the velocity inlet and the pressure outlet boundary conditions were applied for the opposite faces in the longitudinal direction. The top and bottom far field boundaries were defined as velocity inlet while symmetry boundary conditions were used for the vertical centre and side wall boundaries as similarly used by Terziev et al. (2019a). The surface boundary conditions of the hull and rudder were defined as no-slip walls. For the smooth surface condition, the smooth type wall-function was used, whereas the rough type roughness-functions, including the additional term of the roughness function were used for the fouling cases. The difference for the double-body simulations is that the $z = 0$ plane is replaced with a symmetry plane such the simulation does not have the free surface. It is of note that all the simulations were conducted in fixed conditions (i.e. no sink or trim motions were allowed).



Figure 10.2 Geometry of KCS hull with a rudder



Figure 10.3 Geometry of KVLCC2 hull with a rudder

Table 10.1 Principal particulars and conditions of the KCS simulations, adapted from Kim et al. (2001) and Larsson et al. (2013)

Main particulars	Full-scale	Moderate-scale	Model-scale
Scale factor, λ	1	10	31.6
Length between the perpendiculars, L_{PP} (m)	230	23	7.278
Length of waterline, L_{WL} (m)	232.5	23.25	7.358
Beam at waterline, B_{WL} (m)	32.2	3.22	1.019
Depth, D (m)	19	1.9	0.601
Design draft, T (m)	10.8	1.08	0.342
Length-depth ratio, L_{PP}/T	21.30	21.30	21.30
Wetted surface area with a rudder, S (m ²)	9539	95.39	9.553
Displacement, ∇ (m ³)	52030	52.03	1.649
Block coefficient, C_B	0.6505	0.6505	0.6505
Design speed, V (m/s)	12.3456	3.904	2.196
Froude number at the design speed, F_n	0.26	0.26	0.26
Speed range used in simulations, V (m/s)	6.17-13.37	1.95-4.23	1.10-2.38

Table 10.2 Principal particulars and conditions of the KVLCC2 simulations, adapted from Kim et al. (2001) and Larsson et al. (2013)

Main particulars	Full-scale	Moderate-scale	Model-scale
Scale factor, λ	1	10	58
Length between the perpendiculars, L_{PP} (m)	320	32	5.517
Length of waterline, L_{WL} (m)	325.5	32.55	5.612
Beam at waterline, B_{WL} (m)	58	5.8	1.000
Depth, D (m)	30	3	0.517
Design draft, T (m)	20.8	2.08	0.359
Length-depth ratio, L_{PP}/T	15.38	15.38	15.38
Wetted surface area with a rudder, S (m ²)	27467.3	274.673	8.165
Displacement, ∇ (m ³)	312622	312.622	1.602
Block coefficient, C_B	0.8098	0.8098	0.8098
Design speed, V (m/s)	7.9732	2.521	1.047
Froude number at the design speed, F_n	0.142	0.142	0.142
Speed range used in simulations, V (m/s)	4.63-8.74	0.86-1.62	0.61-1.14

Table 10.3 Simulation cases

		Double-body	Double-body	Double-body	Free-surface
		Full-scale	Moderate-scale	Model-scale	Full-scale
KCS	Scale factor, λ	1	10	31.6	1
	Speed range, V (m/s)	6.17-13.37	1.95-4.23	1.10-2.38	6.17-13.37
	F_n range	0.13-0.282	0.13-0.282	0.13-0.282	0.13-0.282
	Re_L range	$1.2-2.7 \times 10^9$	$3.9-8.5 \times 10^7$	$0.7-1.5 \times 10^7$	$1.2-2.7 \times 10^9$
	Surface conditions	Smooth, S20%, M20%, B20%			
KVLCC2	Scale factor, λ	1	10	58	1
	Speed range, V (m/s)	4.63-8.74	0.86-1.62	0.61-1.14	4.63-8.74
	F_n range	0.083-0.156	0.083-0.156	0.083-0.156	0.083-0.156
	Re_L range	$1.2-2.2 \times 10^9$	$3.7-7.1 \times 10^7$	$2.6-5.1 \times 10^6$	$1.2-2.2 \times 10^9$
	Surface conditions	Smooth, S20%, M20%, B20%			

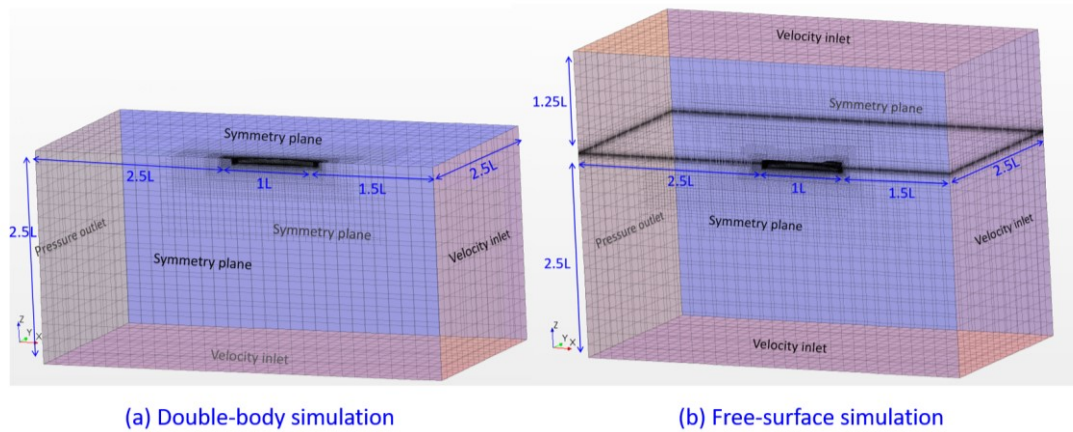


Figure 10.4 Computational domain and the boundary conditions of KCS simulations

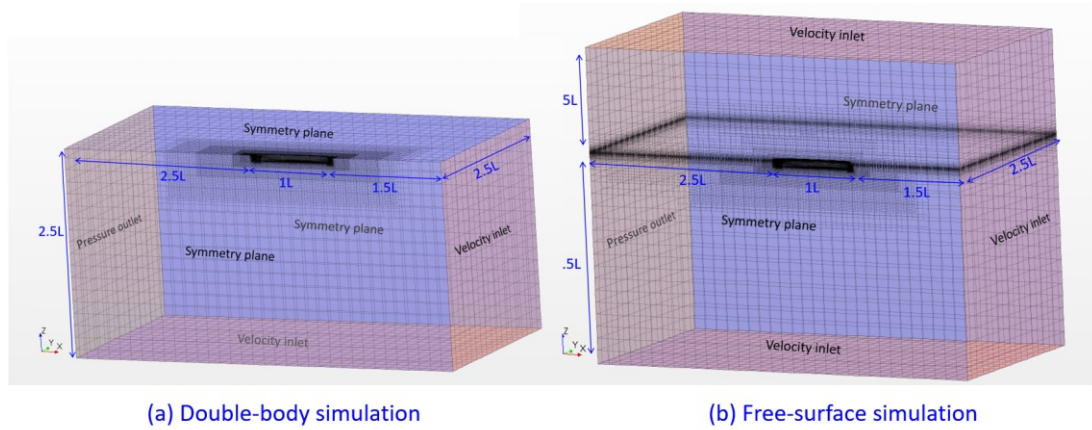


Figure 10.5 Computational domain and the boundary conditions of KVLCC2 simulations

10.2.4. Mesh generation

Cut-cell grids with prism layer mesh on the walls were generated using the built-in meshing tool of STAR-CCM+ (version 13.06). Local refinements were made for finer grids in the critical regions, such as the bulbous bow, rudder, stern, and the region near the free surface (in case of the free-surface simulations), as shown in Figure 10.6. The thickness of the first layer cell on the surface was chosen such that the y^+ values are always higher than 30 and also higher than the k^+ values, as recommended by Demirel et al. (2017b), and Siemens (2019). It is of note that the same mesh was used for all the smooth and rough surface conditions, including the near wall refinement.

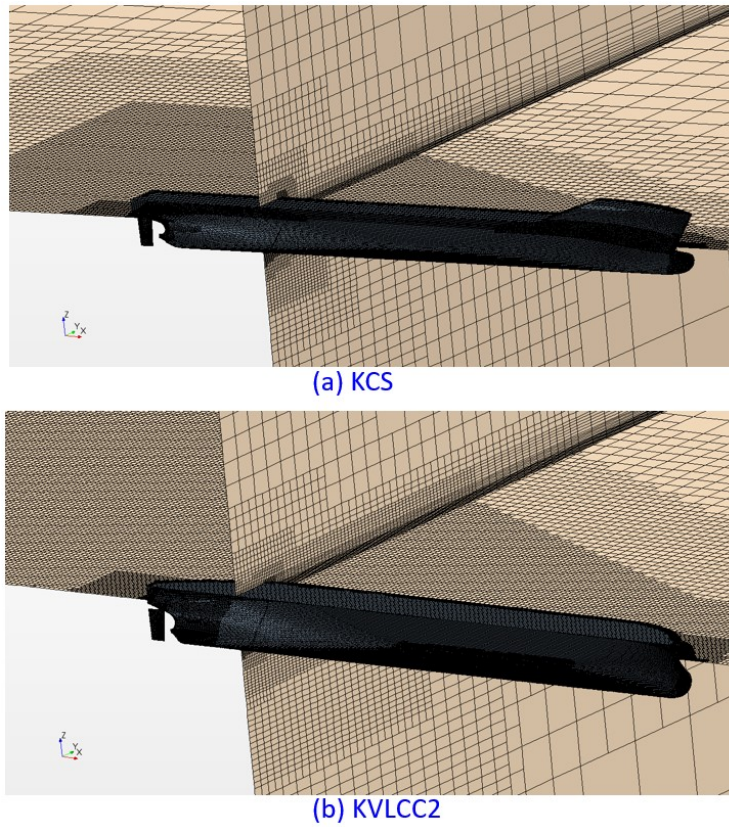


Figure 10.6 Mesh structure of the computational domain of KCS and KVLCC2 simulations (free-surface models)

10.3. Result

10.3.1. Verification study

In order to estimate the numerical uncertainties of the CFD models and also to determine the sufficient grid-spacings and the time-step size (Δt), a verification study was performed by conducting the simulations with three different resolutions of mesh and time steps, namely fine, medium and coarse. Then, the spatial and temporal uncertainties (U_{Grid} and $U_{\Delta t}$) were estimated using the Grid Convergence Index (GCI) method (Celik et al., 2008), as used in Chapter 5 – 8. Further details regarding the GCI method can be found in Section 5.2.7.

Tables 10.4 and 10.5 show the spatial and temporal uncertainties of the KCS and KVLCC simulations, obtained from the grid and time-step convergence study. The spatial and temporal uncertainties were calculated based on the fine mesh and the fine time-step for each case. In this study, the fine mesh and fine time step were used for each case.

Table 10.4 Spatial and temporal convergence study of the KCS simulations

	Double-body Full-scale ($\lambda=1$)		Double-body Moderate-scale ($\lambda=10$)		Double-body Model-scale ($\lambda=31.6$)		Free-surface Full-scale ($\lambda=1$)	
	No.Cells	R_V (N)	No.Cells	R_V (N)	No.Cells	R_V (N)	No.Cells	R_T (N)
Spatial convergence								
Coarse	524,829	591,515	435,628	878.15	229,144	36.083	1,005,230	768,434.74
Medium	695,031	581,901	596,259	875.50	316,815	35.978	1,407,062	767,334.76
Fine	963,216	578,655	815,837	870.96	479,982	35.954	2,019,668	765,293.29
U_{Grid} (Fine)		0.246%		0.909%		0.013%		0.481%
Temporal convergence	Δt (s)	R_V (N)	Δt (s)	R_V (N)	Δt (s)	R_V (N)	Δt (s)	R_T (N)
Coarse	0.04	577,156	0.04	870.55	0.04	35.947	0.04	766,944.79
Medium	0.02	577,717	0.02	870.66	0.02	35.948	0.02	765,097.03
Fine	0.01	578,655	0.01	870.96	0.01	35.954	0.01	765,293.29
$U_{\Delta t}$ (Fine)		0.302%		0.023%		0.005%		0.036%
U_{total}		0.389%		0.909%		0.014%		0.483%

Table 10.5 Spatial and temporal convergence study of KVLCC2 simulations

	Double-body Full-scale ($\lambda=1$)		Double-body Moderate-scale ($\lambda=10$)		Double-body Model-scale ($\lambda=31.6$)		Free-surface Full-scale ($\lambda=1$)	
	No.Cells	R_V (N)	No.Cells	R_V (N)	No.Cells	R_V (N)	No.Cells	R_T (N)
Spatial convergence								
Coarse	712,288	782,485	598,405	1,192.16	578,599	9.289	1,525,249	803,512.69
Medium	1,068,217	775,411	917,246	1,189.64	800,617	9.269	2,267,933	800,629.00
Fine	1,571,155	772,577	1,371,184	1,188.14	1,104,198	9.259	3,543,146	788,229.32
U_{Grid} (Fine)		0.347%		0.283%		0.149%		0.781%
Temporal convergence	Δt (s)	R_V (N)	Δt (s)	R_V (N)	Δt (s)	R_V (N)	Δt (s)	R_T (N)
Coarse	0.08	771,365	0.08	1,188.23	0.04	9.259	0.08	801,500.37
Medium	0.04	771,774	0.04	1,188.09	0.02	9.258	0.04	788,930.44
Fine	0.02	772,577	0.02	1,188.14	0.01	9.259	0.02	788,446.66
$U_{\Delta t}$ (Fine)		0.135%		0.003%		0.001%		0.003%
U_{total}		0.373%		0.283%		0.149%		0.781%

10.3.2. Double-body simulations

10.3.2.1. Roughness effect on C_F and C_V

In order to investigate the roughness effect on the frictional resistance, C_F , and viscous resistance, C_V , the double-body simulations of KCS and KVLCC2 were performed. As mentioned earlier, the total resistance of the vessels calculated in the double-body simulations is assumed to be equal to the viscous resistance (i.e. $C_T = C_V$), while C_F is calculated by simply considering the shear force only in the simulations.

Figures 10.7 and 10.8 show the C_F and C_V values obtained from the KCS and KVLCC2 simulations, respectively, in different surface conditions (Smooth, S20%, M20% and B20%). As shown in the figures, the C_F and C_V values increase significantly due to the hull fouling. For the KCS cases, the percentage increase in the frictional resistance, $\% \Delta C_F$, with the most severe fouling condition (B20%) are up to

93%, 89%, and 86%, at the model, moderate, and full-scales, respectively. And those of KVLCC2 are 79%, 74%, and 69%. One can notice that the $\% \Delta C_F$ values are larger for KCS than KVLCC2, while these values become smaller as the ship length increases. This can be explained by two factors; the relative roughness height, k/L , and the roughness Reynolds number, $k^+ = kU_\tau/\nu$, where, k , U_τ and ν are the roughness height, friction velocity, and the kinematic viscosity, respectively. It is a well-known fact that the skin friction over a rough wall increases with the k/L values (Moody, 1944; Demirel et al., 2019). Therefore, even with the same fouling condition, the roughness effect on C_F is stronger for smaller vessels due to the larger k/L ratios.

On the other hand, considering the significant changes in ship lengths, the changes in $\% \Delta C_F$ with scale are relatively small. For example, while the ship length of KVLCC2 increases 58 times (i.e. the k/L ratio becomes 58 times smaller), the $\% \Delta C_F$ reduces by 10% only. This can be attributed to the fact that the k^+ values increase due to the increasing ship speeds with the scale at the same Fn . Therefore, higher k^+ values result in stronger roughness effects in the turbulent boundary layer, which diminishes the decreasing trends of $\% \Delta C_F$ due to the rapid changes in the k/L ratio. Figure 10.9 compares the k^+ values on the hull of KCS and KVLCC2 at their design speed (constant Fn) with the B20% fouling condition. The k^+ values appear to be higher with larger scales and also higher for KCS due to the higher speeds.

When it comes to the viscous resistance, C_V , similar trends were observed. For the KCS cases, the percentage increase in the viscous resistance, $\% \Delta C_V$, due to the most severe fouling condition (B20%) are up to 88%, 87%, and 84%, at the model, moderate, and full-scales, respectively. And those of KVLCC2 are 78%, 74%, and 71%. It can be also found that the differences between C_V and C_F are larger for KVLCC2 than KCS (including the smooth surface condition), which signifies larger viscous pressure resistance, C_{VP} , and hence larger form factor values, $1 + k$.

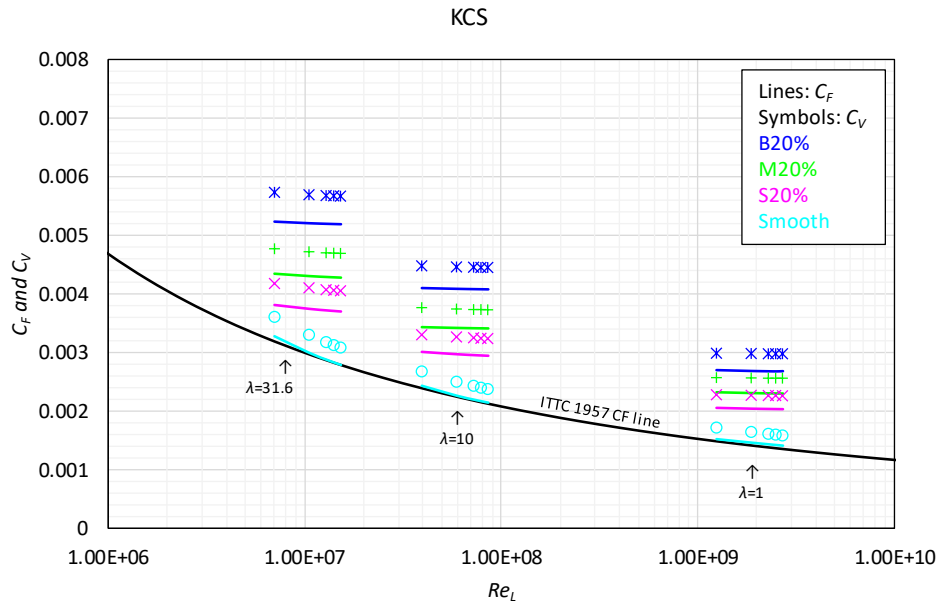


Figure 10.7 C_F and C_V of KCS with different hull conditions at model ($\lambda=31.6$), moderate ($\lambda=10$) and full-scale ($\lambda=1$)

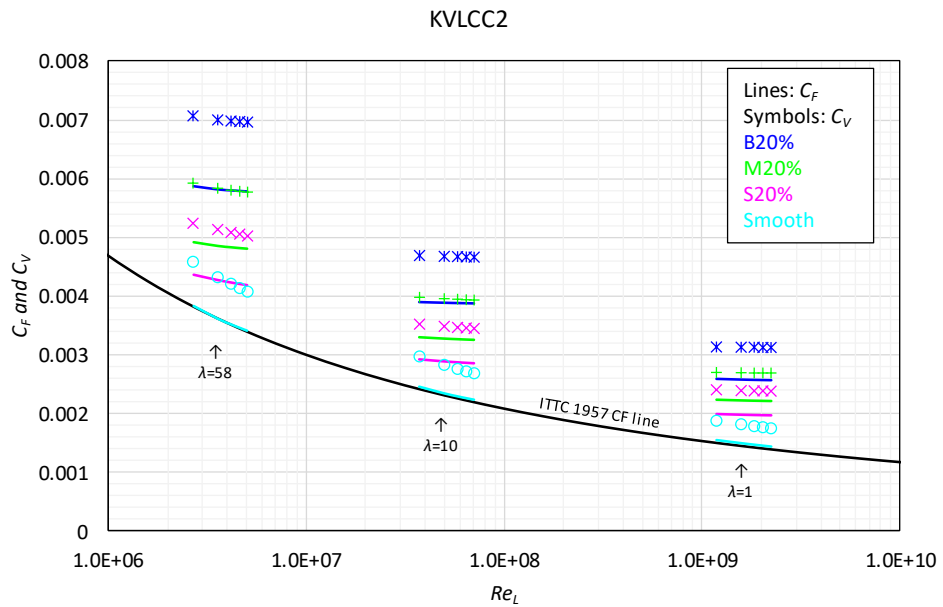


Figure 10.8 C_F and C_V of KVLCC2 with different hull conditions at model ($\lambda=58$), moderate ($\lambda=10$) and full-scale ($\lambda=1$)

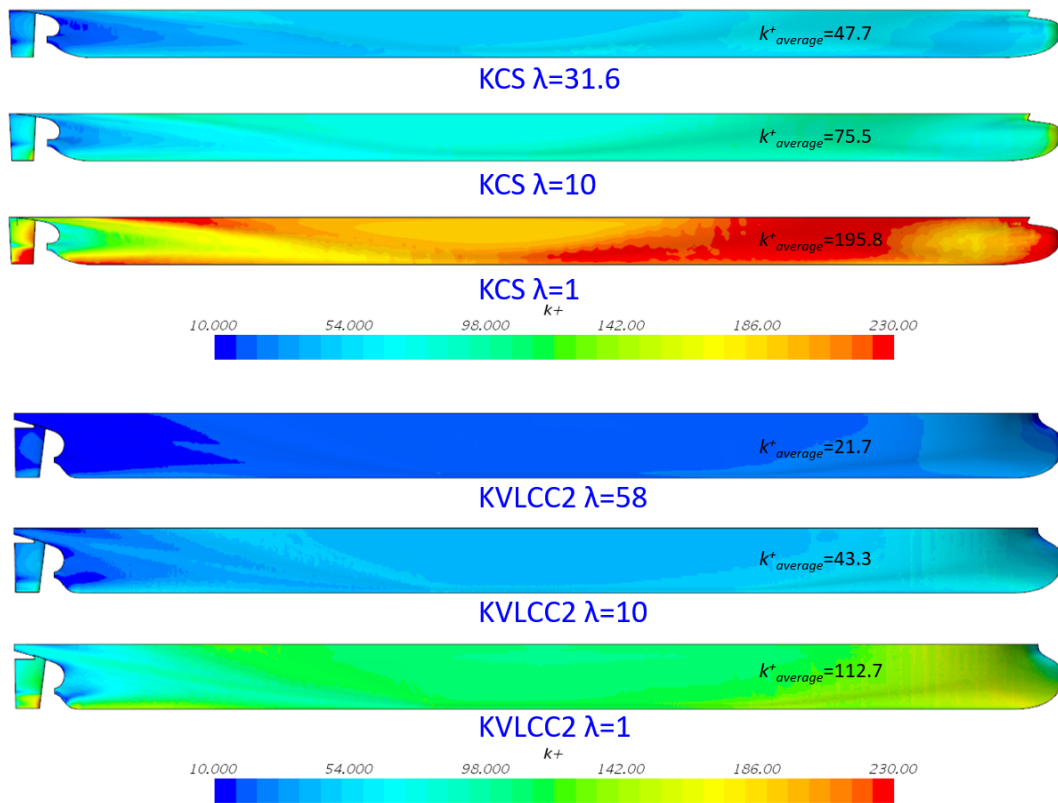


Figure 10.9 k^+ on the hulls of KCS and KVLCC2 with B20% fouling condition

10.3.2.2. Roughness effect on form factor, $1 + k$

Figure 10.10 compares the form factors, $1 + k$, of KCS and KVLCC2 with the different surface conditions. The $1 + k$ values were calculated using the C_F and C_V values obtained from the double-body simulations, as $1 + k = C_V/C_F$. As shown in the figure, the roughness effect of barnacles on the $1 + k$ values showed different trends for KCS and KVLCC2. For the KCS cases, the $1 + k$ values decrease due to hull fouling and these decreases become more significant as the hull size increases. The reduction in the form factor implies that the increase due to hull fouling is more significant for C_F than C_{VP} .

On the other hand, differences were found in the KVLCC2 cases. The roughness effect on the $1 + k$ values of KVLCC2 showed a different trend at each scale. In the model-scale ($\lambda=58$), the $1 + k$ values increase with the presence of hull fouling. The

roughness effect on $1 + k$ become minor at the moderate-scale ($\lambda=10$) and finally the $1 + k$ values decrease at the full-scale ($\lambda=58$). These different trends indicate that the roughness effect of C_{VP} is more significant than that of C_F at small scales but the effect of C_F becomes dominant as the hull size increases, which agrees with the KCS cases.

These differences in the roughness effect on the form factors can be more clearly seen in Figure 10.11 which compares the percentage increase in the frictional and viscous pressure resistance components, $\% \Delta C_F$ and $\% \Delta C_{VP}$. The $y = x$ line was drawn together for comparison, which indicates that $\% \Delta C_F$ and $\% \Delta C_{VP}$ are equal along the line. For KCS, the results shown in Figure 10 are located under the $y = x$ line, which means that the roughness effect of C_F dominates to that of C_{VP} . And the results move to the right-bottom side as the scale increases suggesting that this dominance becomes stronger with larger hull sizes. When it comes to the KVLCC2 case, the results for the model-scale ($\lambda=58$) simulation are found above the $y = x$ line, showing the dominance of the roughness effect of C_{VP} over C_F . But these results move to the right-bottom side of the graph as the scale increases, similarly to the KCS case. The general trend in these differences can be summarised that as the scale increases, the roughness effect of C_F becomes more important than that of C_{VP} for both the vessels.

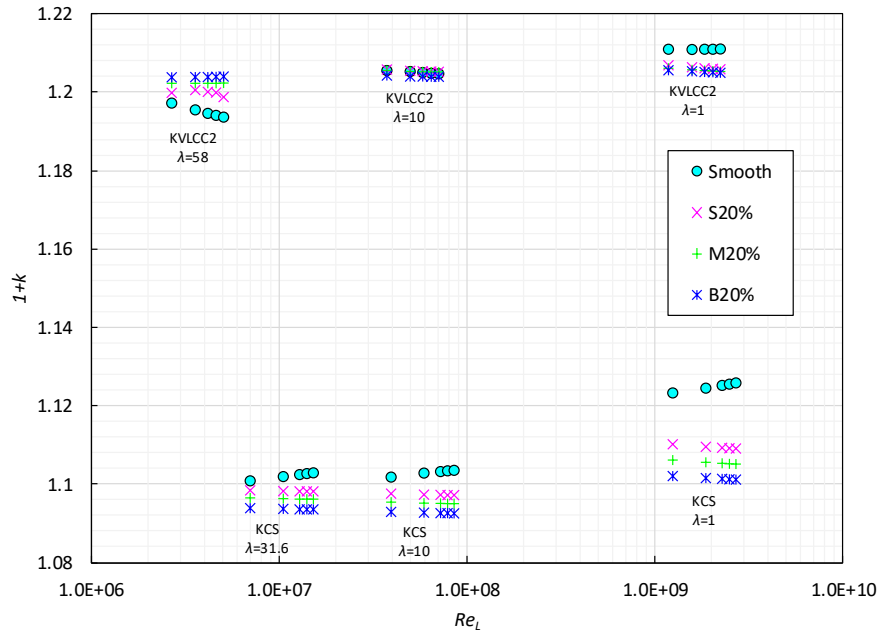


Figure 10.10 $1+k$ of KCS and KVLCC2 for different surface conditions

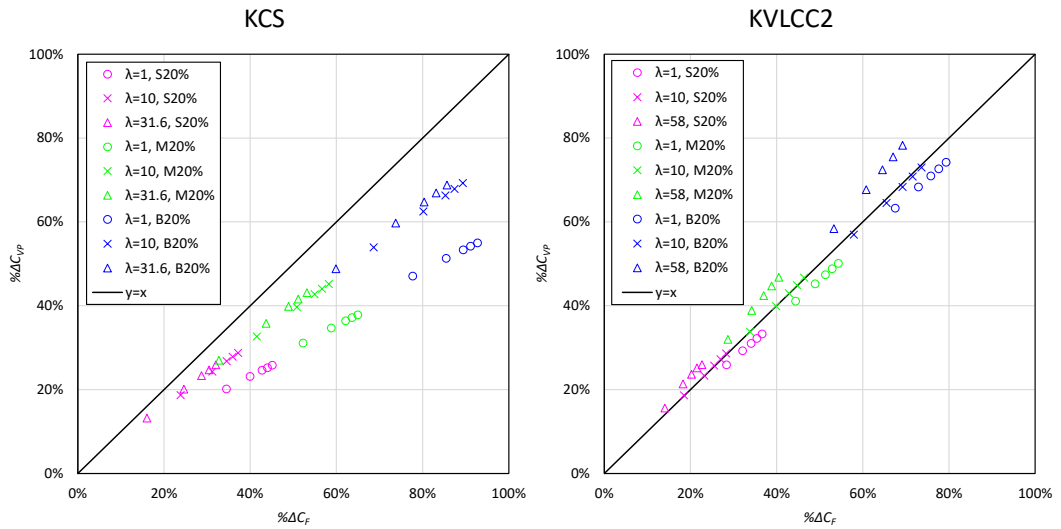


Figure 10.11 $\% \Delta C_F$ vs $\% \Delta C_{VP}$ due to the fouling conditions of KCS (left) and KVLCC2 (right)

10.3.3. Free-surface simulations

10.3.3.1. Roughness effect on C_T

In order to investigate the roughness effect on the total resistance, C_T , free-surface simulations of KCS and KVLCC2 were conducted with varying speeds for the smooth and fouling (S20%, M20%, B20%) surface conditions. As mentioned earlier, these free-surface simulations were conducted in the full-scale only due to the limited time and computational power. Figure 10.12 and 10.13 show the C_T values of KCS and KVLCC2, respectively, with and without the presence of hull fouling. Significant increases in C_T were recorded for both the ships. The percentage increases, $\% \Delta C_T$ due to the most severe fouling condition (B20%) for KCS and KVLCC2 were up to 66% and 78%. It is interesting to note that the KVLCC2 case shows higher $\% \Delta C_T$ values although they have smaller $\% \Delta C_F$ as shown in section 4.2. This can be explained by the fact that KVLCC2 has a higher contribution of the frictional resistance in the total resistance than KCS due to slower speed (lower Fn).

Another interesting feature to note is that the $\% \Delta C_T$ values of KCS show a decreasing trend with the ship speed while those of KVLCC2 show the opposite. In order to find the rationale behind these differences, the total resistance components were divided into different components and discussed in the following sections.

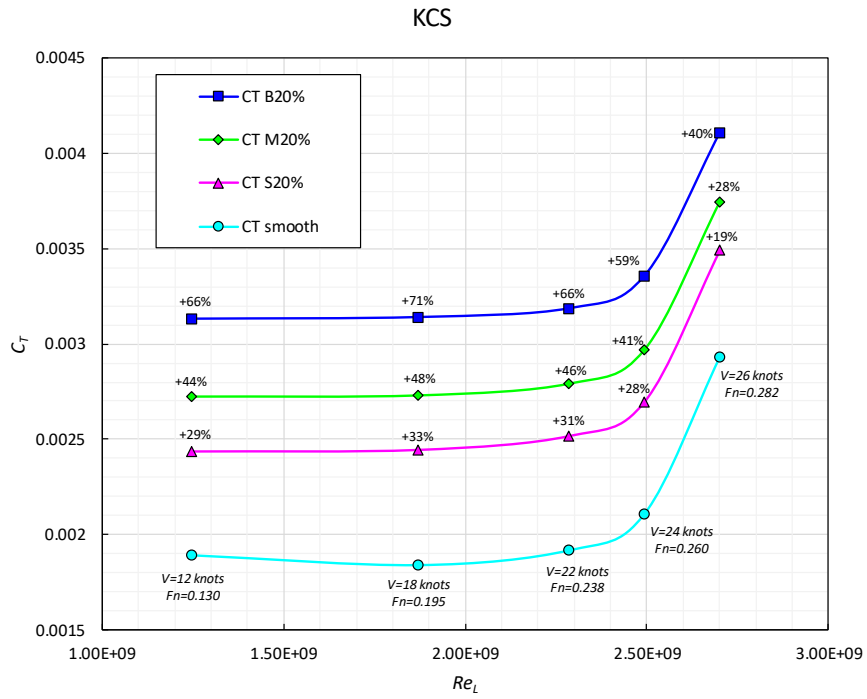


Figure 10.12 C_T of KCS with different hull conditions

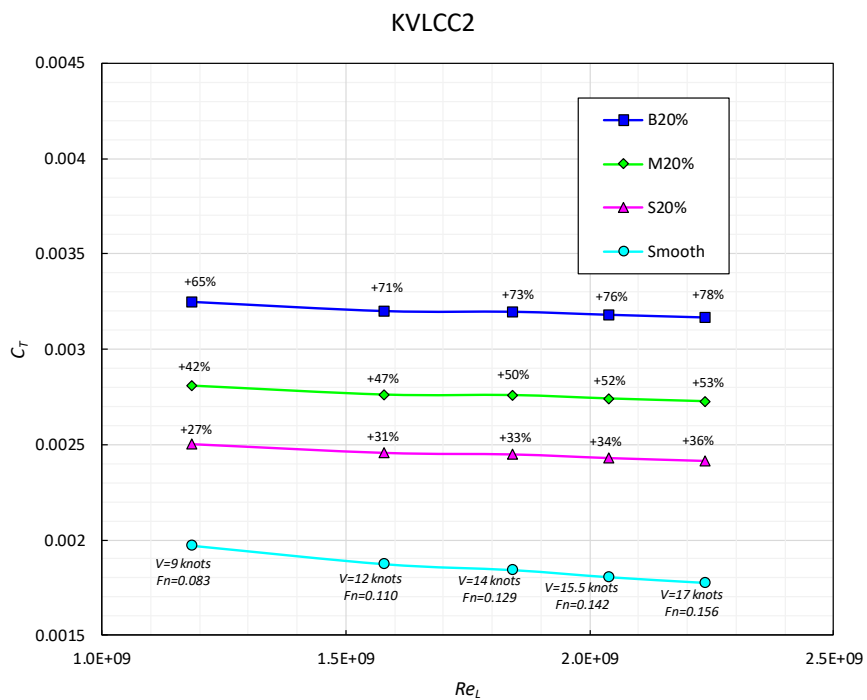


Figure 10.13 C_T of KVLCC2 with different hull conditions

10.3.3.2. Roughness effect on C_F and C_R

The total resistance coefficients, C_T , were decomposed into the frictional resistance coefficients, C_F , and the residuary resistance coefficients, C_R , by simply dividing the total drag acting on the ship into the shear and pressure force components. Figures 10.14 and 10.15 show the C_F and C_R values of the full-scale KCS and KVLCC2 models, respectively, in the smooth and fouled (S20%, M20%, B20%) hull conditions. It is of note that the C_F values in Figures 10.14 and 10.15 are from the free-surface simulations and these values can be slightly different ($\sim 1\%$) from the C_F values of the double-body simulations (Figure 10.7 and 10.8) mainly because of the changes in the wetted surface area due to free surface elevations.

Both the KCS and KVLCC2 simulations showed significant increases in C_F due to the hull fouling as already observed in Figure 10.7 and 10.8, while some differences were observed on C_R of KCS and KVLCC2. The C_R values of KVLCC2 show significant increases due to the hull fouling and these increases are consistent with the varying speeds. On the other hand, the C_R values of KCS showed relatively small increases with hull fouling at low speed. These increases become smaller as the speed increases and eventually turn into decreases at higher speeds. Together with this feature, the increasing dominance of C_R in C_T for the KCS case can be related to the decreasing $\% \Delta C_T$ values of KCS as the speed increases as shown in Figure 10.12.

In order to understand the rationale of the changing trends of the roughness effect on C_R , the residuary resistance values were further decomposed into the viscous pressure resistance, C_{VP} , and the wave making resistance, C_W and discussed in the following section.

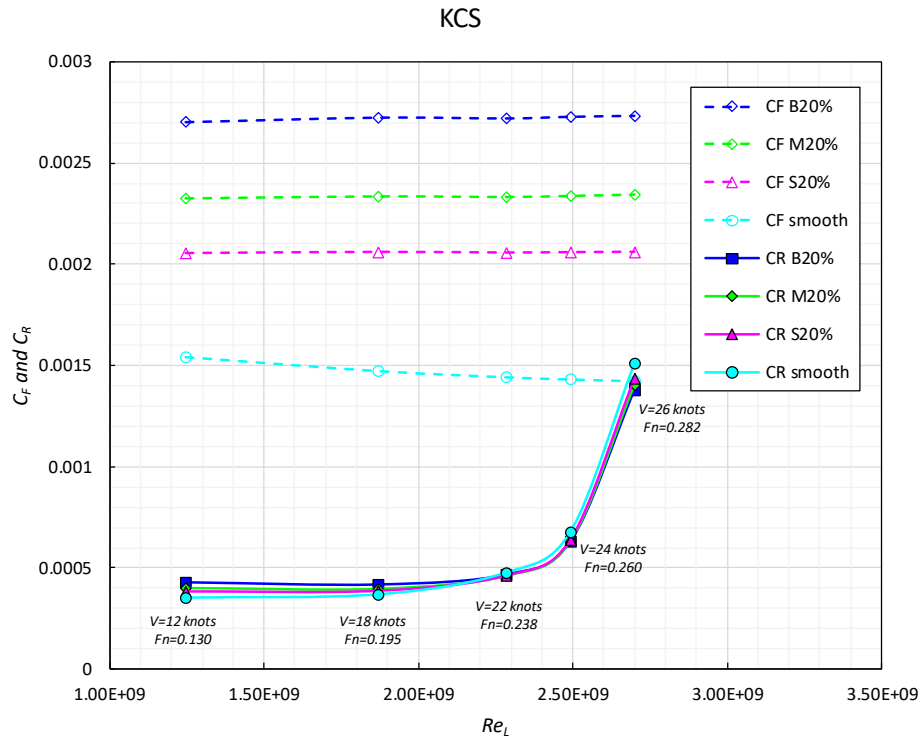


Figure 10.14 C_T of KCS with different hull conditions

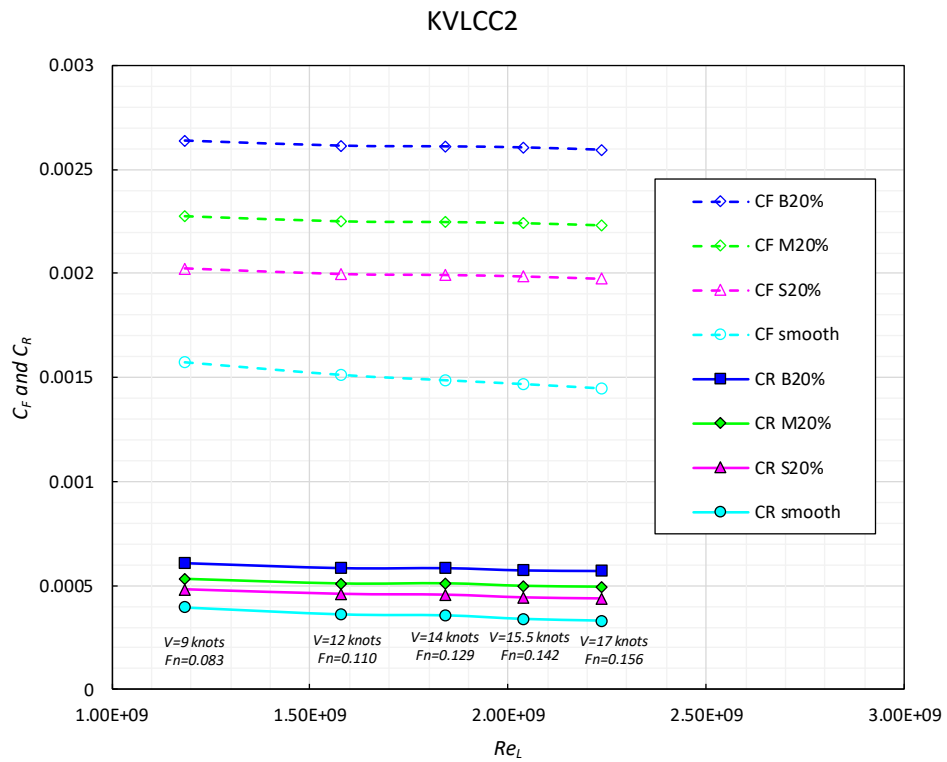


Figure 10.15 C_T of KVLCC2 with different hull conditions

10.3.3.3. Roughness effect on C_{VP} and C_W

The C_R values were decomposed into C_{VP} and C_W using the form factor values obtained from the double-body simulations as

$$C_{VP} = kC_F \quad (10.1)$$

$$C_W = C_R - C_{VP} \quad (10.2)$$

Figures 10.16 and 10.17 show the C_{VP} and C_W values of KCS and KVLCC2, respectively, with the smooth and fouled (S20%, M20%, B20%) hull conditions. In terms of C_{VP} , both the KCS and KVLCC2 cases show significant increases due to the hull fouling. On the other hand, differences were found on C_W between the two hull types.

For the KCS case, the C_W values have relatively high contributions in C_R and these values increase sharply as the speed increases and eventually become dominant over C_{VP} . The roughness effect on the C_W values of KCS is negligible at the lowest speed but the effect becomes clear as the ship speed increases. The C_W values of KCS show decreases due to hull fouling and these decreases become larger as the dominance of C_W increases. Consequently, for the fouled KCS cases, the decreases in C_W cancel the increases in C_{VP} and eventually the C_R values start to increase at higher speeds.

On the other hand, the C_W values of KVLCC2 have minor contributions and remain rather consistent with the speed. Accordingly, for KVLCC2, the roughness effect on C_R follows the trend of C_{VP} . It is interesting that at the high speeds, the roughness effect causes increases in C_W unlike the KCS case. However, these changes in C_W are too small (i.e. $\Delta C_W / C_T < 0.5\%$) to draw any reliable conclusion on their effects, considering that the estimated numerical uncertainty of C_T of the free-surface KVLCC2 simulation is larger than these changes ($U_{\text{total}}=0.78\%$).

This observation suggests that the roughness effect on the wave making resistance can differ by the hull forms and also by the speed. These differences can be correlated with

many different factors (e.g. the block coefficient, and the Froude number, Fn). Further investigations with sufficient variations are required to understand better the correlations between these factors and the roughness effect on C_W

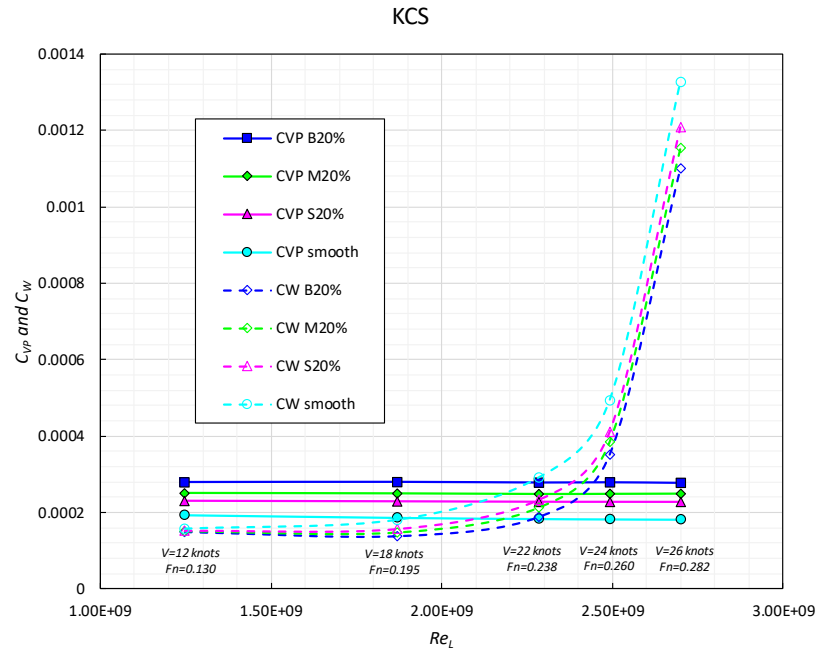


Figure 10.16 C_{VP} and C_W of KCS with different hull conditions

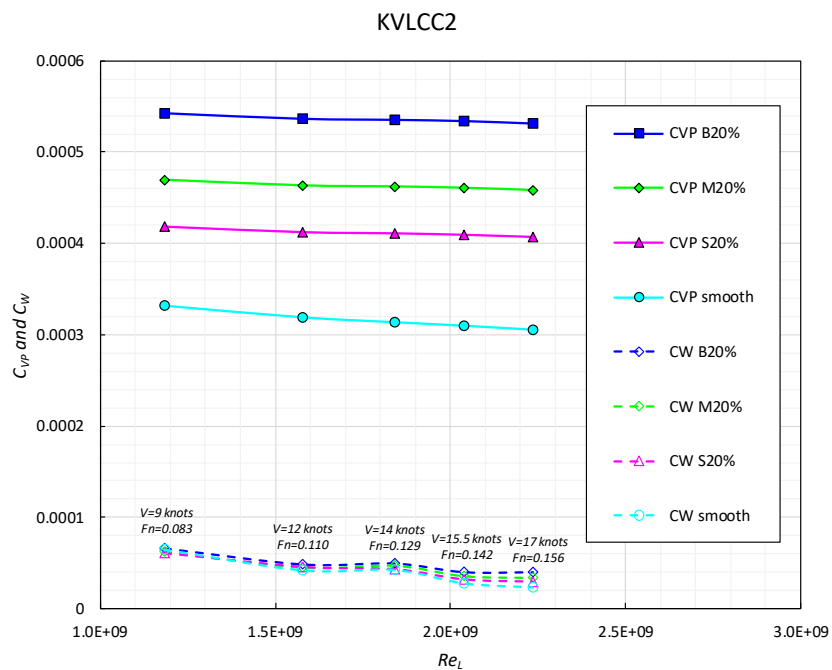


Figure 10.17 C_{VP} and C_W of KVLCC2 with different hull conditions

10.3.4. Roughness effect on the flow field

10.3.4.1. Velocity field

Figures 10.19 and 10.20 show the axial velocity contours around the KCS and KVLCC2 hulls, respectively, in different scales with the smooth surface conditions and the most severe fouling conditions (B20%). The mean axial velocity was normalised by dividing the velocity with the advance speed of the ship (V_x/V_{ship}). As shown in the figures, for both the hull forms at the respective scales, the roughness effect brings significant changes in the velocity field around the hulls. As expected, the smaller sizes with fouling showed larger wake regions due to the decelerated flow velocity at the stern. The roughness effect on the wake field can be more clearly seen in Figure 10.21, which compares the axial velocity contours behind the hull on the propeller plane ($x = 0.0175L_{pp}$).

In order to quantify the increases in the stern wake, the nominal wake fractions, w_n , were calculated by surface averaging the local wake fraction, $w'_x = (V_{ship} - V_x)/V_{ship}$, on the propeller disk (i.e. the disk where the propeller will be located). Figures 10.21 and 10.22 compare the w_n of the KCS and KVLCC2, respectively, with the smooth and most severe fouling conditions (B20%). The inner and outer circles represent the hub diameter and propeller diameter. For both the hull forms, the hull fouling resulted in significant increases in the w_n values. The percentage increases in the w_n of KCS due to the hull fouling at the model, moderate and the full-scale are 53%, 54%, and 45%, while those for the KVLCC2 case are 35%, 43%, and 43%.

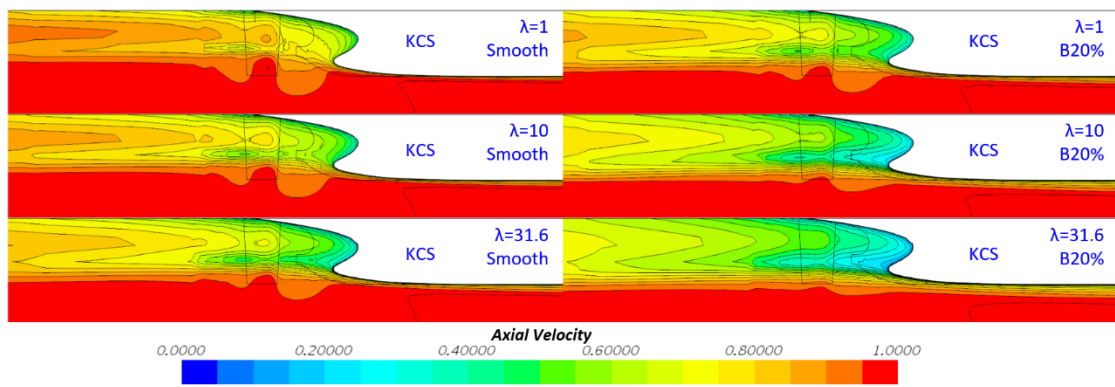


Figure 10.18 Axial velocity (V_x/V_{ship}) around KCS hulls in different scales with smooth and B20% surface conditions (on $y = 0.006L_{pp}$ plane)

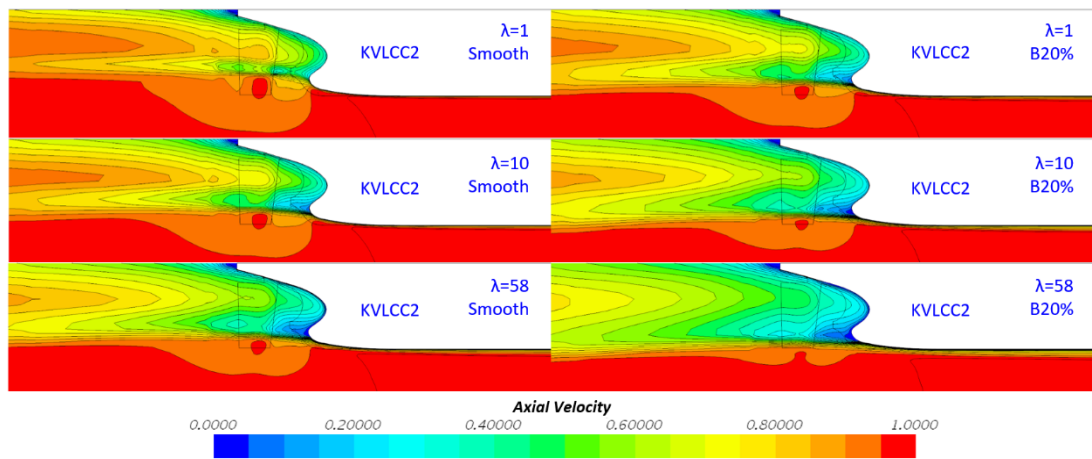


Figure 10.19 Axial velocity (V_x/V_{ship}) around KVLCC2 hulls in different scales with smooth and B20% surface conditions (on $y = 0.006L_{pp}$ plane)

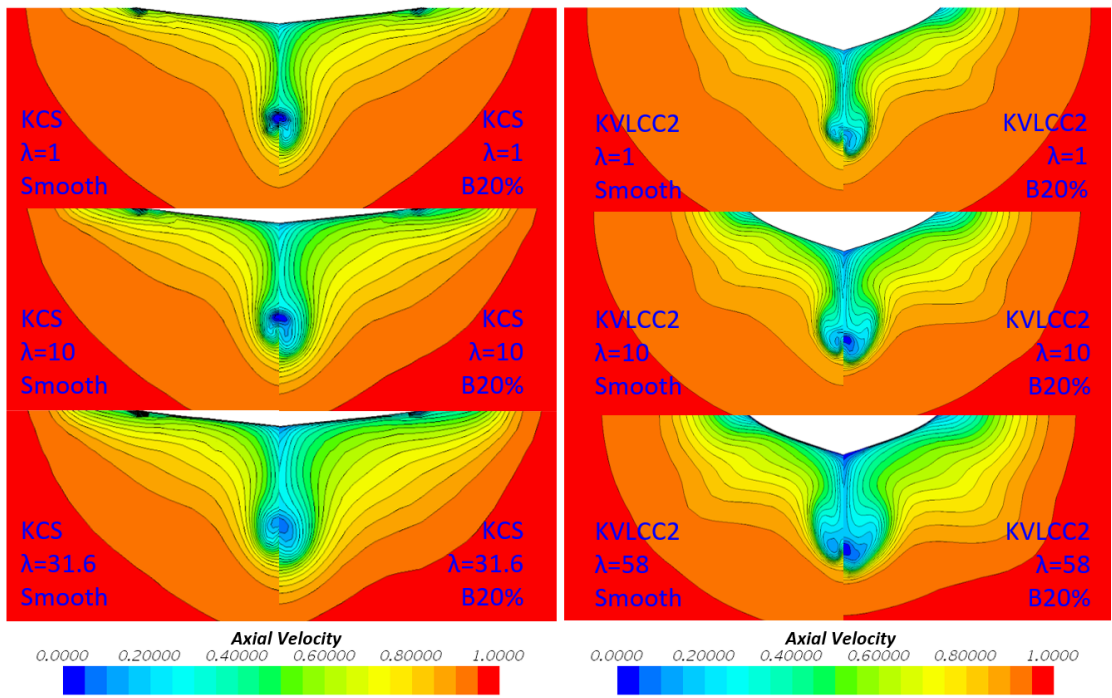


Figure 10.20 Axial velocity (V_x/V_{ship}) behind KCS (left) and KVLCC2 (right) in different scales with smooth and B20% surface conditions (on $x = 0.0175L_{pp}$ plane)

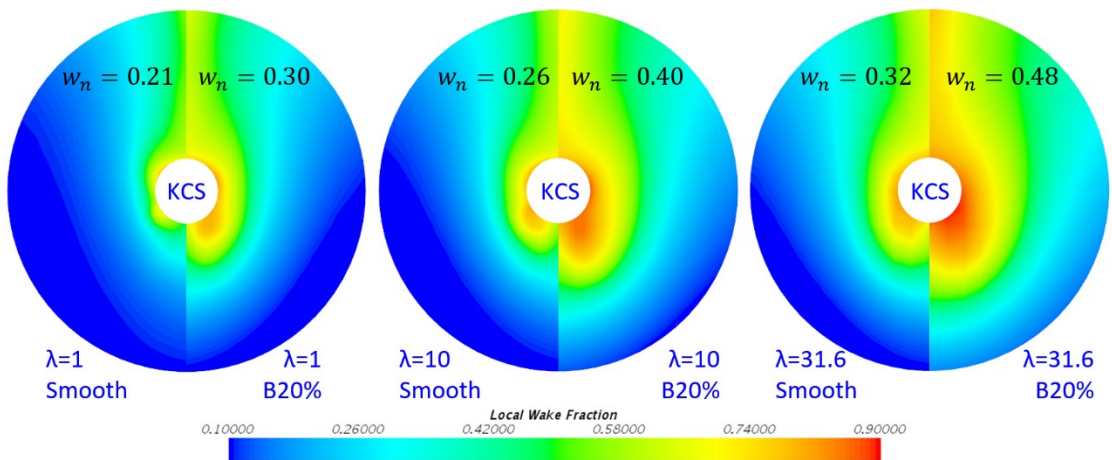


Figure 10.21 Local wake fraction, w_n' , at the propeller plane of KCS in different scales with smooth and B20% surface conditions

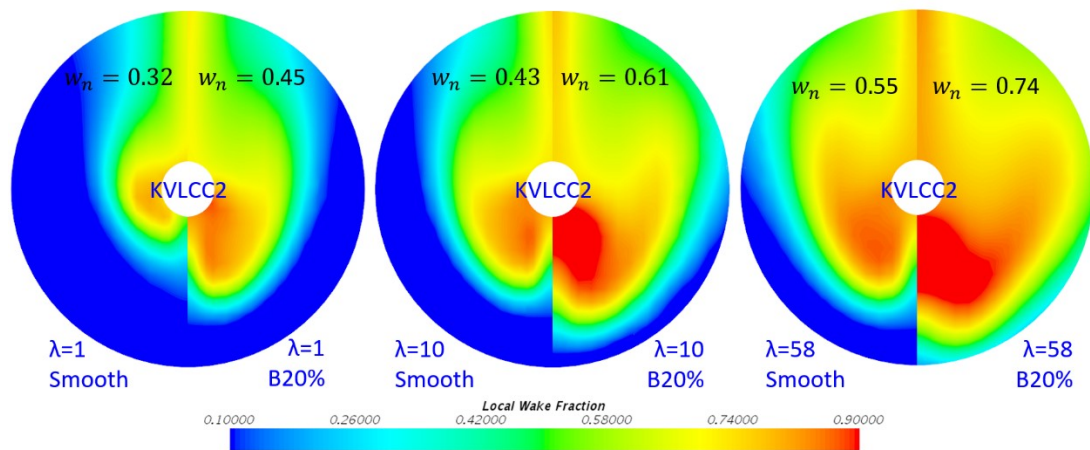


Figure 10.22 Local wake fraction, w_x' , at the propeller plane of KVLCC2 in different scales with smooth and B20% surface conditions

10.3.4.2. Boundary layer thickness

Another notable feature of the fouling effect observed in Figure 10.18 and 10.19 is the increase in the boundary layer thickness, especially on the hull bottom as well as on the aft end region. The increases in the boundary layer thicknesses can be seen more clearly in Figure 10.23 and 10.24 where the boundary layers are represented by the axial velocity contours limited to $V_x/V_{ship} = 0.9$. The figures vividly show the increases in the boundary layer thickness due to the hull fouling (B20%) for both the ships at all the scales. These arguments in the boundary layer thickness with the presence of hull fouling reflect on to the frictional and viscous pressure resistance as discussed earlier.

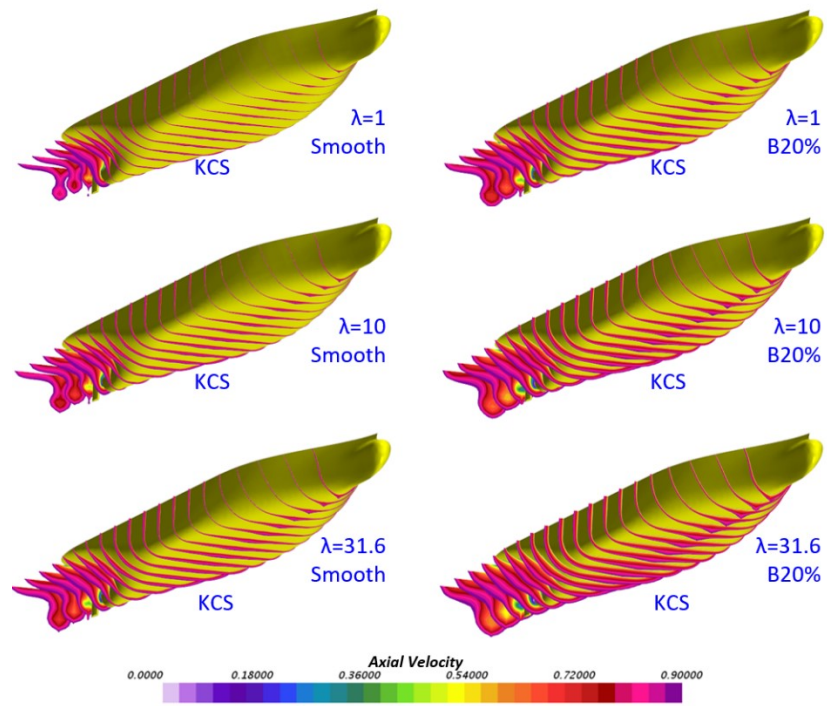


Figure 10.23 Boundary layer represented by slices limited to axial velocity ($V_x/V_{ship} = 0.9$) around KCS hulls in different scales with smooth and B20% surface conditions

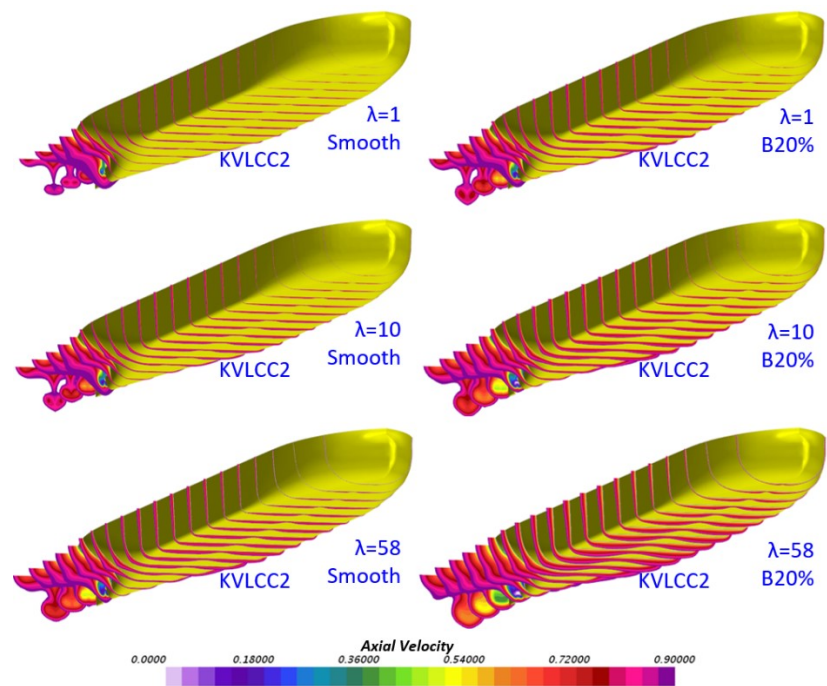


Figure 10.24 Boundary layer represented by slices limited to axial velocity ($V_x/V_{ship} = 0.9$) around KVLCC2 hulls in different scales with smooth and B20% surface conditions

10.3.4.3. Pressure field

Figure 10.25 and 10.26 illustrate the surface pressure distribution on the stern region of KCS and KVLCC2, respectively, in both the smooth and fouled (B20%) conditions. The pressure was normalised by dividing it by the dynamic pressure ($1/2\rho V_{ship}^2$). For both the ship types in all the scales, reduced pressure magnitudes at the stern were observed with the presence of surface fouling, i.e. reduced pressure recovery. Correspondingly, the decreased stern pressures bring increased viscous pressure resistances as shown in Figure 10.16 and 10.17.

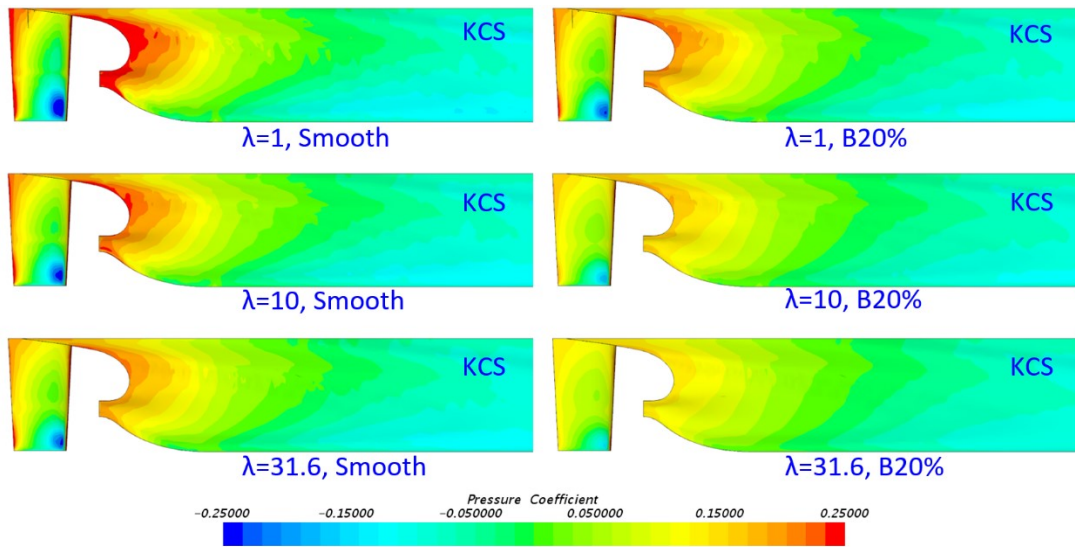


Figure 10.25 Pressure coefficient on stern region of KCS in different scales with smooth and B20% surface conditions

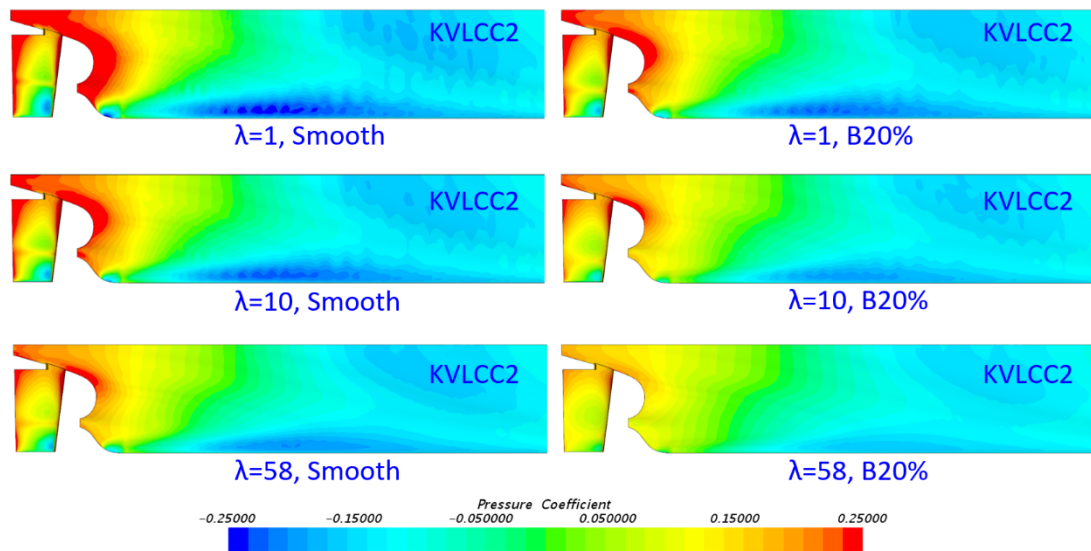


Figure 10.26 Pressure coefficient on stern region of KVLCC2 in different scales with smooth and B20% surface conditions

10.3.4.4. Wave elevation

Figure 10.27 compares the Kelvin wave around the KCS hull with and without the surface fouling at low and high speeds. While considerable differences were observed between the smooth and fouled (B20%) hulls at the high speed ($Fn = 0.282$), almost no effects were noted at the low speed ($Fn = 0.13$). These speed dependant effects of the roughness on the wave elevations are in agreement with those on the wave-making resistance, C_W , of KCS as shown in Figure 16, where the effect was negligible at the low speed whereas the effect becomes substantial as the speed increases.

Likewise, as shown in Figure 10.28, the roughness effect on the Kelvin wave around the KVLCC2 showed correspondences with the roughness effect on the C_W values, also shown in Figure 10.17. For both the low and high speeds, the free surface elevations around the KVLCC2 hull showed almost no differences regardless of the presence of hull fouling.

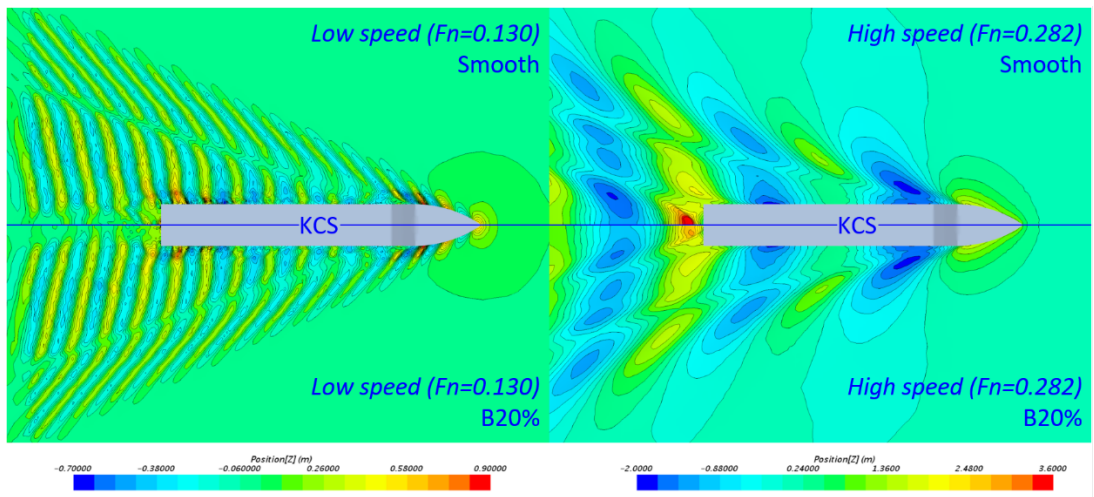


Figure 10.27 Kelvin wave pattern around KCS hulls at low and high speeds with smooth (upper) and B20% (lower) surface conditions

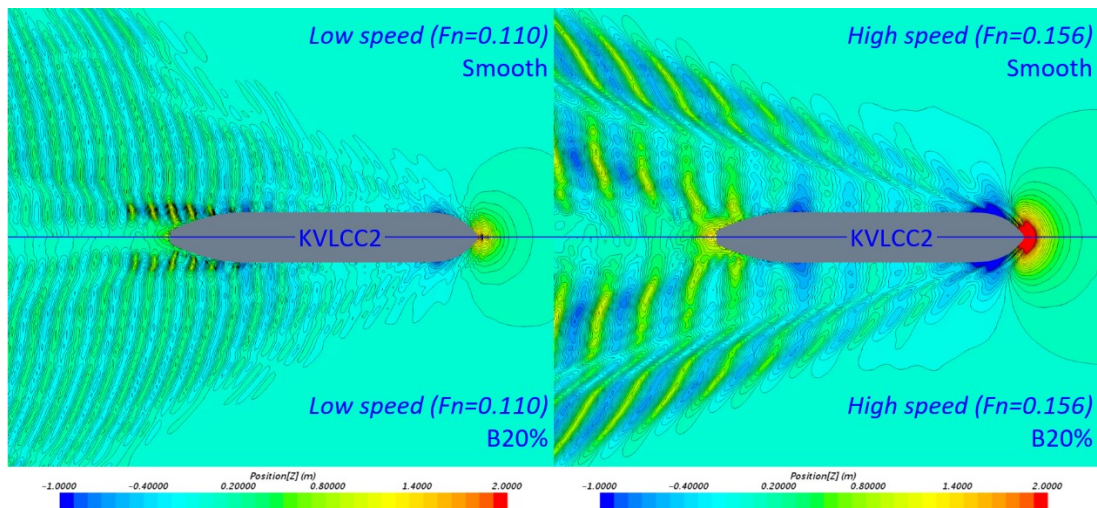


Figure 10.28 Kelvin wave pattern around KCS hulls at low and high speeds with smooth (upper) and B20% (lower) surface conditions

10.4. Chapter summary and conclusions

In the study presented here, URANS based CFD simulation models of two different types of hulls and sizes were developed to investigate the effect of the ship type and scales on the towed resistance of these ships in the presence of fouling. The CFD simulations were performed using the benchmark ship hulls of a container ship (KCS) and a tanker (KVLCC2). For the representation of the roughness effect due to hull fouling, the modified wall-function approach was used with the roughness function of barnacles.

Spatial and temporal convergence studies were performed using the Grid convergence Index (GCI) method, to estimate the numerical uncertainties of the proposed CFD models and to determine sufficient grid-spacings and time steps.

By using two different computational domain types (i.e. double-body and free-surface) the ship resistance was decomposed into individual components. The results showed that the hull fouling causes significant increases in the frictional resistance and the viscous resistance regardless of the hull forms, scales and speeds. On the other hand, the form factors of KVLCC2 showed a different trend at each scale, while those of KCS consistently showed decreases with hull fouling. Differences between the two hull forms were also found in the roughness effect on the wave making resistance. The wave making resistance of KVLCC2 showed almost no differences regardless of the presence of the hull fouling. On the other side, KCS showed considerable roughness effects on the wave making resistance at the high speed, while the effect was negligible at the low speed. Finally, the effect of hull fouling on the flow characteristics around the hulls was examined, including the velocity field, wake field, boundary layer thickness, pressure distribution on the hull and Kelvin wave.

This study provided several important findings such as the different features of the roughness effect for different hull forms, ship size and speeds. However, to establish a more comprehensive understanding of the correlations of the roughness effect with various factors such as block coefficient, Froude number, etc., this study should be further extended with sufficient variations of hull forms, scales and speeds.

11. Conclusions and discussions

11.1. Introduction

This chapter presents a comprehensive summary of the work performed within this PhD thesis. Section 11.2 details the achievement of the aim and objectives, addressing each specific objective and the corresponding chapter where the objective is achieved. The main conclusions are discussed in Section 11.3, while the novelties and contributions to the field are defined in Section 11.4. General discussions are given in Section 11.5, and finally, the recommendations for future works are made in Section 11.6.

11.2. Achievement of research aim and objectives

As discussed in Chapter 1, the aim of this PhD study is '*To develop computational and experimental techniques to investigate the effect of biofouling on ship hydrodynamic performances*' and this aim was achieved by performing novel studies and realising the specific objectives.

The specific objectives of the PhD study and the corresponding chapters where the objectives are realised are listed below:

- Objective 1: To conduct a literature survey to review the state-of-the-art literature and the background knowledge in the field of the effect of hull and propeller fouling on ship hydrodynamic performance.

Objective 1 was achieved in Chapter 2 by conducting an extensive critical review on the relevant subjects of this PhD thesis, including a brief review on the marine biofouling, historic and modern antifouling methods, the impact of biofouling on ship

performance, general information of the background theories, and the current state-of-the-art studies to predict the effect of biofouling on ship performance.

- Objective 2: To perform an experimental study using a towed flat plate and a ship model in smooth and rough surface conditions, to investigate the effect of hull roughness on ship resistance and to validate the similarity law scaling of Granville (1958; 1978).

Objective 2 was achieved in Chapter 4, by performing tank testing of a flat plate and a ship model in smooth and rough surface conditions. The roughness functions of the rough surface (sand-grain) were determined from the flat plate towing tests. Using the obtained roughness functions, the frictional resistance was extrapolated to the length of the ship model following the similarity law scaling of Granville (1958; 1978). The total resistance of the ship model with the rough surface was predicted based on the extrapolated results, by using two different methods based on Froude's and Hughes' approaches. The predicted results agreed well with the towing test of the rough ship model and hence the validity of Granville's method was demonstrated.

- Objective 3: To develop a CFD model to predict the effect of hull roughness on ship resistance and to perform a validation study by comparing the CFD prediction with the experimental result obtained from the ship model towing test.

Objective 3 was achieved in Chapter 5, by developing CFD models to simulate the towing tests conducted in Chapter 4. The flat plate and the ship model were modelled in CFD with the smooth and rough surface conditions. For modelling the roughness effect in the simulations, the roughness function of the sand-grain surface was employed in the wall-function of the CFD models (i.e. modified wall-function approach). The simulation results showed a good agreement with the experimental data, which supports the validity of the CFD method.

- Objective 4: To develop a CFD model of a full-scale towed ship to investigate the effect of biofouling on the resistance components and other hydrodynamic characteristics.
- Objective 5: To develop a CFD model of a full-scale marine propeller to investigate the effect of propeller fouling on the propeller performance in open water.
- Objective 6: To develop a CFD model of a full-scale self-propelled ship to investigate the effect of hull and/or propeller fouling on ship self-propulsion characteristics.

Objective 4, 5 and 6 were achieved in Chapter 6, 7, and 8, respectively, by performing full-scale CFD simulations of a towed-ship, a marine propeller and a self-propelled ship. In order to simulate the roughness effect due to the barnacle fouling, the roughness function of Demirel et al. (2017a) was used with the modified wall-function approach. First, the use of the modified wall-function approach for barnacle fouling was validated against the experimental data of Demirel et al. (2017a) and the approach was applied to the full-scale ship hydrodynamic problems: In Chapter 5, full-scale resistance simulations of KCS were performed to investigate the effect of hull fouling on the ship resistance components, form factor, wake fraction as well as the flow characteristics around the hull. In Chapter 7, full-scale simulations of the KP505 propeller in open water were performed to investigate the effect of propeller fouling on the propeller performances in open water. In Chapter 8, full-scale simulations of the self-propelled KCS were performed with various configurations of hull and/or propeller fouling to investigate the effect of hull and propeller fouling on the ship self-propulsion performance.

- Objective 7: To perform an experimental study using a ship model with heterogeneous hull roughness to investigate the effect of heterogeneous hull

roughness on ship resistance and propose a new prediction method for heterogeneous hull fouling.

Objective 7 was achieved in Chapter 9, by performing tank testing of a Wigley hull model. The ship model was coated with the sand-grain for different hull conditions such as smooth, $\frac{1}{4}$ -bow-rough, $\frac{1}{4}$ -aft-rough, $\frac{1}{2}$ -bow-rough, $\frac{1}{2}$ -aft-rough, and full-rough conditions. The bow-rough conditions showed larger added resistance compared to the aft-rough conditions. Also, a new prediction method was proposed to predict the added resistance due to the heterogeneous hull roughness based on Granville's similarity law scaling and the predictions showed good agreement with the experimental results.

- Objective 8: To perform CFD simulations of different hull forms in different scales and speeds to investigate the effect of hull fouling on different ships.

Objective 8 was achieved in Chapter 10 by performing CFD simulations of different ships. Two different hull forms (KCS and KVLCC2) were modelled in different scales. The same modified wall-function approach was applied to simulate the roughness effect of barnacles on the hull, as used in Chapter 6-8. From the simulations, the effects of hull fouling on the ship hydrodynamic characteristics were examined for different ships, scales and speeds. The rationale for the differences were discussed.

11.3. Main conclusions

The main conclusions drawn from this thesis are listed below:

- From the experimental study in Chapter 4, it was concluded that Granville's similarity law scaling can reasonably predict the added resistance due to the hull roughness. However, the prediction is more accurate when the roughness effect on the viscous pressure resistance is considered together, by using the form factor of the ship.
- From the numerical study in Chapter 5, it was concluded that the CFD method, which involves a modified wall-function, can accurately predict not only the roughness effect on the skin friction but also the total resistance of a 3D hull, which involves the pressure-related resistance components.
- From the numerical study in Chapter 6, it was concluded that the hull fouling significantly increases the frictional resistance of the full-scale KCS, while the residuary resistance can increase or decrease depending on the dominance of the wave-making resistance and the viscous pressure resistance at different speeds. The effects of biofouling on the individual resistance components showed strong correlations with the flow characteristics around the hull.
- From the numerical study in Chapter 7, it was concluded that propeller fouling decreases the thrust coefficient of the full-scale KP505 propeller while the torque coefficient increases. This leads to a significant loss in the propeller open water efficiency. Also, the results showed that the CFD method is

superior over other methods in terms of predicting the fouling effect on the pressure field around the propeller.

- Thanks to the superiority of the CFD method for predicting the roughness effect on the flow field around the propeller, this method could be also used for self-propulsion simulations with hull and propeller fouling. From the numerical study in Chapter 8, it was concluded that the hull and propeller fouling significantly increases the required delivered power of the full-scale KCS for a constant speed. The power penalty prediction based on the towed ship resistance and propeller open water efficiency showed a reasonable agreement with the direct predictions from the self-propulsion simulations, despite its significantly low computational cost compared to the self-propulsion simulations.
- From the experimental study in Chapter 9, it is concluded that the heterogeneous distribution of the hull roughness results in different added resistance. The hull roughness at the bow results in more added resistance than the roughness at the aft part. Additionally, the newly proposed prediction method, which considers the proportions of the wetted surface areas of the individual rough regions, showed reasonable predictions of the added resistance due to the heterogeneous hull roughness.
- From the numerical study in Chapter 10, it was concluded that hull fouling causes significant increases in the frictional resistance and the viscous pressure resistance regardless of the hull forms, scales and speeds. However, the

roughness effect on the wave-making resistance and the form factor can differ by the hull form and the ship speed.

11.4. Novelties and contributions

Several novelties have been introduced within this PhD study and useful contributions have been made to the state-of-the-art.

The main novelties achieved within this PhD study are given as follows:

- To the best of the author's knowledge, this is the first time that Granville's similarity law scaling is validated against tank testing of a 3D ship model. This work also provides the first experimental evidence of the roughness effect on the viscous pressure resistance.
- To the best of the author's knowledge, this is the first time that the CFD approach (i.e. modified wall-function approach) is validated against tank testing of a 3D ship model .

Following contributions were made to the field within this PhD study, to the best of the author's knowledge:

- In Chapter 6, the CFD method was extended not only to cover the fouling effect on ship resistance components, but also the other ship hydrodynamic characteristics including the form factor and nominal wake fraction. Therefore, this can form an important basis for improved understanding of the fouling effect on ship resistance and powering.
- Chapter 7 presents the first-ever CFD simulations were conducted to predict the fouling effect on the full-scale propeller performance. The open water coefficients with fouling conditions can be used to predict the power penalty due to hull fouling.
- Chapter 8 is the first CFD study examining the effect of hull and/or propeller fouling on the full-scale ship self-propulsion performance. The findings of the roughness effect on the self-propulsion efficiencies can be useful to assess the delivered power of ships in service.
- Chapter 9 presents the first-ever experimental study investigating the effect of heterogeneous distributions of hull roughness on ship resistance. The finding of the different added resistance depending on the roughness locations can be useful to increase the understanding of the roughness effect on ship resistance.

- A new prediction method was developed in Chapter 9 based on Granville's method, to predict the added resistance due to heterogeneous hull roughness.
- Chapter 10 presents the first-ever investigation of the different fouling effect on different ship types. The result showed that the roughness effect can differ by the hull forms, scales and speeds. It suggests that the roughness effect on ship resistance cannot be generalised and therefore the research should be continued over different vessels.

11.5. General discussion

This work was built on two different approaches: experiments involved with ship model towing tests and the CFD methods for modelling the roughness effects on ship hydrodynamics. The main results of these studies were summarised and discussed in detail in the previous sections.

In Chapter 4, it was experimentally shown that the hull roughness not only affects the frictional resistance but also the viscous pressure resistance. Therefore, a better prediction was achieved when the roughness effect on the viscous pressure resistance is considered together. In order to take into account this effect, a constant form factor value, $1 + k$, of the smooth KCS hull was used. However, the simulations in Chapter 5, 6, and 10 show conflicting results which suggest that the $1 + k$ values are also affected by the hull roughness. Unfortunately, Prohaska's method cannot be used, in this case, to determine the $1 + k$ values of the rough ship model, because this method involves towing tests of the model at low Froude numbers (i.e. $Fn < 0.2$). At these low speeds, the roughness effect will be very small due to the small roughness Reynolds numbers, k^+ (or there might be even no roughness effect if it falls into the 'hydraulically smooth regime'). It is likely that there exists no effective method of

determining the $1 + k$ value of a rough hull experimentally, and therefore, the transition to CFD is inevitable for detailed analyses of the roughness effect on individual ship resistance components.

Another issue raised during the ship model towing tests in Chapter 4 and 9 was the changes in the model weight due to the applied sand-grit on the hull, which can bring additional uncertainties. In order to verify this issue, the weights of the models were measured before and after the application of sand-grit. Despite the additional weights of the sand-grit (i.e. about 2.4 kg for the Wigley hull in Chapter 9), no visible differences were observed in the waterline depths of the ship models (i.e. draft of the models). This can be attributed to the cancelling effect between the additional weight and the additional buoyancy of the sand-grit on the surface. Therefore, the associated uncertainties were assumed to be neglectable.

It was shown in Chapter 6-8, and 10 that CFD simulations can be effectively used to predict the effect of biofouling on ship hydrodynamic performances. However, some technical difficulties were experienced while running the CFD simulations. The most challenging issue was the instability of the simulations when the modified wall-function is applied, especially at the initial stage of the simulations. This issue was not consistent for different surface conditions, and therefore, different solutions were used after several trials and errors. The most effective solution was initialising the simulations with a smooth surface condition and changing the boundary condition to a rough surface after the simulation settles down. However, some simulations diverged due to the sudden change in the boundary condition, and it was mitigated by using gradually increasing roughness heights in the simulations.

In Chapter 7, it was shown that the propeller fouling reduces the strengths of the tip and hub vortices of the propeller, and it was attributed to the roughness effect in the pressure field around the propeller. This finding suggests a possible benefit of the roughness effect for resolving problems associated with the propeller vortices, such as propeller cavitation and radiation noise. For example, an adequate application of roughness on the propeller tip and hub may result in a remarkable improvement of

radiation noise with a small loss of the propeller performance, which can be beneficial for certain types of vessels (e.g. submarines).

An important point to note in Chapter 8 is the increased propulsive efficiency, η_D , with the presence of hull fouling. This was attributed to the increased hull efficiency, η_H , as a result of the increased stern wake. However, it should be borne in mind that this does not necessarily mean that the energy efficiency is improved with the hull fouling. It only means, the ‘ratio’ between the effective power and the delivered power (i.e. $\eta_D = P_E/P_D$) is increased with the hull fouling. In other words, the fouling impact on P_E is more dramatic than that on P_D . As evidence of this, all the *fouled-hull* cases in Chapter 8 showed significant increases in the delivered power, which means the energy efficiency of the ship has dropped significantly due to the hull fouling.

11.6. Recommendations for future research

- This thesis includes the validations of the similarity law scaling and the CFD method for predictions of the roughness effect on ship resistance against tank testing of a ship model. These studies are useful as they provide experimental support for these prediction methods. However, these validations should be extended to demonstrate the validity of these predictions for full-scale ships. Therefore, it is recommended to conduct studies comparing the predictions against full-scale ship measurements.
- Although the CFD method is validated against the ship model towing test, it is not validated for marine propellers. Therefore, a piece of future work might be to conduct an open water test using a roughened model propeller for validation of the CFD method.

- The full-scale CFD predictions in Chapter 6, 7, 8, and 10 were made using uniformly distributed hull fouling conditions (i.e. homogeneous hull roughness), while the real ships' surfaces are not uniform as discussed in Chapter 9. Therefore, it is recommended to extend the CFD studies to include heterogeneous hull roughness conditions for more realistic predictions.
- The newly proposed method in Chapter 9 does not consider the effect of the roughness location while it considers the wetted surface areas of the different roughness regions. For this reason, discrepancies were observed between the predictions and the experimental results. Therefore, it is recommended to develop a new prediction method that can consider the effect of the locations of the different roughness regions, based on the similarity law scaling.

11.7. Research outputs

The following publications were generated throughout the timespan of the PhD study.

- **Journal Papers (SCI/ SCI Expanded):**

1. **Song, S.**, Demirel, Y. K., & Atlar, M. (2019). An investigation into the effect of biofouling on the ship hydrodynamic characteristics using CFD. *Ocean Engineering*, 175, 122-137. doi:<https://doi.org/10.1016/j.oceaneng.2019.01.056>
2. Demirel, Y. K., **Song, S.**, Turan, O., & Incecik, A. (2019). Practical added resistance diagrams to predict fouling impact on ship performance. *Ocean Engineering*, 186, 106112. doi:<https://doi.org/10.1016/j.oceaneng.2019.106112>
3. **Song, S.**, Kim, S.H, & Paik, K.J. (2019). Determination of linear and nonlinear roll damping coefficients of a ship section using CFD. *Brodogradnja*, 70 (4). doi:<https://doi.org/10.21278/brod70402>
4. **Song, S.**, Demirel, Y. K., & Atlar, M. (2020). Penalty of hull and propeller fouling on ship self-propulsion performance. *Applied Ocean Research*, 94, 102006. doi:<https://doi.org/10.1016/j.apor.2019.102006>
5. **Song, S.**, Demirel, Y. K., Atlar, M., Dai, S., Day, S., & Turan, O. (2020). Validation of the CFD approach for modelling roughness effect on ship resistance. *Ocean Engineering*, 200, 107029. doi:<https://doi.org/10.1016/j.oceaneng.2020.107029>
6. **Song, S.**, Demirel, Y. K., & Atlar, M. (2020). Propeller performance penalty of biofouling: CFD Prediction. *Journal of Offshore Mechanics and Arctic Engineering*, 142(6). doi: <https://doi.org/10.1115/1.4047201>

7. Farkas, A., **Song, S.**, Degiuli, N., Martić, I., & Demirel, Y. K. (2020). Impact of biofilm on the ship propulsion characteristics and the speed reduction. *Ocean Engineering*, 199, 107033. doi:<https://doi.org/10.1016/j.oceaneng.2020.107033>
8. Dogrul, A., **Song, S.** & Demirel, Y. K. (2020). Scale effect on ship resistance components and form factor. *Ocean Engineering*. 209, 107428. doi:<https://doi.org/10.1016/j.oceaneng.2020.107428>
9. **Song, S.**, Demirel, Y. K., Atlar, M. & Shi, W. (2020). Prediction of the fouling penalty on the tidal turbine performance and development of its mitigation measures. *Applied Energy*. 276, 115498. doi:<https://doi.org/10.1016/j.apenergy.2020.115498>
10. **Song, S.**, Dai, S., Demirel, Y. K., Atlar, M., Day, S., & Turan, O. (2020). Experimental and theoretical study of the effect of hull roughness on ship resistance. *Journal of Ship Research*. (accepted/in press)
11. **Song, S.**, Demirel, Y. K., Muscat-Fenech, CM., Atlar, M. (2020). Fouling effect on the resistance of different ship types. *Ocean Engineering* (accepted/in press)

- **Conference papers:**

1. **Song, S.**, Demirel, Y. K., & Atlar, M. (2019). An Investigation Into the Effect of Biofouling on Full-Scale Propeller Performance Using CFD. Paper presented at the ASME 2019 38th International Conference on Ocean, Offshore and Arctic Engineering, Glasgow, UK. <https://doi.org/10.1115/OMAE2019-95315>
2. Marino, A., Ilter, Y. K., **Song, S.**, Shi, W., Atlar, M., & Demirel, Y. K. (2019). Design Specification, Commission and Calibration of the University of Strathclyde's Fully Turbulent Flow Channel (FTFC) Facility. Paper presented at

the The Sixth International Conference on Advanced Model Measurement Technology for The Maritime Industry (AMT'19), Rome, Italy.

3. Ravenna, R., Marino, A., **Song, S.**, Demirel, Y. K., Atlar, M., & Turan, O. (2019). Experimental Investigation on the Effect of Biomimetic Tubercles on the Hydrodynamics of a Flat Plate. Paper presented at the The Sixth International Conference on Advanced Model Measurement Technology for The Maritime Industry (AMT'19), Rome, Italy.

References

- Acharya, M., Bornstein, J., & Escudier, M. P. (1986). Turbulent boundary layers on rough surfaces. *Experiments in Fluids*, 4(1), 33-47. doi:10.1007/BF00316784
- Alzieu, C. L., Sanjuan, J., Deltreil, J. P., & Borel, M. (1986). Tin contamination in Arcachon Bay: Effects on oyster shell anomalies. *Marine Pollution Bulletin*, 17(11), 494-498. doi:https://doi.org/10.1016/0025-326X(86)90636-3
- Andersson, J., Oliveira, D. R., Yeginbayeva, I., Leer-Andersen, M., & Bensow, R. E. (2020). Review and comparison of methods to model ship hull roughness. *Applied Ocean Research*, 99, 102119. doi:https://doi.org/10.1016/j.apor.2020.102119
- Andrewartha, J., Perkins, K., Sargison, J., Osborn, J., Walker, G., Henderson, A., & Hallegraeff, G. (2010). Drag force and surface roughness measurements on freshwater biofouled surfaces. *Biofouling*, 26, 487-496.
- Antonia, R. A., & Krogstad, P. Å. (2001). Turbulence structure in boundary layers over different types of surface roughness. *Fluid Dynamics Research*, 28(2), 139-157. doi:https://doi.org/10.1016/S0169-5983(00)00025-3
- Atlar, M. (2008). An update on marine antifouling. Paper presented at the 25th ITTC Group Discussions 3- Global Warming and Impact on ITTC Activities, Fukuoka.
- Atlar, M., Bashir, M., Turkmen, S., Yeginbayeva, I., Carchen, A. and Politis, G. (2015). Design, Manufacture and Operation of a Strut System Deployed on a Research Catamaran to Collect Samples of Dynamically Grown Biofilms In-Service. Paper presented at the Proceedings of the 4th International Conference on
- Advanced Model Measurement Technology for Maritime Industry (AMT'15), Istanbul, Turkey.
- Atlar, M., Glover, E. J., Candries, M., Mutton, R. J., & Anderson, C. D. (2002). The effect of a foul release coating on propeller performance. Paper presented at the Marine Science and Technology for Environmental Sustainability, Newcastle upon Tyne, UK.
- Atlar, M., Yeginbayeva, I. A., Turkmen, S., Demirel, Y. K., Carchen, A., Marino, A., & Williams, D. (2018). A Rational Approach to Predicting the Effect of Fouling Control Systems on "In-Service" Ship Performance. *GMO SHIPMAR*, 24(213), 5-36.
- Bandyopadhyay, P. R. (1987). Rough-wall turbulent boundary layers in the transition regime. *Journal of Fluid Mechanics*, 180, 231-266. doi:10.1017/S0022112087001794

Bengough, G. D., & Shephard, V. G. (1943). The corrosion and fouling of ships. Paper presented at the The Marin Corrosion Sub-committee of the Iron and Steel Institute and the British Iron and Steel Federation.

Benson, J., Ebert, J., & Beery, T. (1938). Investigation in the NACA tank fo the effect of immersion in salt water on the resistance of plates coated with different shipbottom paints. Retrieved from

Callow, M. E. C., James E. (2002). Marine biofouling: a sticky problem.

Candries, M. (2001). Drag, boundary-layer and roughness characteristics of marine surfaces coated with antifoulings. University of Newcastle upon Tyne,

Candries, M., Atlar, M., Mesbahi, E., & Pazouki, K. (2003). The Measurement of the Drag Characteristics of Tin-free Self-polishing Co-polymers and Fouling Release Coatings Using a Rotor Apparatus (Vol. 19 Suppl).

Carrica, P. M., Castro, A. M., & Stern, F. (2010). Self-propulsion computations using a speed controller and a discretized propeller with dynamic overset grids. *Journal of Marine Science and Technology*, 15(4), 316-330. doi:10.1007/s00773-010-0098-6

Castro, A. M., Carrica, P. M., & Stern, F. (2011). Full scale self-propulsion computations using discretized propeller for the KRISO container ship KCS. *Computers & Fluids*, 51(1), 35-47. doi:https://doi.org/10.1016/j.compfluid.2011.07.005

CD-Adapco. (2017). STAR-CCM+ user guide, version 12.06.

Cebeci, T., & Bradshaw, P. (1977). *Momentum Transfer in Boundary Layer* (Vol. -1).

Celik, I. B., Ghia, U., Roache, P. J., Freitas, C. J., Coleman, H., & Raad, P. E. (2008). Procedure for Estimation and Reporting of Uncertainty Due to Discretization in CFD Applications. *Journal of Fluids Engineering*, 130(7), 078001-078001-078004. doi:10.1115/1.2960953

Chambers, L. D., Stokes, K. R., Walsh, F. C., & Wood, R. J. K. (2006). Modern approaches to marine antifouling coatings. *Surface and Coatings Technology*, 201(6), 3642-3652. doi:https://doi.org/10.1016/j.surfcoat.2006.08.129

Champ, M. A. (2003). Economic and environmental impacts on ports and harbors from the convention to ban harmful marine anti-fouling systems. *Marine Pollution Bulletin*, 46(8), 935-940. doi:https://doi.org/10.1016/S0025-326X(03)00106-1

Chen, X., Zhu, R.-c., Song, Y.-l., & Fan, J. (2019). An investigation on HOBEM in evaluating ship wave of high speed displacement ship. *Journal of Hydrodynamics*, 31(3), 531-541. doi:10.1007/s42241-018-0092-8

Clauser, F. H. (1954). Turbulent Boundary Layers in Adverse Pressure Gradients. *Journal of the Aeronautical Sciences*, 21(2), 91-108. doi:10.2514/8.2938

Coles, D. (1956). The law of the wake in the turbulent boundary layer. *Journal of Fluid Mechanics*, 1, 191-226.

Date, J. C., & Turnock, S. R. (1999). A study into the Techniques Needed to Accrately Predict Skin Friction Using RANS solvers with Validation Against Froude's Historical Flat Plate Experimental Data. Retrieved from Southampton, UK:

Demirel, Y. K. (2015). Modelling the Roughness Effects of Marine Coatings and Biofouling on Ship Frictional Resistance. (PhD), University of Strathclyde, Glasgow.

Demirel, Y. K., Khorasanchi, M., Turan, O., Incecik, A., & Schultz, M. P. (2014). A CFD model for the frictional resistance prediction of antifouling coatings. *Ocean Engineering*, 89, 21-31. doi:https://doi.org/10.1016/j.oceaneng.2014.07.017

Demirel, Y. K., Turan, O., & Incecik, A. (2017). Predicting the effect of biofouling on ship resistance using CFD. *Applied Ocean Research*, 62, 100-118. doi:https://doi.org/10.1016/j.apor.2016.12.003

Demirel, Y. K., Uzun, D., Zhang, Y., Fang, H.-C., Day, A. H., & Turan, O. (2017). Effect of barnacle fouling on ship resistance and powering. *Biofouling*, 33(10), 819-834. doi:10.1080/08927014.2017.1373279

Denny, M. E. (1951). BSRA Resistance Experiments on the Lucy Ashton: Part I: Full-scale Measurements. *Transactions of Royal Institution of Naval Architects*, 93, 21-31.

Eça, L., & Hoekstra, M. (2011). Numerical aspects of including wall roughness effects in the SST $k-\omega$ eddy-viscosity turbulence model. *Computers & Fluids*, 40(1), 299-314. doi:https://doi.org/10.1016/j.compfluid.2010.09.035

Farkas, A., Degiuli, N., & Martić, I. (2018). Towards the prediction of the effect of biofilm on the ship resistance using CFD. *Ocean Engineering*, 167, 169-186. doi:https://doi.org/10.1016/j.oceaneng.2018.08.055

Farkas, A., Degiuli, N., & Martić, I. (2019). Impact of biofilm on the resistance characteristics and nominal wake. *Proceedings of the Institution of Mechanical Engineers, Part M: Journal of Engineering for the Maritime Environment*, 1475090219862897. doi:10.1177/1475090219862897

Farkas, A., Song, S., Degiuli, N., Martić, I., & Demirel, Y. K. (2020). Impact of biofilm on the ship propulsion characteristics and the speed reduction. *Ocean Engineering*, 199, 107033. doi:<https://doi.org/10.1016/j.oceaneng.2020.107033>

Ferziger, J. H., & Peric, M. (2002). *Computational Methods for Fluid Dynamics*: Springer-Verlag Berlin Heidelberg.

Flack, K. A., & Schultz, M. P. (2010). Review of Hydraulic Roughness Scales in the Fully Rough Regime. *Journal of Fluids Engineering*, 132(4), 041203-041203-041210. doi:10.1115/1.4001492

Flack, K. A., & Schultz, M. P. (2014). Roughness effects on wall-bounded turbulent flows. *Physics of Fluids*, 26(10), 101305. doi:10.1063/1.4896280

Flack, K. A., Schultz, M. P., Barros, J. M., & Kim, Y. C. (2016). Skin-friction behavior in the transitionally-rough regime. *International Journal of Heat and Fluid Flow*, 61, 21-30. doi:<https://doi.org/10.1016/j.ijheatfluidflow.2016.05.008>

Flack, K. A., Schultz, M. P., & Shapiro, T. A. (2005). Experimental support for Townsend's Reynolds number similarity hypothesis on rough walls. *Physics of Fluids*, 17(3), 035102. doi:10.1063/1.1843135

Franzini, J. (1997). *Fluid Mechanics with Engineering Applications*: 9th edition (9 ed.). New York: McGraw-Hill.

Fujisawa, J., Ukon, Y., Kume, K., & Takeshi, H. (2000). Local Velocity Field Measurements around the KCS Model. Retrieved from Tokyo:

Gehrke, T., & Sand, W. (2003). Interactions Between Microorganisms and Physiochemical Factors Cause MIC of Steel Pilings in Harbors (ALWC). Paper presented at the CORROSION 2003, San Diego, California. <https://doi.org/>

Gibbs, P. E., & Bryan, G. W. (2009). Reproductive Failure in Populations of the Dog-Whelk, *Nucella Lapillus*, Caused by Imposex Induced by Tributyltin from Antifouling Paints. *Journal of the Marine Biological Association of the United Kingdom*, 66(4), 767-777. doi:10.1017/S0025315400048414

Granville, P. S. (1958). The frictional resistance and turbulent boundary layer of rough surfaces. *J. Ship Res.*, 2(3), 52-74.

Granville, P. S. (1978). Similarity-law characterization methods for arbitrary hydrodynamic roughnesses. Retrieved from Bethesda, MD:

Granville, P. S. (1982). Drag-Characterization Method for Arbitrarily Rough Surfaces by Means of Rotating Disks. *Journal of Fluids Engineering*, 104(3), 373-377. doi:10.1115/1.3241854

Granville, P. S. (1987). THREE INDIRECT METHODS FOR THE DRAG CHARACTERIZATION OF ARBITRARILY ROUGH SURFACES ON FLAT PLATES. *Journal of Ship Research*, 31(No.1), 8 p.

Grigson, C. (1992). Drag losses of new ships caused by hull finish. *Journal of Ship Research*, 36, 182-196.

Hama, F. R. (1954). Boundary-layer characteristics for smooth and rough surfaces, by Francis R. Hama. New York Society of Naval Architects and Marine Engineers.

Haslbeck, E. G. B. (1992). Microbial biofilm effects on drag-lab and field. Paper presented at the Ship Production Symposium Proceedings.

Hino, T. (2005 ed). Proceedings of CFD Workshop Tokyo 2005. Retrieved from

Hiraga, Y. (1934). Experimental investigations on the resistance of long planks and ships. *Zosen Kiokai*, 55, 159-199.

Holm, E., Schultz, M., Haslbeck, E., Talbott, W., & Field, A. (2004). Evaluation of Hydrodynamic Drag on Experimental Fouling-release Surfaces, using Rotating Disks. *Biofouling*, 20(4-5), 219-226. doi:10.1080/08927010400011245

Hunsucker, J. T., Hunsucker, K. Z., Gardner, H., & Swain, G. (2016). Influence of hydrodynamic stress on the frictional drag of biofouling communities. *Biofouling*, 32(10), 1209-1221. doi:10.1080/08927014.2016.1242724

Hunsucker, K. Z., Koka, A., Lund, G., & Swain, G. (2014). Diatom community structure on in-service cruise ship hulls. *Biofouling*, 30(9), 1133-1140. doi:10.1080/08927014.2014.974576

IMO. (2001). International convention on control of harmful anti-fouling systems on ships. In.

IMO. (2011). Resolution MEPC.203(62). Retrieved from

IMO. (2014). Third IMO GHG Study 2014, Executive Summary and Final Report. Retrieved from Suffolk, UK:

ITTC. (2002). Final Report and Recommendations to the 23rd ITTC. Paper presented at the 23rd ITTC.

ITTC. (2011). Specialist Committee on Surface Treatment - Final Report and Recommendations to the 26th ITTC. Retrieved from

ITTC. (2014). General guideline for uncertainty analysis in resistance tests. Retrieved from

Izaquirre-Alza, P., Perez-Rojas, L., & Nunez-Basanez, J. F. (2010). Drag reduction through special paints coated on the hull. Paper presented at the International Conference on Ship Drag Reduction SMOOTH-SHIPS, Istanbul, Turkey.

Izubuchi, T. (1934). Increase in hull resistance through shipbottom fouling. *Zosen Kiokai*, 55.

Ju, S. (1983). Study of Total and Viscous Resistance for the Wigley Parabolic Ship Form: Iowa Institute of Hydraulic Research, University of Iowa.

Karlsson, R. I. (1978). The Effect of Irregular Surface Roughness on the Frictional Resistance of Ships. Paper presented at the International Symposium on Ship Viscous Resistance, Swedish State Ship-building Experimental Tank, Goteborg.

Keirsbulck, L., Labraga, L., Mazouz, A., & Tournier, C. (2001). Surface Roughness Effects on Turbulent Boundary Layer Structures. *Journal of Fluids Engineering*, 124(1), 127-135. doi:10.1115/1.1445141

Kempf, G. (1937). On the effect of roughness on the resistance of ships. *Trans INA*, 79, 109-119.

Kim, W. J., Van, S. H., & Kim, D. H. (2001). Measurement of flows around modern commercial ship models. *Experiments in Fluids*, 31(5), 567-578. doi:10.1007/s003480100332

Kiosidou, E. D., Liarokapis, D. E., Tzabiras, G. D., & Pantelis, D. I. (2017). Experimental Investigation of Roughness Effect on Ship Resistance Using Flat Plate and Model Towing Tests. *Journal of Ship Research*, 61(2), 75-90. doi:10.5957/JOSR.61.2.160044

Korkut, E., & Mehmet, A. (2009). An Experimental Investigation of the Effect of Foul Release Coating Application on Performance, Noise and Cavitation Characteristics of Marine Propellers. Paper presented at the First International Symposium on Marine Propulsors, smp'09, Trondheim, Norway.

Krogstad, P. Å., Antonia, R. A., & Browne, L. (1992). Comparison between rough- and smooth-wall turbulent boundary layers. *Journal of Fluid Mechanics*, 245(599-617).

Krogstad, P. Å., & Antonia, R. A. (1999). Surface roughness effects in turbulent boundary layers. *Experiments in Fluids*, 27(5), 450-460. doi:10.1007/s003480050370

Kumar, N. V. k. R., & Doble, M. (2014). *Polymers in a Marine Environment: Macrofouling and Bioadhesion of Organisms on Polymers: A Smithers Group Company*.

Kunkel, G. J., & Marusic, I. (2006). Study of the near-wall-turbulent region of the high-Reynolds-number boundary layer using an atmospheric flow. *Journal of Fluid Mechanics*, 548, 375-402. doi:10.1017/S0022112005007780

Larsson, L., Stern, F., & Visonneau, M. (2013). CFD in Ship Hydrodynamics—Results of the Gothenburg 2010 Workshop. In L. Eça, E. Oñate, J. García-Espinosa, T. Kvamsdal, & P. Bergan (Eds.), *MARINE 2011, IV International Conference on Computational Methods in Marine Engineering: Selected Papers* (pp. 237-259). Dordrecht: Springer Netherlands.

Lewis, E. V. (1988). *Principles of Naval Architecture : Resistance, Propulsion and Vibration: 2*. Jersey City: The Society of Naval Architects and Marine Engineers.

Lewis, J. (1998). *Marine biofouling and its prevention on underwater surfaces* (Vol. 22).

Lewkowicz, A., & Das, D. (1986). Turbulent boundary layers on rough surface with and without a pliable overlayer: a simulation of marine fouling. *International Shipbuilding Progress*, 33, 174-186.

Lewthwaite, J., Molland, A. & Thomas, K. (1985). An investigation into the variation of ship skin frictional resistance with fouling. *Transactions of Royal Institution of Naval Architects*, 127, 269-284.

Li, C., Atlar, M., Haroutunian, M., Norman, R., & Anderson, C. (2019). An investigation into the effects of marine biofilm on the roughness and drag characteristics of surfaces coated with different sized cuprous oxide (Cu₂O) particles. *Biofouling*, 1-19. doi:10.1080/08927014.2018.1559305

Little, B. J., & Depalma, J. R. (1988). 3 - Marine Biofouling. In D. F. Hasson & C. R. Crowe (Eds.), *Treatise on Materials Science & Technology* (Vol. 28, pp. 89-119): Elsevier.

Loeb, G., Laster, D., & Gracik, T. (1984). The influence of microbial fouling films on hydrodynamic drag of rotating discs. In: J. D. Costlow, R. C. Tipper (Eds.), *Marine Biodeterioration: An Interdisciplinary Study*, 88-94.

Luo, J. Y., Issa, R. I., & Gosman, A. D. (1994). Prediction of impeller induced flows in mixing vessels using multiple frames of reference. Paper presented at the 8th European conference on mixing; INSTITUTION OF CHEMICAL ENGINEERS SYMPOSIUM SERIES, Cambridge.

Maréchal, J.-P., & Hellio, C. (2009). Challenges for the development of new non-toxic antifouling solutions. *International journal of molecular sciences*, 10(11), 4623-4637. doi:10.3390/ijms10114623

McEntee, W. (1915). Variation of frictional resistance of ships with condition of wetted surface. *Trans. Soc. Nav. Arch. Mar. Eng.*, 24, 37-42.

McEntee, W. (1916). Notes from Model Basin. *Transactions of the Society of Naval Architects and Marine Engineers*.

Menter, F. R. (1994). Two-Equation Eddy-Viscosity Turbulence Models for Engineering Applications. *AIAA Journal*, 32(8), 1598-1605.

Mizzi, K., Demirel, Y. K., Banks, C., Turan, O., Kaklis, P., & Atlar, M. (2017). Design optimisation of Propeller Boss Cap Fins for enhanced propeller performance. *Applied Ocean Research*, 62, 210-222. doi:<https://doi.org/10.1016/j.apor.2016.12.006>

Monty, J. P., Dogan, E., Hanson, R., Scardino, A. J., Ganapathisubramani, B., & Hutchins, N. (2016). An assessment of the ship drag penalty arising from light calcareous tubeworm fouling. *Biofouling*, 32(4), 451-464. doi:10.1080/08927014.2016.1148140

Morton, L. H. G., Greenway, D. L. A., Gaylarde, C. C., & Surman, S. B. (1998). Consideration of some implications of the resistance of biofilms to biocides. *International Biodeterioration & Biodegradation*, 41(3), 247-259. doi:[https://doi.org/10.1016/S0964-8305\(98\)00026-2](https://doi.org/10.1016/S0964-8305(98)00026-2)

Mosaad, M. A. A.-R. (1986). Marine propeller roughness penalties. (PhD), Newcastle University, Newcastle Upon Tyne.

Mutton, R. J., Atlar, M., & Anderson, C. D. (2005). Drag Prevention Coatings for Marine Propellers. Paper presented at the 2nd International Symposium on Seawater Drag Reduction, Busan, Korea.

Nikuradse, J. (1933). Laws of flow in rough pipes. *NACA Technical Memorandum*, 1292.

Owen, D., Demirel, Y. K., Oguz, E., Tezdogan, T., & Incecik, A. (2018). Investigating the effect of biofouling on propeller characteristics using CFD. *Ocean Engineering*. doi:<https://doi.org/10.1016/j.oceaneng.2018.01.087>

- Patel, V. C. (1998). Perspective: Flow at High Reynolds Number and Over Rough Surfaces—Achilles Heel of CFD. *Journal of Fluids Engineering*, 120(3), 434-444. doi:10.1115/1.2820682
- Perry, A., & Li, J. D. (1990). Experimental support for the attached-eddy hypothesis in zero-pressure-gradient turbulent boundary layers. *Journal of Fluid Mechanics*, 218, 405-438.
- Raupach, M. R., Antonia, R. A., & Rajagopalan, S. (1991). Rough-Wall Turbulent Boundary Layers. *Applied Mechanics Reviews*, 44(1), 1-25. doi:10.1115/1.3119492
- Redfield, A. C., Hutchins, L. W., Redfield, A. C., E. S. Deevy, J., Ayers, J. C., Turner, H. J., . . . Todd, D. (1952). Marine fouling and its prevention. Retrieved from Annapolis, Maryland:
- Reichel, M. (2009). Influence of rudder location on propulsive characteristics of a single screw container ship. Paper presented at the First International Symposium on Marine Propulsors smp'09, Trondheim, Norway.
- Richardson, L. F. (1910). The approximate arithmetical solution by finite differences of physical problems involving differential equations, with an application to the stresses in a masonry dam. *Transactions of the Royal Society of London. Series A*, 210, 307-357.
- Schetz, J. A. (1993). *Boundary Layer Analysis*: Prentice Hall.
- Schlichting, H. (2017). *Boundary-Layer Theory* (9th Ed.). Berlin Heidelberg: Springer-Verlag.
- Schoenherr, K. E. (1932). Resistance of flat surfaces moving through a fluid. *Trans SNAME*, 40, 279-313.
- Schultz, M. P. (2002). The Relationship Between Frictional Resistance and Roughness for Surfaces Smoothed by Sanding. *Journal of Fluids Engineering*, 124(2), 492-499. doi:10.1115/1.1459073
- Schultz, M. P. (2004). Frictional Resistance of Antifouling Coating Systems. *Journal of Fluids Engineering*, 126(6), 1039-1047. doi:10.1115/1.1845552
- Schultz, M. P. (2007). Effects of coating roughness and biofouling on ship resistance and powering. *Biofouling*, 23(5), 331-341. doi:10.1080/08927010701461974
- Schultz, M. P., Bendick, J. A., Holm, E. R., & Hertel, W. M. (2011). Economic impact of biofouling on a naval surface ship. *Biofouling*, 27(1), 87-98. doi:10.1080/08927014.2010.542809

Schultz, M. P., & Flack, K. A. (2003). Turbulent Boundary Layers Over Surfaces Smoothed by Sanding. *Journal of Fluids Engineering*, 125(5), 863-870. doi:10.1115/1.1598992

Schultz, M. P., & Flack, K. A. (2005). Outer layer similarity in fully rough turbulent boundary layers. *Experiments in Fluids*, 38(3), 328-340. doi:10.1007/s00348-004-0903-2

Schultz, M. P., & Flack, K. A. (2007). The rough-wall turbulent boundary layer from the hydraulically smooth to the fully rough regime. *Journal of Fluid Mechanics*, 580, 381-405. doi:10.1017/S0022112007005502

Schultz, M. P., & Flack, K. A. (2009). Turbulent boundary layers on a systematically varied rough wall. *Physics of Fluids*, 21(1), 015104. doi:10.1063/1.3059630

Schultz, M. P., & Myers, A. (2003). Comparison of three roughness function determination methods. *Experiments in Fluids*, 35(4), 372-379. doi:10.1007/s00348-003-0686-x

Schultz, M. P., & Swain, G. W. (1999). The Effect of Biofilms on Turbulent Boundary Layers. *Journal of Fluids Engineering*, 121(1), 44-51. doi:10.1115/1.2822009

Schultz, M. P., & Swain, G. W. (2000). The influence of biofilms on skin friction drag. *Biofouling*, 15(1-3), 129-139. doi:10.1080/08927010009386304

Schultz, M. P., Walker, J. M., Steppe, C. N., & Flack, K. A. (2015). Impact of diatomaceous biofilms on the frictional drag of fouling-release coatings. *Biofouling*, 31(9-10), 759-773. doi:10.1080/08927014.2015.1108407

Seo, K.-C., Atlar, M., & Goo, B. (2016). A Study on the Hydrodynamic Effect of Biofouling on Marine Propeller. *Journal of the Korean Society of Marine Environment and Safety*, 22(1), 123-128.

Seok, J., & Park, J.-C. (2020). Numerical simulation of resistance performance according to surface roughness in container ships. *International Journal of Naval Architecture and Ocean Engineering*, 12, 11-19. doi:https://doi.org/10.1016/j.ijnaoe.2019.05.003

Shapiro, T. A. (2004). The Effect of Surface Roughness on Hydrodynamic Drag and Turbulence. Retrieved from

Siemens. (2018). STAR-CCM+, user guide, version 13.06. In.

Tachie, M. F., Bergstrom, D. J., & Balachandar, R. (2000). Rough Wall Turbulent Boundary Layers in Shallow Open Channel Flow. *Journal of Fluids Engineering*, 122(3), 533-541. doi:10.1115/1.1287267

Taylor, D. W. (1943). *The speed and power of ships: a manual of marine propulsion*. Washington: U.S. G.P.O.

Terziev, M., Tezdogan, T., & Incecik, A. (2019). Application of eddy-viscosity turbulence models to problems in ship hydrodynamics. *Ships and Offshore Structures*, 1-24. doi:10.1080/17445302.2019.1661625

Terziev, M., Tezdogan, T., Oguz, E., Gourlay, T., Demirel, Y. K., & Incecik, A. (2018). Numerical investigation of the behaviour and performance of ships advancing through restricted shallow waters. *Journal of Fluids and Structures*, 76, 185-215. doi:https://doi.org/10.1016/j.jfluidstructs.2017.10.003

Tezdogan, T., & Demirel, Y. K. (2014). An overview of marine corrosion protection with a focus on cathodic protection and coatings. *Brodogradnja*, 65, 49–59.

Tezdogan, T., Demirel, Y. K., Kellett, P., Khorasanchi, M., Incecik, A., & Turan, O. (2015). Full-scale unsteady RANS CFD simulations of ship behaviour and performance in head seas due to slow steaming. *Ocean Engineering*, 97, 186-206. doi:https://doi.org/10.1016/j.oceaneng.2015.01.011

Titah-Benbouzid, H., & Benbouzid, M. (2015, 2015-09-06). *Marine Renewable Energy Converters and Biofouling: A Review on Impacts and Prevention*. Paper presented at the EWTEC 2015, Nantes, France.

Townsend, A. A. (1961). Equilibrium layers and wall turbulence. *Journal of Fluid Mechanics*, 11(1), 97-120. doi:10.1017/S0022112061000883

Townsin, R. L. (2003). The Ship Hull Fouling Penalty. *Biofouling*, 19(sup1), 9-15. doi:10.1080/0892701031000088535

Townsin, R. L., & Dey, S. (1990). The correlation of roughness drag with surface characteristics. Paper presented at the The RINA International Workshop on Marine Roughness and Drag.

TQC. (2019). *Hull Roughness Gauge*. Retrieved from <https://www.tqcsheen.com/en/product/hull-roughness-gauge-en/>

Ulman, A., Ferrario, J., Forcada, A., Seebens, H., Arvanitidis, C., Occhipinti-Ambrogi, A., & Marchini, A. (2019). Alien species spreading via biofouling on recreational vessels in the Mediterranean Sea. 56(12), 2620-2629. doi:10.1111/1365-2664.13502

Ünal, B. (2012). Effect of surface roughness on the turbulent boundary layer due to marine coatings. (PhD), Istanbul Technical University,

UNCTAD. (2017). Review of Maritime Transport. Retrieved from Geneva, Switzerland:

Uzun, D., Demirel, Y. K., Coraddu, A., & Turan, O. (2019). Time-dependent biofouling growth model for predicting the effects of biofouling on ship resistance and powering. *Ocean Engineering*, 191, 106432. doi:<https://doi.org/10.1016/j.oceaneng.2019.106432>

Uzun, D., Ozyurt, R., Demirel, Y. K., & Turan, O. (2020). Does the barnacle settlement pattern affect ship resistance and powering? *Applied Ocean Research*, 95, 102020. doi:<https://doi.org/10.1016/j.apor.2019.102020>

van Manen, J. D., & Oossanen, v. (1988). Chapter V: Resistance: The Society of Naval Architecture & Marine Engineering.

Van Rompay, B. (2012). Surface treated composites white book: Tahoka Press.

Vargas, A., & Shan, H. (2016). A Numerical Approach for Modeling Roughness for Marine Applications.

Videla, H. A. (1996). Manual of biocorrosion. Boca Raton, Florida, US: CRC Press.

von Karman, T. (1934). Skin Friction and Turbulence. *Journal of the Aeronautical Science*, 1(1).

Watanabe, S., Nagmatsu, N., Yokoo, K., & Kawakami, Y. (1969). The augmentation in frictional resistance due to slime. *J. Kansai Soc. Nav. Arc.*, 131(45-51).

White, F. M. (2011). Fluid Mechanics: McGraw Hill.